Aerodynamic Interactions on Airbus Helicopters' Compound Helicopter RACER

A thesis accepted by the Faculty of
Aerospace Engineering and Geodesy of the University of Stuttgart
in partial fulfilment of the requirements for the degree of
Doctor of Engineering Sciences (Dr.-Ing.)

by
Felix Frey
born in Backnang

Main-referee: Prof. Dr.-Ing. Ewald Krämer
Co-referee: Prof. dr. ir. Leo L. M. Veldhuis

Date of defence: 31.08.2022

Institute of Aerodynamics and Gas Dynamics
University of Stuttgart
2023

Contents

Abstract

In the course of recent years' efforts of extending helicopters' flight envelopes towards higher cruise speed, nonconventional configurations have increasingly come into focus of various manufacturers, spawning a multitude of developments with different designs. Among these, Airbus Helicopters' compound helicopter RACER is equipped with a box wing and lateral pusher rotors. In combination with the main rotor, these components are expected to be subjected to mutual interactions, which influence their individual aerodynamic performance. Consequently, understanding the interactional phenomena is also vital for the evaluation of the helicopter's overall system.

For this reason, the present thesis addresses the mutual effects of RACER's main rotor, wings, and lateral rotors under different flight conditions. In order to isolate the interactional phenomena, trimmed high-fidelity computational fluid dynamics (CFD) simulations are not only conducted on a detailed representation of the full compound helicopter but also on reduced configurations which are created by sequentially removing the respective other components of interest. By comparing the aerodynamic performance of main rotor, wings, and lateral rotors for the different computations, mutual influences can consequently be determined. These are further divided into first- and second-order effects, where the latter only manifest themselves via the respective third component.

With the help of a loose coupling between the comprehensive analysis (CA) tool HOST and the CFD solver FLOWer, realistically trimmed free-flight conditions are determined for the relevant flight states. The first of these is RACER's cruise flight at 220 kts, which is of particular interest as it represents the operating condition the compound helicopter was specifically designed for. Due to the elevated advance ratio of over 0.5 and the resulting azimuthal variation of main rotor inflow, a strong asymmetry is witnessed in unsteady Reynolds-averaged Navier–Stokes (URANS) simulations, where most of the interactional phenomena originating from or affecting the advancing side of the rotor disk are significantly stronger than on the retreating side. This does not only become manifest in characteristic influences of left wings and lateral rotor on the superjacent region's main rotor thrust, resulting in a decrease of total thrust mostly through first-order effects, but the highly loaded advancing main rotor blades vice versa also cause a stronger deflection of the subjacent flow. On the left wings, this leads to a reduction of effective angle of attack and consequently lift, whereas the small first-order gain in thrust on the left lateral rotor is prevented by the wings' presence and reverted into a net decrease due to second-order effects. Interactions between lateral rotors and wings, in contrast, show

relatively symmetrical characteristics. Here, the suction of the lateral rotors affects the specifically swept box wing design by inducing an upward deflection in the lower wings' inflow which consequently experience a lift increase. Vice versa, mostly as a result of the wing tip vortex both lateral rotors' thrust is immensely increased due to their favourable sense of rotation.

In order to account for the large regions of separated flow below the wings, RACER's hover as the second flight condition of interest is analysed by means of delayed detached-eddy simulations (DDES). It is not only that second-order effects generally play a more important role for this flight state, but that asymmetries in aerodynamic interactions are not linked to the main rotor and its thrust distribution but rather to the different operating conditions of the lateral rotors where the right-hand rotor generates reverse thrust to provide anti-torque. While this does not affect the wings' minor influence on main rotor thrust via a blocking effect of the downwash, conversely, the main rotor's generation of download on the wings, in fact, shows distinctly asymmetric second-order effects of the lateral rotors. Apart from this, the significantly lower download on the lower wings illustrates the box wing concept's effect of shading them from the downwash. The main rotor's first-order effect causes a thrust increase on both lateral rotors by inducing changes in the inflow's axial and tangential velocity components. On the left lateral rotor, however, this is reversed into a cumulative decrease of thrust by the wings' second-order deflection of the downwash, similar to cruise flight. Vice versa, despite causing characteristic differences in main rotor thrust distribution in the superjacent regions of the rotor disk, the lateral rotors have no effect on total main rotor thrust. As a result of its generation of reverse thrust, the right lateral rotor shows hardly any influence of the downstream wings' presence, whereas on its left-hand counterpart minor beneficial wing-induced first-order effects occur, which clearly resemble the interactions in cruise flight. However, these are significantly overcompensated by a strong second-order influence where the wings, in combination with the downwash, generate a reversed wing tip vortex. While, conversely, the lateral rotors' minor first-order induction of wing lift is widely limited to the latter's regions directly upstream or downstream of the rotors, second-order effects expand their influence over the whole span of the wings and mostly result in the generation of download.

Zusammenfassung

Im Rahmen der Bemühungen der letzten Jahre, die Flugenveloppe von Hubschraubern hin zu höheren Reisegeschwindigkeiten auszudehnen, rückten unkonventionelle Konfigurationen zunehmend in den Fokus vieler Hersteller, was eine Vielzahl von Entwicklungsprojekten verschiedenster Designs hervorbrachte. Als eines hiervon ist Airbus Helicopters' Compound-Hubschrauber RACER mit einem Boxwing und seitlichen Druckrotoren ausgestattet. In Kombination mit dem Hauptrotor ist davon auszugehen, dass diese Komponenten wechselseitigen Interaktionen unterliegen, die ihr jeweiliges aerodynamisches Verhalten beeinflussen. Folglich ist ein Verständnis der Interaktionsphänomene auch unerlässlich für die Bewertung des Hubschraubers als Gesamtsystem.

Aus diesem Grund befasst sich diese Arbeit mit den gegenseitigen Effekten von RACERs Hauptrotor, Flügeln und seitlichen Rotoren in verschiedenen Flugzuständen. Um die Interaktionsphänomene zu isolieren, werden getrimmte, hochaufgelöste CFD-Simulationen (computational fluid dynamics) nicht nur für ein detailliertes Abbild des kompletten Compound-Hubschraubers durchgeführt, sondern auch für reduzierte Konfigurationen, bei denen jeweils die relevanten Komponenten nicht beinhaltet sind. Durch Vergleiche des aerodynamischen Verhaltens von Hauptrotor, Flügeln und seitlichen Rotoren zwischen den verschiedenen Berechnungen können somit wechselseitige Einflüsse bestimmt werden. Diese werden weiter unterteilt in Effekte erster und zweiter Ordnung, wobei letztere sich nur mittels der jeweiligen dritten Komponente auswirken.

Mithilfe einer schwachen Kopplung zwischen dem Programm HOST zur Flugmechanikanalyse und dem CFD-Löser FLOWer werden realistisch getrimmte Freiflugbedingungen für die relevanten Flugzustände bestimmt. Der erste hiervon ist RACERs Reiseflug bei 220 kts, der von besonderem Interesse ist, da er den Betriebspunkt darstellt, für den der Compound-Hubschrauber spezifisch entworfen wurde. Durch den erhöhten Fortschrittsgrad von über 0.5 und die daraus resultierende azimuthale Schwankung der Hauptrotoranströmung ist in URANS-Simulationen (unsteady Reynolds-averaged Navier–Stokes) eine starke Asymmetrie zu beobachten, durch die die meisten der Interaktionsphänomene, die von der vorlaufenden Seite der Rotorkreisscheibe ausgehen oder diese betreffen, deutlich stärker sind als auf der rücklaufenden Seite. Dies wirkt sich nicht nur in charakteristischen Einflüssen von linken Flügeln und seitlichem Rotor auf die darüberliegenden Gebiete des Hauptrotorschubs aus, die hauptsächlich durch Effekte erster Ordnung zu einer Abnahme des Gesamtschubs führen, sondern umgekehrt auch dadurch, dass die hochbelasteten vorlaufenden Hauptrotorblätter eine stärkere Ablenkung der darunterliegenden

Strömung verursachen. An den linken Flügeln führt dies zu einer Abnahme des effektiven Anstellwinkels und folglich auch des Auftriebs, wohingegen der kleine Schubgewinn erster Ordnung am linken seitlichen Rotor durch die Anwesenheit der Flügel verhindert und mittels Effekten zweiter Ordnung in eine Nettoabnahme umgekehrt wird. Die Interaktionen zwischen seitlichen Rotoren und Flügeln weisen hingegen relativ symmetrische Charakteristika auf. Hier beeinflusst das Ansaugen der seitlichen Rotoren das Boxwing-Design mit seiner spezifischen Pfeilung dadurch, dass in der Anströmung der unteren Flügel eine Aufwärtsströmung verursacht wird, welche hierdurch einen Auftriebsanstieg erfahren. Umgekehrt wird hauptsächlich durch den Flügelspitzenwirbel der Schub beider seitlicher Rotoren aufgrund ihrer vorteilhaften Drehrichtung immens erhöht.

Um den großen Gebieten abgelöster Strömung unter den Flügeln Rechnung zu tragen, wird RACERs Schwebeflug als der zweite Betriebspunkt von Interesse mithilfe von DDES (delayed detached-eddy simulations) untersucht. Für diesen betrachteten Flugzustand spielen Effekte zweiter Ordnung im Allgemeinen eine größere Rolle. Zudem sind die Asymmetrien der aerodynamischen Interaktionen nicht mit dem Hauptrotor und seiner Schubverteilung verknüpft, sondern mit den verschiedenen Betriebspunkten der seitlichen Rotoren, von denen der rechte Rotor Gegenschub liefert, um zum Drehmomentausgleich beizutragen. Während dies den geringen Flügeleinfluss auf den Hauptrotorschub mittels einer Verblockung des Abwinds nicht beeinträchtigt, weist die Erzeugung von Flügelabtrieb durch den Hauptrotor umgekehrt tatsächlich deutlich asymmetrische Effekte zweiter Ordnung durch die seitlichen Rotoren auf. Davon abgesehen veranschaulicht der erheblich niedrigere Abtrieb der unteren Flügel das Prinzip des Boxwing-Konzepts, diese vom Abwind abzuschatten. Der Hauptrotor-Effekt erster Ordnung verursacht eine Schubzunahme auf beiden seitlichen Rotoren, indem in der Zuströmung Änderungen der axialen und tangentialen Geschwindigkeitskomponenten induziert werden. Ähnlich wie beim Reiseflug jedoch kehrt dies am linken seitlichen Rotor in zweiter Ordnung die Ablenkung des Abwinds durch die Flügel zu einer Gesamtabnahme des Schubs um. Obwohl die seitlichen Rotoren in darüberliegenden Gebieten der Rotorkreisscheibe charakteristische Veränderungen der Hauptrotorschubverteilung verursachen, haben sie umgekehrt keinen Einfluss auf den Gesamtschub des Hauptrotors. Aufgrund der Erzeugung von Gegenschub weist der rechte seitliche Rotor kaum Einflüsse der stromab liegenden Flügel auf, wohingegen auf seinem linken Gegenpart geringe positive flügelinduzierte Effekte erster Ordnung auftreten, die deutlich den Interaktionen im Reiseflug ähneln. Allerdings werden diese bei Weitem durch einen starken Effekt zweiter Ordnung überkompensiert, bei dem die Flügel in Kombination mit dem Abwind einen umgekehrten Flügelspitzenwirbel verursachen. Während umgekehrt die Erzeugung von Flügelauftrieb durch die seitlichen Rotoren weitgehend auf die Bereiche direkt stromauf oder stromab der Rotoren beschränkt ist, erweitern Effekte zweiter Ordnung diesen Einfluss auf die komplette Flügelspannweite und resultieren größtenteils in der Erzeugung von Abtrieb.

Notation

Latin letters

a	Speed of sound (m/s)
b	Wingspan (m)
c	Chord length (m)
$c_l c$	Section lift coefficient (m), $c_l c = {}^{l}/_{(\frac{1}{2}\rho_\infty v_\infty^2)}$
c_p	Pressure coefficient, $c_p = {}^{(p-p_\infty)}/_{(\frac{1}{2}\rho_\infty v_\infty^2)}$
c_{pz}	Vertical component of surface pressure coefficient, $c_{pz} = c_p n_z$
E	Specific energy (J/kg)
F	Force (N)
$\vec{F}_C$	Vector of convective fluxes
$\vec{F}_V$	Vector of viscous fluxes
I	Helicopter mass moment of inertia ($\mathrm{kg\,m^2}$)
L	Lift (N)
l	Section lift force (N/m)
M	Moment (N m)
M	Section Mach number
$M^2 c_n$	Section normal force coefficient, $M^2 c_n = {}^{n}/_{(\frac{1}{2}\rho_\infty a_\infty^2 c)}$
m	Helicopter mass (kg)
$\dot{m}$	Mass flow (kg/s)
n	Number of rotor revolutions
n	Section normal force in rotor frame (N/m)
n_{it}	Number of (inner) iterations
n_z	Vertical component of wall-normal vector
P	Power (W)
p	Static pressure (Pa)
Q	Mass flux ($\mathrm{kg/s\,m^2}$)
$\vec{Q}$	Vector of source terms
R	Rotor radius (m)
r	Radial position (m)
S	Surface ($\mathrm{m^2}$)
T	Temperature (K)
T	Thrust (N)
$\vec{v}$	Velocity vector (m/s)
v_i	Induced velocity of main rotor (m/s), $v_i = \sqrt{{}^{2T_{MR}}/_{(\rho_\infty \pi R_{MR}^2)}}$
W	Helicopter weight (N)
$\vec{W}$	Vector of conservative variables

x, y, z	Helicopter axes pointing back, right, up in pilot's view (m)
y^+	Dimensionless wall distance

Greek letters

α	Angle of attack (°)
α	Vertical flow deflection angle (°)
α	Relaxation factor
β_C	Main rotor longitudinal flapping angle (°)
η	Propulsive efficiency
η	Flap deflection angle (°)
$\eta_{0,wing}$	Wing flap collective deflection angle (°)
$\eta_{\Delta,wing}$	Wing flap differential (left-right) deflection angle (°)
$\eta_{\Delta,lwing}$	Left wing flap differential (upper-lower) deflection angle (°)
$\eta_{\Delta,rwing}$	Right wing flap differential (upper-lower) deflection angle (°)
Θ	Helicopter pitch attitude (°)
θ	Rotor control angle (°)
θ_0	Main rotor collective control (°)
θ_C	Main rotor lateral cyclic control (°)
$\theta_{0,LR}$	Lateral rotor collective control (°)
$\theta_{\Delta,LR}$	Lateral rotor differential control (°)
θ_S	Main rotor longitudinal cyclic control (°)
λ_2	Vortex criterion ($1/s^2$)
μ	Advance ratio, $\mu = {}^{v_\infty}/_{\Omega R}$
ρ	Air density (kg/m^3)
Φ	Helicopter roll attitude (°)
Ψ	Helicopter yaw attitude (°)
Ψ	Azimuth angle (°)
Ω	Control volume (m^3)
Ω	Rotor rotational frequency (1/s)
$\vec{\omega}$	Vorticity vector (1/s)

Subscripts

avg	Average
ax	Axial
eff	Effective
$elev$	Elevator
i	Iteration
ll	Left lower wing
lu	Left upper wing
res	Resulting

rl	Right lower wing
ru	Right upper wing
rud	Rudder
tan	Tangential
∞	Free-stream conditions

Symbols

Δ	Difference
$\lvert\ \rvert$	Absolute value (modulus)
$\bar{}$	Mean value

Abbreviations

AD	Actuator disk
AFDD	Aeroflightdynamics Directorate, U.S. Army
AH	Airbus Helicopters
AL	Actuator line
ALE	Arbitrary Lagrangian Eulerian
AMR	Adaptive mesh refinement
BEMT	Blade element momentum theory
BET	Blade element theory
BPF	Blade passing frequency
BVI	Blade-vortex interaction
CA	Comprehensive analysis
CA^{3}TCH	Coupled Aerodynamic-Aeroacoustic Analysis of a Trimmed Compound Helicopter
CFD	Computational fluid dynamics
CMA	Cumulative moving average
CSD	Computational structural dynamics
DDES	Delayed detached-eddy simulation
DES	Detached-eddy simulation
DIM	Dynamic inflow model
DLR	Deutsches Zentrum für Luft- und Raumfahrt, German Aerospace Center
DNS	Direct numerical simulation
DOF	Degree of freedom
EMS	Emergency medical services
eVTOL	Electric vertical take-off and landing
FFT	Fast Fourier transform
FM	Flight mechanics
FOM	Figure of merit

FVM	Free-vortex wake model
HLRS	High Performance Computing Center Stuttgart
HPC	High performance computing
IAG	Institute of Aerodynamics and Gas Dynamics, University of Stuttgart
JAXA	Japan Aerospace Exploration Agency
JST	Jameson–Schmidt–Turkel
L/D	Lift-to-drag ratio
LES	Large-eddy simulation
LIM	Linearized inflow model
LR	Lateral rotor
MBB	Messerschmitt–Bölkow–Blohm
MPI	Message passing interface
MR	Main rotor
MTOW	Maximum take-off weight
NASA	National Aeronautics and Space Administration
ONERA	Office National d'Études et de Recherches Aérospatiales, French Aerospace Lab
PVM	Prescribed-vortex wake model
RACER	Rapid And Cost-Effective Rotorcraft
RANS	Reynolds-averaged Navies–Stokes
RBF	Radial basis function
rev	Rotor revolution
RMS	Root mean square
RSM	Reynolds-stress model
SAR	Search and rescue
SST	Shear-stress transport
TR	Tail rotor
TSA	Time-synchronous average
URANS	Unsteady Reynolds-averaged Navies–Stokes
VPM	Vortex particle method
VTM	Vorticity transport method
VTOL	Vertical take-off and landing
WENO	Weighted essentially non-oscillatory

1 Introduction

During the multi-faceted era of manned flight, helicopters have proven to be an indispensable means of transport. With their abilities of vertical take-off and landing (VTOL) as well as hovering, they are relied on in a variety of missions and fields of application, such as emergency medical services (EMS), search and rescue (SAR), law enforcement, and special transport of passengers and cargo. The flexibility of helicopters with their significantly reduced requirement of complex and spacious infrastructure on landing sites oftentimes makes them superior to fixed-wing aircraft.

However, the flight envelope of helicopters is limited to flight speeds of up to 180 kts (Sikorsky CH-53K) [1] due to detrimental aerodynamic effects on the main rotor (MR). As the rotor blades experience an inflow where the flight speed is superposed by the rotational velocity, in high-speed forward flight this leads to significantly increasing drag on the advancing side of the rotor disk, whereas the retreating side suffers from flow separation and reverse inflow, and consequently the breakdown of thrust generation [2].

In contrast, fixed-wing aircraft with turboprop engines can reach up to 400 kts (Piaggio Avanti EVO) [3], which is even surpassed by aircraft with turbofan or turbojet engines. Due to their lacking VTOL capabilities, this leaves what Blacha et al. [4] refer to as a "Mobility Gap" as illustrated in Fig. 1.1, where accessibility describes the availability of airlift regarding required infrastructure.

In order to close this gap, in recent years numerous manufacturers increasingly started developing novel aircraft configurations which are aimed at overcoming the limits of traditional layouts by extending the maximum flight speed of conven-

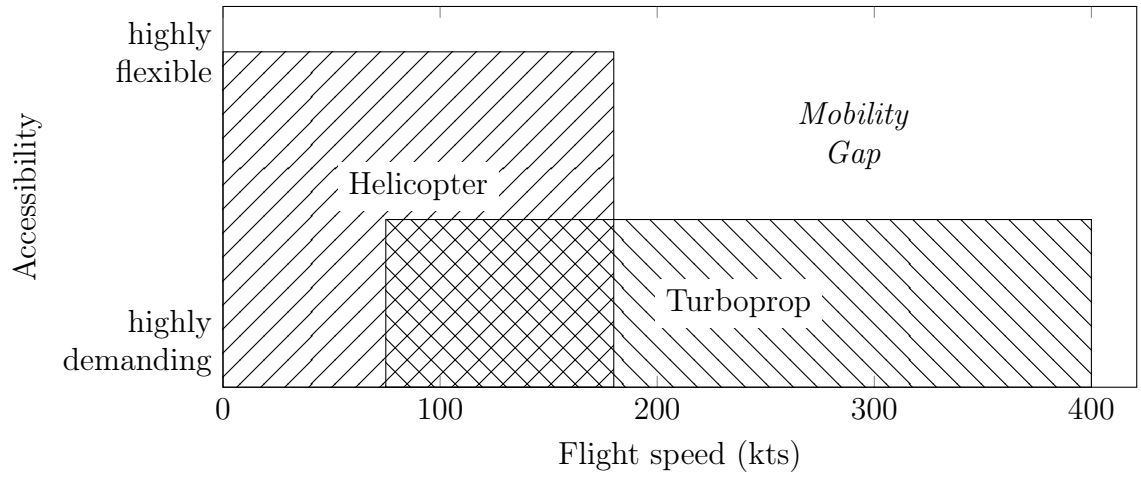

Figure 1.1: Operation envelope of helicopters and turboprop fixed-wing aircraft.

Figure 1.2: Airbus Helicopters RACER. Courtesy of Airbus Helicopters.

tional helicopters while still maintaining their flexibility in accessible airlift. One of the approaches is Airbus Helicopters' (AH) compound helicopter demonstrator RACER (Rapid And Cost-Effective Rotorcraft, see Fig. 1.2). Equipped with a box wing and pusher propellers or lateral rotors (LR), RACER's design significantly deviates from conventional helicopters.

1.1 Motivation

The addition of wings and lateral rotors heavily influences the aerodynamics of RACER as these components are intended to unload the main rotor by delivering lift and thrust depending on the flight conditions. Furthermore, the lateral rotors replace the tail rotor (TR) of a conventional helicopter and are therefore responsible for anti-torque [5]. Consequently, taking box wing and lateral rotors into account clearly is absolutely essential when analysing the aerodynamic behaviour and performance of this compound helicopter. This also applies to the related topics such as flight mechanics and stability.

However, considering the different components as isolated protagonists might not be sufficient at this point. With the wide range of flight conditions experienced by a helicopter and the complex flow phenomena accompanying them, main rotor, wings, and lateral rotors are likely to have an influence on each other's performance in at least some of these conditions. This becomes especially relevant due to the positioning of these components, where the lateral rotors are directly attached to the joined wing tips of the box wing and the latter is mounted to the fuselage below the main rotor.

For this reason, the mutual effects of the main aerodynamic components might be a key factor in their respective performance. Understanding the general phenomena

of the interactions and assessing their beneficial or detrimental nature therefore is essential in analysing the overall system.

This becomes relevant in various stages of a compound helicopter's development and operation, starting with the conceptual and preliminary design process, where Ormiston [6] considers the lacking capability of prediction methodology to cope with innovative advanced concepts to be one of the main obstacles in the development of such concepts. For an initial sizing, basic rotor principles such as blade element momentum theory (BEMT) are used to achieve a targeted flight envelope and payload [2]. Heavily depending on the performance figures of the individual components such as propulsive efficiency, figure of merit (FOM) and lift-to-drag ratio (L/D), these estimates have to be adjusted by additional factors taking into account the mutual influences.

In the detailed design study following the initial sizing, the helicopter's performance is analysed with the help of wind tunnel tests and computational fluid dynamics (CFD). Due to restraints in cost, available wind tunnel facilities or computational performance, this often comprises studies on individual components rather than the complete system. Deducing the overall performance of the latter consequently requires factoring in the occurring interactional effects. For a conventional helicopter, these are particularly the mutual influences of main rotor, fuselage, and tail rotor, which are taken into account with the help of both empirical data and specific analyses—by experimental or numerical methods—of these effects [2]. For a compound helicopter, this naturally translates to analyses of interactions between main rotor, wings, and lateral rotors.

The general understanding of interactional phenomena emerging from this is furthermore required in defining specific flight states where these might be particularly critical to the overall performance or stability of the helicopter. Only after determining the basic aerodynamic mechanisms coming into play between the various components it is possible to deduce under which conditions they are likely to become most detrimental. Paying particular attention to these flight states not only is part of the de-risking during the detailed design study but also the following flight tests. At this stage, the prior assumptions for interactional influences are verified both by assessing the performance of the helicopter over its flight envelope and by examining flight states previously defined most critical.

Furthermore, understanding interactional effects and the underlying flow physics is necessary for developing models of advanced rotorcraft configurations for comprehensive analysis (CA) [7] as well as for flight dynamics [8]. With the former being used not only as a low- or mid-fidelity alternative to CFD in analyses of aerodynamics and performance but also in coupled CFD-CA environments, and the latter enabling flight control development and real-time piloted simulation, these models and their correct representation of aerodynamic interactions play an important role over the whole period of rotorcraft development and operation.

1.2 Compound Helicopters

As Fig. 1.1 clearly illustrates, closing the "Mobility Gap" can be achieved from two directions: adding VTOL capability to fixed-wing turboprop aircraft would extend their operation envelope towards more flexibility in accessible airlift, whereas increasing the maximum flight speed of helicopters would close the velocity gap while maintaining accessibility.

The first of these approaches underlies the concept of tiltrotor aircraft, where the orientation of the propellers can be altered during flight in order to tilt the thrust vector. Furthermore, compared to a conventional turboprop aircraft, the propeller radius is increased, allowing for sufficient thrust for VTOL and hover, and blade pitch control is extended from collective to cyclic control. This measure is necessary to achieve a trimmed flight state in vertical and transition flight. Recently developed tiltrotor aircraft include the AgustaWestland AW609 (see Fig. 1.3(a)) and the Bell V-280 Valor (see Fig. 1.3(b)) which is an evolution of the Bell Boeing V-22 Osprey, the only tiltrotor model broadly in operation.

A variation of the tiltrotor configuration is the tiltwing concept, where the propellers or rotors remain fixedly attached to the wings, which can be rotated as a whole in relation to the fuselage.

Extending the operation envelope of helicopters towards a higher flight speed in order to close the "Mobility Gap" is the idea behind compound helicopters. With the aforementioned detrimental effects in high-speed forward flight of significantly increasing drag and noise on the advancing blade due to compressibility effects and retreating blade stall, this concept aims at unloading the main rotor. As the latter is responsible both for lift and propulsion in forward flight, this can be achieved in two different ways: on the one hand, the helicopter can be provided with wings to generate additional lift (lift compounding); on the other hand, thrust compounding is enabled by adding means of propulsion [2].

First compound helicopter concepts in the 1950s were fitted with a tip-driven main rotor that was merely used for autorotation in forward flight (McDonnell XV-1, Fairey Rotodyne), whereas following approaches were mostly based on existing helicopter models with a conventional main rotor. Consistently fitted with auxiliary wings for lift compounding, thrust compounding was achieved in varying ways. On the Sikorsky S-61F, Lockheed XH-51A, or Bell HPH, turbojet engines were mounted to fuselage or wings, whereas the Piasecki 16H-1 Pathfinder or Lockheed AH-56A Cheyenne had a single—optionally ducted—pusher propeller at their tail for propulsion. In contrast, the Sikorsky XH-59A did not include wings to achieve lift compounding but was fitted with coaxial rotors instead to overcome the detrimental main rotor effects in high-speed flight; propulsion was provided by two turbojet engines [6].

(a) AgustaWestland AW609 (b) Bell V-280 Valor

Figure 1.3: Tiltrotor aircraft. (a) Courtesy of Leonardo. (b) Courtesy of Bell Textron.

Despite their largely successful expansion of helicopter flight envelopes with record breaking flight speeds, none of these concepts was developed into a production model. The increased complexity of the compound design lead to technical difficulties as well as cost overruns in development and operation [6]. Together with the general downside of this concept with an increased empty weight due to the additional components and an inferior performance in hover and climb caused by the download penalty of the wings [2], this was the reason for a decades-long hiatus of compound helicopters.

In the 2000s, however, helicopter manufacturers started picking up the investigation of the compound helicopter configuration, with Piasecki revisiting their idea of a ducted pusher propeller in the form of the X-49A and Sikorsky building another coaxial helicopter configuration (see Fig. 1.4(a)). In contrast to their previous XH-59A with its twin turbojets, the X2 was fitted with a single pusher propeller at the tail. This demonstrator proved to be very successful, achieving an unofficial flight speed record of 253 kts in July 2010 [6] and eventually spawning the Sikorsky S-97 Raider and Sikorsky-Boeing SB>1 Defiant compound helicopter configurations.

In parallel to the Sikorsky X2, Eurocopter launched the development of their compound helicopter demonstrator X^3. As illustrated in Fig. 1.4(b), this was provided with wings for lift compounding, whereas thrust compounding was enabled by auxiliary tractor propellers attached to the wing tips. In contrast to compound designs with a single pusher propeller at the tail or turbojet engines at the fuselage, the lateral position of these propellers also allowed to provide anti-torque through differential thrust and therefore made a tail rotor obsolete.

After setting an unofficial flight speed record of 255 kts in June 2013 [9] and thereby even surpassing the Sikorsky X2, newly branded Airbus Helicopters decided to benefit from the gained experience and develop an evolved compound helicopter

(a) Sikorsky X2 (b) Eurocopter X^3

Figure 1.4: Compound helicopters. (a) Courtesy of Lockheed Martin. (b) Courtesy of Airbus Helicopters.

demonstrator under the Fast RotorCraft section of the European Research Program Clean Sky 2 with a design cruise speed of 220 kts [4].

While maintaining the general concept of X^3's auxiliary wings and propellers or lateral rotors, the resulting RACER design features distinctive changes on both components as illustrated in Fig. 1.2. Instead of a single wing, it is equipped with a joined wing or box wing for structural and safety reasons. According to Blacha et al. [4], also a reduction of detrimental wing download in hover through the staggering of the wings and the resulting shielding of the lower wing from the main rotor downwash was intended. Furthermore, a pusher configuration was selected for RACER's lateral rotors to increase safety of the passengers during boarding and emergency exit.

1.3 State of the Art

With the revival of the compound helicopter configuration, research effort has significantly grown in the last two decades and culminated in publications on various topics related to this field of study. In one of the first of these publications, Orchard and Newman [10] delivered an overview of design variations as well as an insight into the research conducted during the early days of compound helicopter development. One of the conclusions they drew was the necessity of a better understanding regarding the interference effects between main rotor, wings, and auxiliary propulsion systems in order to maximize efficiency.

Ormiston [6] complemented Orchard and Newman's work by adding recent projects of compound helicopter research and development. Furthermore, key topics were identified and recommendations given to expedite the realization of compound helicopter configurations.

A performance analysis of two different compound helicopter configurations was conducted by Ferguson and Thomson [11], whereas Rand and Khromov [12] presented a process of optimizing such a design. Further topics of recent years' research on compound helicopters include flight mechanics [13] and trim optimization [14,15].

The development of Airbus Helicopters' RACER demonstrator has also spawned multiple publications, starting with an overview of the configuration by Blacha et al. [4]. This was followed by research on interactions of the main rotor and rotor head wake with the tail unit [16], aerodynamic design of the vertical fin [17] and main rotor blade roots [18], structural design of the wings [19], and flight mechanics [5]. Recently, Thiemeier [20] furthermore published his findings of a trim condition variation of RACER's cruise flight and the associated influence on efficiency.

Multiple further publications related to RACER involved the author of the present thesis. An introduction of a multidisciplinary, coupled CFD-CA tool chain for simulations on this compound configuration was given by Öhrle et al. [21]. This also included the author's preliminary findings on interaction phenomena in hover and cruise flight, as well as an insight into aeroacoustics in hover. RACER's behaviour in hover under crosswind conditions was subsequently analysed by Thiemeier et al. [22] with regards to various topics such as flight mechanics and performance. A validation of the tool chain was finally delivered by Öhrle et al. [23] by applying it to RACER's predecessor X^3 and correlating simulation results in high-speed flight with respective flight test data.

Due to the decades-long hiatus of compound helicopter development and the lack of production models up to the present day, research on aerodynamic interactions for such configurations in general and for their main rotor, wings, and lateral rotors in particular is limited. However, as findings on interactional phenomena might be transferable from other aircraft configurations to the compound geometry of RACER, the following sections give an overview of selected investigations on rotor-rotor interaction and rotor-wing interaction in general. For this purpose, all propulsive devices with rotating blades are referred to as rotors, assuming overall similar characteristics in interactional behaviour for main rotors, tail rotors, lateral rotors, and propellers, regardless of differences in orientation (vertical, longitudinal or lateral axis), articulation (cyclic, collective or fixed), or stiffness (elastic or rigid) that are associated with the different terms.

The section is concluded with remarks on the application of coupled high-fidelity simulations in the field of rotorcraft aerodynamics.

1.3.1 Investigations of Rotor-Rotor Interaction

With the placement of two lateral rotors below the main rotor of the RACER configuration, a mutual interactional effect of these rotors can be expected. While Orchard and Newman [10] identified this effect as an "unknown factor" for compound heli-

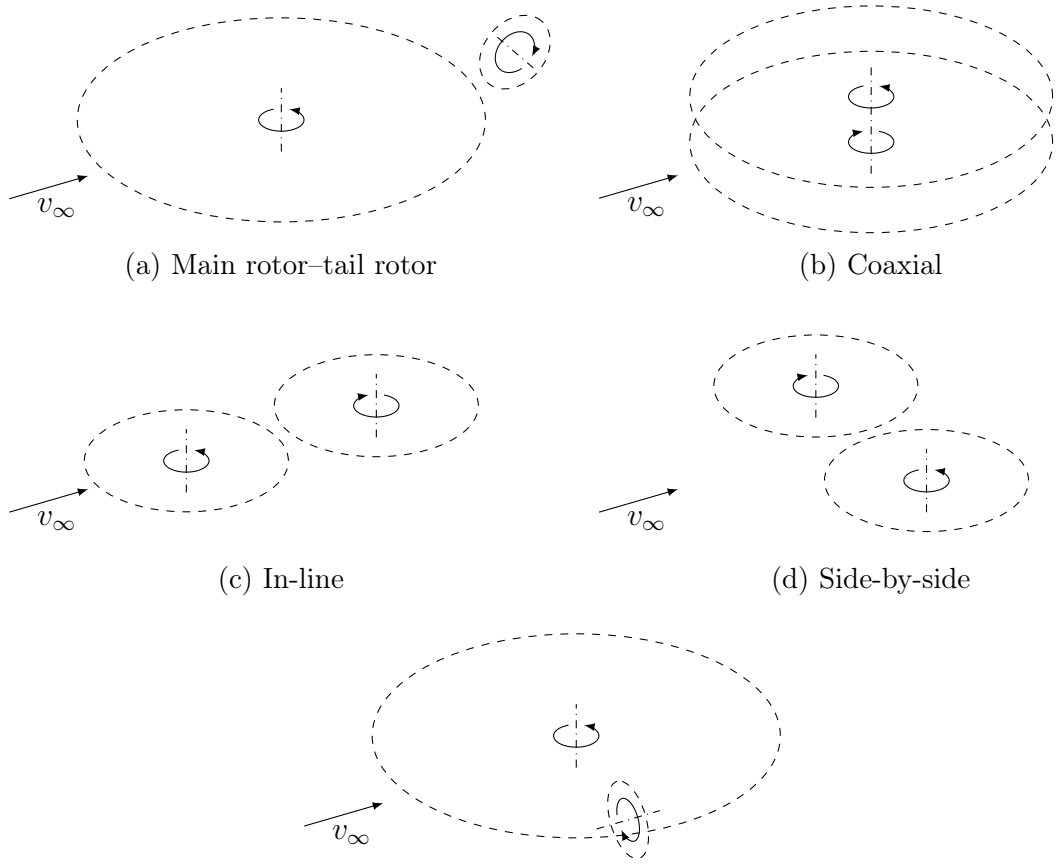

(a) Main rotor–tail rotor

(b) Coaxial

(c) In-line

(d) Side-by-side

(e) Main rotor–lateral rotor

Figure 1.5: Rotor-rotor configurations.

copters, they assumed it to be transferable from findings on main rotor–tail rotor interaction for conventional helicopters (see Fig. 1.5(a)), albeit only for selected flight conditions.

As illustrated in Table 1.1, this interaction was investigated by conducting numerical analyses of varying degrees of fidelity. In contrast to studies using methods that are commonly classified as mid-fidelity [24] and often embedded in CA tools, such as free-vortex wake model (FVM) [25, 26], vortex particle method (VPM) [26], or vorticity transport method (VTM) [27], Jude et al. [28] applied high-fidelity CFD methods in the form of detached-eddy simulations (DES). The examined helicopter configurations were mostly generic geometries solely consisting of main rotor and tail rotor, whereas Visingardi et al. [26] analysed the interactions on a Messerschmitt–Bölkow–Blohm (MBB) BO-105 helicopter by conducting simulations on a full and reduced geometry and comparing them to results of wind tunnel experiments.

For a range of flight states, the studies found the main rotor to be the cause of performance fluctuations on the tail rotor [27, 28]; however, a similar, yet smaller effect was also witnessed vice versa in hover [25]. Overall, the work on main rotor–

Table 1.1: Overview of selected investigations of rotor-rotor interaction. H: Hover, T: Transition, C: Cruise.

Configuration		Reference	Year	Geometry	Flight conditions			Numerical analysis	Experimental analysis
					H	T	C		
MR-TR	Generic	Yin & Ahmed [25]	2000	MR + TR & reduced	×	×		FVM	
	MBB BO-105	Visingardi et al. [26]	2006	Full & reduced		×	×	FVM, VPM	Wind tunnel
	Generic	Fletcher et al. [27]	2008	MR + TR & reduced		×	×	VTM	
	Generic	Jude et al. [28]	2018	MR + TR & reduced			×	CFD (DES)	
Coaxial	Generic	Dingeldein [29]	1954	Rotor + rotor & reduced	×	×	×		Wind tunnel
	Generic	Ramasamy [30]	2015	Rotor + rotor & reduced	×				Wind tunnel
	Sikorsky X2	Klimchenko et al. [31]	2017	Rotor + rotor			×	FVM, CFD (URANS)	
	Sikorsky XH-59A	Sharma et al. [32]	2020	Rotor + rotor			×	FVM, VPM, CFD (DES)	
	Generic	Keller et al. [8]	2020	Full & reduced	×	×	×	LIM, FVM	
	Sikorsky X2	Juhasz et al. [33]	2020	Full	×		×	DIM, FVM	Flight tests
In-line	Generic	Dingeldein [29]	1954	Rotor + rotor & reduced	×	×	×		Wind tunnel
	Generic	Lee et al. [34]	2009	Rotor + rotor & reduced	×	×	×	FVM	
	Generic	Ramasamy [30]	2015	Rotor + rotor & reduced	×				Wind tunnel
	Generic	Healy et al. [35]	2020	Rotor + rotor & reduced			×	CFD (DES)	
	Boeing CH-47D	Guner et al. [36]	2020	Rotor + rotor	×	×		DIM	
	Generic	Stokkermans et al. [37]	2021	Rotor + rotor & reduced			×		Wind tunnel
Side-by-side	Generic	Ramasamy [30]	2015	Rotor + rotor & reduced	×				Wind tunnel
	Generic	Zhou et al. [38]	2017	Rotor + rotor & reduced	×				Wind tunnel
	Airbus Vahana	Droandi et al. [39]	2018	Full, rotors as AD	×	×	×	FVM, CFD (RANS)	
	Generic	Ventura Diaz et al. [40]	2019	Full & reduced			×	CFD (DES)	
	Generic	Alvarez et al. [41]	2020	Rotor + rotor & reduced	×			VPM, CFD (URANS)	
MR-LR	Generic	Bain & Landgrebe [42]	1967	Full & reduced		×	×		Wind tunnel
	AH RACER	Wentrup et al. [43]	2018	Full, MR as AD			×	CFD (RANS)	
	Generic	Boisard [44]	2018	MR + LR & reduced	×	×	×	FVM, CFD (URANS)	
	AH RACER	Decours et al. [45]	2019	Full & reduced		×	×	FVM, CFD (URANS)	
	AH RACER	Yin et al. [46]	2019	Full & reduced		×	×	FVM	
	AH RACER	Stokkermans et al. [47, 48]	2020	Full & reduced, MR as AD	×		×	CFD (URANS)	

tail rotor interaction shows a strong dependency on flow conditions and the resulting convection of wakes and blade tip vortices.

In hover, a conventional helicopter's tail rotor is not impinged on by the main rotor downwash due to its aft positioning. A similar convection of the main rotor downwash past RACER's lateral rotors can be expected in cruise flight; however, the axial direction of this convection—opposed to the tangential passing of the tail rotor—together with the additional inflow's influence are likely to lead to significantly different interactional phenomena. For a conventional helicopter's cruise flight, in contrast, the placement of the tail rotor in the main rotor wake leads to blade-vortex interactions (BVI), whereas a similar effect on the compound helicopter's lateral rotors can only be expected for specific low speed conditions. Consequently, the findings of main rotor–tail rotor interaction that can be transferred to the compound configuration of RACER are limited due to the lack of comparable flow conditions.

Another helicopter configuration with significant rotor-rotor interaction is the coaxial helicopter (see Fig. 1.5(b)). Despite the lack of a tail rotor, the two stacked, counter-rotating main rotors—allowing for the omission of dedicated anti-torque generation systems—interact heavily due to their close proximity and the resulting placement of one of the rotors in the wake of the other rotor over most of the flight conditions. The mutual effects were studied experimentally on generic rotors in the wind tunnel by Dingeldein [29] and Ramasamy [30], whereas other studies employed numerical analyses [8,31–33]. As illustrated by the overview in Table 1.1, the spectrum of the applied methods ranges from low-fidelity such as linearized inflow models (LIM) and dynamic inflow models (DIM) [24] over mid-fidelity to high-fidelity CFD analysis with unsteady Reynolds-averaged Navier–Stokes (URANS) simulations. In addition to generic configurations, Sikorsky's coaxial compound helicopters XH-59A and X2 were analysed in these studies, even allowing for validation of the numerical results with flight test data [33].

Depending on flight conditions, the authors observed a variety of interactional phenomena such as the upper rotor's downwash impinging on the lower rotor, a mutual influence of the rotating pressure fields, or BVI. The effect of this was found to be a loss in rotor efficiency [30], distinct fluctuations of thrust and resulting noise generation [32], and a change in flight dynamics [8], for instance. However, as RACER's main and lateral rotors are neither positioned coaxially nor in similarly close proximity, the aerodynamic interactions cannot be directly compared to a coaxial rotor configuration.

Besides this, the experimental studies of Dingeldein [29] and Ramasamy [30] also analysed another multirotor layout for rotor-rotor interactions; on the in-line or tandem configuration (see Fig. 1.5(c)), the two rotors are not installed coaxially but with a longitudinal offset of the axes, either one after another or with an overlap as in the work of Lee et al. [34]. While such a configuration is currently in use on the

Boeing CH-47D—investigated by Guner et al. [36]—recent research is mainly aimed at the potential application of in-line rotors on electric VTOL (eVTOL) aircraft for urban air mobility [35, 37] or cargo missions.

In hover, Ramasamy [30] found the rotors to perform similar to isolated rotors for an offset of more than 20 % of the rotor radius, with the interaction consequently being negligible. For rotors with a smaller offset or even an overlap, a general loss in efficiency was visible, with the exception of directly adjoining, staggered rotors where the lower rotor showed a small benefit due to the interaction with blade tip vortices of the upper rotor. With increasing flight speed, an interactional effect can be witnessed on the rear rotor for significantly larger rotor distances. Stokkermans et al. [37] associated the deficit in thrust and efficiency with the influence of the front rotor's convecting downwash, consequently inducing a reduction of effective angle of attack on the superjacently passing blades of the rear rotor. With only RACER's lateral rotors having a similarly coplanar orientation and the fuselage in between making their direct rotor-rotor interaction unlikely, the phenomena observed for in-line rotors cannot be transferred to the compound configuration.

The same holds true for the similar side-by-side configuration (see Fig. 1.5(d)) with laterally instead of longitudinally offset rotors. Aerodynamic interactions have been investigated with a variety of numerical and experimental methods (see Table 1.1) for its application in eVTOL aircraft, both unmanned [38,41] or manned [39, 40]. An example of the latter is the prototype Vahana with four tiltwings and two side-by-side rotors each, developed by Airbus and analysed by Droandi et al. [39] for rotor-rotor interactions by means of FVM and steady-state Reynolds-averaged Navier–Stokes (RANS) simulations, with rotors represented by actuator disks (AD).

With the lack of horizontal convection, the behaviour of side-by-side and in-line rotors is identical in hover. The additional inflow in forward flight, however, leads to a different behaviour for the side-by-side configuration, as none of the rotors is positioned downstream of the other. Despite this, Ventura Diaz et al. [40] witnessed a different performance for directly adjacent rotors compared to isolated ones. Furthermore, they found that the gain in L/D of the side-by-side rotors was even increased for intermeshing rotors, where a difference of thrust generation was noticeable particularly but not exclusively in the overlapping region of the rotor disks. Maximum rotor efficiency was achieved for an overlap of 30 % of the rotor radius.

Besides this variety of rotor configurations, also the combination of main rotor and lateral rotor(s) (see Fig. 1.5(e)) as it can be found on RACER was the subject of numerous investigations on rotor-rotor interaction. During compound helicopters' first period of prosperity, an extensive wind tunnel study was conducted by Bain and Landgrebe [42], who determined an effect of the main rotor on the lateral rotors in forward flight despite the lack of directly impinging downwash. They attributed this effect, becoming manifest in increasing lateral rotor bending moments with rising main rotor thrust, to the change in effective angle of attack—and consequently

thrust distribution—caused by the main rotor momentum downwash angle. Bain and Landgrebe found a reduction of this phenomenon for higher flight velocities and were able to trace this back to the smaller downwash angle and its reduced influence on the effective angle of attack. In contrast, the larger distance between lateral rotors and downwash emerging from the same effect was found to play no role in the reduced interaction. The reverse influence of lateral rotors on main rotor performance was also detected by Bain and Landgrebe, as the load data of the wind tunnel experiments similarly showed increasing main rotor blade moments with growing lateral rotor thrust.

In contrast to these investigations of a full compound helicopter including wing and fuselage, Boisard [44] conducted FVM and URANS simulations of a main rotor and a single lateral rotor—combined and isolated—over a variety of flight conditions in order to analyse their mutual influence. In cruise flight, Boisard observed an increased level of thrust on the lateral rotor in relation to an isolated rotor and associated it with the main rotor's inductive influence on axial and tangential velocity in the lateral rotor's inflow. Vice versa, the lateral rotor's presence had no significant influence on the total main rotor thrust; however, the respective thrust distribution showed a characteristic shift superjacent to the lateral rotor's inflow and wake. Boisard witnessed a similar influence in hover with thrust fluctuations on the main rotor blades passing above the lateral rotor. For these flight conditions, the latter, for its part, was directly subjected to the main rotor downwash and therefore showed significant performance fluctuations due to the asymmetric, non-axial inflow.

While the investigations of Bain and Landgrebe [42], and Boisard [44] were carried out on generic rotor configurations, multiple analyses of rotor-rotor interaction in recent years were specifically dedicated to the RACER compound helicopter. In the context of efforts aimed at the aerodynamic optimization of its wings, Wentrup et al. [43] conducted steady-state RANS simulations of the full helicopter configuration with the main rotor represented by an actuator disk replacing the discrete, rotating blades. Their observation of a larger maximum thrust on the left lateral rotor despite the higher overall thrust of the right lateral rotor lead them to the conclusion that the asymmetric influence of the main rotor was responsible for this, where the highly loaded advancing side induced larger downward velocities in the subjacent flow regions than the retreating side with its partially reverse inflow and significantly smaller thrust generation.

A study for optimizing the aerodynamic and acoustic characteristics of RACER's lateral rotors was conducted by Decours et al. [45] with the help of FVM and URANS simulations. In its course, they found the lateral rotors to be subjected to a decelerated axial inflow in forward flight and attributed this effect to the rotation of the main rotor tip vortices passing between main and lateral rotors. Decours et al. as-

sumed this influence to have a positive installation effect on lateral rotor propulsive efficiency.

RACER's acoustics and the role the rotor-rotor interactions play in its mechanisms of noise generation were investigated by Yin et al. [46] by conducting FVM simulations in forward flight. Their comparison of results for the full setup with reduced configurations and isolated components showed the main rotor to be responsible for thrust fluctuations on the lateral rotors due to asymmetric, non-axial inflow as described by Boisard [44]. Furthermore, they confirmed the different susceptibility of the left and right lateral rotor to the main rotor's interactional influence observed by Wentrup et al. [43] and attributed to the asymmetric main rotor thrust generation.

Most recently, Stokkermans et al. [47] published their findings on aerodynamic interactions for RACER's lateral rotors in hover and cruise flight, including the effect of the main rotor, which was represented by an actuator disk in their URANS simulations. By comparing the results of a helicopter configuration solely lacking the tail geometry with reduced geometries individually omitting main rotor, lateral rotors, wings, and fuselage, they were able to isolate the respective influence of these components on the remaining helicopter's aerodynamic performance. While they observed an increase of lateral rotor thrust, power, and efficiency in cruise flight due to the presence of the main rotor and attributed this to the vertical deflection of the lateral rotor inflow previously hypothesized by Wentrup et al. [43], Stokkermans et al. also confirmed the latter's findings of an asymmetry between the effect of the main rotor's advancing and retreating side. The respective influence in hover was not isolated with the help of simulations omitting the main rotor; however, Stokkermans et al. witnessed a strong sinusoidal fluctuation of the lateral rotors' blade loading and, in agreement with Boisard [44], accredited it to the vertically impinging downwash and its influence on the lateral rotor inflow.

1.3.2 Investigations of Rotor-Wing Interaction

In contrast to interactions between a conventional helicopter's main and tail rotor, its lack of static lifting surfaces—disregarding the relatively small stabilizers—does not allow for any transfer of comparable rotor-wing interactions to RACER's compound configuration, where a mutual influence between main rotor and wings, on the one hand, and lateral rotors and wings, on the other hand, can be expected.

However, the wide range of aircraft configurations overall provides for multiple manifestations of such effects, with the most obvious being the fixed-wing propeller aircraft. As illustrated by the overview in Table 1.2, rotor-wing interactions have been investigated on this type of aircraft, arguably the most classical configuration of manned flight, over a long period of time and with miscellaneous methods.

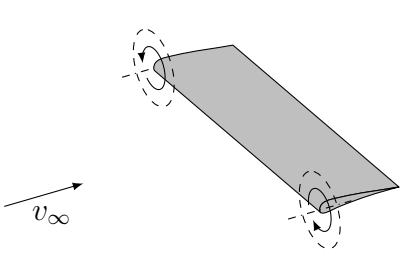

(a) Fixed-wing tractor propeller aircraft

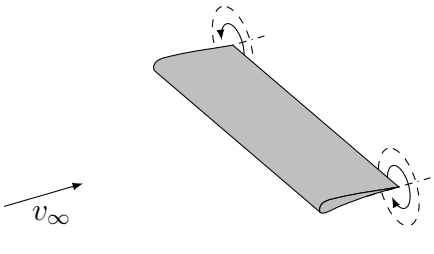

(b) Fixed-wing pusher propeller aircraft

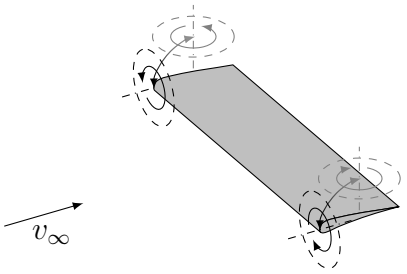

(c) Tiltrotor aircraft

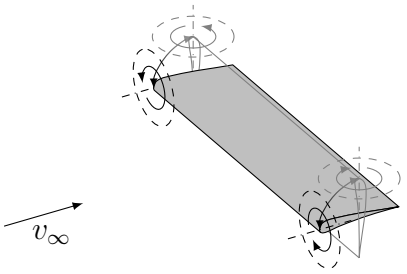

(d) Tiltwing aircraft

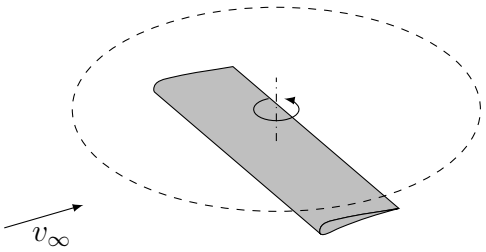

(e) Compound helicopter (lift)

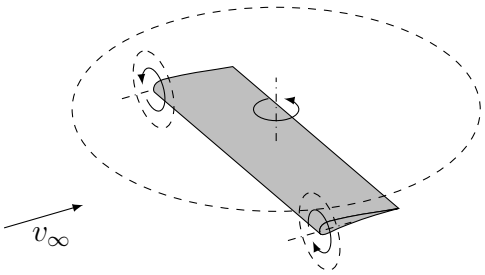

(f) Compound helicopter (lift and thrust)

Figure 1.6: Rotor-wing configurations.

After conducting an analytical study of a wing fitted with wing-tip-mounted propellers, both in tractor (see Fig. 1.6(a)) and pusher (see Fig. 1.6(b)) configuration, Miranda and Brennan [49] published their findings of significant potential performance benefits originating from the mutual interaction of these components. Their prescribed-vortex wake model (PVM) simulations showed a strong influence of the wing tip vortex on the propulsive efficiency of a pusher propeller, with the nature of this influence depending on the propeller's sense of rotation. A significant detrimental installation effect was observed for propellers co-rotating with the wing tip vortex. In contrast, Miranda and Brennan found the reverse, inboard-up sense of rotation to cause a beneficial interactional effect. As this configuration is similar to RACER's combination of lateral rotors and wing, albeit with a box wing geometry, a comparable efficiency benefit in forward flight can be expected for this compound helicopter.

Table 1.2: Overview of selected investigations of rotor-wing interaction. H: Hover, T: Transition, C: Cruise.

Configuration		Reference	Year	Geometry	Flight conditions			Numerical analysis	Experimental analysis
					H	T	C		
Fixed-wing propeller aircraft	Generic	Miranda & Brennan [49]	1986	Rotor + wing & reduced			×	PVM	
	Generic	Patterson & Bartlett [50]	1987	Half-span & reduced			×		Wind tunnel
	Generic	Janus et al. [51]	1996	Half-span & reduced			×	CFD (Euler)	
	Generic	Veldhuis [52]	2005	Half-span & reduced			×	FVM, CFD (RANS)	Wind tunnel
	Generic	Stokkermans et al. [53]	2019	Rotor + wing & reduced			×	CFD (URANS)	
	Generic	Schollenberger et al. [54]	2020	Rotor (AL) + wing & reduced			×	CFD (URANS)	
	NASA X-57	Jayasundara et al. [55]	2020	Half-span & reduced			×	CFD (DDES)	
Tiltrotor/-wing aircraft	Bell Boeing V-22	Felker & Light [56]	1988	Rotor + wing & reduced	×				Ground tests
	Airbus Vahana	Droandi et al. [39]	2018	Full, rotors as AD	×	×	×	FVM, CFD (RANS)	
	Bell XV-15	Lim [57]	2019	Rotor + wing & reduced			×	CFD (URANS)	
	Bell XV-15	Tran et al. [58, 59]	2019–20	Half-span & reduced	×	×	×	CFD (DES)	Flight tests
	Generic	Quackenbush et al. [7]	2020	Rotors + wing		×		FVM	
Compound helicopter	Bell	Lynn [60]	1966	Helicopters + wings	×	×	×		Flight tests
	Generic	Bain & Landgrebe [42]	1967	Full & reduced		×	×		Wind tunnel
	Generic	Felker & Light [56]	1988	MR + wing	×				Ground tests
	Generic	Tanabe & Sugawara [61–63]	2016–20	MR + wing & reduced	×		×	CFD (URANS)	Wind tunnel
	AH RACER	Wentrup et al. [43]	2018	Full, MR as AD	×	×	×	CFD (RANS)	
	AH RACER	Decours et al. [45]	2019	Full & reduced		×	×	FVM, CFD (URANS)	
	AH RACER	Yin et al. [46]	2019	Full & reduced		×	×	FVM	
	Boeing AH-64	Brouwers et al. [64]	2019	Full & reduced	×	×	×		Wind tunnel
	Generic	Yeo [65]	2019	Full			×	PVM	
	AH RACER	Stokkermans et al. [47, 48]	2020	Full & reduced, MR as AD	×		×	CFD (URANS)	

The wind tunnel tests of Patterson and Bartlett [50] on a half-span model of a fixed-wing aircraft with a wing-tip-mounted pusher propeller confirmed the positive installation effect of the wing tip vortex on a counter-rotating propeller. They attributed the decreased power consumption for constant thrust to an increase in effective angle of attack on the propeller blades. Furthermore, Patterson and Bartlett discovered a reverse effect on the performance of the wing, equally depending on the propeller's sense of rotation. They observed a gain in wing lift in case of an inboard-up rotating propeller, which they related to the dampening effect of the propeller wake on the wing tip vortex, resulting in an increased effective angle of attack in the wing's outboard region. With this effect additionally reducing the induced drag of the wing, Patterson and Bartlett consequently found the installation effect to be beneficial in three respects: regarding propeller propulsive efficiency, wing lift, and wing drag.

With the subsequent advance in CFD methods, the interaction between propellers and wings on fixed-wing aircraft was numerically analysed with increasing fidelity by conducting Euler [51], RANS [52], URANS [53,54], or delayed detached-eddy simulations (DDES) [55]. Janus et al. [51] confirmed the experimental results of Patterson and Bartlett with their analysis of the same generic geometry and an analysis of the lift breakdown by components for different setups omitting propeller and nacelle. The studies of Veldhuis [52], Stokkermans et al. [53], and Schollenberger et al. [54] focussed on the influence of propeller thrust level and position, respectively, with the propellers represented by actuator lines (AL) in the latter analysis, whereas Jayasundara et al. [55] investigated the unsteady aerodynamic phenomena of the National Aeronautics and Space Administration (NASA) X-57's wing-tip-mounted (tractor) propeller and the resulting interaction-related noise characteristics.

Besides fixed-wing propeller aircraft, recent years' efforts to close the "Mobility Gap" have lead to investigations of rotor-wing interaction on novel aircraft configurations. Tiltrotor (see Fig. 1.6(c)) and tiltwing (see Fig. 1.6(d)) configurations, for their part, were not only studied in their conventionally-powered form like for example on the Bell XV-15 [57–59] and Bell Boeing V-22 Osprey [56] but lately also for eVTOL aircraft like the Airbus Vahana [39].

Ground tests of Felker and Light [56] on the rotor of the Bell Boeing V-22 Osprey in hover showed that—at constant rotor power—the addition of the aircraft's wing increased the rotor thrust by 3 %. They attributed this to the "ground effect" generated by the wing, where the blockage of the downwash improves the performance of a rotor. In contrast, when mimicking the aircraft's symmetry with the help of an image plane, the rotor thrust was 1.6 % lower than for the isolated rotor, irrespective of the wing's presence. While the latter effect, emerging from a region of recirculation at the symmetry plane, cannot be transferred to RACER, the beneficial effect of the wake blockage on rotor performance can be similarly expected for the compound helicopter's main rotor in hover. Vice versa, Felker and Light observed the rotor

downwash to generate a significant amount of download on the wing, amounting to as much as 10 % of the total rotor thrust, largely independent of the rotor's thrust coefficient. As RACER's wings are similarly situated in the main rotor downwash during hovering condition, a comparable influence is likely to occur.

While numerical studies of Lim [57] on the V-22's predecessor, the tiltrotor demonstrator Bell XV-15, showed a positive installation effect in cruise flight on the rotors' thrust and efficiency as well as on the wings' lift and drag, the interactional phenomena can hardly be transferred to RACER's combination of wings and lateral rotors due to the tiltrotors' upstream position. The high-fidelity DES analysis of Tran et al. [58] for the same configuration, however, confirmed the results of Felker and Light by yielding a similar amount of download generated by the wing in hover. Furthermore, Tran et al. witnessed a region of increased thrust above the wing in the rotor thrust distribution and attributed it to the blades' passage of the high pressure region caused by the blockage of the downwash, which is the same phenomenon that Felker and Light had previously described as a quasi-"ground effect" of the wing on rotor performance. Additional studies of Tran and Lim [59] on mutual effects in medium speed conversion mode showed a significant effect of the—only slightly tilted—rotors on the wings by reducing their lift despite the lack of direct wake impingement. Consequently, a similar inductive influence of RACER's main rotor on wing lift can be expected for transition and cruise flight conditions. While Tran and Lim found the wings, in turn, not to affect the mean thrust of the tiltrotors for this conversion flight, the circulation induced by the wings locally caused the blade tip vortices to interact differently with the rotors than for an isolated case.

Similar to these conventional tiltrotor aircraft, the Airbus Vahana eVTOL configuration studied by Droandi et al. [39] is fitted with tractor rotors in cruise flight. Consequently, the significant gradients in spanwise lift distribution indicating a heavy downstream influence of the rotor wakes on the canard and wing can hardly be transferred to RACER's combination of wings and lateral (pusher) rotors. Furthermore, the tilting of Vahana's canard and wing in hover prevents the resulting rotor-wing interaction to be comparable to what can be expected for RACER's main rotor and wings in these flight conditions. Therefore, while Droandi et al. observed pronounced longitudinal forces—instead of download—to be generated by the rotor-induced convection over the (tilted) canard and wing, this impact on the overall longitudinal trim condition is not expected to be an issue for the compound helicopter configuration.

Most relevantly, rotor-wing interaction has also been investigated for compound helicopter configurations, starting with experimental studies by Lynn [60]. His flight tests of conventional Bell helicopters fitted with wings (see Fig. 1.6(e)) showed an increase in the main rotor's induced power in hover due to the wing's download effect, whereas the wings significantly improved the helicopters' performance in forward

flight. Here, Lynn witnessed little effect of the wing on the main rotor performance but rather an indirect influence on longitudinal control due to the unloading in terms of lift but not propulsive force and a consequently larger tilt angle of the tip path plane in comparison to a conventional helicopter. With RACER's additional lateral rotors providing thrust (see Fig. 1.6(f)), however, this is not a limiting factor for this compound configuration. The reverse effect of the main rotor on wing performance, in contrast, where Lynn assumed the main rotor downwash to reduce the angle of attack of the wing and consequently its lift, is likely to apply to RACER in a similar fashion.

The same effect was witnessed by Bain and Landgrebe [42] during extensive wind tunnel tests on a generic compound helicopter model. Here, in forward flight conditions an increase of main rotor lift—and consequently downwash momentum angle—resulted in a reduction of wing lift at constant wing incidence, with the strength of this detrimental effect depending on wing size and position. Furthermore, Bain and Landgrebe witnessed an asymmetric characteristic of this effect, where the wing lift is noticeably more affected below the advancing side of the main rotor. They assumed the circulation of the rotor blade bound vortex, which induces a reduction of inflow velocity below the advancing side of the main rotor and an increase below its retreating side, to cause this phenomenon. Vice versa, a theoretical analysis of Bain and Landgrebe found the bound vortex of the wing to affect the inflow of the main rotor, mainly by inducing a downward velocity in the aft region of the rotor disk. While their experimental results indeed showed the presence of the wing to cause a harmonic shift of the main rotor flapwise bending moment's time history, the change in thrust distribution presumably responsible for this did not lead to larger offsets in overall main rotor thrust—and power—for most of the relevant forward flight conditions.

In addition to their analysis of rotor-wing interaction on a tiltrotor geometry, Felker and Light [56] also conducted ground tests on a compound helicopter configuration. Here, the wing's download generated by the impinging downwash showed a slightly larger sensitivity to rotor thrust; however, other factors such as flap deflection, wing incidence or vertical distance between rotor and wing proved to have a more pronounced influence on download.

The experimental findings of Felker and Light were largely confirmed by the numerical study of Tanabe and Sugawara [61], where URANS simulations were conducted for the same configuration in hover and showed trends similar to the ground test data. In addition, spanwise distributions of wing download were analysed which manifested a slight asymmetry between right- and left-hand side, particularly with increasing levels of thrust. Additionally, the same authors investigated a combination of main rotor and wing in cruise flight [62]. Here, they not only found the main rotor to reduce the wing lift, as previously described by Lynn [60], but also confirmed the asymmetric nature of this effect observed by Bain and Landgrebe [42]. While the

latter attributed this to the additive and subtractive influence of the rotor blades' bound vortex on the wing's inflow velocity, Sugawara and Tanabe traced it back to the induced velocity of the main rotor, which is already the source of the general decrease in wing lift by reducing the effective angle of attack and which is asymmetric due to the difference in thrust distribution between advancing and retreating side of the rotor disk in forward flight. However, in contrast to the detrimental mean effect on wing lift, which is stronger below the advancing blades, Sugawara and Tanabe observed the fluctuations of wing lift caused by the interaction to be larger below the retreating blades. Most of these findings on main rotor–wing interaction were confirmed in an additional study of Tanabe et al. [63], where wind tunnel tests and URANS simulations were conducted for hover and forward flight on a configuration additionally including a fuselage.

Besides the studies on generic compound helicopter configurations, in recent years rotor-wing interaction has also been investigated specifically for the RACER demonstrator. In addition to their work on rotor-rotor interaction, Wentrup et al. [43] analysed their steady-state RANS simulations regarding mutual influence of main/lateral rotors and box wing. In hover, they found the lower wings to account only for 25 % of the total wing download caused by the impinging main rotor downwash and attributed this to the shielding effect of the upper wings which is a special feature of the box wing design. Wentrup et al. observed an asymmetry in vertical force on the wings for different flight conditions: on the one hand, they attributed the slight asymmetry of download generated in hover to the additional influence of the lateral rotors—in contrast to Tanabe and Sugawara [61] who witnessed it even without lateral rotors; on the other hand, they found a difference in lift distribution between right- and left-hand wings in cruise flight, particularly for the upper wings, and assigned this effect to the asymmetric main rotor thrust distribution in forward flight, in accordance with previous publications [42, 62]. Concerning a wing–lateral rotor interaction, Wentrup et al. determined an increase of thrust and efficiency of the lateral rotors with increasing wing lift and attributed it to the effect of the induced velocity behind the wing and the beneficial influence of the wing tip vortex on the inboard-up rotating rotor which was previously described for fixed-wing pusher propeller aircraft by Miranda and Brennan [49], and Patterson and Bartlett [50].

For the RACER configuration, this effect was also witnessed in the aforementioned study by Decours et al. [45]. Additionally, they assumed a second interactional mechanism to play a role in lateral rotor thrust, where the velocity deficit in the box wing's wake is the source of load fluctuations—and noise—on the passing rotor blades. Decours et al. found a correlation between wing flap deflection and lateral rotor efficiency caused by the former effect and an inverse proportionality between wing-rotor distance and thrust fluctuations due to the second effect.

The study of Yin et al. [46] on RACER's lateral rotor noise showed that these thrust fluctuations on rotor blades passing the wings' wake are not only caused

by the associated velocity deficit, which was not considered in the inviscid FVM simulations, but also by the vertical velocity component induced directly behind the wings. Yin et al. attributed the weaker occurrence of this effect behind the lower wings to their generally lower level of lift and the consequently smaller downward velocity in their wake. Concerning the main rotor–wing interaction, surprisingly—and somewhat implausibly—they found the main rotor to cause an upwash below its retreating side and consequently assumed an increase of wing lift over the full span of the right wings.

Within the development of the Boeing Advanced AH-64, a compound version of the conventional Apache helicopter, Brouwers et al. [64] conducted extensive wind tunnel studies over a wide range of flight conditions. In cruise flight, they observed the main rotor's influence to noticeably reduce the pressure coefficient on the wings and attributed it to a reduction of effective angle of attack by 3.0° and 1.1° below the advancing and retreating rotor blades, respectively. This confirmed both the overall detrimental effect of the main rotor downwash and its asymmetric nature linked to the thrust distribution. Vice versa, Brouwers et al. found the wings' presence to affect the main rotor loads, with a change in flap loads—steady loads as well as fluctuations—likely caused by an effect on main rotor thrust distribution. In this context, they showed the longitudinal position of the wing to significantly influence the intensity of main rotor–wing interactional effects in both directions.

The PVM analysis of a generic compound helicopter in cruise flight by Yeo [65] not only confirmed the detrimental influence of the main rotor on wing lift but also illustrated the reverse effect induced by the wing's circulation which was initially postulated by Bain and Landgrebe [42]. As a consequence of the relatively high wing loading, contributing 93 % of total lift, Yeo witnessed a significant upward velocity induced in the main rotor disk ahead of the wing, whereas a similarly large downward induced velocity occurred in the main rotor's aft region. On the advancing side of the main rotor, he expected this effect to have a beneficial influence on main rotor performance for a configuration with a small distance between wing and main rotor, changing to a detrimental influence with growing vertical distance; in contrast, no significant interference effect was found in the performance of the mostly unloaded retreating side of the main rotor.

In addition to the investigation of rotor-rotor interaction, the recent study of Stokkermans et al. [47] on Airbus Helicopters' RACER demonstrator also included an analysis of rotor-wing interaction. Their URANS simulations in cruise flight showed a distinct increase of the lateral rotors' propulsive efficiency caused by the presence of the wings. Stokkermans et al. found two different effects to be responsible for the underlying thrust increase: on the one hand, an axial velocity deficit in the wings' wake lead to a local reduction of advance ratio on the passing lateral rotor blades; on the other hand, the tangential velocity of the induced flow from the lower wing's pressure side to the upper wing's suction side, comparable to a single wing's

tip vortex, resulted in an increased angle of attack on large parts of the lateral rotor disk. A larger pitch angle of the helicopter was found to increase the latter effect owing to the higher wing lift. In addition, Stokkermans et al. described a reverse effect of the lateral rotors on the wings' aerodynamic performance, where lift was increased over large parts of the lower wings, whereas the upper wings experienced a minor loss. For the hovering RACER, they witnessed the wings to cause a thrust increase of 10.5 % on the—downstream positioned—left lateral rotor, while the respective effect on the reversely operating and therefore upstream positioned right lateral rotor was significantly smaller with only +1.5 %. On the former, Stokkermans et al. traced the influence back to a performance benefit on rotor blades between the bottom and inboard position; despite the lack of comparable inflow data in the absence of the wings, they argued that the wings' shielding effect in this region likely allows the rotor blades to operate in relatively static conditions. In addition, a contrary influence was detected where the upper wing deflected the main rotor downwash and thereby locally increased the left lateral rotor's axial inflow; however, this thrust penalty was assumed to be less dominant, overall leading to the rotor's performance benefit.

1.3.3 Coupled High-Fidelity Simulations

For numerical studies on (rotorcraft) aerodynamics, the validity of results and their transferability to real-world problems depends on a wide range of factors. First of all, the correct representation of flow physics by the applied numerical method is essential for predicting aerodynamic phenomena. This requirement is closely linked to the fidelity of the method, where low- and mid-fidelity simulations such as FVM and VPM are sufficiently accurate to obtain a relatively quick estimate of macroscopic flow phenomena and performance trends. For more challenging flow conditions and a detailed analysis, high-fidelity CFD simulations are required, ranging from steady-state RANS over unsteady URANS to (D)DES methods, large-eddy simulations (LES) or even direct numerical simulations (DNS).

Another important aspect in conducting numerical analyses is the sufficiently accurate representation of the respective geometry. While the inclusion of every detail of the real-world problem is neither feasibly nor necessary for many fields of study, adequate simplifications have to be thoroughly assessed when laying out the simulation setup, as an oversimplification might limit the validity of the results. Specifically for rotorcraft, numerical studies are conducted either on isolated rotors, with the inclusion of dummy components, or with the highly detailed representation of the full configuration. Furthermore, rotors can optionally be included as actuator disks or actuator lines instead of discrete, rotating blades. Conversely, the accuracy of the latters' depiction can further be increased by representing them as elastic structures and deforming them accordingly with the help of computational structural

dynamics (CSD) methods. In recent years, the application of fluid-structure coupling has even lead to extending this elastic representation onto further components of the rotorcraft, which allowed for the analysis of complex phenomena such as tail shake [66].

Besides the geometry, also the flow conditions of a numerical simulation have to correctly represent the respective real-world problem. This can be directly achieved for more abstract or basic cases by prescribing these flow conditions in the numerical analysis, whereas for rotorcraft aerodynamics this often becomes a challenging task. With the helicopter's flight condition being a direct result of its aerodynamic forces, conducting numerical simulations by simply defining any flow condition does not allow for an analysis of a realistic helicopter flight. Thus, the rotorcraft's flight mechanics (FM) have to be taken into account. For this purpose, CA tools combine the aerodynamic analysis of low- or mid-fidelity numerical methods with FM capabilities in order to achieve a trimmed flight state.

The resulting trim condition, consisting of helicopter attitude, rotor controls and possible further degrees of freedom (DOF), together with the aforementioned deformation of flexible rotors provided by the CA tool's CSD feature, can then be provided to a high-fidelity numerical method in order to conduct simulations with more realistic flow conditions. However, this trim state is achieved with aerodynamic methods that are usually based on polars and lookup tables in combination with prescribed- or free-vortex wake methods. Consequently, their accuracy is limited, especially under challenging flight conditions.

In order to overcome these shortcomings, the subsequent high-fidelity simulations can be used as a corrective measure, where the aerodynamic loads of the CFD are fed back to the CA tool and used to determine a new free-flight trim state which is then provided to conduct further CFD simulations. This coupling procedure between CA and CFD can be implemented in two different ways, as described by Altmikus et al. [67] or Potsdam et al. [68]. For the computationally less challenging implementation, the weak or loose coupling, the unsteady CFD simulations are conducted for a sufficient number of time steps to provide the CA tool with periodic rotor loads in the form of radial and azimuthal distributions, whereas the loads on the remaining coupled components are transferred in time-averaged form. For the strong or tight coupling, in contrast, a correction of the trim conditions is repeated after every time step by respectively transferring the CFD loads and determining a new trim state. While it is more complex to implement this method in a computationally efficient manner, it allows for the simulation of dynamic flight conditions and maneuvers.

On most examples of studies on rotor-rotor interaction and rotor-wing interaction with high-fidelity CFD methods in Tables 1.1 and 1.2, only generic flight conditions or an initial trim state were applied. These uncoupled analyses include all studies on Airbus Helicopters' RACER. In contrast, the work of Klimchenko et al. [31] on the Sikorsky X2's coaxial rotors is based on loosely coupled simulations that combine

an in-house CA code of the University of Maryland with the U.S. Department of Defense's CREATE-AV HELIOS framework [69]. HELIOS is a very potent modular tool in the field of CFD in general and coupled simulations in particular that not only embodies a plethora of CFD solvers for different applications and allows for their concurrent operation but also offers a wide range of additional functionalities such as grid generation, adaptive mesh refinement (AMR) or interfaces to CA/CSD tools. Specifically for Klimchenko et al.'s study, NASA's structured CFD solver OVERFLOW [70] was used in conjunction with HELIOS' native Cartesian off-body solver SAMCart.

While HELIOS and the same combination of CFD solvers were also utilized in the study of Sharma et al. [32] on the Sikorsky XH-59A's coaxial rotors, they were loosely coupled to RCAS [71] in this case, a CA tool that was developed by the U.S. Army's Aeroflightdynamics Directorate (AFDD) and incorporates a wide range of features such as FM, CSD and low- to mid-fidelity aerodynamics. Similar functionalities are also included in Johnson Aeronautics' CAMRAD II [72], which was loosely coupled to NASA's OVERFLOW—in this case not wrapped in HELIOS but as a stand-alone solver—in the work of Ventura Diaz et al. [40] on side-by-side rotors. Tran et al.'s [58, 59] study on rotor-wing interactions on the Bell XV-15, in turn, is based on a combination of the aforementioned tools, as they used both RCAS and CAMRAD II within loosely coupled simulations of HELIOS. Here, not only the structured near-body respectively Cartesian off-body solvers OVERFLOW and SAMCart were applied but also NASA's unstructured CFD solver FUN3D [73].

Fully independent of this range of CA and CFD codes, Sugawara and Tanabe [62] conducted loosely coupled simulations on a generic main rotor–wing combination. For this purpose, they utilized the multi-disciplinary toolchain rFlow3D [74], which was developed by the Japan Aerospace Exploration Agency (JAXA) and incorporates CFD, CSD and FM functionalities.

In contrast to these studies applying loose coupling for the analysis of rotor-rotor or rotor-wing interaction, Juhasz et al. [33] utilized a tight coupling in their work on the Sikorsky X2's coaxial rotors. Due to the dynamic nature of the phenomena under investigation, they used this more complex coupling scheme, yet not combining University of Maryland's CA tool HeliUM [75] with a high-fidelity CFD solver but with the mid-fidelity MFW [76], a FVM code also developed by the University of Maryland.

Beyond the analysis of interaction-related topics, various combinations of RCAS/CAMRAD II and HELIOS respectively its CFD solvers in stand-alone mode have been utilized to conduct coupled simulations. Notable examples include the validation studies on flight test data of the Sikorsky UH-60A main rotor with Potsdam et al.'s loosely coupled CAMRAD II–OVERFLOW environment [68] and Bhagwat et al.'s tightly coupled RCAS-OVERFLOW environment [77].

In one of the pioneering works in this field, Altmikus et al. [67] combined Eurocopter's—nowadays Airbus Helicopters—CA tool HOST [78] with Euler simulations of the CFD solvers FLOWer [79], originally developed by the German Aerospace Center (Deutsches Zentrum für Luft- und Raumfahrt, DLR) and fundamentally enhanced by University of Stuttgart's Institute of Aerodynamics and Gas Dynamics (IAG), and WAVES [80], developed by the French Aerospace Lab (Office National d'Études et de Recherches Aérospatiales, ONERA), and compared the results of loose and tight coupling with wind tunnel data of ONERA's 7A model rotor. Loose coupling with HOST and FLOWer was subsequently extended to full helicopter configurations by Dietz et al. [81] and Embacher et al. [82] for wind-tunnel trim and free-flight trim, respectively, whereas Beaumier et al. [83] coupled HOST with WAVES' successor, ONERA's CFD solver elsA [84], and Pahlke and van der Wall [85] combined FLOWer with DLR's CA code S4 [86].

An overview of coupling environments and their validation on the HART II wind tunnel data of a MBB BO-105 rotor was given by Smith et al. [87], comparing the work of different research groups including the aforementioned U.S. Army AFDD, NASA, and DLR.

1.4 Objectives of the Thesis

According to Ormiston [6], research and development of new (rotorcraft) technology requires—among other measures—"developing [the] fundamental understanding [of], e.g., fluid flow or dynamics phenomena". With advanced rotorcraft configurations, targeted at closing the "Mobility Gap" by extending the flight envelope of conventional helicopters, new and unexpected flow phenomena are likely to occur and consequently have to be investigated thoroughly.

As a direct consequence of these flow phenomena, aerodynamic interactions play an important role in the required investigation, especially as they are critical in a variety of aspects within the rotorcraft's development and operation (see Section 1.1). For this reason, this thesis is aimed at the analysis of aerodynamic interactions, with the specific configuration of study being Airbus Helicopters' compound helicopter RACER.

This helicopter demonstrator is selected due to the author's involvement in the project CA^{3}TCH (Coupled Aerodynamic-Aeroacoustic Analysis of a Trimmed Compound Helicopter), IAG's contribution to RACER's risk reduction prior to its first flight and a co-operation with Airbus Helicopters within the Fast Rotorcraft section of European Commission's Clean Sky 2 research framework.

RACER's additional box wing and lateral rotors for lift and thrust compounding in combination with its main rotor are likely to spawn a variety of interactional phenomena, highly depending on the flight conditions. As illustrated in Sections 1.3.1

and 1.3.2, rotor-rotor and rotor-wing interactions have been the subject of various studies on multiple configurations, with some of the results possibly transferable to the RACER compound helicopter. Even on this particular demonstrator, interactions were recently analysed as the main subject or side topic of several publications; however, these studies have miscellaneous shortcomings. First of all, they were entirely based on uncoupled simulations, leading to limited validity of the results regarding their representation of realistic flow phenomena (see Section 1.3.3). Furthermore, the applied CFD methods were either steady-state [43], inviscid mid-fidelity [46], included only a subset of RACER's geometry [46], or represented the main rotor as an actuator disk [43, 47].

In contrast, for this thesis high-fidelity unsteady CFD simulations are performed on a comprehensive geometry of RACER, where main and lateral rotors are represented as discrete, rotating, and—in the case of the main rotor—elastic blades. Furthermore, a loose coupling is applied between CFD and CA in order to achieve a trimmed flight state. More details on the simulation setup and the necessary preliminary studies are included in Chapters 2 and 3.

Among previous studies on RACER, Wentrup et al. [43] tried to isolate the interactional phenomena by comparing the aerodynamic results of lateral rotors and wings for different helicopter attitudes; a discrimination between interactional effects and the change in flow conditions as a cause for potential differences is consequently difficult. In contrast, Stokkermans et al. [47] compared different setups omitting individual components in order to isolate the respective interactions. Their focus on lateral rotors and the resulting lack of specific isolated configurations as well as the lateral rotors' retrim for selected cases, however, limited the comprehensiveness of their analysis.

For this thesis, the approach for the isolation of aerodynamic interactions similarly is based on numerical simulations of different setups of RACER, increasingly reducing the full geometry by individually removing the relevant components, namely main rotor, wings, and lateral rotors. In this manner, not only their direct or first-order interactional effects can be identified but also the indirect or second-order influences of the respective components, which were mostly disregarded in previous studies on compound helicopter interactions. Details on this approach can be found in Chapter 4.

With the extension of helicopters' flight envelopes towards a higher flight speed being the main intention behind the development of compound helicopters, cruise flight at RACER's design cruise speed of 220 kts is one of the flight conditions analysed in this thesis. The results on aerodynamic interactions of main rotor, wings, and lateral rotors in cruise flight are illustrated in Chapter 5.

Despite RACER's focus on increasing flight speed, the VTOL capability remains a vital aspect in the operation of compound helicopters, which is why hover is

selected as another relevant flight condition for this thesis. Chapter 6 illustrates the respective interactional effects of main rotor, wings, and lateral rotors in hover.

As these two flight conditions are antipodal in RACER's flight envelope, they give a good impression of possible interactional phenomena overall; for other flight conditions, the effects can—to some extent—be interpolated and superposed from the results from cruise flight and hover, which are summarized in Chapter 7's conclusions and outlook.

2 Simulation Setup

This thesis' analysis of aerodynamic interactions is based on high-fidelity numerical simulations with the CFD solver FLOWer. For the reasons elaborated in Section 1.3.3, however, representing a realistic flight state additionally requires the coupling to a CA tool. In a first step, FLOWer is therefore coupled to the CA tool HOST in order to achieve a trimmed flight state, which is subsequently applied to all the CFD simulations used for the isolation of interactional effects.

With a tight coupling scheme, achieving helicopter trim is challenging regarding computational efficiency as well as convergence of the trim solution [68]. Due to the loose coupling's characteristic of naturally resulting in a trimmed flight state based on its periodic approach, this scheme is selected instead for this purpose. As illustrated in Fig. 2.1, the coupling is realized with the help of the coupling manager HeliCATS which coordinates the CA and CFD tools and transfers the respective data between them within each trim cycle.

This process is initialized by the CA tool which determines a trim state based on the user-defined trim law with the help of the integrated low- to mid-fidelity numerical methods for aerodynamic modelling. The resulting trim controls together with the rotor deformations provided by the CSD capability are subsequently processed by the coupling manager and, where required, transformed to the required input format of the CFD solver. The latter then conducts high-fidelity simulations until a converged, periodic solution is available.

Within a last step of the coupling cycle, the coupling manager extracts the aerodynamic forces from the CFD solution and transfers them back to the CA tool. In contrast to the tight coupling scheme, where this loop is repeated after every time step of the CFD simulation, the loads have to be provided to the CA tool in an azimuth-dependent form for the loose coupling.

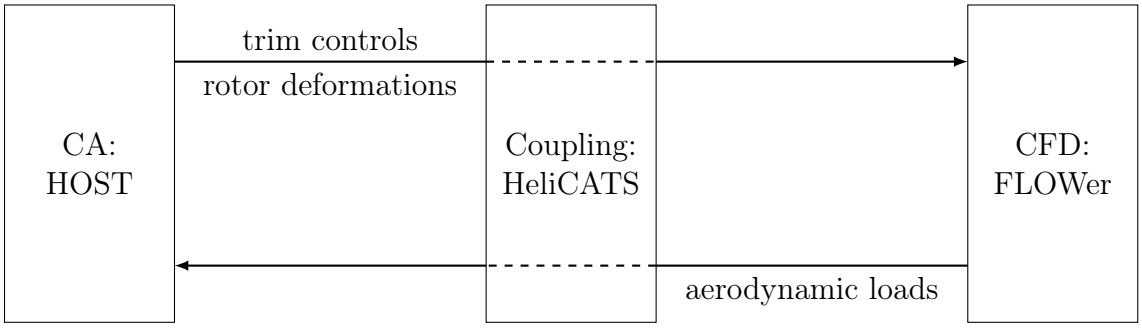

Figure 2.1: Toolchain for loose coupling of simulations required to achieve a trimmed flight state.

The general idea of the coupling process is to use these forces F and moments M—gained with a high-fidelity numerical method—as a corrective measure for the low- or mid-fidelity integrated aerodynamics of the CA tool. For this reason, at the beginning of all subsequent coupling iterations i the difference in forces and moments during the previous trim cycle $i-1$ are determined:

$$\Delta F/M_{i-1} = F/M_{CFD,i-1} - F/M_{CA,i-1}\,. \tag{2.1}$$

This difference is then used to correct the CA loads of the new iteration:

$$F/M_i = F/M_{CA,i} + \Delta F/M_{i-1}\,. \tag{2.2}$$

Optionally, a relaxation factor α can be applied to prevent the trim controls from oscillating over multiple cycles, taking into account the corrections from more than one previous iterations:

$$F/M_i = F/M_{CA,i} + \alpha\,\Delta F/M_{i-1} + (1-\alpha)\,\Delta F/M_{i-2}\,. \tag{2.3}$$

After determining a new trim state with these corrected forces and moments, this is again provided to the CFD solver to conduct new simulations. A converged trim state is reached, when the trim controls over multiple subsequent cycles remain within an acceptably small range that highly depends on the complexity of the trim law and flight conditions.

2.1 Coupling: HeliCATS

The loose coupling between CA and CFD is provided by HeliCATS, a coupling manager that was jointly developed and is continuously enhanced by Airbus Helicopters and IAG. It is implemented in Python and executed on a local workstation.

Data transfer is performed fully file-based and, in the case of the aerodynamic loads delivered by the CFD solver, includes additional steps of processing in order to meet the CA tool's requirements for input. As the loose coupling is based on periodicity, all loads have to be provided in azimuth-dependent form. For rotors, HeliCATS therefore assembles time-dependent load distributions of the individual blades to full polars of the force and moment components. Aerodynamic loads on the remaining helicopter components are not only bundled in accordance with the individual segmentation in the CA modelling but also time-averaged.

2.2 CA: HOST

RACER's CA modelling is realized with the help of HOST [78], which was developed by Airbus Helicopters and, in recent years, complemented by the python wrapper GHOST (Generalized HOST). Within the scope of this study, GHOST is executed on a local workstation with a model of RACER provided by Airbus Helicopters.

2.2.1 Features

The aerodynamic modelling of RACER's rotors is realized with a combination of blade element theory (BET), where two-dimensional airfoil polars of the rotor sections are provided, and two different inflow models, which are FISUW [78] for the main rotor and Meijer-Drees [88] for the lateral rotors. The aerodynamics of the remaining compound helicopter is modelled by means of individual three-dimensional look-up tables of fuselage, box wing, wing flaps, horizontal and vertical stabilizer, as well as rotor head, where the respective polars originate from previous CFD and wind tunnel analyses.

In contrast to the lateral rotors, which are considered to be rigid in this study, the main rotor is represented by an elastic blade model based on a quasi one-dimensional elastic Euler–Bernoulli beam. The blades' DOFs are reduced by applying a modal Rayleigh–Ritz approach and, based on the findings of a previous study, only a limited number of mode shapes are included for flap (4), lag (3) and torsional motion (3). With the help of a specific interface, the resulting deformations are exported in a format suitable for the CFD solver, on a discretization of 77 nodes along the blade span and with 15 temporal harmonics for each of the six translational and rotational DOFs.

2.2.2 Trim in Cruise Flight

Based on the forces and moments derived from its on-board aerodynamics capabilities, for non-initial iterations additionally corrected as indicated in Eqs. 2.2 or 2.3, HOST's FM feature determines RACER's trim state with the help of a trim law specific to the selected flight conditions. For this study, a free-flight trim is selected, which means that an equilibrium of forces and moments in all directions has to be achieved for a steady, non-accelerated flight:

$$\sum F_{x,y,z} = 0\,, \tag{2.4}$$

$$\sum M_{x,y,z} = 0\,. \tag{2.5}$$

Consequently, in vertical direction the lift has to counteract the helicopter's weight, whereas all remaining forces and moments are required to be balanced.

Table 2.1: Free-flight trim law in cruise flight.

Trim objectives	Trim controls	Prescribed trim variables
$\sum F_{x,y,z} = 0$, L_{MR},	θ_0, θ_C, θ_S, $\theta_{0,LR}$, Φ,	Ω, $\theta_{\Delta,LR}$, $\Theta = \Psi = 0$,
$\sum M_{x,y,z} = 0$, β_C	η_{elev}, η_{rud}, $\eta_{0,wing}$	$\eta_{\Delta,wing} = \eta_{\Delta,lwing} = \eta_{\Delta,rwing} = 0$

Due to RACER's compound configuration, its total number of body and control DOFs significantly exceeds a conventional helicopter's: attitude (3), main rotor controls (3), lateral rotor controls (2), wing flaps (4), elevator (1), rudder (1), and rotor rotational frequency (1) amount to 15 DOFs overall. In order to reduce the resulting arbitrary number of possible flight states, further trim objectives are required and redundant controls have to be prescribed. A study on the optimization of associated efficiencies has been conducted by Thiemeier [20].

The cruise flight investigated for this study is conducted at RACER's design cruise speed of 220 kts, in an altitude of 6000 ft, and at maximum take-off weight (MTOW). While this defines the total lift required for a trimmed free-flight, additionally the main rotor lift L_{MR} is prescribed as a trim objective in order to achieve a lift share of roughly 50 % with the help of the main rotor collective control θ_0 at a prescribed rotor rotational frequency Ω. Due to the pitch attitude Θ and yaw attitude Ψ being fixed to 0°, the residual lift is controlled by the wing flaps, which are not deflected individually but collectively ($\eta_{0,wing}$) and the differential flap angles ($\eta_{\Delta,wing}$, $\eta_{\Delta,lwing}$, $\eta_{\Delta,rwing}$) consequently set to 0°.

Longitudinal force balance is achieved with the lateral rotors' collective pitch control $\theta_{0,LR}$, whereas the main rotor's share in propulsive force is prescribed as an additional trim objective by means of its longitudinal flapping angle β_C. The trim control responsible for this is the main rotor lateral cyclic θ_S. Furthermore, the respective longitudinal cyclic control θ_C enables the trim of the lateral force balance.

The equilibrium of the helicopter is completed with roll angle Φ, elevator deflection η_{elev}, and rudder deflection η_{rud} allowing for the balance of rolling, pitching, and yawing moment, whereas the lateral rotors' contribution to the latter is eliminated by prescribing their differential pitch control $\theta_{\Delta,LR}$. The full eight DOF free-flight trim law is summarized in Table 2.1.

Convergence of the individual controls during the trim process is illustrated in Fig. 2.2 and shows multiple distinct changes. Most prominently, a significant leap in nearly all controls can be witnessed between the initial solution—referred to as iteration 0—and the first retrim, originating from the corrective influence of the high-order CFD solution and emphasizing the necessity of coupling to achieve a trimmed, representative flight state. In further course, the changes between subsequent trim iterations quickly decrease, only interrupted by a distinct step in lateral rotor collective control at iteration 9. The underlying change in longitudinal force balance

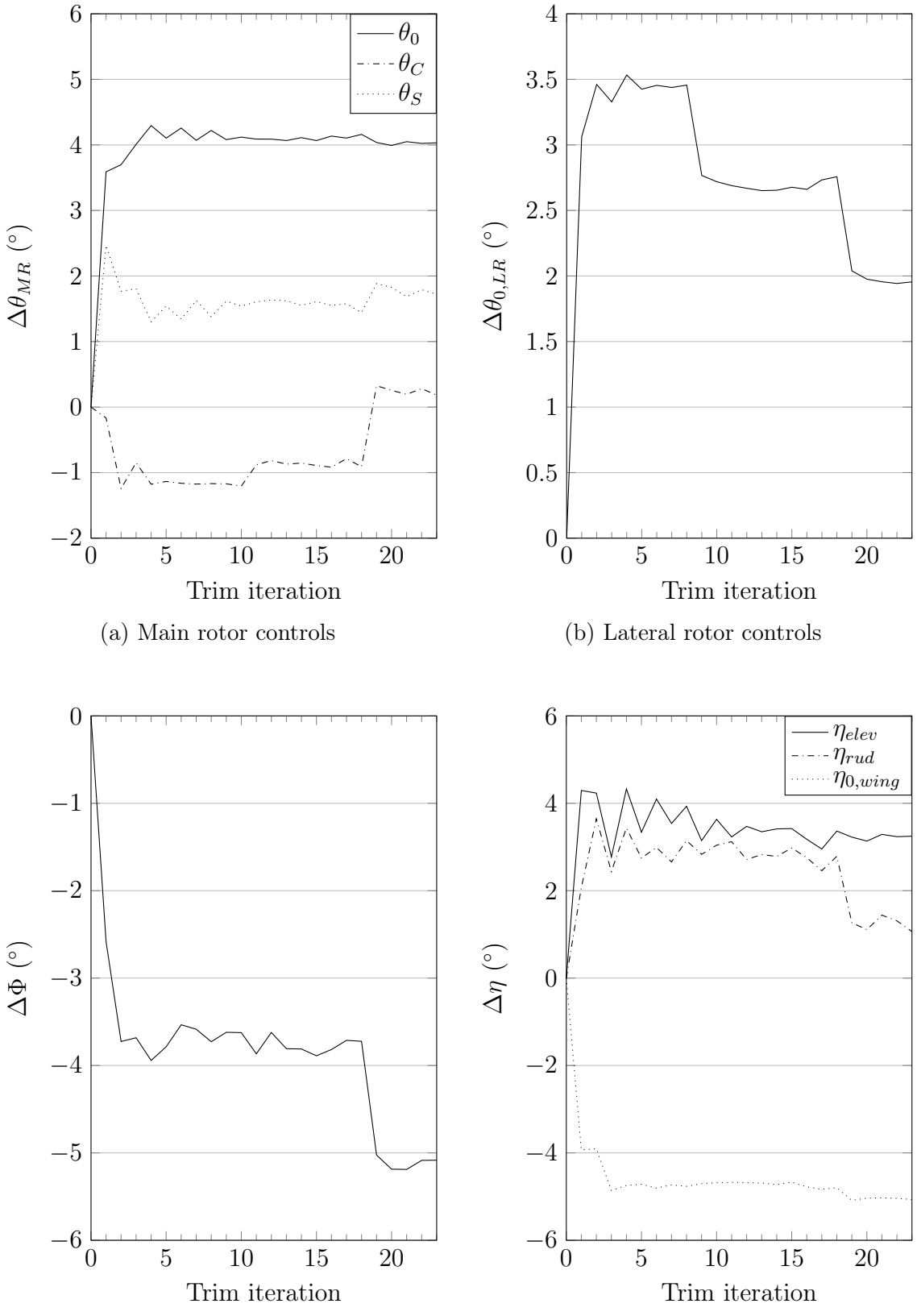

(a) Main rotor controls

(b) Lateral rotor controls

(c) Helicopter attitude

(d) Flap angles

Figure 2.2: Trim convergence of the cruise flight simulations. Relative to initial trim.

Table 2.2: Residual translational and rotational accelerations of the cruise flight simulations prior to the final trim iteration.

$\ddot{x}$	$-0.006\,\mathrm{m/s^2}$
$\ddot{y}$	$+0.023\,\mathrm{m/s^2}$
$\ddot{z}$	$+0.012\,\mathrm{m/s^2}$
$\ddot{\Phi}$	$-1.1\,^\circ/\mathrm{s^2}$
$\ddot{\Theta}$	$-0.9\,^\circ/\mathrm{s^2}$
$\ddot{\Psi}$	$+2.3\,^\circ/\mathrm{s^2}$

is caused by the additional inclusion of—mostly propulsive—forces originating from the engine.

In order to expedite the trim process, the first 10 iterations are adopted from a very similar cruise flight case, where the wing flaps can be deflected asymmetrically at the expense of additionally prescribing the main rotor's lateral flapping angle as a trim objective. Consequently, releasing this constraint while eliminating the differential wing flap deflection is reflected in a slight step of the longitudinal cyclic control.

Lastly, the significant change at iteration 19 is the result of correcting a faultily defined boundary condition in the CFD setup. While this affects only a small portion of the simulated domain, the positioning of this boundary condition close to RACER's right nacelle explains the strong influence on rudder control and lateral rotor collective control; however, the resulting change in trim state extends to almost all remaining trim controls.

As illustrated in Fig. 2.2, changes in trim controls become relatively small after iteration 20. While rudder deflections remain in a range of 0.4°, all other controls are even converged to a significantly higher degree, with most of them lying in a range of less than 0.1°. Convergence can be further confirmed by investigating the loads equilibrium achieved in the respective CFD simulations. Based on the residual loads, including aerodynamic and inertial forces and moments, translational and rotational accelerations can be calculated with the help of helicopter mass m and mass moment of inertia $I_{xx,yy,zz}$:

$$\ddot{x}, \ddot{y}, \ddot{z} = \frac{\sum F_{x,y,z}}{m}\,, \tag{2.6}$$

$$\ddot{\Phi}, \ddot{\Theta}, \ddot{\Psi} = \frac{\sum M_{x,y,z}}{I_{xx,yy,zz}}\,. \tag{2.7}$$

The individual residual accelerations achieved in the simulations of iteration 22 are listed in Table 2.2. With maximum values of $0.023\,\mathrm{m/s^2}$ and $2.3\,^\circ/\mathrm{s^2}$, the accelerations are in a very similar range to the convergence Embacher et al. [89] achieved for loosely coupled simulations of a Eurocopter EC145 in cruise flight at 136 kts. As

the latter additionally observed a trend of growing residual accelerations for higher flight speed, reaching a comparable convergence at 220 kts is deemed sufficient for this study. Consequently, HOST's subsequent retrim in iteration 23 is defined as the trimmed free-flight state for the investigations on aerodynamic interactions in cruise flight.

2.2.3 Trim in Hover

For the analysis of aerodynamic interactions in hover, a flight state at sea level out of ground effect is selected. Similar to the cruise flight, a free-flight trim is aimed for; consequently, the equilibrium of forces and moments according to Eqs. 2.4 and 2.5 must be adhered to. As no further trim objectives are defined for this flight state, the resulting six DOF trim law accordingly requires a reduction of the aforementioned 15 potential trim controls.

Due to the lack of longitudinal convective inflow to wings and stabilizers, all flaps remain undeflected. Consequently, with the main rotor being the sole contributor of lift to the vertical force balance, the main rotor collective control θ_0 is trimmed to achieve the required lift at a prescribed rotor rotational frequency Ω. The cyclic controls θ_C and θ_S additionally enable the trim of lateral and longitudinal force balance. The lateral rotors' contribution to the latter is prescribed via a fixed collective pitch control $\theta_{0,LR}$, as in hover the lateral rotors are not responsible for propulsion but rather generation of anti-torque. Collective pitch control is selected in a way that allows for an anti-torque ratio of 70 %/30 % between left and right lateral rotor. The smaller contribution of the right lateral rotor is caused by its unfavourable operating condition in reverse thrust.

Lateral rotor differential pitch control $\theta_{\Delta,LR}$, in contrast, is trimmed to achieve sufficient total anti-torque for yawing moment balance, whereas roll attitude Φ and pitch attitude Θ are responsible for equilibrium in rolling and pitching moment. Yaw attitude Ψ, however, has no significance in hover and therefore is prescribed to 0° in the trim law. An overview of the six DOF free-flight trim law can be found in Table 2.3.

The convergence of these controls during the trim process is illustrated in Fig. 2.3. Similar to the convergence of the simulations in cruise flight (see Fig. 2.2), the corrective influence of the high-order CFD results is reflected in significant leaps of the main rotor collective and lateral rotor differential control at the first retrim.

Table 2.3: Free-flight trim law in hover.

Trim objectives	Trim controls	Prescribed trim variables
$\sum F_{x,y,z} = 0$,	θ_0, θ_C, θ_S,	Ω, $\theta_{0,LR}$, $\Psi = 0$, $\eta_{elev} = \eta_{rud} = 0$,
$\sum M_{x,y,z} = 0$	$\theta_{\Delta,LR}$, Φ, Θ	$\eta_{0,wing} = \eta_{\Delta,wing} = \eta_{\Delta,lwing} = \eta_{\Delta,rwing} = 0$

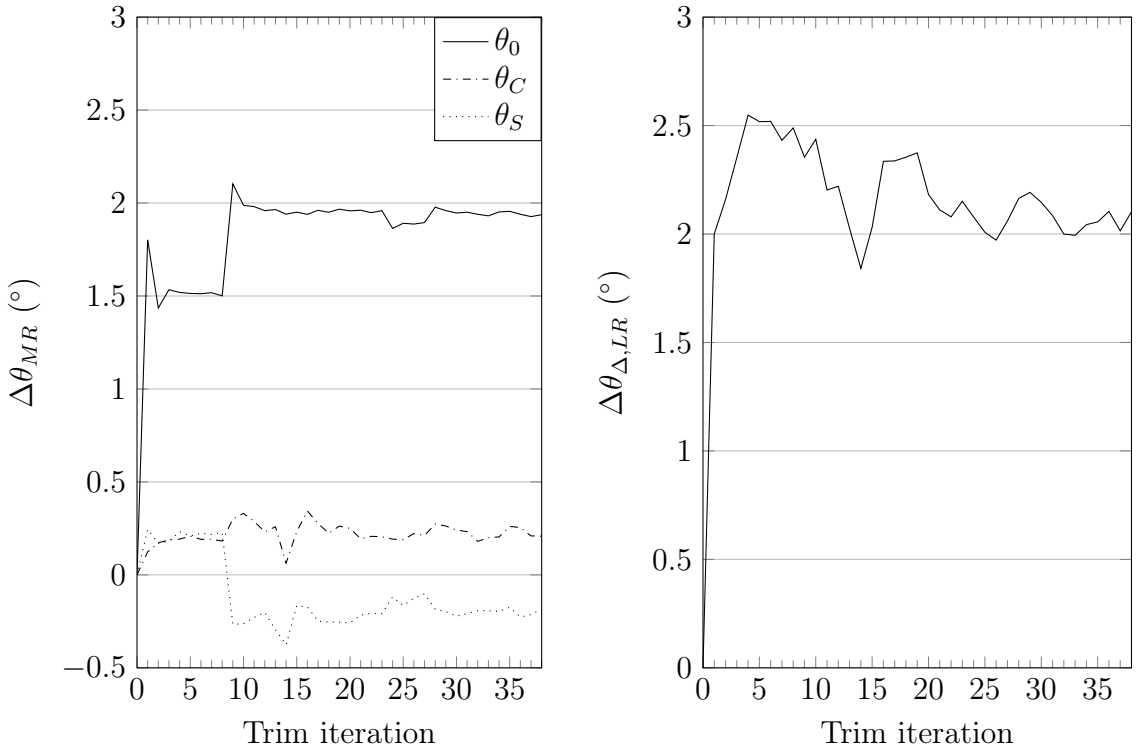

(a) Main rotor controls

(b) Lateral rotor controls

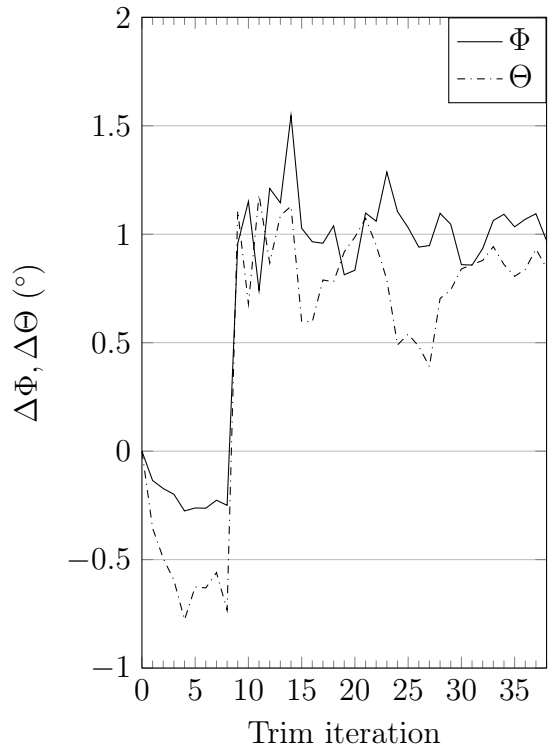

(c) Helicopter attitude

Figure 2.3: Trim convergence of the hover simulations. Relative to initial trim.

Table 2.4: Residual translational and rotational accelerations of the hover simulations prior to the final trim iteration.

$\ddot{x}$	$+0.023\,\mathrm{m/s^2}$
$\ddot{y}$	$+0.034\,\mathrm{m/s^2}$
$\ddot{z}$	$-0.024\,\mathrm{m/s^2}$
$\ddot{\Phi}$	$-0.2\,^\circ/\mathrm{s^2}$
$\ddot{\Theta}$	$-0.3\,^\circ/\mathrm{s^2}$
$\ddot{\Psi}$	$+1.8\,^\circ/\mathrm{s^2}$

The main rotor cyclic controls and the helicopter's pitch and roll attitude at trim iteration 1, in contrast, remain relatively close to HOST's initial solution.

While all trim controls converge to relatively constant values after roughly five iterations, only the loads of main and lateral rotors are corrected with delta loads according to Eq. 2.2 at this stage. With the additional coupling of fuselage, wings, horizontal and vertical stabilizers at iteration 9 as well as the concurrent consideration of engine forces, considerable changes are visible in Fig. 2.3, particularly for the main rotor collective control and helicopter attitude. Furthermore, the full coupling of the helicopter's loads leads to larger fluctuations of the trim controls between consecutive iterations.

In order to eliminate the resulting oscillations, a relaxation of the delta loads is introduced in iteration 17 for lateral rotors, fuselage, and stabilizers. The load correction of these components is therefore applied according to Eq. 2.3 with a relaxation factor of $\alpha = 0.6$. A similar relaxation for the wing loads is subsequently added with iteration 29, leading to a reduction of spikes in the trim controls' convergence history.

Consequently, remaining oscillations are largely reduced after iteration 35, and the rotor controls remain in a range of well below 0.1°. The pitch and roll attitude are almost similarly well-converged.

After determining the residual loads achieved in the simulations of iteration 37, the induced translational and rotational accelerations can be calculated according to Eqs. 2.6 and 2.7. The resulting values listed in Table 2.4 are very similar to the accelerations achieved for the cruise flight simulations (see Table 2.2). The associated loads equilibrium is therefore considered to confirm sufficient convergence, and HOST's subsequent retrim in iteration 38 is selected as the trimmed free-flight state for the investigations on aerodynamic interactions in hover.

2.3 CFD: FLOWer

The CFD simulations this study of RACER's aerodynamic interactions is based on are conducted with FLOWer. This CFD solver was originally developed by DLR [90]

and significantly extended by IAG, for instance regarding its high performance computing (HPC) capabilities.

2.3.1 Numerical Methods

The basic idea of CFD is solving the governing equations of fluid dynamics for a given problem in order to predict the behaviour of the fluid and its interaction with solid bodies. For this purpose, the underlying conservation laws of mass, momentum and energy are combined in the Navier–Stokes equations which, according to Blazek [91], can be written in integral form as follows:

$$\frac{\partial}{\partial t}\int_{\Omega}\vec{W}\,\mathrm{d}\Omega+\oint_{\partial\Omega}\left(\vec{F}_C-\vec{F}_V\right)\mathrm{d}S=\int_{\Omega}\vec{Q}\,\mathrm{d}\Omega\,. \tag{2.8}$$

Here, the first term describes the variation in time of the vector $\vec{W}$—representing the unknown conservation variables of mass, momentum and energy—in the control volume Ω. The second term comprises the respective fluxes traversing the control volume's surface S and consists of the convective fluxes $\vec{F}_C$ and the viscous fluxes $\vec{F}_V$. The equilibrium is completed by the source term $\vec{Q}$, comprising external influences like body forces or heating.

The Navier–Stokes equations are a system of five equations which contain the seven unknown flow field variables ρ, v_x, v_y, v_z, E, p, and T. Consequently, two additional equations are required to close the system, accounting for the thermodynamics of the fluid. Typically, in CFD solvers the ideal gas law is applied for this purpose.

By neglecting any viscous effects, the Navier–Stokes equations are simplified significantly, and the resulting Euler equations can be solved with relatively low computational effort to describe an inviscid fluid. The simulation of turbulence, however, is considerably more challenging and the application of DNS only possible at low Reynolds numbers and for relatively simple flow conditions [91].

In order to overcome these limitations, various approaches to approximate the effect of turbulence have been developed, reducing the computational cost of the corresponding simulations while also sacrificing a certain degree of accuracy. The least invasive turbulence modelling is applied with LES, as it only affects small scales in the form of relatively simple subgrid-scale models, whereas the larger scale flow features are directly resolved.

In a more extensive approach of approximation, the flow variables in the Navier–Stokes equations are decomposed into mean and fluctuating parts and subsequently time-averaged. The resulting RANS equations additionally contain the Reynolds-stress tensor and the turbulent heat-flux vector, which have to be determined by means of the variety of RANS turbulence models. These range from the relatively complex and computationally costly Reynolds-stress models (RSM) to the simpler

zero-, one-, or two-equation models which express the Reynolds stresses with the help of a turbulent eddy viscosity and subsequently determine the latter based on semi-empirical results. As the RANS simulations with one- or two-equation models provide a good compromise between computational effort and accuracy, they are particularly popular for engineering applications. Amongst these, the one-equation model of Spalart and Allmaras [92] as well as the k-ω two-equation model of Wilcox [93] and Menter's shear-stress transport (SST) model [94]—a combination of the k-ω and k-ϵ models—are most widely applied.

Finally, a hybrid RANS/LES approach is available in the form of DES, where RANS with respective turbulence models is applied in the attached boundary layers within a flow field, whereas the larger turbulent structures in the detached flow are resolved by means of LES. This additionally requires a shielding mechanism that is responsible for the discrimination between the two different treatments.

2.3.2 Features

FLOWer uses a finite volume formulation of the governing equations with a block-structured discretization of the control volume. For the present study, computations were carried out with a cell-centered scheme, whereas FLOWer also offers the application of a cell-vertex approach [90]. Among the available schemes for spatial discretization, the second-order central difference Jameson–Schmidt–Turkel (JST) [95] scheme is applied as well as the sixth-order weighted essentially non-oscillatory (WENO) scheme according to Borges et al. [96], which was implemented in FLOWer at IAG [97].

Simulations can be conducted both in steady and time accurate mode, where the time discretization of the latter is realized with the help of a second-order implicit dual-time stepping method [98]. Convergence acceleration is achieved by means of a three-level multigrid approach.

While FLOWer originally was only capable of conducting Euler and (U)RANS simulations, IAG's implementation of hybrid RANS/LES methods and experimental DES shielding functions [99] further extended its scope, together with the modelling of laminar-turbulent transition [100]. For the study at hand, however, the flow is treated to be fully turbulent.

FLOWer's arbitrary Lagrangian Eulerian (ALE) formulation allows for the treatment of rotating and deforming structures and therefore makes it well-suited for the simulation of rotorcraft. The addition of the IAGCOUPle library furthermore enables a radial basis function (RBF) based mesh deformation and facilitates post-processing via the output of various types of loads for arbitrary structures [101, 102].

2.3.3 Mesh Topology

Due to its Chimera overset grid technique, FLOWer allows for the decomposition of the computational domain into individual structures and therefore significantly increases flexibility in the elaborate generation of structured meshes. For the RACER geometry, which is represented in high detail within the CFD simulations for this study, the surface was therefore divided into smaller subdomains which were fitted with individual structured grids in a collaboration of the author with his colleagues Constantin Öhrle and Jakob Thiemeier. The full helicopter consequently is assembled from 101 near-body grids. An overview of the mesh can be seen in Fig. 2.4 from Frey et al. [103] (note: only every second grid line is shown in the central illustration for the sake of clarity).

RACER's representation within the CFD simulation is fitted with a main rotor with five discrete, clockwise rotating blades. These are treated as elastic structures and therefore deformed according to the HOST output provided via coupling, which combines the elasticity and dynamics of the blades with their control angles θ_0, θ_C, and θ_S. As illustrated in Detail (a) of Fig. 2.4, the rotor hub is modelled in detail and includes the blade roots and interblade dampers, which are equally deformed to account for the kinematics of blade pitch, flap and lag.

Deformation is furthermore applied to deflect wing flaps as well as flaps and rudders on elevator and fins corresponding to their respective controls $\eta_{0,wing}$, $\eta_{\Delta,wing}$, $\eta_{\Delta,lwing}$, $\eta_{\Delta,rwing}$, η_{elev}, and η_{rud} provided by HOST's trim state (see Detail (b)). Another feature of RACER's CFD setup is the representation of the engines, not only geometrically as inlet ducts (see Detail (c)) and exhaust nozzles but also by specific boundary conditions. Hereby, a prescribed mass flux and exhaust temperature is distributed uniformly over the engine outlets, whereas the iterative adjustment of the inlets' pressure at every time step ensures mass conservation of each engine flow [104].

The engine exhausts additionally comprise a cooling flow, which furthermore is also implemented on the lateral rotors' nacelles. The respective outlet upstream of the spinners is illustrated in Detail (d), together with the attachment of the six discrete, inboard-up rotating blades constituting each lateral rotor. In order to allow for a pitching movement of the latter's meshes according to the respective control angles $\theta_{0,LR}$ and $\theta_{\Delta,LR}$ provided by HOST, a slight modification of the geometry was necessary at the transition between blades and spinner. In contrast to the main rotor, the blades of the lateral rotors are treated as rigid structures due to their significantly larger stiffness and consequently smaller deformations.

Unless explicitly stated otherwise, the lateral rotors are represented by these discrete rotating blades. For selected analyses, however, the two lateral rotors are replaced by actuator disks, which prescribe a specific force distribution exerted by

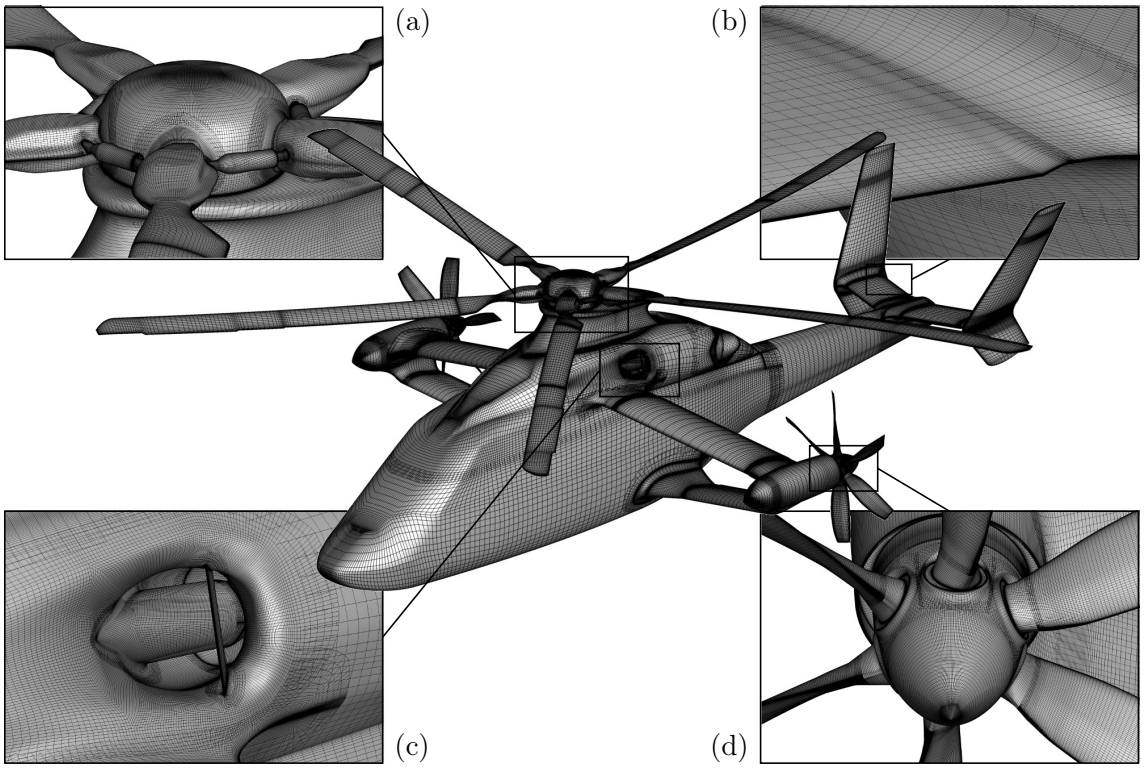

Figure 2.4: Overview of the CFD mesh (center, every second grid line shown) with details of (a) rotor hub, (b) deformed flap, (c) engine inlet, and (d) lateral rotor spinner [103].

the lateral rotors onto the flow field. The respective input for the loads is derived from corresponding simulations with discrete rotating blades.

The spatial resolution of the main rotor blades is based on a grid convergence study by Öhrle et al. [105], resulting in an O-type mesh with 2.0 million cells for each of the blades ($152 \times 228 \times 52$ cells in chordwise, spanwise and normal direction, respectively), which includes the trim tabs in the outer region. A similar study was conducted for the grids of RACER's wings and lateral rotors by Frey et al. [106], the findings of which the CFD setup of this thesis is based on. The normal grid spacing of these meshes is selected to guarantee a dimensionless wall distance in the surface cells of $y^+ < 1$, equally to all remaining near-body grids, which are furthermore designed to accurately represent the helicopter's geometry. In total, these 101 near-body structures amount to 103.4 million cells; an overview of the individual contribution of different components is given in Table 2.5.

By means of the Chimera technique, these near-body grids are embedded in a Cartesian off-body grid, which extends over the full simulation domain. As illustrated in Fig. 2.5, this spans over roughly $14R$ in each dimension for the simulations of cruise flight, whereas the lack of forced flow convection in hover requires a significantly larger computation domain ($\approx 69R$) to avoid any effects of its borders

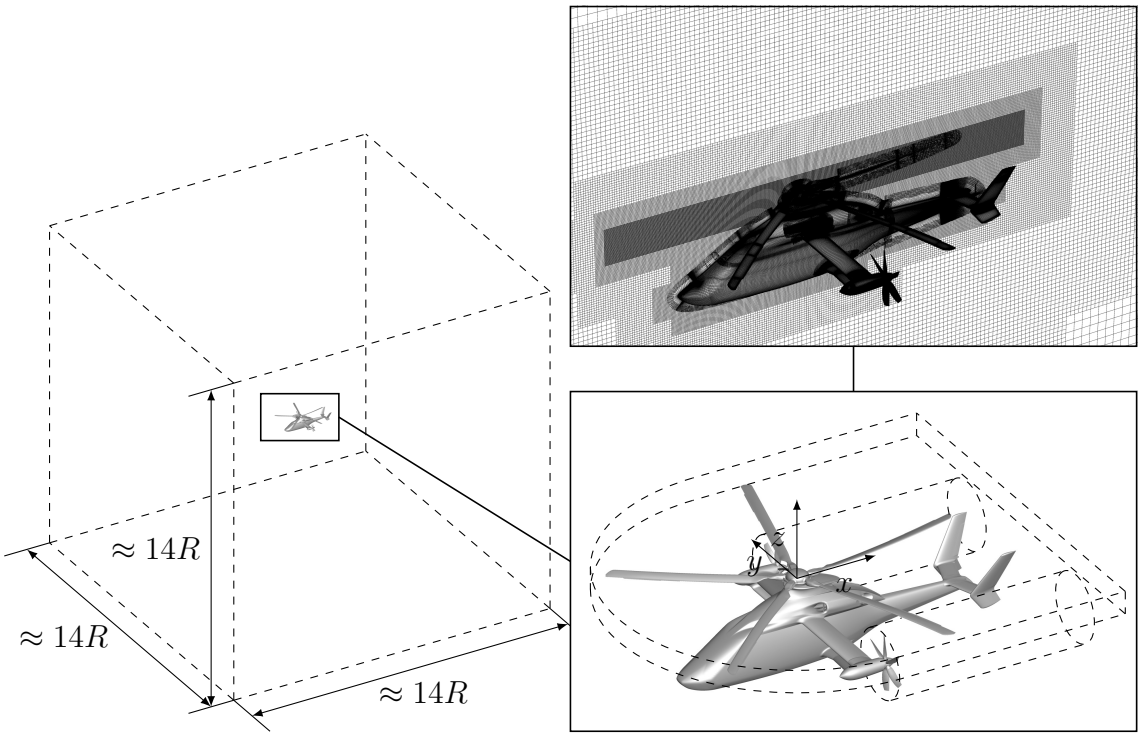

(a) Cruise flight

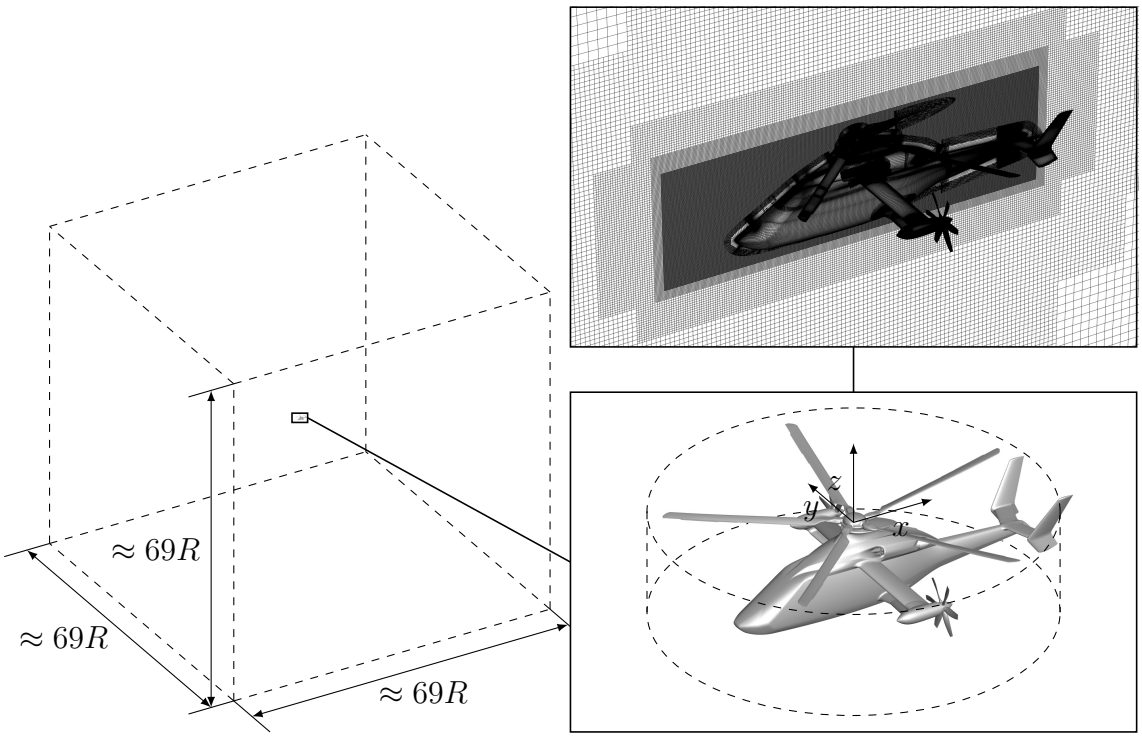

(b) Hover

Figure 2.5: Simulation domain with wake refinement, coordinate system, and mesh slice.

Table 2.5: Breakdown of number of cells in near-body grids.

Component	Number of cells (million)
Main Rotor	9.9
Wings	11.6
Lateral Rotors	23.4
Fuselage	8.8
Tailboom	2.3
Empennage	10.1
Nacelles	8.1
Rotorhead	12.3
Engine	17.0
Total	103.4

and their far field boundary conditions onto the flow around the helicopter. Both dimensions were determined in a preliminary study.

In the airframe's vicinity, the resolution of the Cartesian off-body grid is roughly $10\,\%\,c_{MR}$—similar to the maximum spacing of the near-body meshes—whereas it is coarsened with growing distance from the helicopter with the help of hanging grid nodes. In order to account for particularly sensitive flow features and their conservation, an additional refinement is provided towards the main rotor ($\approx 5\,\%\,c_{MR}$) and the lateral rotors ($\approx 10\,\%\,c_{LR}$).

While an AMR was implemented in FLOWer in recent years [107], this feature is not used for the present study. Therefore, the refined resolution of approximately $5\,\%\,c_{MR}$ is also applied to the regions of the expected rotor wakes. As illustrated in Fig. 2.5(a), this refinement extends from the respective rotors up to the passage of the helicopter's tail in case of cruise flight, whereas in hover the expected downwash region encompasses the entirety of RACER's airframe except for the empennage, guaranteeing the adequate representation of occurring interactions.

The resulting off-body grids comprise 54.9 and 88.1 million cells for the cruise flight and hover simulations, respectively. Together with the near-body meshes, this amounts to a total of 158.3 and 191.5 million cells for the two different CFD setups.

2.3.4 Simulations in Cruise Flight

For the cruise flight condition at 220 kts described in Section 2.2.2, RANS simulations are conducted on the respective CFD setup. Based on long experience at IAG with various of FLOWer's turbulence models, Wilcox' two-equation k-ω model [93] is selected as it was found to cover most of a helicopter's flow features sufficiently accurate [108].

An overview of the most relevant CFD settings applied during the different phases of computations is given in Table 2.6. The simulations for the previously described

Table 2.6: CFD settings for the simulations in cruise flight.

Computation		$\Delta\Psi_{MR}$	n_{MR}	$n_{MR,avg}$	n_{it}	WENO
Trim process		steady	—	—	1000	
	0–4	1.5°	2	1	40	
	5–14	1°	2	1	40	
	15–18	0.5°	2	1	30	×
	19–22	0.5°	1.2	1	30	×
Evaluation		steady	—	—	1000	
		1°	2	—	60	×
		0.5°	2	—	30	×
		0.25°	2	1	30	×

trim process (see Fig. 2.2) are initialized by a steady computation with a number of iterations of $n_{it} = 1000$. This is followed by unsteady simulations for each of the trim iterations, which are always restarted from the flow solution of the previous step with only the respective trim controls and main rotor deformations adapted according to HOST's retrim.

In order to accelerate trim convergence, the initial time step for the simulations is selected relatively large with a corresponding main rotor azimuthal step of $\Delta\Psi_{MR} = 1.5°$. With progressing trim iterations, this is repeatedly reduced to improve the accuracy of the simulations and consequently the trim state. The number of inner iterations of the dual-time stepping scheme n_{it} is accordingly selected and guarantees a sufficient convergence of the individual time steps.

For each of the trim iterations, the aerodynamic loads of the simulations are averaged over one main rotor revolution ($n_{MR,avg}$) and subsequently provided to HOST to determine a new trim state. Due to the high velocity of the examined flight state and the resulting quick convection of the flow field around the helicopter, the necessary transition following a retrim until the solution is converged to periodicity and the evaluation interval can be started is equally fast. Consequently, the simulation of $n_{MR} = 2$ main rotor revolutions per trim cycle is sufficient for the first 18 iterations, whereas subsequently this can be even further reduced to 1.2 due to the small changes in trim controls associated with the retrim.

With its superior robustness and relatively low computational cost, the second-order JST [95] scheme is used for spatial discretization for the first 14 trim iterations. In order to increase accuracy and reduce the dissipation of flow features, for the subsequent iterations the sixth-order WENO [96] scheme is applied to the off-body mesh, which benefits most from this due to its Cartesian structure.

Following this trim process, the converged trim state (see Section 2.2.2) is used to conduct the computations for the analysis of aerodynamic interactions in the scope of this study. As illustrated in Table 2.6, this is also initialized with the

help of steady RANS simulations. For the subsequent unsteady computations, the azimuthal step of the main rotor associated with the time step is progressively reduced from 1° to 0.25°. More details on the selection of this final time step are included in Section 3.1. The evaluation interval used for the analysis of aerodynamic interactions is determined to one main rotor revolution according to the findings of the preliminary study described in Section 3.2.

2.3.5 Simulations in Hover

Conducted on the respective CFD setup, the simulations for the hover conditions specified in Table 2.7 are generally similar to the previously described computations on cruise flight. However, the lack of forced flow convection necessitates significantly longer simulation intervals in order to convect flow features solely through the propagation of main rotor downwash and lateral rotor wakes. Consequently, after an initialization with steady RANS simulations, URANS computations of five main rotor revolutions are required to establish a flow field the trim process can be based on.

Furthermore, the interval used for averaging the loads provided to HOST is increased to two main rotor revolutions beginning with trim iteration 23 in order to account for a weaker periodicity of the solutions compared to the cruise flight. This additionally requires raising the simulation period for these computations to three main rotor revolutions.

As illustrated in Table 2.7, the simulation period is also significantly longer for the computations used for the analysis of aerodynamic interactions in hover—based on the converged trim state from Section 2.2.3—than they are for the respective evaluation of the cruise flight state. For each of the phases of decreasing time steps, 5–10 main rotor revolutions are computed. Following the findings of the preliminary

Table 2.7: CFD settings for the simulations in hover.

Computation		$\Delta\Psi_{MR}$	n_{MR}	$n_{MR,avg}$	n_{it}	WENO	DES
Trim process		steady	—	—	1000		
		1°	5	—	60		
	0–7	1°	2	1	60		
	8–22	0.5°	2	1	30	×	
	23–37	0.5°	3	2	30	×	
Evaluation		steady	—	—	1000		
		1°	5	—	60		
		1°	5	—	60	×	
		0.5°	5	—	30	×	×
		0.25°	10	5	30	×	×

study on periodicity in Section 3.2, the flow field is evaluated for five full main rotor revolutions for the analysis of aerodynamic interactions within this study.

While the schemes for spatial discretization are handled similarly to the simulations in cruise flight—JST on the near-body structures and off-body mesh switched from JST to WENO—the k-ω turbulence model is only universally applied during the trim process and the first phases of evaluation computations. For the final CFD simulations, however, based on the results of a preliminary study on turbulence modelling (see Section 3.3) DES computations are conducted instead of RANS simulations.

2.3.6 HPC

In order to efficiently conduct CFD simulations on millions of cells, parallelization of the computations is absolutely essential. For this purpose, FLOWer makes heavy use of the message passing interface (MPI), the application of which has been significantly optimized over the years to improve code performance for massive parallel scaling [102, 109, 110]. This allows for efficient computations on large high-performance computing systems using several thousand processors.

All CFD computations in the scope of this study have been conducted on the Hazel Hen Cray XC40 cluster of the High Performance Computing Center Stutt-

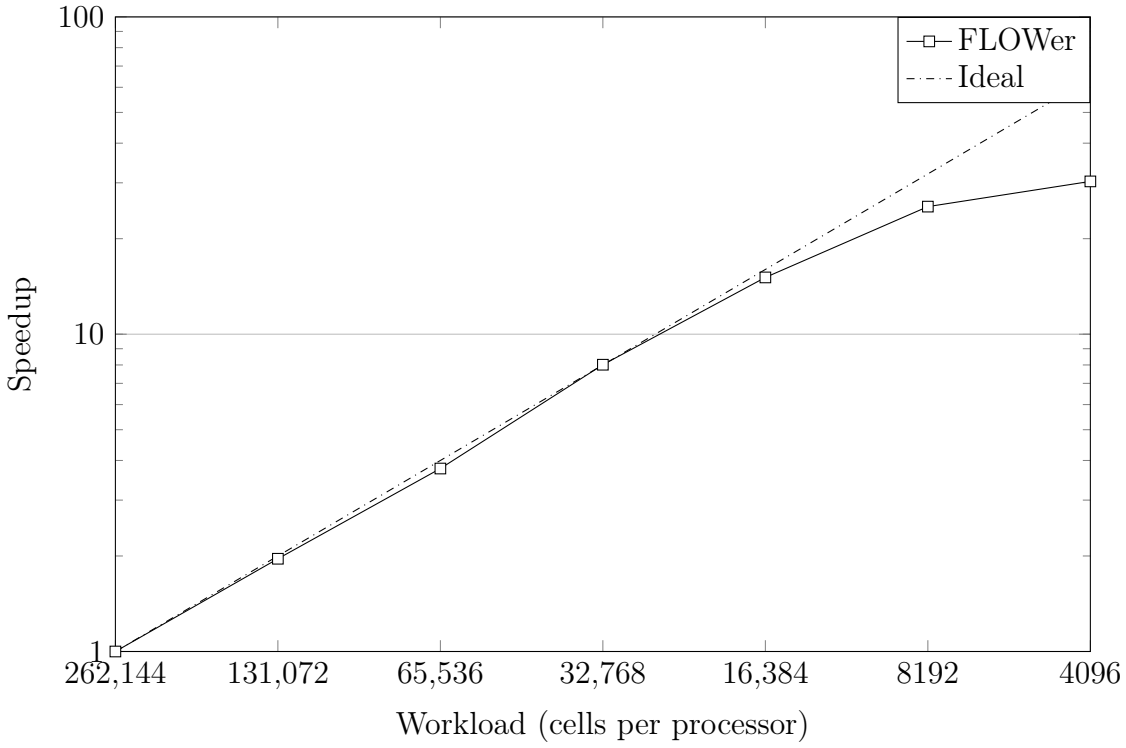

Figure 2.6: Strong scaling of FLOWer on Hazel Hen Cray XC40 with a CFD setup of 134 million cells. Adapted from Letzgus et al. [110].

gart (HLRS). For this purpose, the grids for cruise flight and hover described in Section 2.3.3 were split beforehand to achieve an average workload of 16,384 cells per processor. Such a parallelization was found to be optimal in a previous study by Letzgus et al. [110] on FLOWer's strong scaling with a similarly large CFD setup (see Fig. 2.6).

The simulations described in Sections 2.3.4 and 2.3.5 consequently were conducted on 9816 and 11,880 processors, respectively. With this parallelization, a full main rotor revolution on the finest temporal resolution ($\Delta\Psi_{MR} = 0.25°$), hence with 1440 time steps, was accomplished in roughly 10 h wall clock time.

3 Preliminary Studies

The generation of the underlying setups as well as the actual computation of the simulations described in Chapter 2 are strongly based on best practice and experience gained for CFD simulations in general and the flow solver FLOWer in particular. While for many of the relevant parameters a relatively universal guideline can be followed, others depend heavily on the specific geometry and flight condition examined, as well as on the scope of the analysis.

For this reason, preliminary studies are required to correctly select the respective settings of the computations. In the first of the following sections, the impact of the temporal resolution on the CFD solutions is assessed and the time step for the simulations described in Sections 2.3.4 and 2.3.5 is defined; this analysis is based on Frey et al. [106].

In addition to the temporal resolution, also the evaluation period is critical for the validity of the results and the conclusions drawn from them. This chapter therefore additionally contains an examination of the simulations' periodicity.

It is concluded by an analysis of different approaches for turbulence modelling, which is of particular interest for the simulations in hover and the resulting investigation of aerodynamic interactions. The respective section is based on Frey et al. [111].

3.1 Temporal Resolution

With the focus of the present study lying on the interactions between main rotor, wings, and lateral rotors, the selection of the time step for the CFD simulations is especially important to guarantee the correct representation of these effects. While the temporal discretization for previous studies on RACER [21] was set to 0.5° of the main rotor azimuth—with larger time steps of 1–1.5° during the first iterations of the trim process—the effect of a further reduction in two steps is analysed here.

For this purpose, the simulation setup of RACER described in Section 2.3 is used for three different computations of cruise flight at 220 kts with a time step of $\Delta\Psi_{MR} = 0.5°$, 0.25° and 0.125°, respectively, in their final phase. A comparison of the global main rotor loads is illustrated in Fig. 3.1(a) as the relative changes of forces and moments in relation to the largest time step.

A converging behaviour can be found for the longitudinal and lateral forces (F_x, F_y) with changes of hardly over 1 %, whereas the lift F_z shows no notable deviations for all three temporal discretizations. The same accounts for the torque M_z—and consequently main rotor power—with changes of less than 0.5 %. Significantly

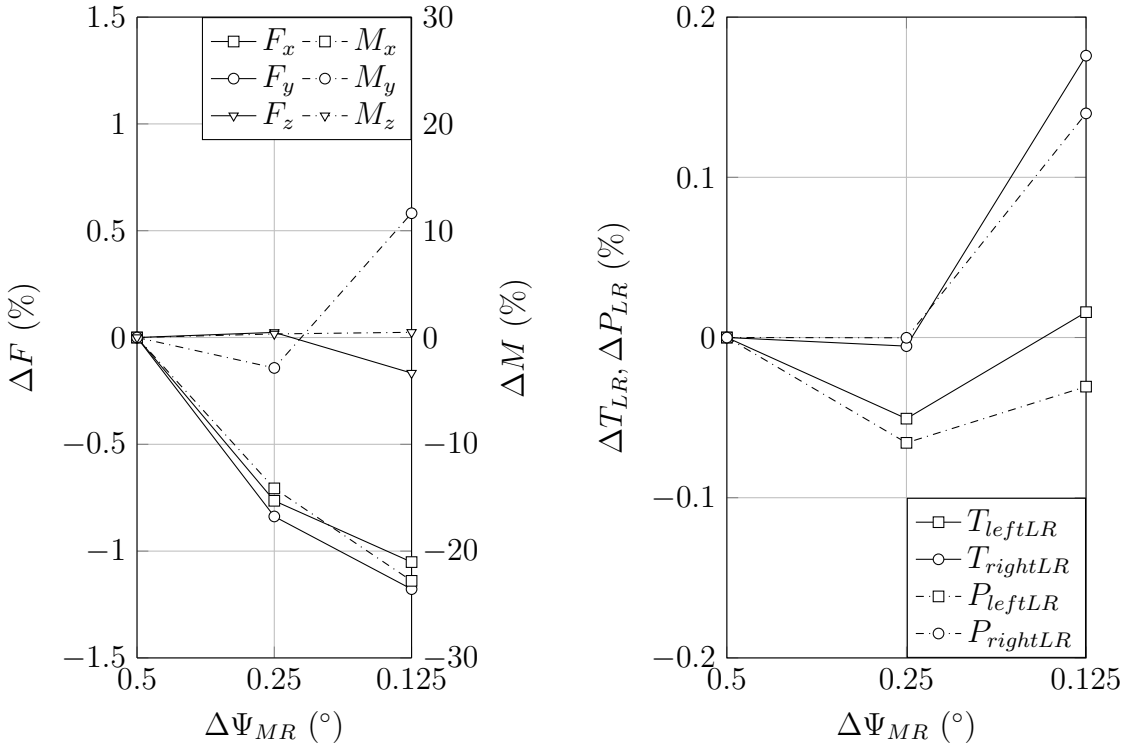

(a) Main rotor loads

(b) Lateral rotor thrust and power

Figure 3.1: Relative change of rotor loads and power with different temporal discretization. Averaged over one main rotor revolution [106].

larger relative changes can be found for the rolling and pitching moments (M_x, M_y); however, these are caused by the small absolute values of these loads, strongly emphasizing their variation for different time steps.

Besides the aerodynamic performance of the main rotor also the behaviour of the lateral rotors is of particular interest within this temporal resolution study, not only as the focus of this analysis of aerodynamic interactions is also aimed at these components, but also as the fixed gearing ratio between main rotor and lateral rotors leads to a roughly six times larger azimuthal step on the latter. Nevertheless, this step size needs to be sufficiently small to capture the aerodynamic effects on the lateral rotor blades. In order to analyse the sensitivity of the lateral rotor performance towards the temporal resolution, Fig. 3.1(b) illustrates both lateral rotors' changes in thrust and power for the three different time steps.

While the changes of thrust and power on the left lateral rotor are significantly smaller than 0.1 % for all three time steps, the right lateral rotor shows increasing deviations for the smallest discretization of $\Delta\Psi_{MR} = 0.125°$. However, these values are sufficiently small at $\Delta T_{rightLR}, \Delta P_{rightLR} \approx 0.15\,\%$ and therefore below the accuracy requirements of this study.

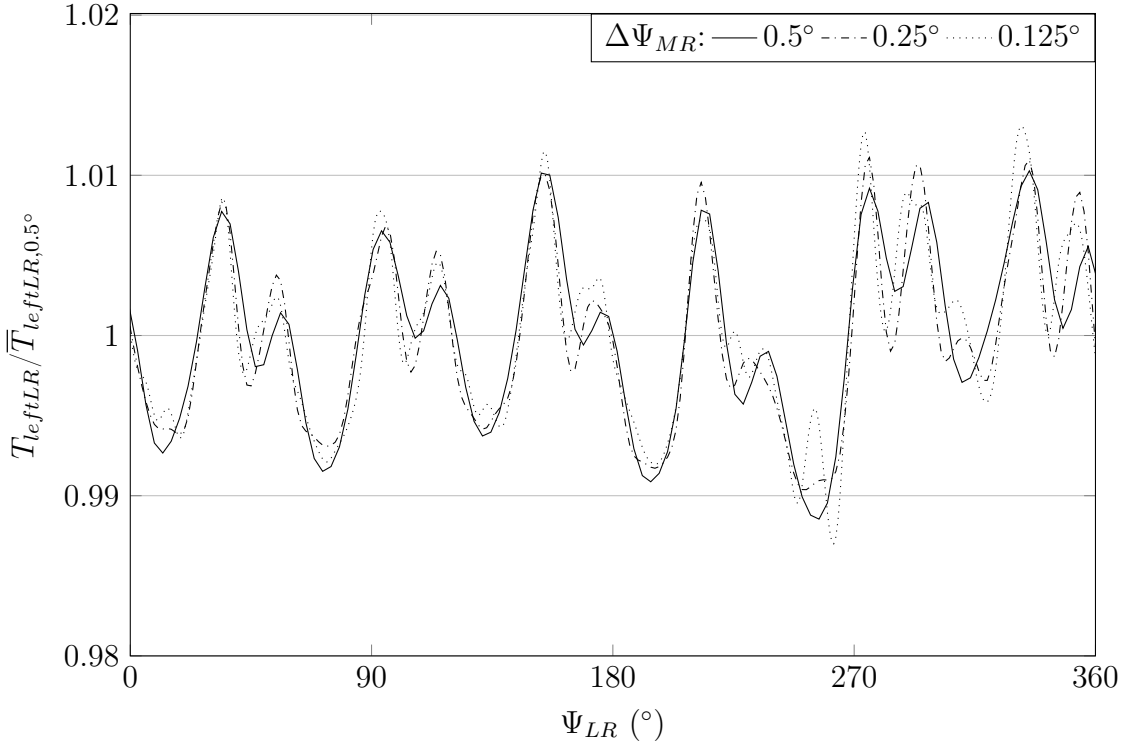

Figure 3.2: Thrust of left lateral rotor with different temporal discretization. Normalized with average thrust of lateral rotor for largest time step [106].

With this thesis' scope on the interactional effects between main rotor, wings, and lateral rotors, not only the average loads are of particular interest, but also the load fluctuations need to be represented accurately in order to analyse their changes under the influence of other components. For this reason, the global thrust of the left lateral rotor is exemplarily illustrated in Fig. 3.2 for all three temporal discretizations over the course of one lateral rotor revolution.

A sharper representation of the fluctuation's peaks can be observed for the first refinement of time steps at $\Delta\Psi_{MR} = 0.25°$, furthermore indicating the inclusion of higher harmonics. The second refinement towards the smallest time step, however, does not alter the characteristics of the load fluctuations in a way that would justify the additional computational cost.

Together with the conclusions from main rotor loads and lateral rotor performance, the medium temporal resolution with a time step of $\Delta\Psi_{MR} = 0.25°$ is therefore decided to be sufficient to resolve the aerodynamic effects in the scope of this work. While a further refinement would lead to another doubling of the computational cost, it has only limited effect on the analysed results and can therefore be deemed unnecessary.

3.2 Periodicity

With the inclusion of rotating structures and occurrence of unsteady phenomena, no convergence in a steady manner can be achieved for the simulations in the scope of this study. Instead, all analyses have to be based on results from a specific evaluation period, the selection of which is crucial for their validity. Due to the rotating nature of RACER's geometry in flight, an inherent periodicity of the flow field and the underlying phenomena can be expected, dominating over stochastic effects that might require a significantly longer evaluation window for their adequate representation in the resulting analysis.

In order to assess the effect of both periodic and stochastic effects on results relevant for the evaluation of aerodynamic interactions, the cumulative moving average (CMA) of main and lateral rotor thrust as well as wing lift is calculated for the final stages of the CFD simulations in cruise flight and hover (see Tables 2.6 and 2.7). This does not determine the average of all available values for a force F but gives a transient progression with an evaluation window over all values prior to the respective number of main rotor revolutions n_{MR}:

$$\mathrm{CMA}F\left(n_{MR}\right) = \frac{\sum_{i=1}^{i(n_{MR})} F}{i\left(n_{MR}\right)}\,. \tag{3.1}$$

The resulting CMA of thrust and lift over one main rotor revolution of cruise flight is displayed in Fig. 3.3(a). On the main rotor, the strong change of inflow conditions experienced by the blades over the course of one revolution leads to fluctuations with a periodicity of $\Psi_{MR} = 72°$ or $n_{MR} = 0.2$, respectively, as a result of the total number of five blades. Consequently, an evaluation is only advisable over a full number of periods, which, in turn, yields almost constant CMA values mostly within a range of 0.1 %.

The periodicity of the main rotor thrust as well as the marginal influence of otherwise induced or stochastic effects is supported by Fig. 3.4's comparison of the five cycles during this main rotor revolution, illustrated by means of their deviation from the phase-averaged mean cycle or time-synchronous average (TSA), respectively. With cycle-to-cycle variations clearly playing only a minor role, the analysis of the main rotor regarding aerodynamic interactions can be expected to deliver reliable results with an evaluation window over a full number of periods.

While, according to Fig. 3.3(a), fluctuations on lateral rotor thrust and wing lift additionally show characteristics of the lateral rotors' periodicity with six rotor blades and a roughly six times larger rotational frequency, a clear periodicity originating from the main rotor is visible on lateral rotors and right wings with relatively constant CMA values for multiples of $n_{MR} = 0.2$. As the CMA of the left wings remains within a range of less than 0.2 % at $0.8 < n_{MR} < 1$—thus indicating a

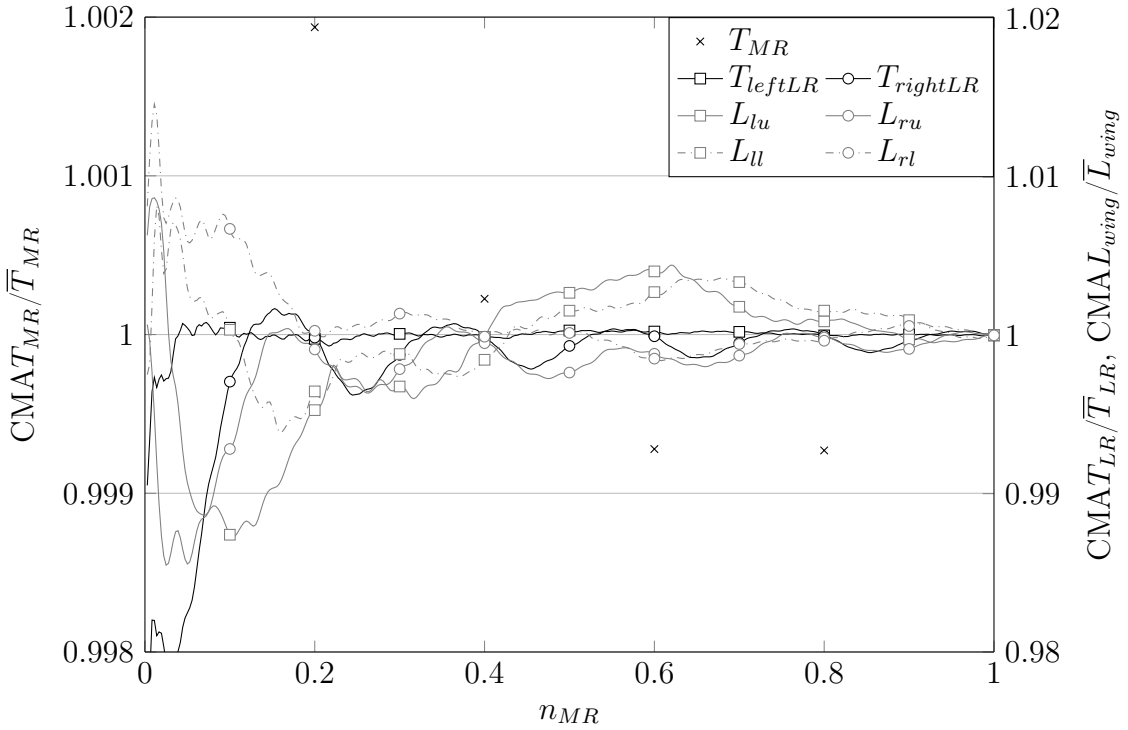

(a) Cruise flight

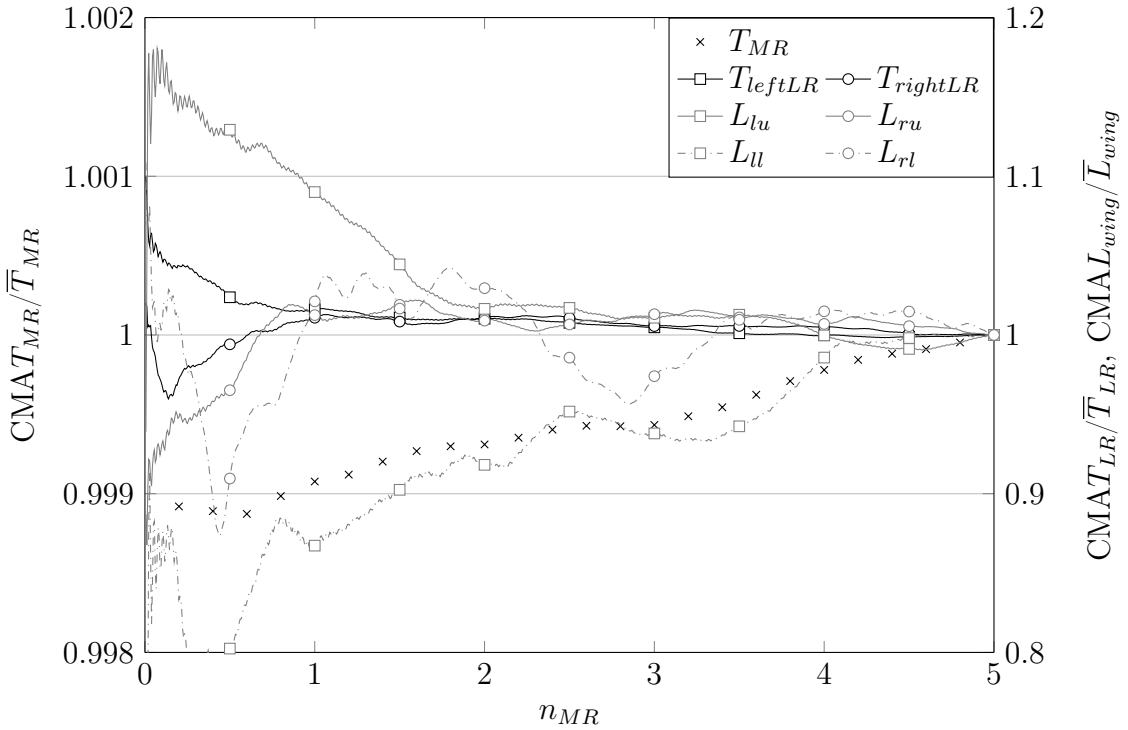

(b) Hover

Figure 3.3: CMA of rotor thrust and wing download with increasing width of averaging window. Only values for full periods included for main rotor thrust. Normalized with average rotor thrust and wing download for maximum averaging window.

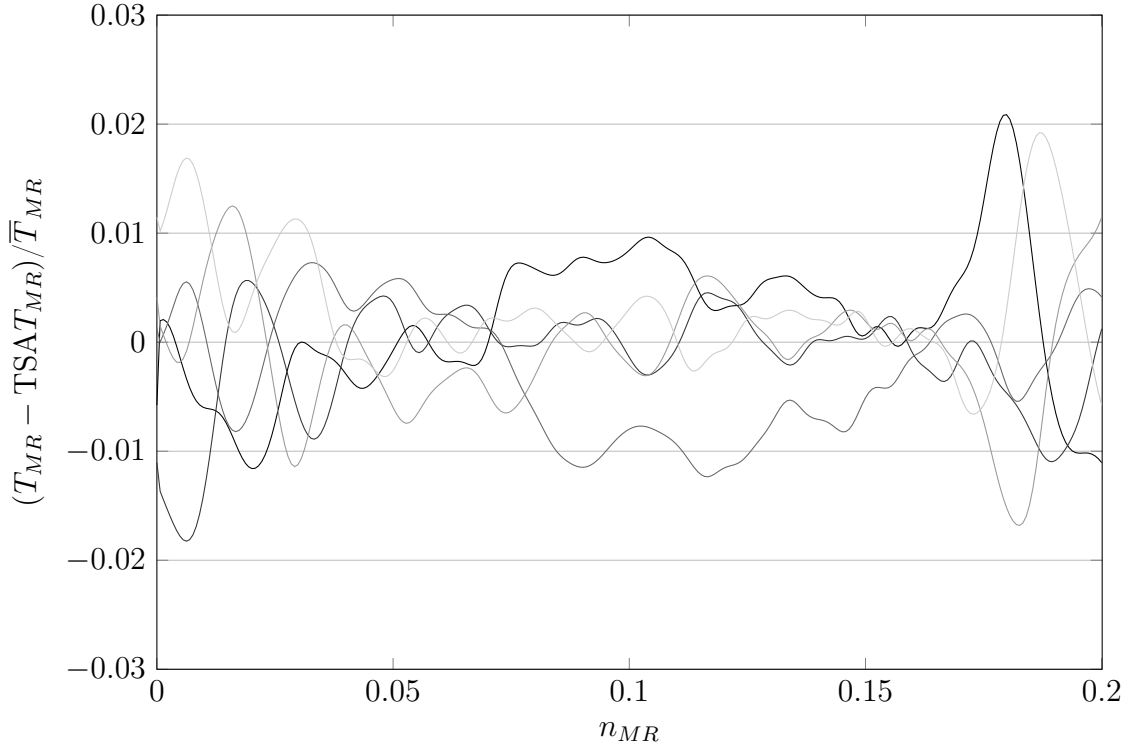

Figure 3.4: Deviation of main rotor thrust from phase-averaged mean cycle in cruise flight for five consecutive cycles over one main rotor revolution. Normalized with average thrust of main rotor.

negligible influence of stochastic effects—an evaluation window over one main rotor revolution is selected for the analysis of aerodynamic interactions in cruise flight.

With the lack of forced convection, the periodicity of the main rotor loads can be expected to play a significantly smaller role for the hover simulations. In light of the present thesis' focus on interactions with subjacent components, however, selecting an evaluation window over a full number of periods nevertheless remains sensible. According to Fig. 3.3(b), the absence of notable stochastic effects leads to a particularly small range of CMAT_{MR} over a period of five main rotor revolutions. While a certain influence of the lateral rotors' periodicity can be witnessed on lateral rotor thrust and wing lift by means of high-frequency fluctuations for small evaluation windows ($n_{MR} < 0.5$), the dominance of stochastic phenomena is clearly illustrated by medium- and long-term drifts of the respective CMA.

This leads to the requirement of a significantly longer evaluation period than for the cruise flight simulations. As the CMA of all relevant loads remains within a range of 2 % for $4 < n_{MR} < 5$, the evaluation of the hover simulations regarding aerodynamic interactions over five main rotor revolutions is considered to be a reasonable trade-off with the resulting computational cost.

3.3 Turbulence Modelling

In long experience at IAG with various of FLOWer's turbulence models, Wilcox' two equations $k-\omega$ model [93] was found to cover most of a helicopter's flow features sufficiently accurately [108]. For this reason, URANS simulations with this turbulence modelling are selected as an appropriate basis for the analysis of aerodynamic interactions on RACER in cruise flight, where a relatively conventional flow regime can be expected.

For the analysis of hover, however, where large regions of separated flow can be expected below the wings, in combination with this study's focus on interactions, which are likely affected by this flow separation, the use of Menter's widely applied SST turbulence model [94] is considered.

In addition to these URANS simulations, within a preliminary study, DDES with Menter SST as underlying RANS model is carried out for the evaluation computations illustrated in Table 2.7. The hybrid RANS/LES capabilities were implemented into FLOWer in recent years [99] and were found by Letzgus et al. [112] to show a good agreement of separated flows with experimental data "regarding size and shape of incoherent vortical structures". As the impingement of such structures shed from the upper wings onto the lower wings is one of the main interactional features in this study's scope, their accurate representation is considered particularly important, with the DDES approach consequently being a promising alternative to URANS simulations.

Figure 3.5 illustrates the vorticity magnitude on a longitudinal slice through the wings for the three different approaches, namely URANS with Wilcox and Menter SST turbulence model, and DDES with Menter SST. Clearly, the distributions generally show very good agreement both qualitatively and quantitatively. The blade tip vortices convect and dissolve into smaller structures in a similar manner; the conservation of the vorticity in the boundary layers shed from the main rotor blades and convecting downwards is equally provided.

While the separated flow structures below the wings differ to a certain degree, the highly unsteady nature of this phenomenon makes it difficult to compare them based on a momentary impression. However, all three distributions show distinct vortical structures of varying scales, in contrast to unphysical uniformly large-scale structures.

As the characteristics of the flow separation influences the loads of the wings both at the shedding and the impingement, a closer look on these forces is necessary. Figure 3.6 therefore illustrates the change in vertical force on all four wings in relation to the respective forces for the Wilcox URANS simulation.

On the upper wings, the URANS loads differ by roughly 2 % for the two different turbulence models, whereas the discrepancy is significantly larger on the lower wings. However, this is not only caused by a different representation of the impinging

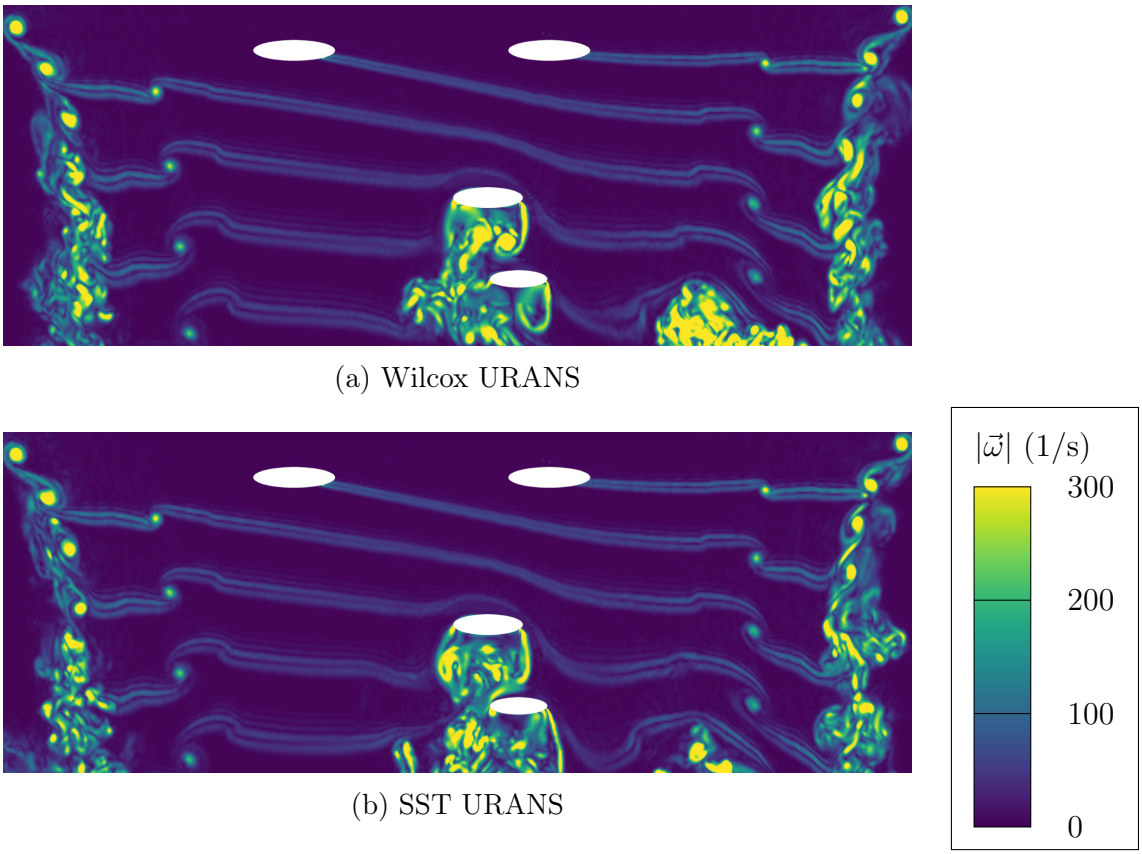

(a) Wilcox URANS

(b) SST URANS

(c) SST DDES

Figure 3.5: Distribution of vorticity magnitude with different turbulence modelling on longitudinal slice at $y/b = -0.33$ [111].

separated flow structures but also by the generally relatively low loads on the lower wings which quickly leads to larger relative changes. In comparison with the URANS results of the same turbulence model, except for the left upper wing, the DDES simulations mostly show little or no difference in wing lift.

In addition to the average loads, the flow separation also affects the load fluctuations. For this reason, a fast Fourier transform (FFT) of the vertical wing forces obtained from the three different approaches is conducted over three main rotor revolutions, where an almost full number of lateral rotor cycles is achieved. The

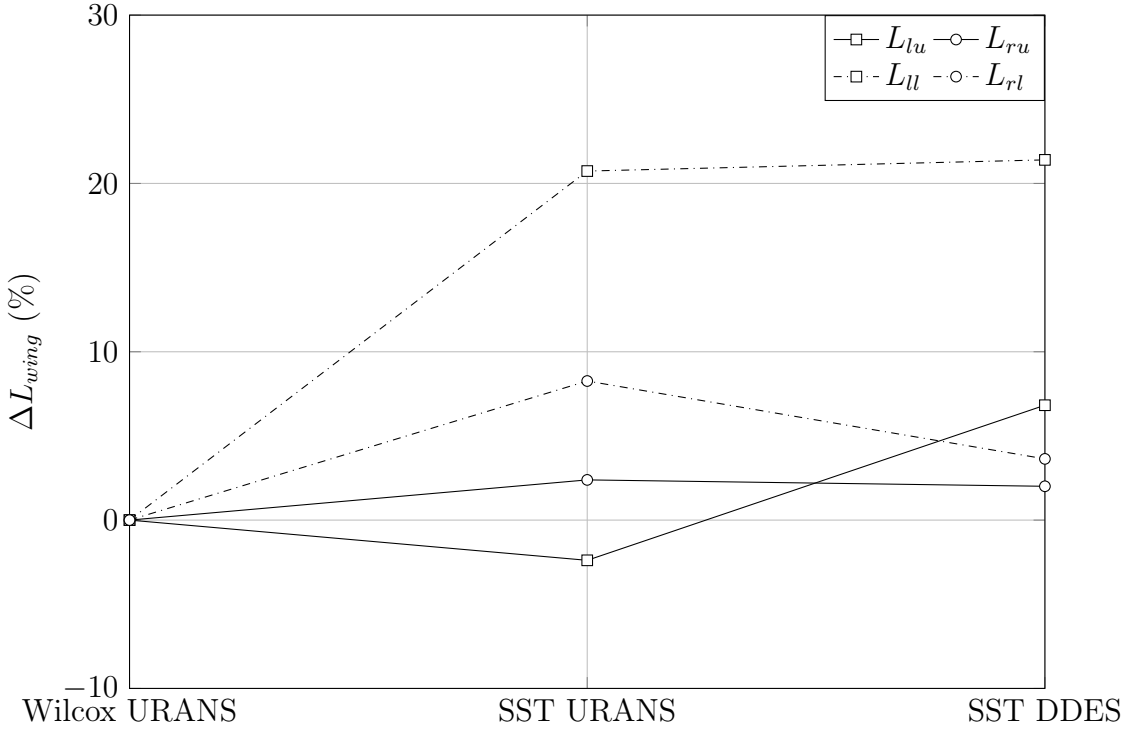

Figure 3.6: Relative change of wing lift with different turbulence modelling. Averaged over five main rotor revolutions [111].

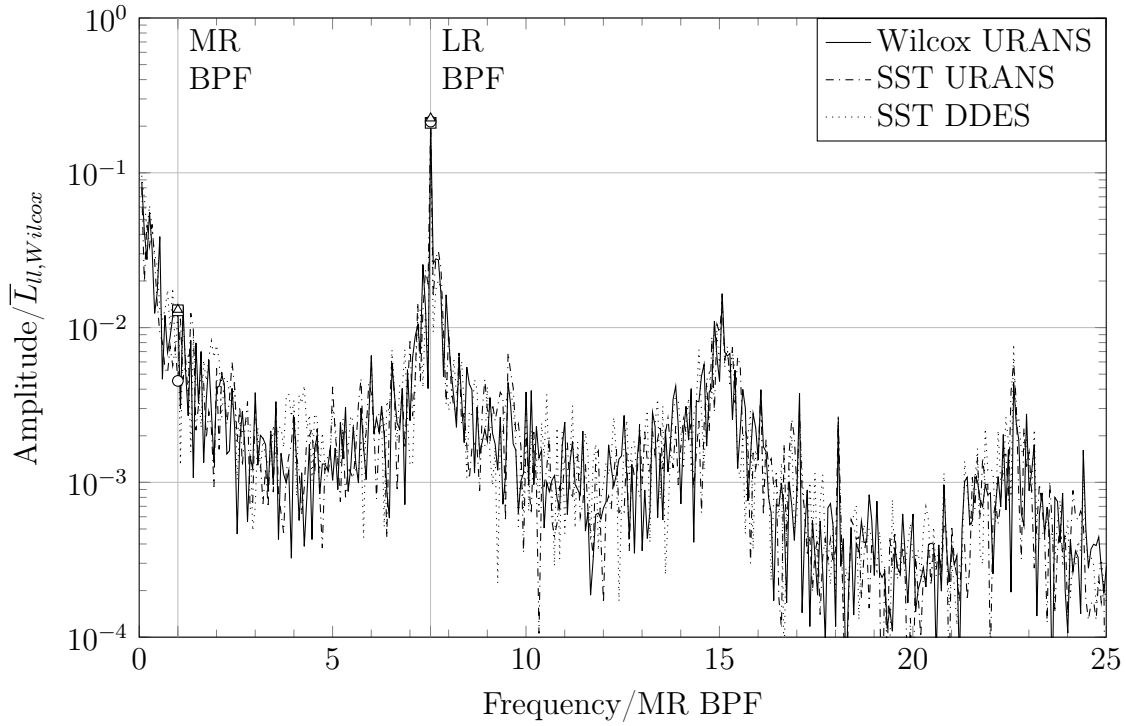

Figure 3.7: Frequency spectrum of download on left lower wing with different turbulence modelling. Normalized with average download of wing with Wilcox URANS [111].

resulting frequency spectra are displayed in Fig. 3.7 for the left lower wing with the largest deviations in average loads (see Fig. 3.6).

Most notably, the distinct peaks at the blade passing frequency (BPF) of the lateral rotors are almost identical for all simulations. Furthermore, small stochastic fluctuations can be consistently witnessed over a large range of frequencies. Both URANS and DDES show a broad range of vortical scales as shown by the lack of significant non-BPF peaks in Fig. 3.7, which supports the conclusions drawn from the vorticity distributions in Fig. 3.5.

Based on these criteria, with all three simulations showing relatively similar results independent of the turbulence model or the use of DDES, none of them can be considered particularly superior. As the application of DDES in combination with the Menter SST turbulence model has proven to deliver very good agreement with experimental data on separated flows [112] and with (D)DES being increasingly applied for the investigation of rotorcraft and their interaction phenomena [28, 40, 55, 59], it is decided to use this approach for the simulations underlying the analysis of interactional effects in hover within this study.

4 Approach for the Investigation of Interactions

For a conventional helicopter, the aerodynamic performance is strongly dominated by the performance of the main rotor. With RACER's concept of lift and thrust compounding, however, realized by the addition of box wings and lateral rotors, two additional components play an important role in this respect. Based on the previous findings on rotor-rotor and rotor-wing interaction illustrated in Sections 1.3.1 and 1.3.2, all three components are very likely to mutually influence their aerodynamic performance, the consideration of which is relevant for the reasons given in Section 1.1.

By directly affecting the aerodynamics of the respective other components, six different first-order interactional effects might occur as illustrated in Fig. 4.1(a). With the analysis of three components, though, the overall influence of the interactions is not limited to this direct share, but rather an indirect effect might additionally contribute in each case. The nature of these second-order interactions is pictured in Fig. 4.1(b), where one component affects another via its influence on the aerodynamic behaviour of the respective third component.

Solely based on the analysis of the full helicopter's performance, the interactional effects of main rotor, wings, and lateral rotors are difficult—if not impossible—to extract; the analysis is somewhat limited to speculations about qualitative influences. Among recent studies on RACER, Wentrup et al. [43] attempted to overcome this limitation by comparing simulation results for different helicopter attitudes. While provoking variations in aerodynamic performance that are required for the assess-

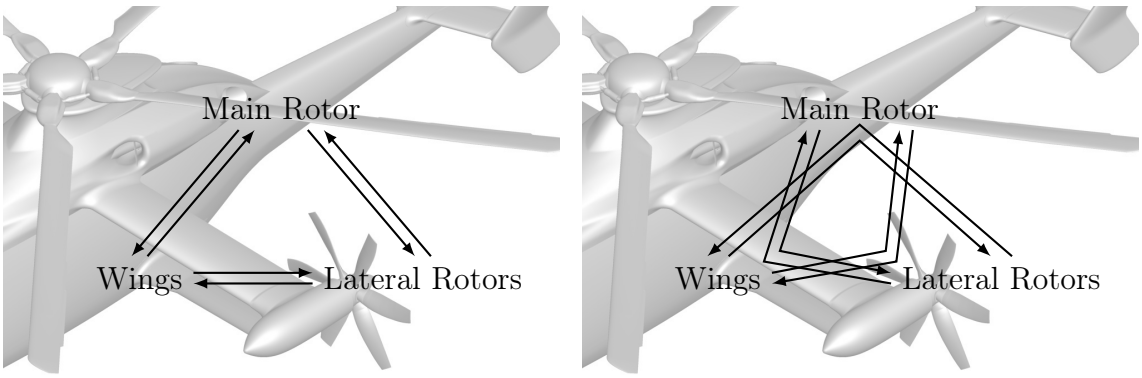

(a) First-order interactions (b) Second-order interactions

Figure 4.1: Aerodynamic interactions analysed in the scope of this study. Adapted from Frey et al. [113].

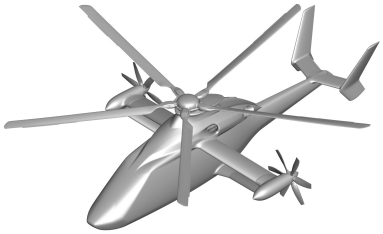

(a) Full configuration

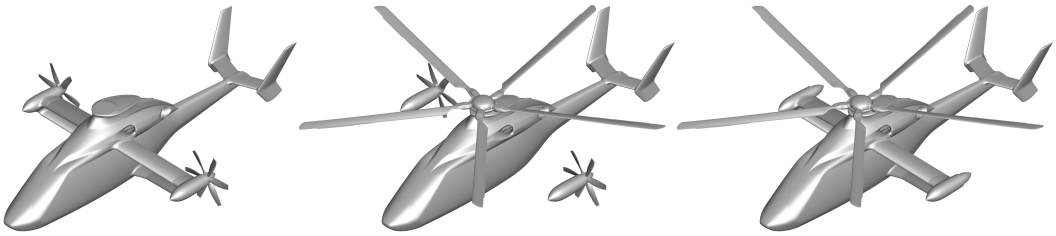

(b) Configurations reduced by one component: without main rotor (left), wings (center), and lateral rotors (right)

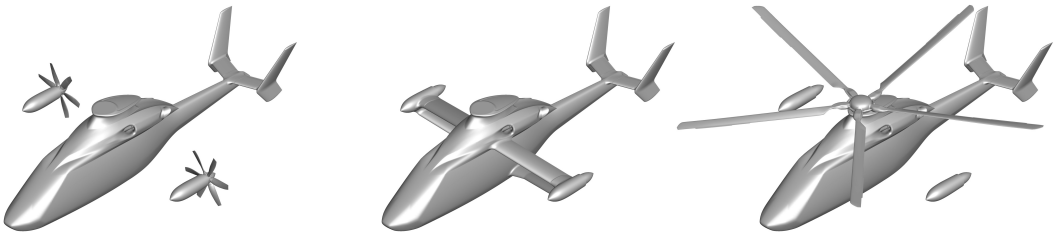

(c) Configurations reduced by two components: without main rotor and wings (left), main rotor and lateral rotors (center), and wings and lateral rotors (right)

Figure 4.2: Configurations simulated for the analysis of aerodynamic interactions [111].

ment of interactions, the consequently changing flow conditions, however, also narrow the conclusions that can be drawn from this.

For this study, in contrast, simulations are repeated at identical flight conditions for helicopter configurations with a geometry respectively reduced by the relevant components. This approach recently was also used for the analysis of interactions on tiltrotor and compound configurations, respectively, in studies by Tran and Lim [59], and Stokkermans et al. [47]. Consequently, in addition to the full RACER geometry illustrated in Fig. 4.2(a) computations are conducted on setups lacking main rotor, wings, or lateral rotors (see Fig. 4.2(b)), as well as on geometries with two of these components omitted each (see Fig. 4.2(c)).

While an individual trim process for all configurations is not necessary but would rather hamper the analysis due to the differing operating conditions of the components, the seven different setups are analysed using the identical trim state—obtained with the full configuration—for cruise flight and hover, respectively. For

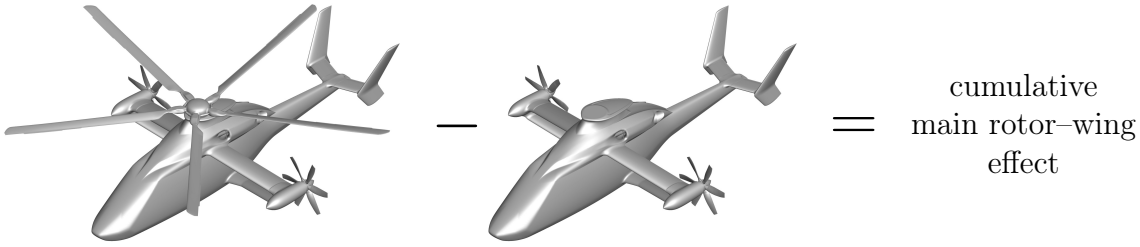

(a) With lateral rotors

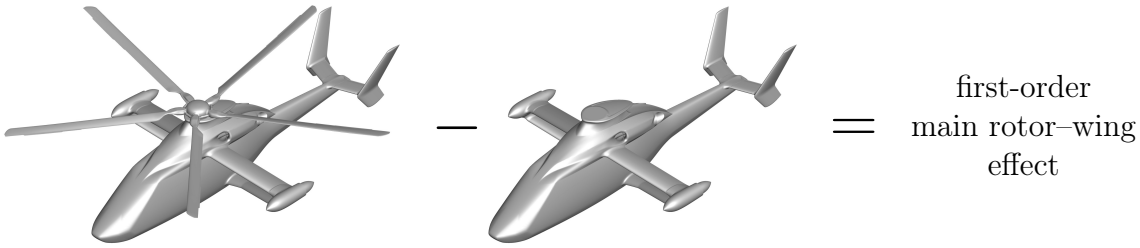

(b) No lateral rotors

Figure 4.3: Schematic of the analysis of cumulative and first-order effects on the example of main rotor–wing interaction.

each of these setups, individual evaluation computations are then conducted according to Tables 2.6 and 2.7. With the omission of one or two of the aerodynamic components and their corresponding mesh structures, the number of cells is equivalently reduced compared to the numbers given in Table 2.5. This is also reflected in the parallelization of the respective CFD simulations, where the number of processors used for the full configuration's HPC computations (see Section 2.3.6) is adjusted in order to maintain the average loading of the processors.

For both flight conditions, the simulations of all seven configurations are examined over the evaluation period regarding the performance of main rotor, wings, and lateral rotors. By comparing these results, the interactional effects are subsequently isolated and analysed within the following chapters of this study. In order to determine the overall influence of component A onto component B, the aerodynamic performance of the latter is assessed both for the full configuration as well as for the configuration lacking component A. Clearly, the resulting difference in component B's performance originates from component A's presence, which not only has a first-order effect but also a second-order influence by affecting component C's aerodynamic behaviour. The schematic of this analysis of the cumulative interactional effect on the example of the main rotor–wing interaction, thus the influence of the main rotor on the wings, is illustrated in Fig. 4.3(a)'s schematic (note: throughout this study the interactions' denotation indicates the influence of the former component onto the latter).

In order to isolate the second-order effect from this analysis, a similar comparison is drawn between two respective setups additionally lacking the third component. With the latter's absence, consequently only first-order effects can arise between the other two components (see Fig. 4.3(b) for the example of main rotor–wing interaction).

While the difference between cumulative and first-order effects is clearly caused by second-order phenomena due to the third component's presence, these indirect effects are not further isolated by a similar subtraction. The reason for this is the inherent complexity and non-linearity of the phenomena, which the explicit assessment of second-order effects by subtracting the results of four different simulations would exceedingly disregard. Instead, the results for cumulative and first-order effects are directly juxtaposed within this analysis of aerodynamic interactions.

5 Aerodynamic Interactions in Cruise Flight

As RACER is designed to significantly extend the flight envelope of a helicopter towards cruise flight at higher flight speeds, this condition is of particular interest for the design of this compound helicopter. For this reason, the following chapter addresses the aerodynamic interactions between main rotor, wings, and lateral rotors in cruise flight with the approach outlined in Chapter 4 and with the help of the coupled and trimmed CFD simulations described in Chapter 2. Each of the six interactional effects (see Fig. 4.1) is analysed regarding its first- and second-order nature in a separate section, where the interactions' respective denotation indicates an influence of the former component on the latter. This chapter is based on Frey et al. [103], with some of the analyses—particularly from Section 5.2—originating from an earlier version of this publication [106] and those regarding second-order interactions added for this thesis.

With a design cruise flight at 220 kts, an advance ratio $\mu = {}^{v_\infty}/_{\Omega R}$ of over 0.5 is reached, considerably surpassing the advance ratio of conventional helicopters. In order to get an overview of the flow phenomena occurring under these conditions,

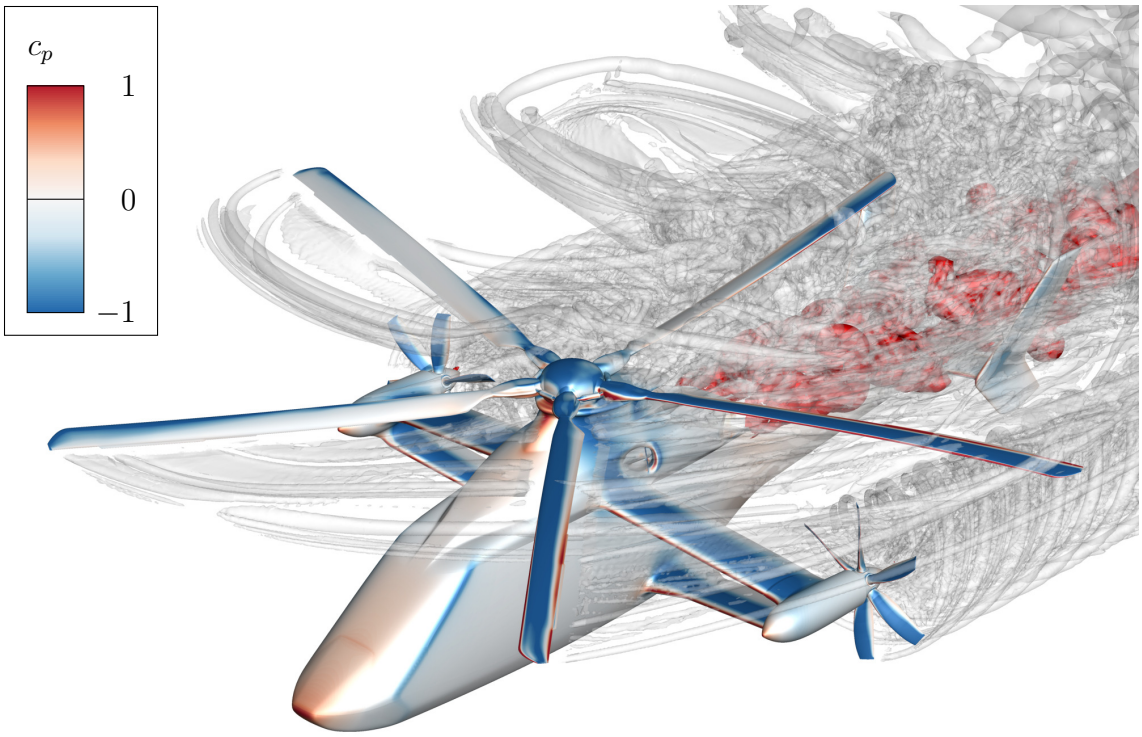

Figure 5.1: λ_2 flow field visualization of RACER in cruise flight with temperature isosurface of exhaust gases and pressure coefficient on helicopter surface [103].

the general flow features in cruise flight are illustrated in Fig. 5.1 with the help of λ_2 isosurfaces of the vortex structures and a temperature isosurface of the exhaust gases.

5.1 Main Rotor–Wing Interaction

In a previous study involving the author of the present thesis [21], a difference had been found in lift generation during cruise flight between right and left wings. The cause for this was assumed to be the highly asymmetrical main rotor thrust distribution, resulting in an asymmetrical influence on the wings' effective angle of attack. While Bain and Landgrebe [42] also witnessed this asymmetry in wing lift generation during an extensive wind tunnel study on compound helicopter configurations, they rather attributed it to the bound vortex of each main rotor blade inducing a reduction of inflow velocity below the advancing side and an increase below the retreating side. Recent years' studies of Sugawara and Tanabe [62, 63], in contrast, also related this effect to the asymmetric main rotor thrust distribution and consequently induced (vertical) velocity.

In order to examine the main rotor's influence on the wing lift more deeply, according to the approach described in Chapter 4 the results of RACER's cruise flight are compared to additional simulations where the main rotor geometry is omitted (see Fig. 4.2(b), left). For both setups, the resulting lift distribution of all four individual wings is displayed in Fig. 5.2 with the help of the section lift coefficient $c_l c$ derived from the section lift force l:

$$c_l c = \frac{l}{\frac{1}{2}\rho_\infty v_\infty^2}\,. \tag{5.1}$$

In accordance with previous results, the full setup shows a larger lift on the right-hand side, especially on the upper but also on the lower wings. When neglecting the main rotor, however, the left-hand wings experience a lift increase. While this increase is relatively constant on the lower wing, on the upper wing it grows with decreasing spanwise position and—due to the dihedral—decreasing vertical distance from the main rotor, which is highly loaded above the left-hand wings.

This is illustrated in Fig. 5.3, where for each spanwise position of the wings the main rotor's section normal force coefficient is averaged over the superjacent lateral section of the rotor disk. Using the example of a thrust distribution of RACER at a flight with 175 kts from Thiemeier [20], this averaging approach is illustrated in Fig. 5.4. The section normal force coefficient $M^2 c_n$ is determined from the main rotor thrust in the form of the section normal force n (evaluated in the rotor frame) as follows:

$$M^2 c_n = \frac{n}{\frac{1}{2}\rho_\infty a_\infty^2 c}\,. \tag{5.2}$$

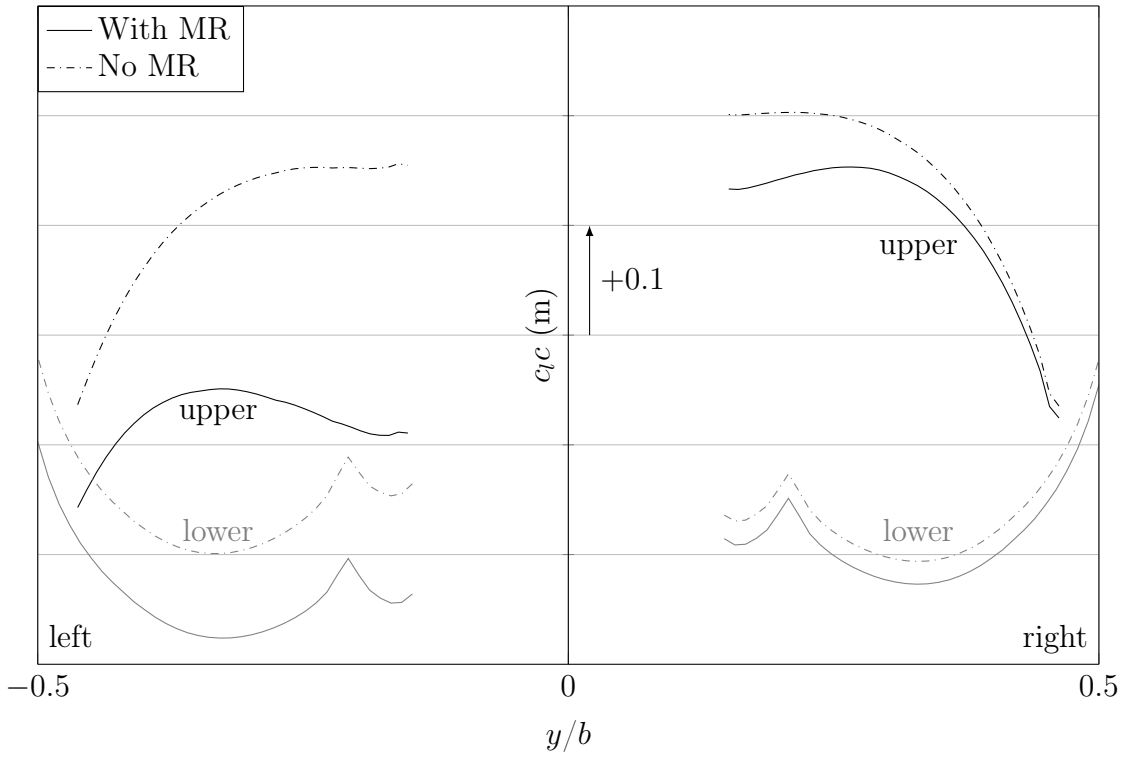

Figure 5.2: Distribution of wing lift with and without main rotor. Section lift coefficient. Averaged over one main rotor revolution [103].

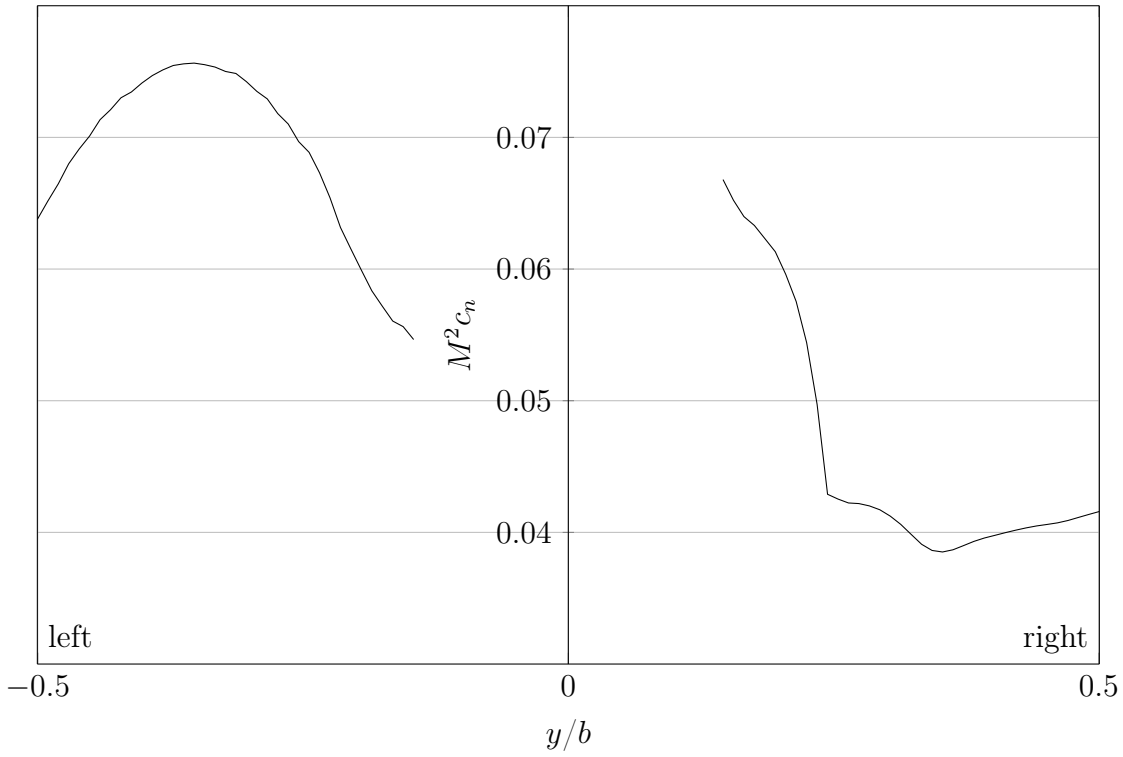

Figure 5.3: Spanwise main rotor thrust distribution. Section normal force coefficient averaged for lateral sections of main rotor disk [103].

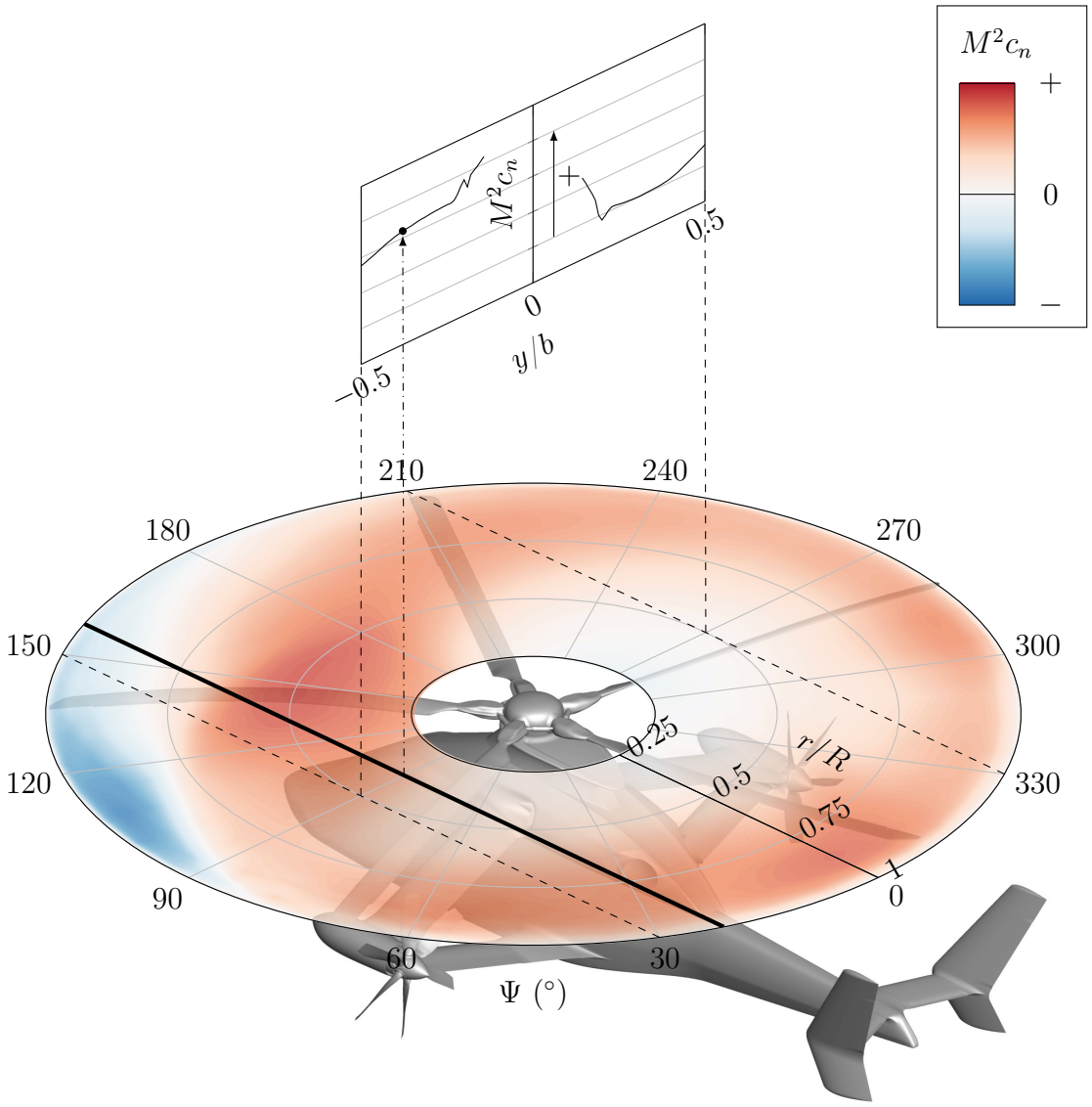

Figure 5.4: Illustration of the analysis of spanwise main rotor thrust distribution. Section normal force coefficient averaged for lateral sections of main rotor disk. Exemplary main rotor thrust distribution at 175 kts from Thiemeier [20].

The thrust distribution of the main rotor also explains the much smaller difference between the two setups on the right-hand wings, as the retreating rotor blades partly operate under reverse flow conditions and mostly produce lift on a significantly smaller scale. However, the general influence of the main rotor—constant shift on lower wing, growing shift on upper wing with decreasing spanwise position—is also clearly visible here. Consequently, the specific distribution of $\Delta c_l c$ is a combination of main rotor thrust distribution and vertical distance towards the wings.

Without the main rotor influence, the wing lift distributions in Fig. 5.2 are relatively symmetrical which is to be expected due to the lack of yawing angle and the

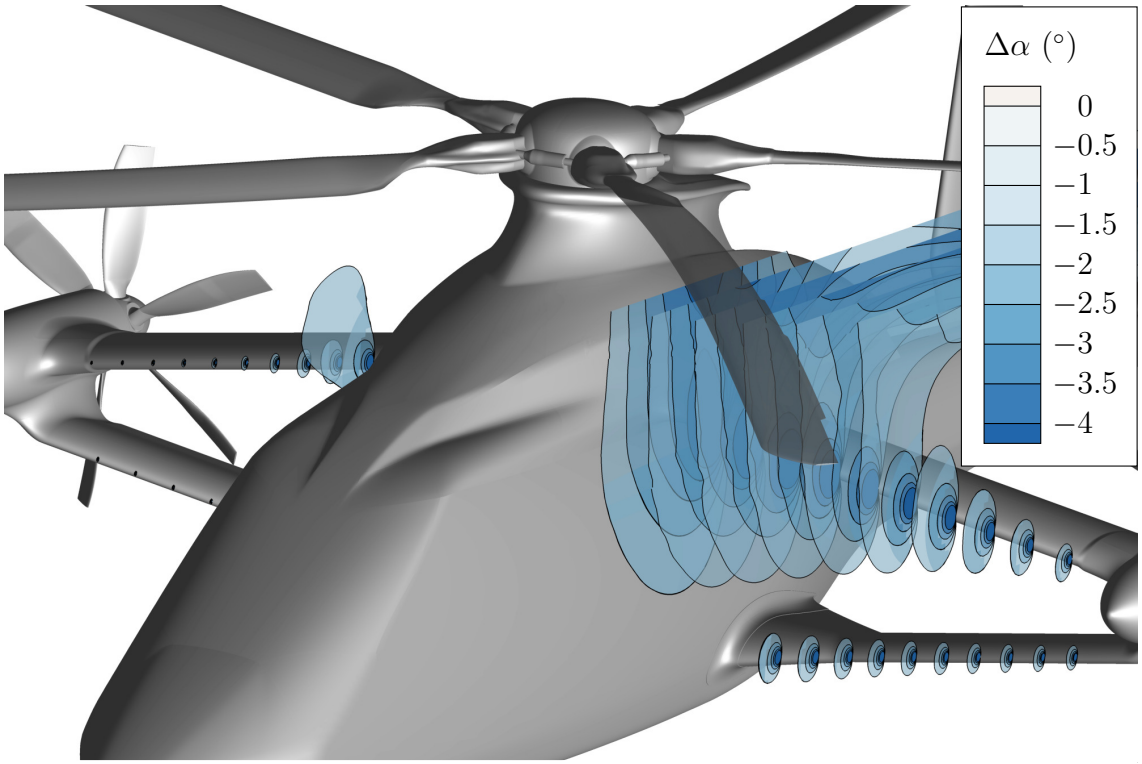

Figure 5.5: Distribution of vertical flow deflection induced by main rotor on planes across wingspan. Values above −2° blanked. Averaged over one main rotor revolution [103].

symmetrical geometry of fuselage and wings. However, a minor difference is visible between the upper wings' root regions. This can be explained with their proximity to the respective engine inlets (see Detail (c) in Fig. 2.4), which create a distinct region of suction. As the engine flow is modelled with specific boundary conditions which iteratively aim at achieving a target mass flow by prescribing a static pressure in the engine inlet, small asymmetries can accrue from this iterative process. The slightly lower static pressure and consequently higher mass flow on the right inlet is mirrored in the lift increase on the right upper wing's root.

In order to quantify the main rotor's influence on the wings' inflow, the respective flow fields of setups with and without main rotor are averaged over one main rotor revolution and subtracted. Figure 5.5 illustrates the resulting vertical flow deflection that can consequently be traced back to the main rotor's influence. On planes in the wings' inflow, $\Delta\alpha$ shows that, originating from the main rotor's region of high thrust, the upper left wing's inboard region experiences a reduction of effective angle of attack. This results in the lift decrease displayed in Fig. 5.2.

Consistently with both main rotor thrust distribution and wing lift distribution, the vertical flow deflection decreases towards the left lateral rotor, while it is relatively constant in the left lower wing's inflow. At maximum spanwise position, the

effect on upper and lower wing is relatively similar due to their smallest vertical distance. On the right wings, in contrast, the vertical flow deflections show only minor influence of the main rotor's significantly unloaded retreating side.

Consequently, the reduction of overall wing lift, which was previously found in the experimental studies of Lynn [60] as well as Bain and Landgrebe [42], and was attributed to the detrimental effect of downwash momentum angle on the wings' effective angle of attack, can be traced back predominantly to the advancing side of the main rotor in RACER's cruise flight with its characteristic advance ratio and lift share. The significant asymmetry was recently confirmed in wind tunnel tests on the Boeing Advanced AH-64 compound helicopter by Brouwers et al. [64], who found a reduction of effective angle of attack of 3.0° and 1.1° below the advancing and retreating rotor blades, respectively. While in recent numerical studies on RACER Wentrup et al. [43] witnessed an effect of the main rotor on the wing lift similar to the present results, Yin et al. [46] surprisingly found the main rotor to cause an upwash below its retreating side and consequently assumed an increase of wing lift over the full span of the right wings, which is implausible and contradicts the results of other studies on this topic.

In order to discriminate between contributions of first- and second-order effects to the main rotor's influence on wing lift, following the schematic outlined in Fig. 4.3 the difference in section lift coefficient induced by the main rotor is not only extracted from the distributions illustrated in Fig. 5.2 but also from respective results of simulations additionally lacking the lateral rotors (see configurations in Fig. 4.2(b), right and 4.2(c), center). For all four wings, the distributions of $\Delta c_l c$ induced by the main rotor in the presence and absence of lateral rotors are contrasted in Fig. 5.6.

Clearly, the first-order effect of the main rotor which can be observed without the lateral rotors is very similar to its previously discussed cumulative effect. As the presence of the lateral rotors consequently is rather negligible for the underlying interactional phenomena, second-order effects play no significant role in this case.

Additionally to influencing the mean inflow conditions of the wings, the passing main rotor blades likely also induce a fluctuation of these conditions and consequently the wing loads. For this reason, an FFT of the wings' individual lift difference between the two setups with and without main rotor is conducted and the resulting frequency spectrum is representatively displayed in Fig. 5.7 for the upper wings. The lower wings' fluctuations show characteristics similar to their upper counterparts.

Both upper wings show a distinct fluctuation at the main rotor BPF. While it is only slightly stronger for the right wing, this corresponds well with results of Sugawara and Tanabe [62] who similarly found the fluctuations of wing lift to be larger below the retreating blades of the main rotor despite the generally larger detrimental effect of the advancing side. The amplitude of the present fluctuations, however, is relatively small with 0.6–0.7 %. The amplitudes of the higher harmonics quickly

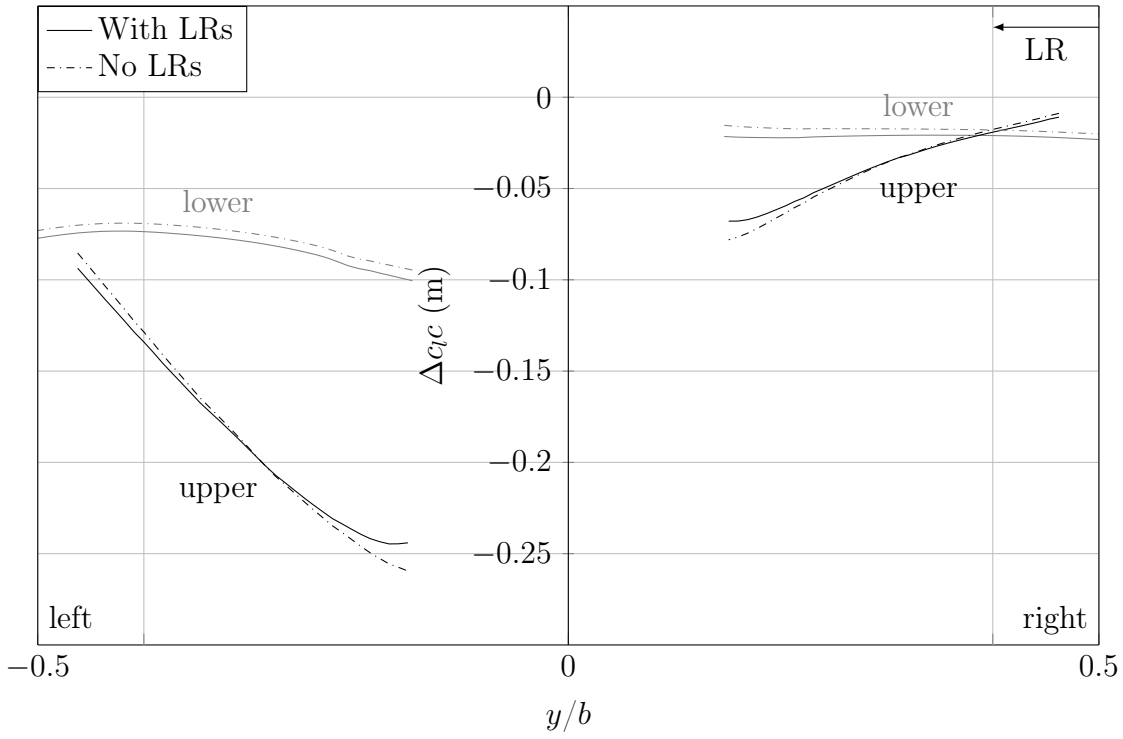

Figure 5.6: Distribution of difference in wing lift induced by main rotor with and without lateral rotors. Section lift coefficient. Averaged over one main rotor revolution. Approximate location of lateral rotors indicated.

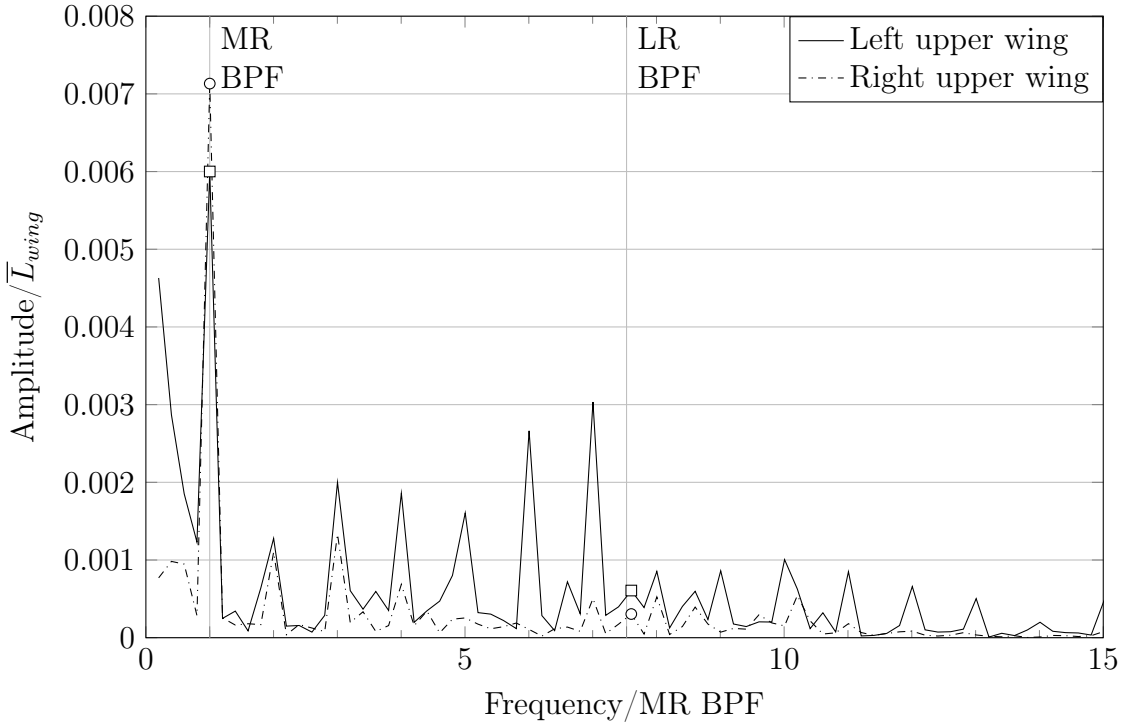

Figure 5.7: Frequency spectrum of lift difference on upper wings induced by main rotor. Normalized with average lift of respective wing in full configuration [103].

decrease on the right upper wing, whereas they are responsible for a significant share of the left upper wing's fluctuations.

5.2 Wing–Main Rotor Interaction

The reverse influence of the wings on the main rotor similarly cannot be of convective nature with direct wake interactions, but nevertheless, an inductive effect might also arise in this direction, manifesting itself in circulation-induced changes of velocity or angle of attack. In order to assess the occurrence of such interactions, the full setup is compared to additional simulations conducted on a reduced setup lacking the helicopter's wings (see Fig. 4.2(b), center). The resulting main rotor thrust distributions in terms of $M^2 c_n$ from Eq. 5.2 are subtracted and the difference—consequently originating from the presence of the wings—is displayed in Fig. 5.8(a).

While the first quadrant is clearly affected by a thrust decrease due to the wings' influence, this abruptly changes to a, yet smaller, thrust increase in the second quadrant, explaining the change in flapwise bending moments that Bain and Landgrebe [42] as well as Brouwers et al. [64] witnessed when adding wings during their wind tunnel tests on compound helicopters. On the retreating side of the main rotor, in contrast, no such effect can be observed, with a thrust decrease only emerging between 330° and 0° which is less uniform due to the stochastic nature of the passing rotor head wake.

The reason for this behaviour becomes clear when examining the vertical flow deflection α caused by the wings. This is achieved by subtracting the averaged flow field of the reduced setup without wings from the respective flow field of the full setup. The resulting distribution of $\Delta\alpha$ on planes across the wingspan is displayed in Fig. 5.9. By highlighting only regions of $\Delta\alpha > 0.5°$ and $\Delta\alpha < -0.5°$, it becomes apparent that in front of the wings the flow is deflected upwards. Behind the wings, however, a downward deflection can be observed. This can be explained by the effect of the wings' circulation on the flow around the helicopter.

On the main rotor's advancing side, this deflection causes a decrease in effective angle of attack and consequently thrust in the first quadrant, while, in front of the wings, the upward deflection is the source of the additional thrust. In contrast, the retreating blades are hardly affected by the wings as they are much less prone to changes in effective angle of attack due to their smaller dynamic pressure or even reverse inflow.

The effect of wing circulation on the main rotor's advancing side was witnessed by Yeo [65] for a compound helicopter with a wing generating as much as 93 % of total lift. As shown by the present results, this interactional phenomenon clearly also comes into play for a more balanced lift share.

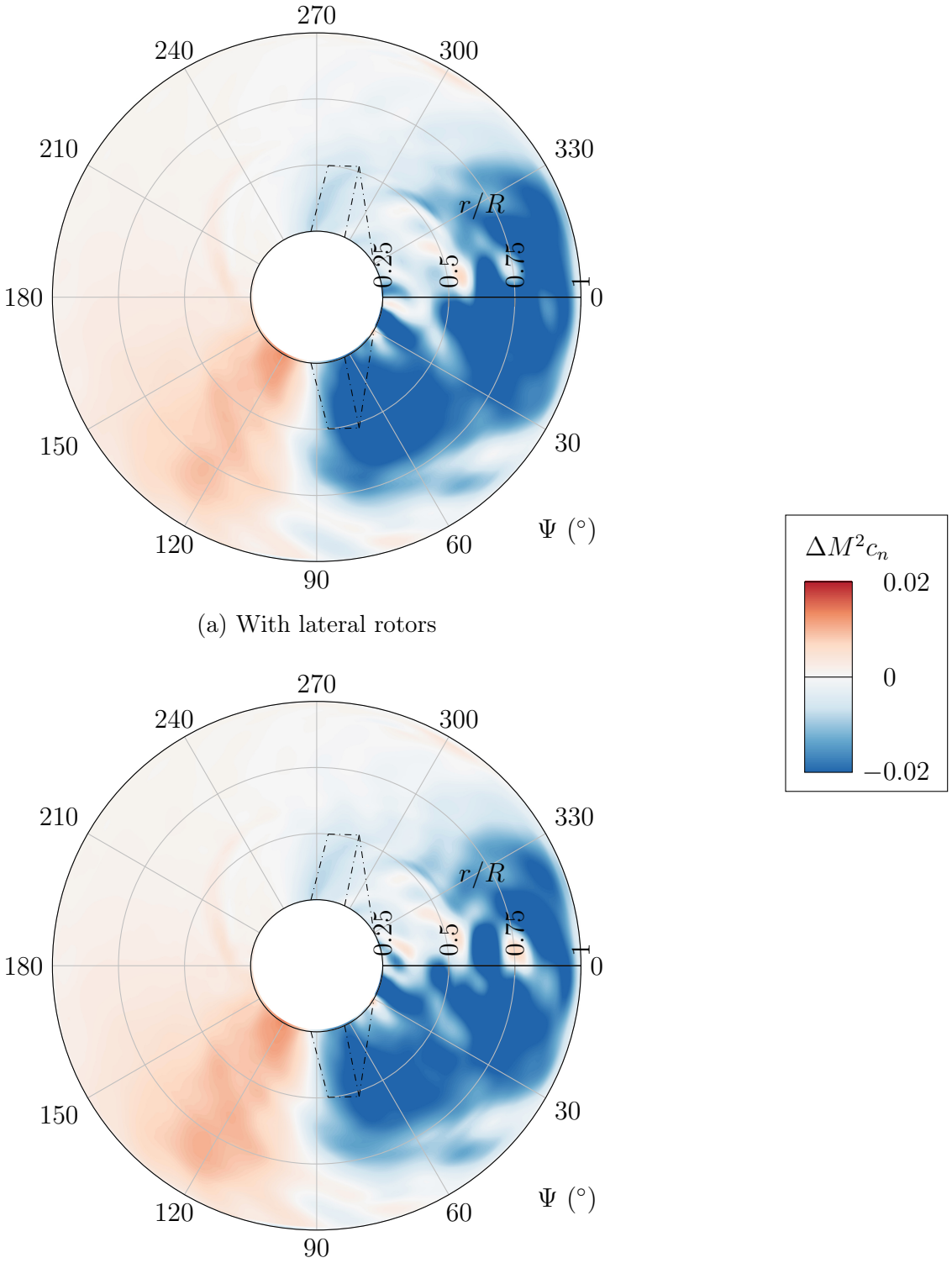

(a) With lateral rotors

(b) No lateral rotors

Figure 5.8: Distribution of thrust difference on main rotor induced by wings with and without lateral rotors. Section normal force coefficient. Frequency filtered above 20/rev. Approximate location of wings indicated. View from above. Adapted from Frey et al. [106].

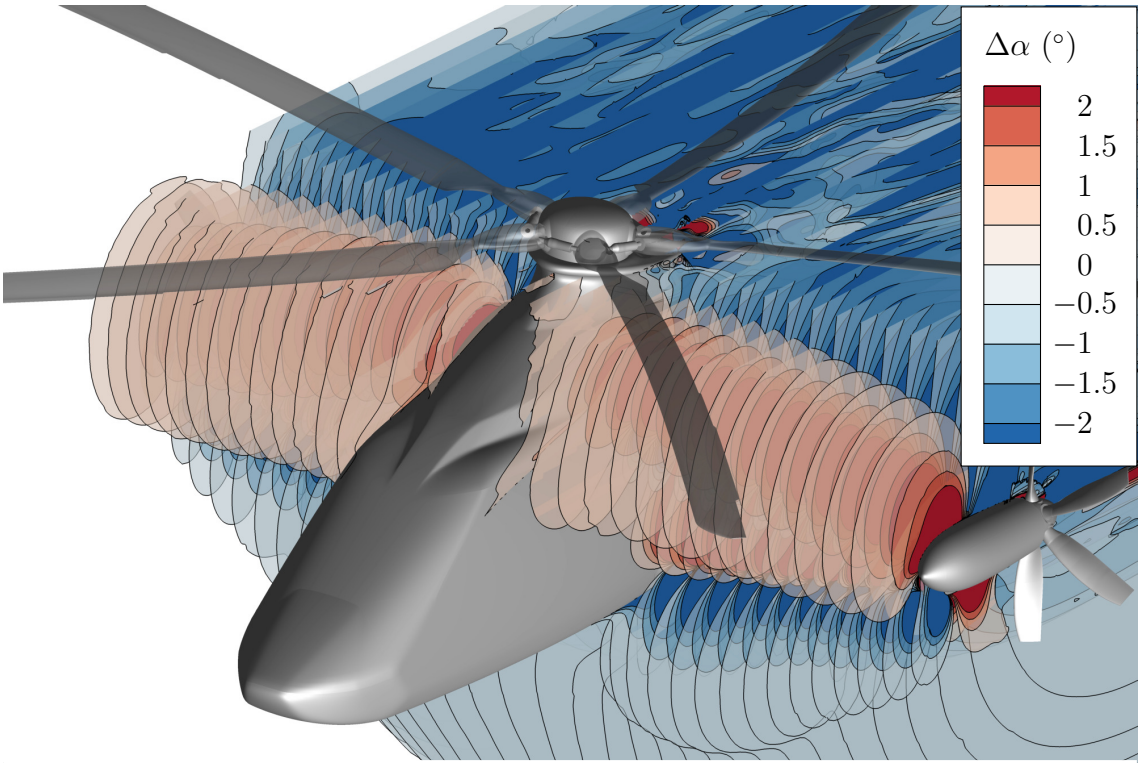

Figure 5.9: Distribution of vertical flow deflection induced by wings on planes across wingspan. Values between −0.5° and 0.5° blanked. Averaged over one main rotor revolution [106].

The difference in thrust distribution displayed in Fig. 5.8(a) also affects the global performance of the main rotor. While the lacking influence of the wings results in a thrust gain of 9.3 % for the reduced configuration, the required power experiences a similar increase of 8.1 %.

In order to differentiate between first- and second-order effects, Table 5.1 additionally includes the differences in main rotor thrust and power caused by the omission of the wings in the absence of lateral rotors (see configurations in Fig. 4.2(b), right and 4.2(c), right). The general trends of the resulting first-order phenomena are relatively similar to the cumulative effect with the lateral rotors present; however, particularly regarding thrust generation, a second-order effect intensifies the overall detrimental influence of the wings on main rotor performance. This is supported by the respective distribution of first-order thrust difference in Fig. 5.8(b), which shows very similar characteristics to the previously discussed distribution in the lateral rotors' presence but with a slightly more pronounced region of thrust gain in front of the left-hand wings and a marginally weaker loss behind them.

The comparison in Table 5.1, however, is not suited to assess RACER's performance but purely to examine the aerodynamic interactions. Not only is a wing-less configuration in the given context completely pointless, but it would also require a

Table 5.1: Changes in main rotor thrust and power. Normalized with respective configuration with wings.

	No wings, with lateral rotors	No wings, no lateral rotors
ΔT_{MR}	+9.3 %	+7.5 %
ΔP_{MR}	+8.1 %	+7.4 %

retrim of the flight state in order to achieve the respective trim targets. While the required main rotor thrust would necessitate an adjustment of collective main rotor pitch, also the cyclic pitch input had to be adapted due to the significant pitching moment arising from the tail-heavy change in thrust distribution.

5.3 Main Rotor–Lateral Rotor Interaction

Similar to the main rotor's influence on the wings discussed in Section 5.1, no convective effects on the lateral rotors can be expected. In extensive wind tunnel tests, Bain and Landgrebe [42] nevertheless found the main rotor to induce bending moments on the lateral rotors, likely via an influence of the downwash momentum angle on effective angle of attack and consequently thrust distribution. A comparison of the lateral rotor performance with results from computations omitting the main rotor geometry (see Fig. 4.2(b), left) shows a considerable difference, especially on the left lateral rotor. Here, the average thrust increases by 4.6 % when omitting the main rotor, while the power requirement almost equally rises by 4.0 %, leading to an almost unchanged propulsive efficiency η. The effects on the right lateral rotor, meanwhile, are of a significantly smaller scale as listed in Table 5.2; this asymmetric susceptibility to the main rotor's presence was confirmed in recent studies by Wentrup et al. [43] and Yin et al. [46].

In order to investigate this asymmetry more closely, the flow field is examined in a plane 0.25 m upstream of the lateral rotors. As the lateral rotor performance can be influenced by a change in axial or tangential inflow velocity, Fig. 5.10(a) first

Table 5.2: Changes in lateral rotor thrust and power. Normalized with respective configuration with main rotor.

	No main rotor, with wings	No main rotor, no wings
ΔT_{leftLR}	+4.6 %	−2.2 %
$\Delta T_{rightLR}$	+1.5 %	+0.1 %
ΔP_{leftLR}	+4.0 %	−1.7 %
$\Delta P_{rightLR}$	+1.3 %	+0.1 %

(a) Difference in velocity magnitude induced by main rotor

(b) Velocity magnitude RMS of full configuration

Figure 5.10: Distribution of velocity magnitude on lateral rotor inflow. Averaged/calculated over one main rotor revolution. View from behind [103].

of all illustrates the main rotor's influence on the velocity magnitude and shows a different effect of the advancing and retreating blades on the subjacent flow field.

Owing to the asymmetric main rotor loading (see spanwise thrust distribution in Fig. 5.3), RACER's left-hand side experiences a significant influence on the passing flow originating from the highly loaded inner section of the main rotor. This is particularly strong in the upper half of the left lateral rotor inflow. Similar to the influence on the wings discussed in Section 5.1 and illustrated in Fig. 5.2, however, the right-hand side is much less affected with relatively constant velocity magnitude. While the effect in thrust generation highly depends on the orientation of the induced velocities, the generally larger difference in velocity magnitude below the advancing main rotor blades indicates a more substantial effect on the left lateral rotor as described above.

The causative effects are illustrated on the left lateral rotor with its higher levels of thrust change; the right lateral rotor, however, generally shows similar characteristics. In order to examine the origin of the difference in global thrust under main rotor influence, the left lateral rotor's thrust distributions of the two differ-

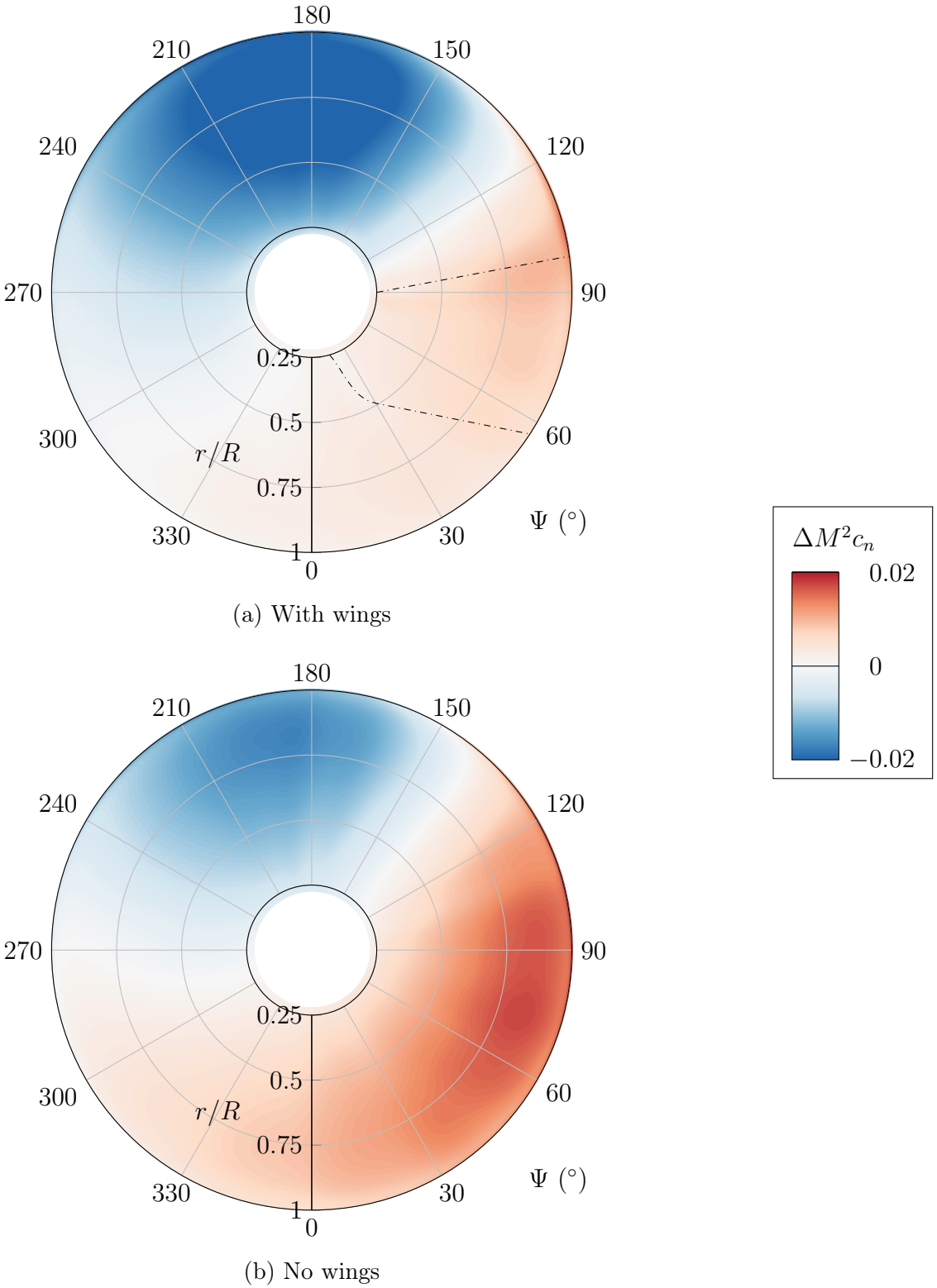

(a) With wings

(b) No wings

Figure 5.11: Distribution of thrust difference on left lateral rotor induced by main rotor with and without wings. Section normal force coefficient. Averaged over one main rotor revolution. Approximate location of wings indicated. View from behind. Adapted from Frey et al. [103].

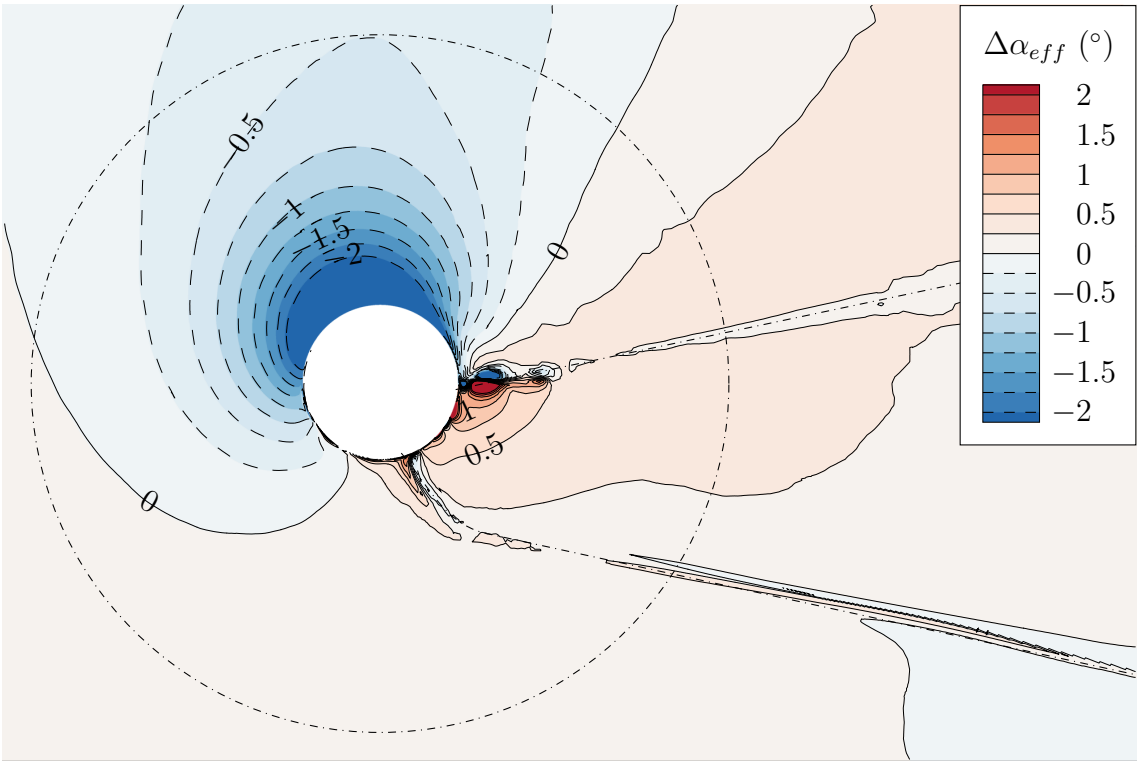

Figure 5.12: Distribution of difference in effective angle of attack on left lateral rotor inflow induced by main rotor. Based on local rotational velocity. Averaged over one main rotor revolution. Approximate location of wings indicated. View from behind [103].

ent setups (with and without main rotor) are compared. The resulting $\Delta M^2 c_n$ is illustrated in Fig. 5.11(a).

While the first quadrant, situated behind the wings, shows only a minor effect of the main rotor's presence with a slight increase in thrust, the upper half of the polar is dominated by a noticeably smaller thrust, leading to the aforementioned overall decrease in lateral rotor thrust due to the main rotor. In order to examine this thrust difference more deeply, Fig. 5.12 displays the main rotor's effect on the lateral rotors' effective angle of attack which is calculated from the tangential and axial velocity components (v_{tan} and v_{ax}) of both configurations' inflow and the local rotational velocity of the lateral rotor blades (v_{Blade}):

$$\begin{aligned}\Delta\alpha_{eff} &= \arctan\frac{v_{tan,MR}+v_{Blade}}{v_{ax,MR}} - \arctan\frac{v_{tan,noMR}+v_{Blade}}{v_{ax,noMR}} \\ &= \arctan\frac{v_{tan,MR}+\Omega_{LR}r}{v_{ax,MR}} - \arctan\frac{v_{tan,noMR}+\Omega_{LR}r}{v_{ax,noMR}}\,. \end{aligned} \tag{5.3}$$

This effect is mainly caused by a, in relation to the lateral rotor, tangential velocity component of the main rotor's induction on the flow, whereas a small flow

deceleration due to the presence of the main rotor, especially in the upper part of the lateral rotor inflow, is only responsible for a minor extent of this change in effective angle of attack. Originating from the highly loaded inner section of the advancing main rotor blades (see Fig. 5.3), a counterclockwise rotating effect on the inflow is visible in the upper and outer parts of the lateral rotor disk, concordant with the blades' sense of rotation.

At the same time, an increase of effective angle of attack could be expected on the upstroking side of the polar. Wentrup et al. [43] assumed this to cause a significant thrust gain on the upstroking lateral rotor blades. Owing to RACER's configuration, however, the wings partly shield the lateral rotors from the inductive effect of the main rotor, rectifying the lateral rotor inflow in their wake and leading to relatively undeflected flow conditions in the first quadrant of Fig. 5.12.

This second-order effect in the presence of the wings becomes clear when comparing Fig. 5.11(a)'s distribution of thrust difference to the respective change induced by the main rotor in the wings' absence, computed with the configurations in Fig. 4.2(b), center and 4.2(c), left. The significantly more pronounced region of thrust gain in Fig. 5.11(b)'s first-order influence indicates a lacking rectification by the wings, whereas the losses in the upper part of the rotor disk are additionally reduced compared to the cumulative effect in the wings' presence. The occurrence of regions with increased and decreased thrust generation clearly contradicts the assumption of Decours et al. [45] who found the positive installation effect of the main rotor on lateral rotor thrust to be driven by the main rotor blade tip vortices passing above the lateral rotors and consequently inducing a reduction of axial velocity in the latter's inflow.

The shift between Fig. 5.11's thrust distributions also becomes manifest in global lateral rotor thrust, where the changes in Table 5.2 show a loss in left lateral rotor thrust with the main rotor's omission in the wings' absence, in contrast to the previously discussed gain due to cumulative effects. In accordance with the present results, a positive first-order installation effect with a lateral rotor thrust increase induced by the main rotor was not only discovered in recent studies on RACER by Decours et al. [45] and Stokkermans et al. [47] but also by Boisard [44] who exposed a single isolated lateral rotor to the advancing side of an isolated main rotor for significantly smaller advance ratios of up to $\mu = 0.25$. However, he achieved this with not only a presumably largely different main rotor loading due to the more than 50 % lower advance ratio but interestingly also an opposite, inboard-down, sense of rotation of the lateral rotor.

Matching with Boisard's results, the fluctuations on the left lateral rotor are of a very small scale. This is displayed in Fig. 5.13's illustration of a frequency spectrum of both lateral rotors' thrust difference between the two setups with and without main rotor. The right lateral rotor, however, shows fluctuations more than 10 times larger for the first main rotor BPF. Despite this, the general trend witnessed on the

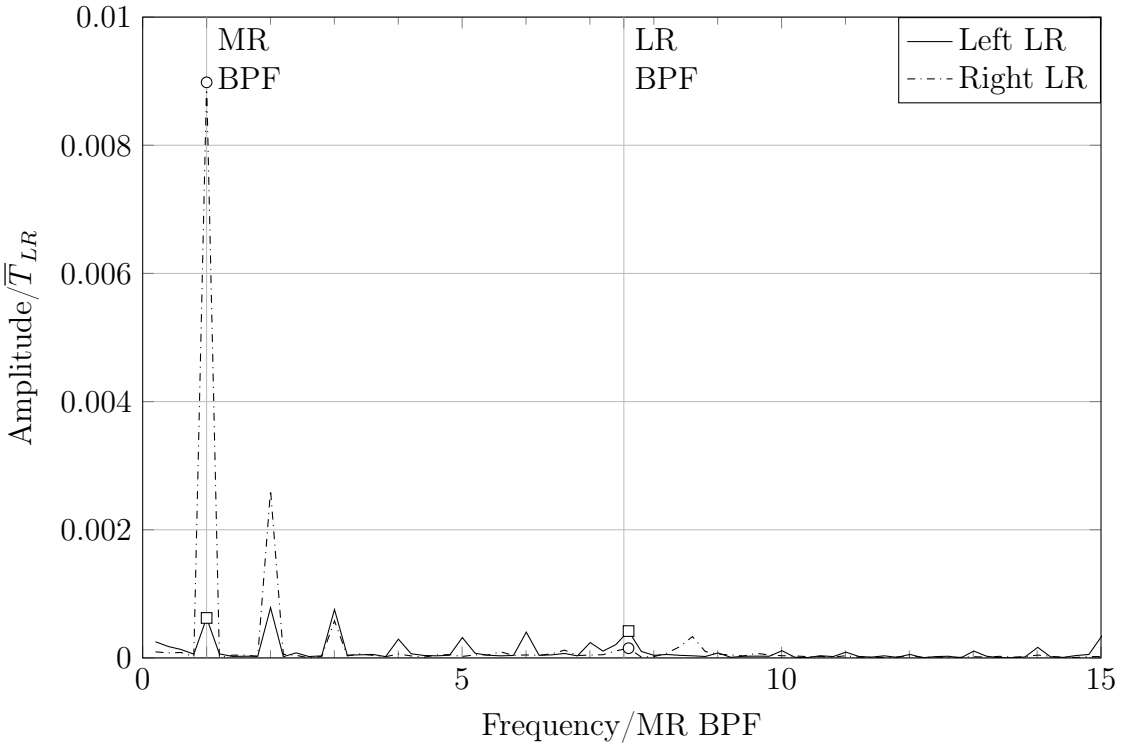

Figure 5.13: Frequency spectrum of thrust difference on lateral rotors induced by main rotor. Normalized with average thrust of respective lateral rotor in full configuration [106].

main rotor's influence on wing lift fluctuations in Fig. 5.7 is confirmed here as the higher harmonics similarly are much more pronounced below the advancing blades than below the retreating blades.

In order to investigate the source of the right lateral rotor's larger thrust fluctuations, the thrust curve over the lateral rotor azimuth is computed by averaging the thrust curves of the lateral rotor's six blades over all lateral rotor revolutions taking place during the evaluation period of one main rotor revolution. Additionally, their root mean square (RMS) is evaluated. While the left lateral rotor shows hardly any significant RMS, neither in standard configuration nor without the main rotor, confirming the low level of induced fluctuations observed in Fig. 5.13, the right lateral rotor indeed features larger standard deviations in thrust with the influence of the main rotor (see Fig. 5.14).

Here, not only the decrease of thrust in the upper half of the lateral rotor disk in the main rotor's presence can be observed that was also visible on the left lateral rotor in Fig. 5.11(a). Additionally, thrust fluctuations with an amplitude similar to this decrease in mean value occur over the same range of azimuth (RMS values without the main rotor are comparably small and therefore not included in Fig. 5.14). The source of the asymmetric main rotor influence on the lateral rotor thrust fluctuations

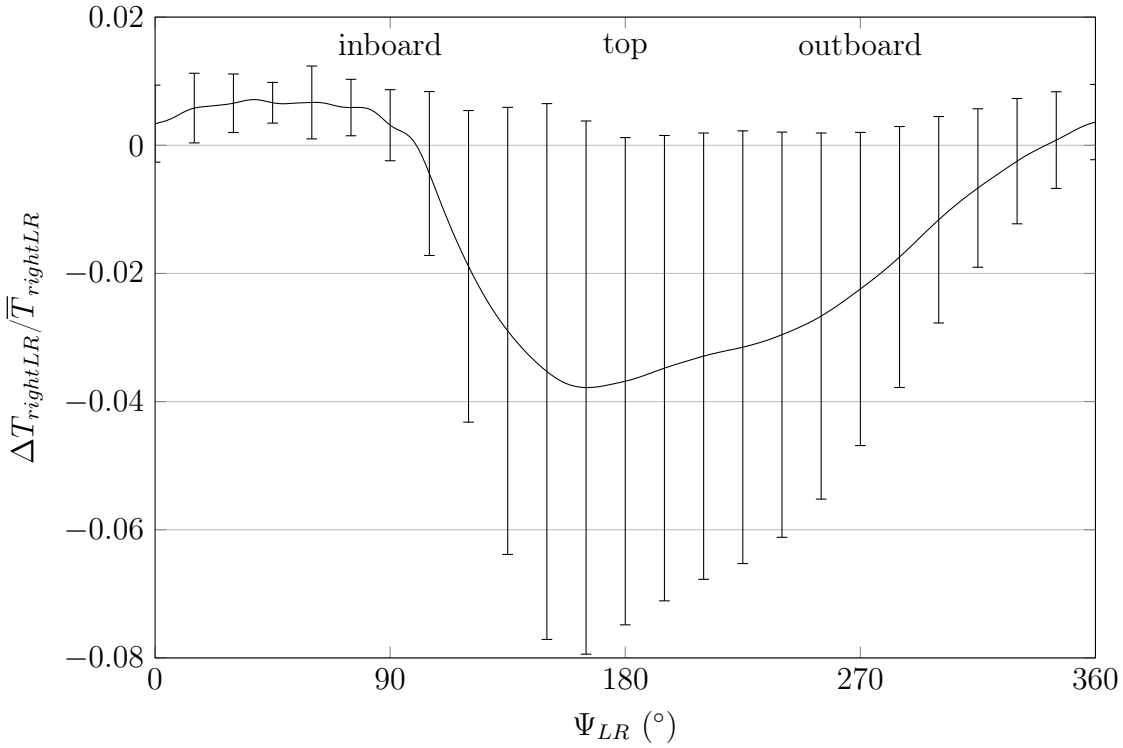

Figure 5.14: Thrust difference on right lateral rotor induced by main rotor with standard deviation in full configuration. Normalized with average thrust of lateral rotor in full configuration. Averaged over one main rotor revolution [103].

is illustrated in Fig. 5.10(b). In contrast to the induced effect on the *average* velocity magnitude, which is significantly larger on the left-hand—advancing—side (see Fig. 5.10(a)), the *fluctuations* in velocity magnitude originating from the main rotor extend further downwards below the right-hand—retreating—side. Therefore, they induce fluctuations in effective angle of attack and consequently thrust in the upper half of the right lateral rotor's disk as witnessed in Fig. 5.14. As discussed in Section 5.1, the two asymmetric effects illustrated in Fig. 5.10 were similarly witnessed by Sugawara and Tanabe [62] in their study of main rotor influence on average wing lift and its fluctuations.

5.4 Lateral Rotor–Main Rotor Interaction

With the wings' notable influence on main rotor performance described in Section 5.2, a similar investigation is conducted for the interaction between lateral rotors and main rotor despite an equally lacking convective effect in this case. The comparison of the full setup's main rotor thrust with the results of an additional simulation omitting the lateral rotor blades (see Fig. 4.2(b), right) shows a slight increase of 4.1 % without the influence of the lateral rotors. The main rotor power,

meanwhile, is not affected by the presence of the lateral rotors and remains almost completely unchanged.

A comparison of the two setups' respective main rotor thrust polars reveals the source of the thrust decrease due to the lateral rotor influence. The distribution of this thrust difference is illustrated in Fig. 5.15(a) and shows a distinct pattern with almost the complete $\Delta M^2 c_n$ being situated in the advancing half of the main rotor disk.

The losses in main rotor thrust are concentrated in a region where the left lateral rotor is located, slightly behind the main rotor hub and at roughly 60 % of the main rotor radius. As the lateral rotor induces an acceleration of the inflow, leading to a contraction of the streamtube, a deflective effect on the surrounding flow can be expected. In order to quantify this effect, the averaged flow fields of the setups with and without lateral rotors are subtracted and the resulting difference in vertical flow deflection is displayed in Fig. 5.16 on planes across the wingspan.

Here, a negative vertical flow deflection can be observed extending up to the main rotor with angles less than $-0.4°$. As this is exactly the region of decreased thrust in Fig. 5.15(a), the effect can be traced back to smaller effective angles of attack on the advancing main rotor blades passing the left lateral rotor's contracting streamtube.

While the right lateral rotor has the same effect on the flow field, due to the large advance ratio in this flight condition the retreating main rotor blades experience a significantly decreased dynamic pressure or even reverse inflow and therefore are less prone to changes in effective angle of attack.

Boisard's results [44] show an opposite trend of this interaction with—depending on the advance ratio—no effect on main rotor thrust or even a small thrust increase due to the lateral rotor influence. In contrast to the reverse interaction in the previous section, this is not caused by the inboard-down sense of rotation of the lateral rotor but rather by its relative position to the main rotor. While RACER's lateral rotors are positioned notably behind the main rotor hub, Boisard's lateral rotor is situated significantly further upstream. Thus, the main rotor thrust distribution still shows a decrease above the lateral rotor, but, further downstream, it features a compensating or even overcompensating region of thrust gain due to the lateral rotor influence. The reason for this was found to be the blocking effect of the lateral rotor's wake of accelerated flow, reducing the downward deflection below the highly loaded region of the main rotor disk and therefore inducing an increase of effective angle of attack.

For the investigations at hand, the same effect is visible downstream of the region of thrust decrease in Fig. 5.15(a). However, due to the longitudinal position of the lateral rotor, the main rotor thrust cannot benefit from this increase in effective angle of attack in a region large enough to compensate or even overcompensate for the thrust decrease.

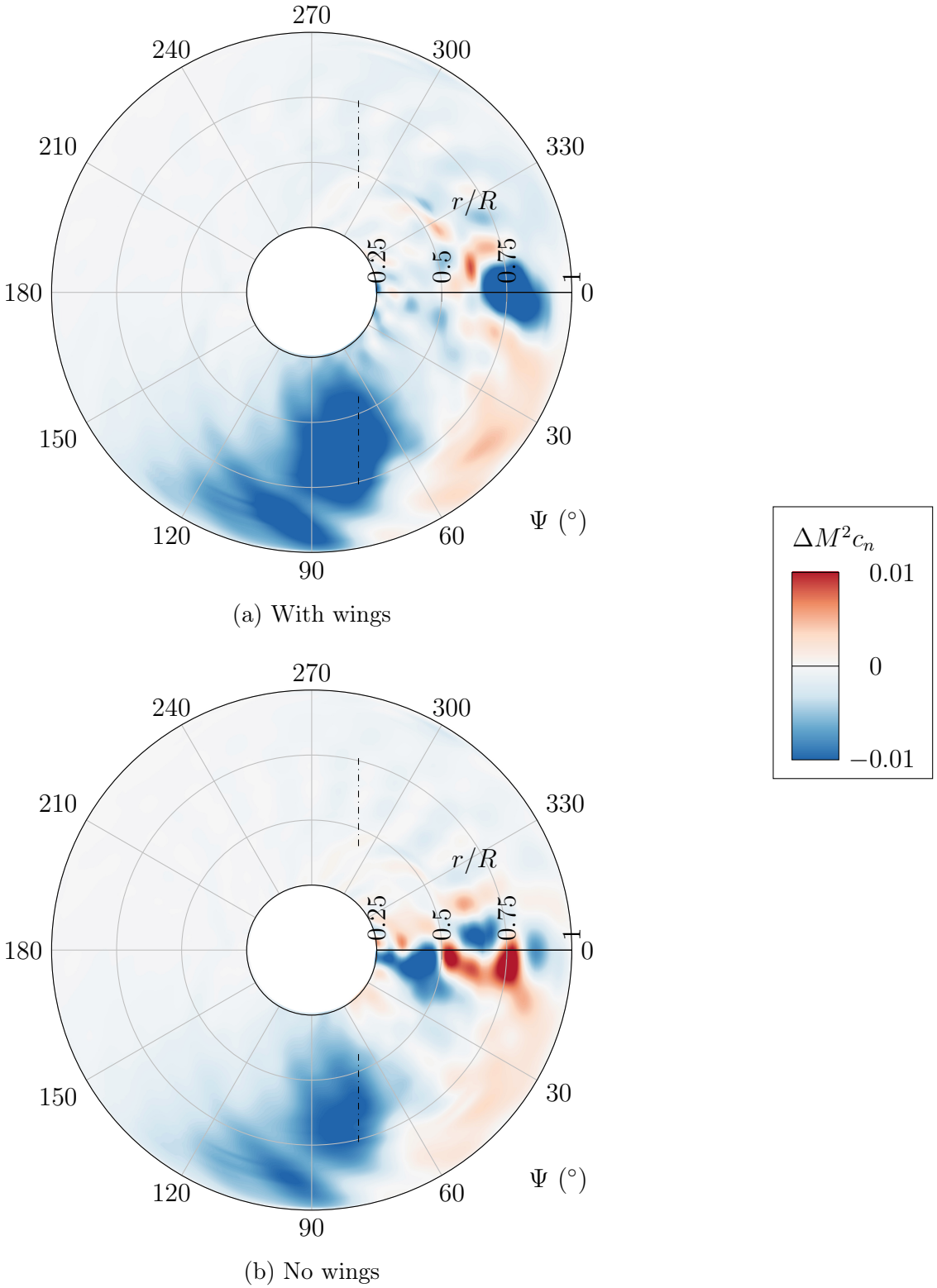

(a) With wings

(b) No wings

Figure 5.15: Distribution of thrust difference on main rotor induced by lateral rotors with and without wings. Section normal force coefficient. Frequency filtered above 20/rev. Approximate location of lateral rotors indicated. View from above. Adapted from Frey et al. [103].

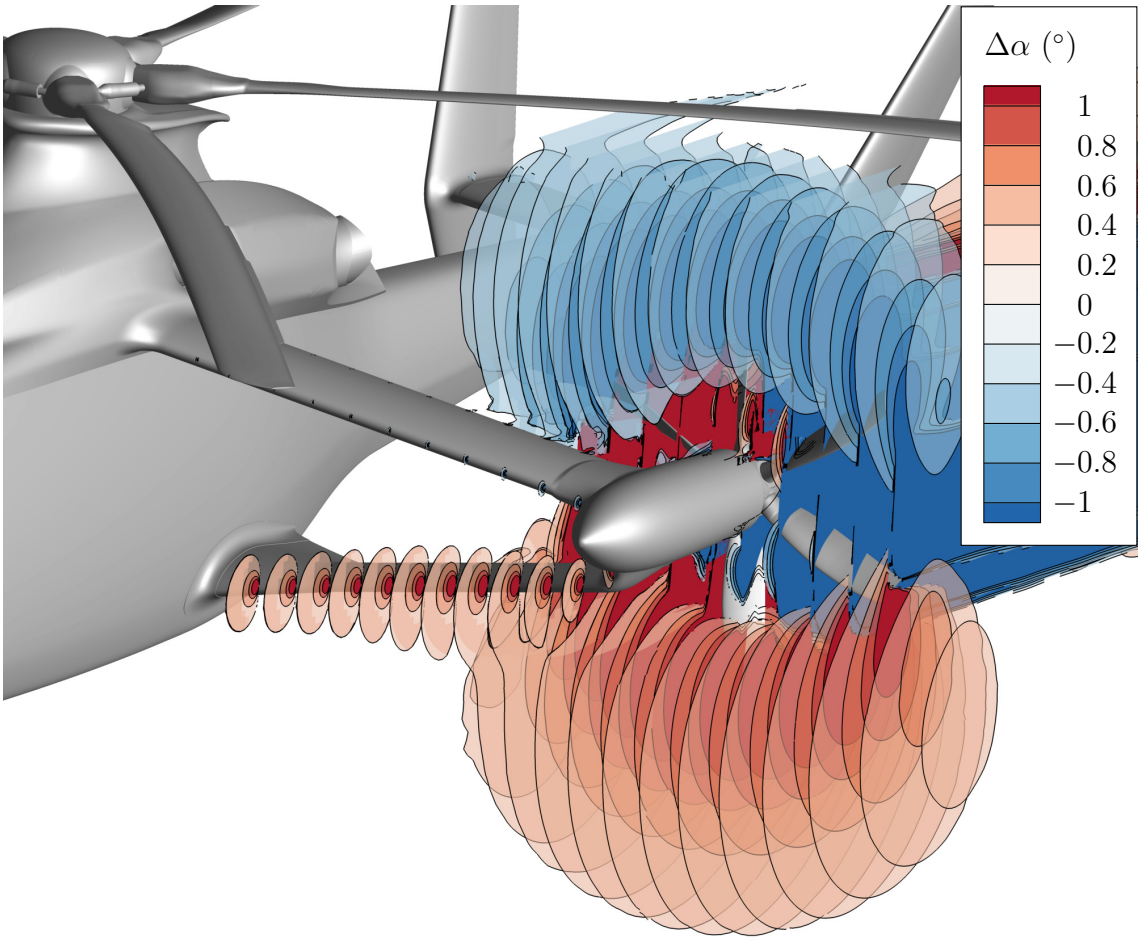

Figure 5.16: Distribution of vertical flow deflection induced by left lateral rotor on planes across wingspan. Values between $-0.4°$ and $0.4°$ blanked. Averaged over one main rotor revolution [103].

In order to differentiate between first- and second-order effects in the witnessed lateral rotor influence, the respective interaction is additionally assessed in the absence of wings (see configurations in Fig. 4.2(b), center and 4.2(c), right). The resulting distribution of thrust difference in Fig. 5.15(b) shows the same characteristic region of thrust decrease above the left lateral rotor. Similar to the equally observable thrust gain further downstream, however, it is less distinct compared to Fig. 5.15(a)'s cumulative phenomena in the wings' presence. This indicates an amplifying nature of the second-order effects and also becomes manifest in the comparison of lateral rotor–induced changes of global main rotor thrust with and without wings in Table 5.3.

While distinct regions of thrust difference occur in the rotor head wake, these are presumably caused by the stochastic nature of this wake's local flow phenomena, rather than a characteristic first- or second-order influence of the lateral rotors' presence. This is supported by the distributions of Fig. 5.15 differing particularly

Table 5.3: Changes in main rotor thrust and power. Normalized with respective configuration with lateral rotors.

	No lateral rotors, with wings	No lateral rotors, no wings
ΔT_{MR}	+4.1 %	+2.4 %
ΔP_{MR}	+0.0 %	−0.7 %

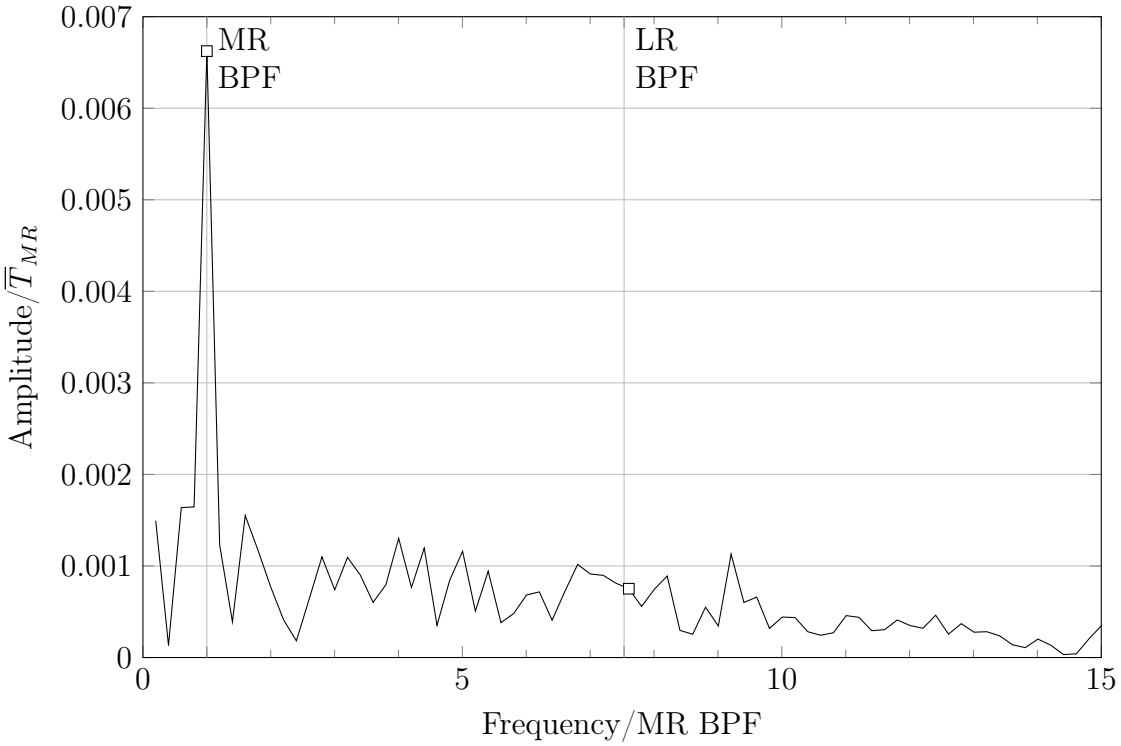

Figure 5.17: Frequency spectrum of thrust difference on main rotor induced by lateral rotors. Normalized with average thrust of main rotor in full configuration [106].

in this region despite their aforementioned overall agreement, which makes a characteristic effect on the rotor head wake highly unlikely.

The frequency spectrum of the main rotor's global thrust difference induced by the lateral rotors (see Fig. 5.17) does not show any fluctuations with the lateral rotor BPF. This indicates no effect of the lateral rotor blades' rotating pressure fields on the main rotor thrust generation. The effect on the mean flow, however, with the vertical deflection discussed before, is also visible here, as it induces additional fluctuations with the main rotor BPF. At roughly 0.7 % of the average thrust, though, they remain relatively small. This effect was also described by Bain and Landgrebe [42] who witnessed increasing main rotor blade moments for growing lateral rotor thrust in their wind tunnel tests.

5.5 Wing–Lateral Rotor Interaction

In contrast to the interactions discussed in the previous sections, the effect of the wings on the lateral rotors is of convective—wake-induced—nature and was expected to be beneficial for the lateral rotor performance in a prior publication involving the author of the present thesis [21]. In order to assess its magnitude, the performance of the installed lateral rotors is compared with respective results of a setup omitting the wings (see Fig. 4.2(b), center). The changes in thrust and required power of both lateral rotors are listed in Table 5.4 in relation to the full setup.

Without the influence of the wings, the lateral rotor thrust decreases significantly by 30–35 %—explaining the amplifying second-order effect in Section 5.4 in the wings' presence (see Fig. 5.15)—whereas the savings in required power are distinctly smaller. While no statement can be made about the influence on propulsive efficiency due to the different levels of thrust, Stokkermans et al. [114] found a gain of $\Delta\eta = 0.06$–0.11 with increasing wing lift, when comparing to an isolated lateral rotor at equal thrust.

Owing to the rather symmetrical trends, the following investigations are conducted on the left lateral rotor with the general findings, however, also applying to the right lateral rotor.

In order to locate the regions where the wings induce the thrust benefit on the lateral rotors, thrust polars of the two setups with and without wings are subtracted; the resulting distribution of thrust change is illustrated in Fig. 5.18(a). This clearly shows a thrust benefit not only in the direct wake of the upper and lower wing but also in the region between both wings and above the upper wing as well as—on a smaller scale—over the remaining rotor disk.

As the wings are likely to influence the lateral rotor inflow in a way that changes the rotor blades' effective angle of attack, the individual mechanisms are illustrated in detail in Fig. 5.19. Essentially, the underlying effect of the wings' induction is twofold: On the one hand, the wing wake alters the axial inflow velocity from $v_{ax,noWing}$ to $v_{ax,Wing}$. In combination with the blade section's local rotational speed v_{Blade} resulting from the rotational frequency Ω_{LR} and the radial position r,

Table 5.4: Changes in lateral rotor thrust and power. Normalized with with respective configuration with wings/nominal lateral rotor sense of rotation.

	No wings, with main rotor	No wings, no main rotor	Reverse lateral rotors	Reverse lateral rotors, retrim T_{LR}
ΔT_{leftLR}	−29.5 %	−34.1 %	−49.6 %	−1.6 %
$\Delta T_{rightLR}$	−34.4 %	−35.2 %	−57.5 %	−1.6 %
ΔP_{leftLR}	−24.6 %	−28.7 %	−42.9 %	+18.6 %
$\Delta P_{rightLR}$	−29.5 %	−30.3 %	−51.3 %	+22.6 %

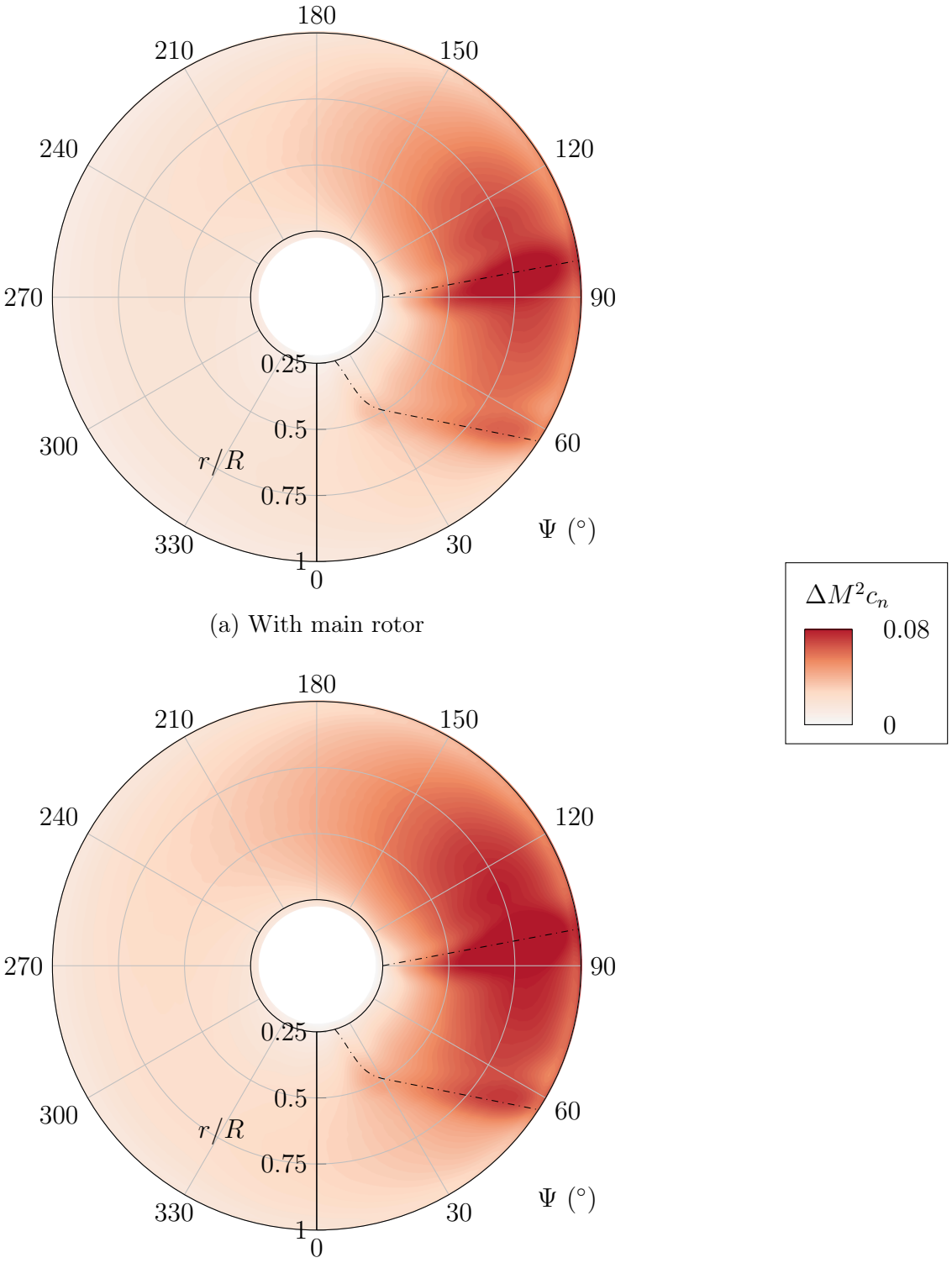

(a) With main rotor

(b) No main rotor

Figure 5.18: Distribution of thrust difference on left lateral rotor induced by wings with and without main rotor. Section normal force coefficient. Averaged over one main rotor revolution. Approximate location of wings indicated. View from behind. Adapted from Frey et al. [103].

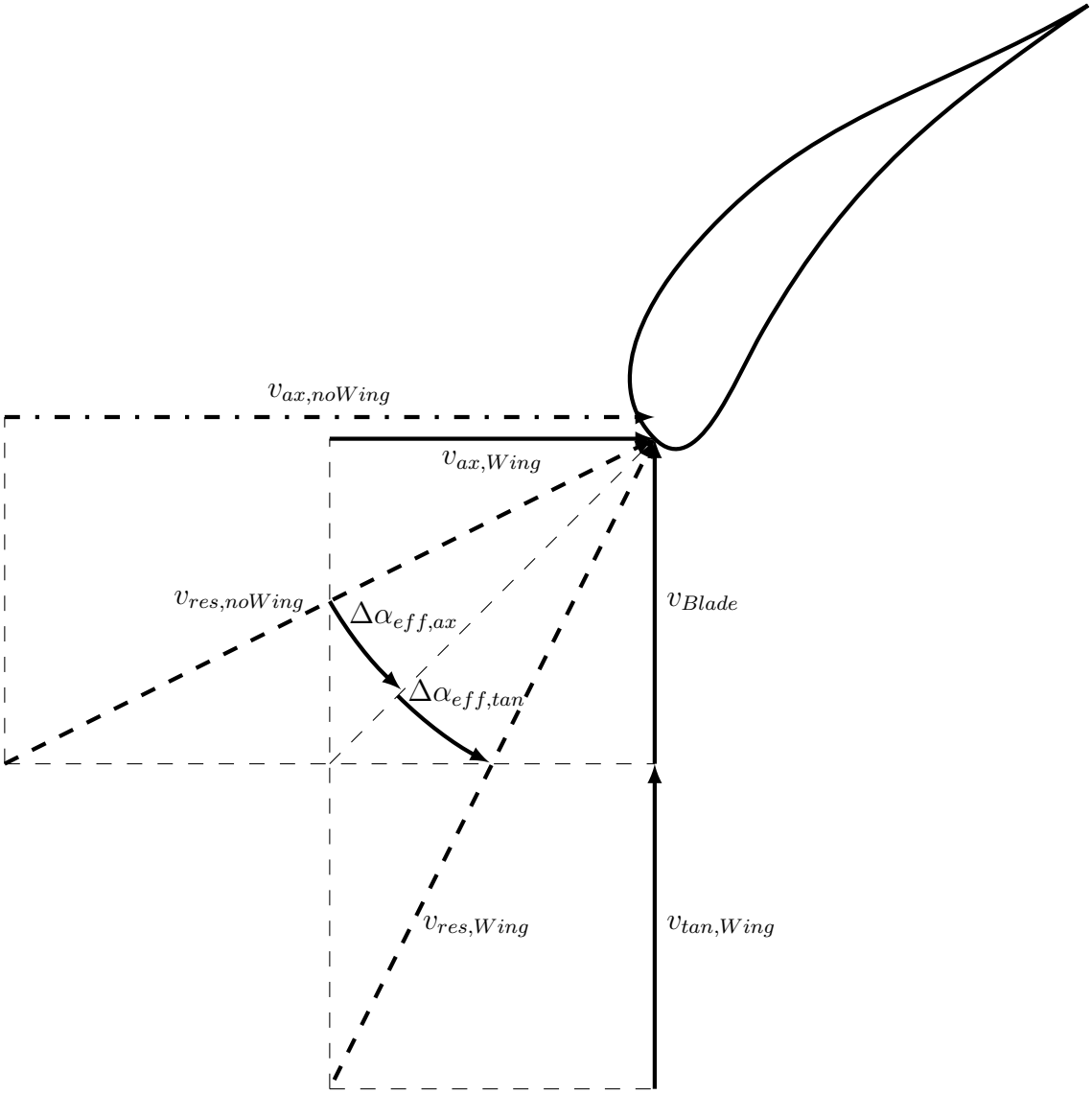

Figure 5.19: Sketch of inflow on lateral rotor blades and difference in effective angle of attack induced by wings [103].

this deflects the resulting inflow velocity $v_{res,noWing}$ by the difference in effective angle of attack $\Delta\alpha_{eff,ax}$ (note: the negligible tangential inflow velocity in the wings' absence $v_{tan,noWing}$ is included for the sake of completeness):

$$\begin{aligned}\Delta\alpha_{eff,ax} &= \arctan\frac{v_{tan,noWing}+v_{Blade}}{v_{ax,Wing}} - \arctan\frac{v_{tan,noWing}+v_{Blade}}{v_{ax,noWing}} \\ &= \arctan\frac{v_{tan,noWing}+\Omega_{LR}r}{v_{ax,Wing}} - \arctan\frac{v_{tan,noWing}+\Omega_{LR}r}{v_{ax,noWing}}\,. \end{aligned} \tag{5.4}$$

On the other hand, the wings' circulation and the wing tip vortex induce a tangential velocity $v_{tan,Wing}$ in the lateral rotor inflow. This results in an additional difference

in effective angle of attack $\Delta\alpha_{eff,tan}$ contributing to the overall deflection between the resulting inflow velocities $v_{res,noWing}$ and $v_{res,Wing}$:

$$\begin{aligned}\Delta\alpha_{eff,tan} &= \arctan\frac{v_{tan,Wing}+v_{Blade}}{v_{ax,Wing}} - \arctan\frac{v_{tan,noWing}+v_{Blade}}{v_{ax,Wing}} \\ &= \arctan\frac{v_{tan,Wing}+\Omega_{LR}r}{v_{ax,Wing}} - \arctan\frac{v_{tan,noWing}+\Omega_{LR}r}{v_{ax,Wing}}\,. \end{aligned} \tag{5.5}$$

The influence of the first effect is displayed in Fig. 5.20(a)'s distribution of $\Delta\alpha_{eff,ax}$, computed from the average inflow of the left lateral rotor for the two setups with and without wings according to Eq. 5.4. In large parts, it shows only minor influence of the wings on the axial velocity with the wings' circulation leading to a deceleration of the subjacent flow and consequently values of $\Delta\alpha_{eff,ax} \geq 0°$ as well as the opposite effect above the wings. In contrast, the flow deceleration in the wings' wake clearly has a notable impact on the lateral rotor blades' effective angle of attack. Here, $\Delta\alpha_{eff,ax}$ reaches between $+2°$ and $+8°$ with positive values indicating an increased effective angle of attack due to the wing influence, being responsible for the thrust increase behind the wings' trailing edges illustrated in Fig. 5.18(a).

The wings' effect on the tangential lateral rotor inflow velocity, illustrated in Fig. 5.20(b)'s distribution of $\Delta\alpha_{eff,tan}$ according to Eq. 5.5, extends over a larger region. The flow channelled between upper and lower wing experiences a general downward deflection due to the wings' circulation which was also observed in recent studies on RACER by Wentrup et al. [43] and Yin et al. [46]. Owing to the inboard-up sense of rotation of the lateral rotor blades, this results in the effective angle of attack's increase by 1–5°.

Furthermore, a characteristic influence of the wing tip vortex described by Miranda and Brennan [49] as well as Patterson and Bartlett [50] for fixed-wing propeller aircraft and recently also witnessed for RACER [43, 45, 47] comes into effect, leading to a clockwise rotation of the flow around the nacelle and therefore additionally increasing the effective angle of attack of the counterclockwise rotating left lateral rotor. This becomes most obvious on the transition between upper wing's suction side and nacelle, but is visible on a large part of the blades' radius over most of the azimuth. In combination with the decelerating effect of the wing wakes this tangential deflection accounts for the distribution of thrust increase due to the wings in Fig. 5.18(a), the outwards shift between the two distributions arising from the radially varying rotational velocities and, consequently, dynamic pressure.

While the first effect, illustrated in Fig. 5.20(a), is independent of the lateral rotors' sense of rotation as it acts via the axial inflow velocities, the second and seemingly larger effect only increases the lateral rotor blades' effective angle of attack due to their favourable inboard-up sense of rotation. In order to examine

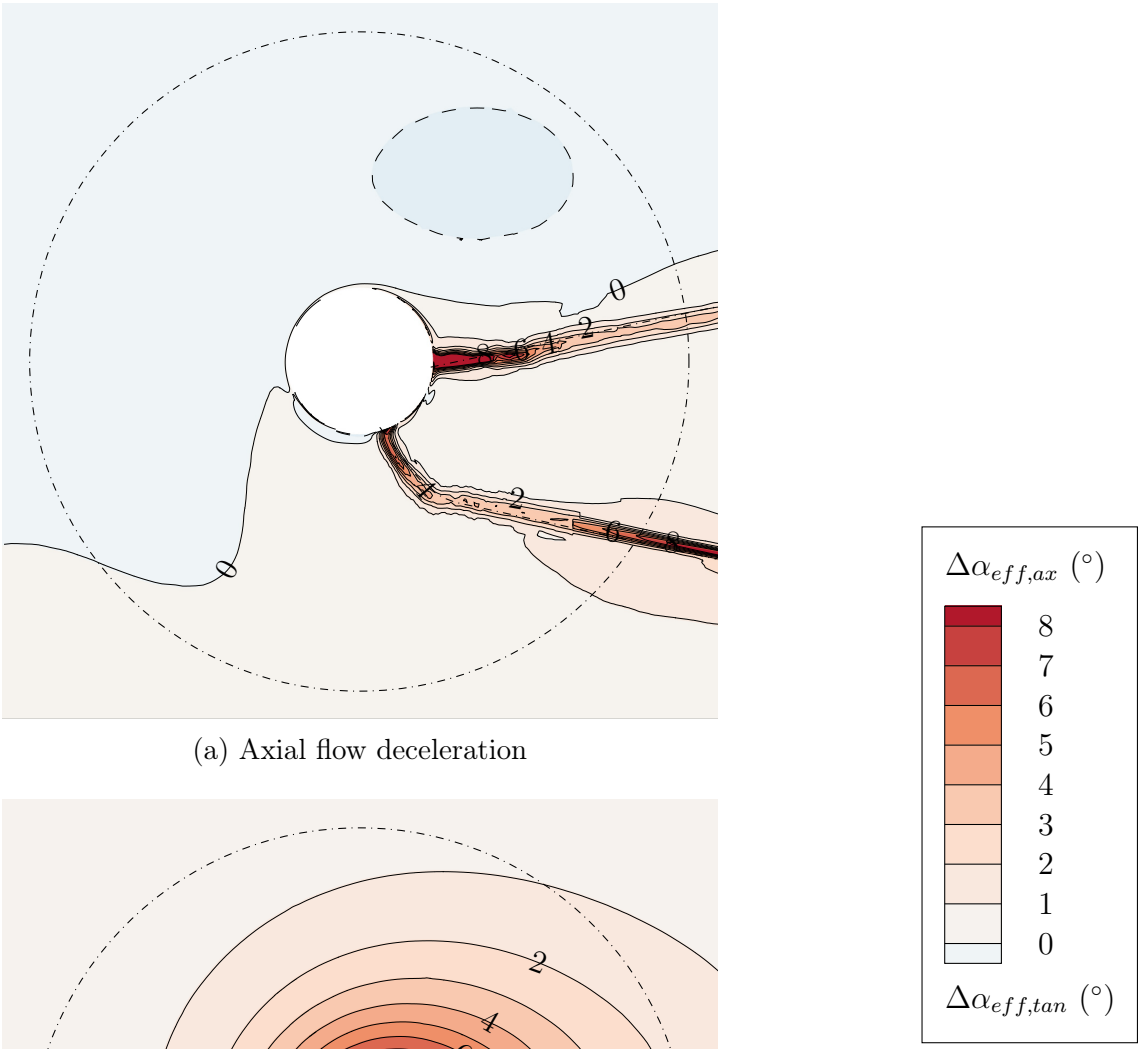

(a) Axial flow deceleration

(b) Tangential flow deflection

Figure 5.20: Distribution of difference in effective angle of attack on left lateral rotor inflow induced by different effects of wings. Based on local rotational velocity. Averaged over one main rotor revolution. Approximate location of wings indicated. View from behind [103].

the interplay of these two mechanisms more deeply, additional simulations are conducted on a full RACER configuration with reverse lateral rotor sense of rotation on mirrored blades (note: blades remain on their respective lateral rotor, airfoils are mirrored). The respective thrust and power of the lateral rotors modified in such a way, normalized with their respective values on the basic configuration, are also included in Table 5.4.

This shows an important effect of the lateral rotors' sense of rotation on their performance in combination with the wing influence. At equal blade pitching angles, they generate 50–60 % less thrust with an inboard-down sense of rotation due to the influence of the identically oriented wing tip vortex and the flow's downward deflection behind the wings caused by their circulation. As already deduced from the distributions of $\Delta\alpha_{eff,tan}$ and $\Delta\alpha_{eff,ax}$ in Fig. 5.20, this effect is stronger than the—independently of the sense of rotation—positive effect of the flow deceleration in the wing wakes.

The decrease in power requirement for the reverse lateral rotors, listed in Table 5.4, is noticeably smaller than the loss in thrust. In order to assess the lateral rotor efficiency on a more comparable operating point, both lateral rotors are retrimmed manually towards their thrust on the nominal configuration by increasing their respective blade pitching angles.

This is realized by increasing the left lateral rotor's blade pitch by 6.05°, while the right lateral rotor requires an additional 7.0°. The results on lateral rotor performance are included in Table 5.4. In order to achieve almost equal thrust ($-1.6\,\%$) to the nominal configuration, the retrimmed lateral rotors with reverse sense of rotation require roughly 20 % more power than with inboard-up sense of rotation. For a comparable flight condition, this configuration consequently suffers losses of 17–20 % in lateral rotor efficiency. Not being designed for this operating point at reverse sense of rotation, the lateral rotor blades are affected by incipient flow separation at their tips.

The resulting difference in thrust distribution between the two setups with similar net thrust but contrary sense of rotation on their lateral rotors is displayed in Fig. 5.21. While the nominal configuration clearly profits from the wing tip vortex energy recovery and the general downward deflection between the wings (see $60° \leq \Psi \leq 120°$), the difference is less pronounced directly in the wings' wakes where both configurations' effective angle of attack is increased due to the flow deceleration. The overall thrust increase in the inboard region, however, has to be compensated in the outer parts of the lateral rotor disk's outboard half, resulting from the increased blade pitching angles associated with the retrim.

In addition to its dependency on the lateral rotors' sense of rotation, this interactional effect also is affected by the presence of the main rotor. This becomes clear by additionally computing the thrust difference induced by the wings in the main rotor's absence from the configurations illustrated in Fig. 4.2(b), left and 4.2(c),

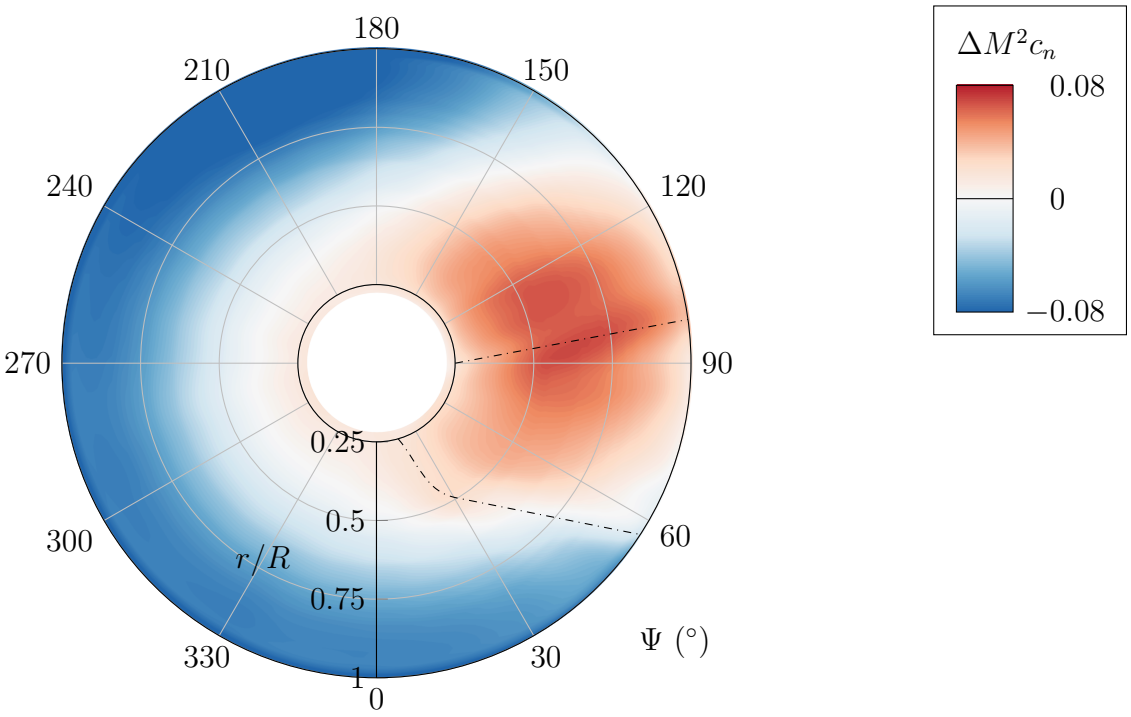

Figure 5.21: Distribution of thrust difference on left lateral rotor between nominal and reverse sense of rotation. Trimmed to similar net thrust. Section normal force coefficient. Averaged over one main rotor revolution. Approximate location of wings indicated. View from behind [103].

left. The resulting distribution of $\Delta M^2 c_n$ in Fig. 5.18(b) shows a slightly larger thrust gain caused by first-order effects than cumulatively which is confirmed by the respective difference in total lateral rotor thrust included in Table 5.4. While the underlying effect of axial flow deceleration with its velocity deficit in the wings' wake is induced by the latter's drag, the tangential flow deflection in contrast is driven by the wings' lift which in turn is affected by the main rotor as discussed in Section 5.1. Consequently, the (asymmetrical) detrimental effect of the main rotor on wing lift results in a similarly detrimental second-order effect in the wings' influence on lateral rotor thrust which slightly reduces the prevailing first-order interaction particularly on the left-hand side.

5.6 Lateral Rotor–Wing Interaction

A notable upstream effect of the lateral rotors on the—especially lower—wings was already found to occur in a previous study involving the author of the present thesis [21]. In order to investigate it more closely, similar to the approach in Section 5.1 the wings' individual lift for the full configuration is compared to the respective loads on a reduced setup omitting the lateral rotors' blades (see Fig. 4.2(b), right). The

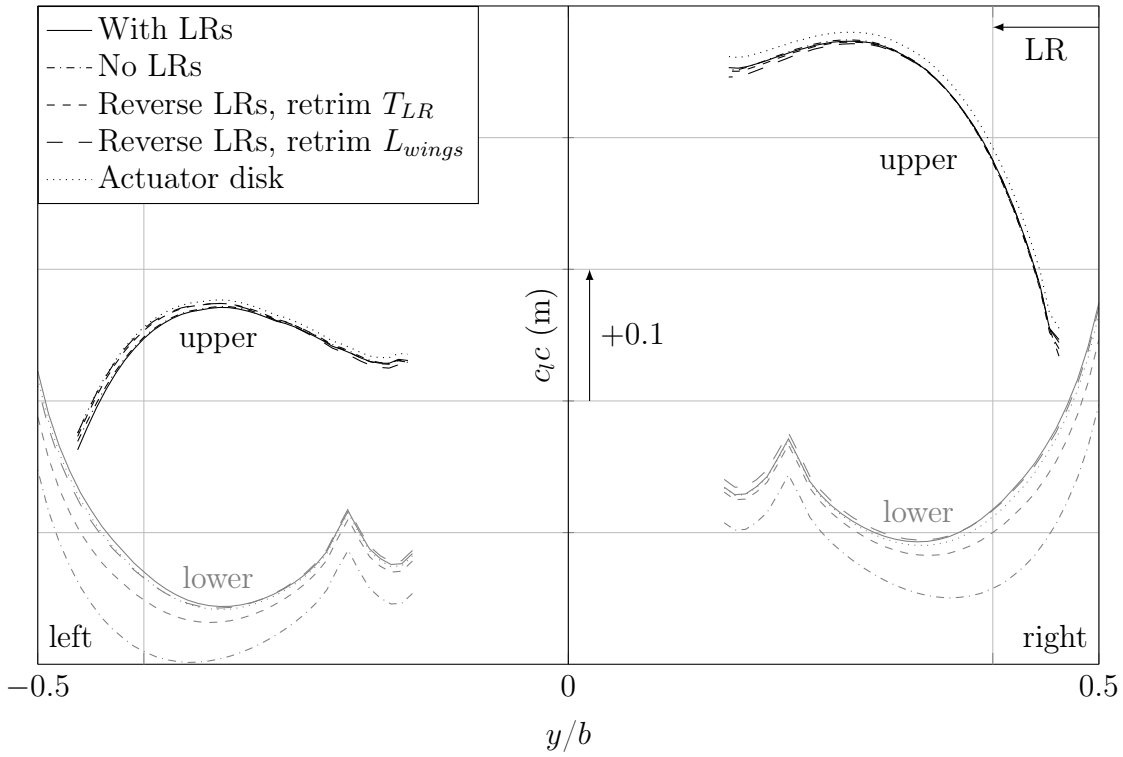

Figure 5.22: Distribution of wing lift with and without lateral rotors. Section lift coefficient. Averaged over one main rotor revolution. Approximate location of lateral rotors indicated [103].

resulting distributions of section lift coefficient (see Eq. 5.1) for both configurations are displayed in Fig. 5.22.

While the upper wings show hardly any difference in lift generation due to the presence of the lateral rotors, the lower wings experience a notable increase in lift not only on the outer regions—in the direct vicinity of the lateral rotor disks—but over the complete wingspan. Both trends were confirmed in a recent study on RACER by Stokkermans et al. [47]. As the lateral rotors are unlikely to have a large effect on the dynamic pressure outside of their streamtubes, the benefit in wing performance caused by their presence rather originates from an increase in effective angle of attack.

The resulting difference in wing lift is displayed in Fig. 5.23. With the help of the ideal lift curve slope of 2π/rad, a change in effective angle of attack required to generate the additional lift on the lower wings is estimated in the order of 0.5°. Albeit also caused by a rise in dynamic pressure within the streamtube, the relatively large additional lift in the wings' outer region would require a larger increase in effective angle of attack, whereas $\Delta\alpha_{eff}$ drastically drops with increasing distance from the rotors.

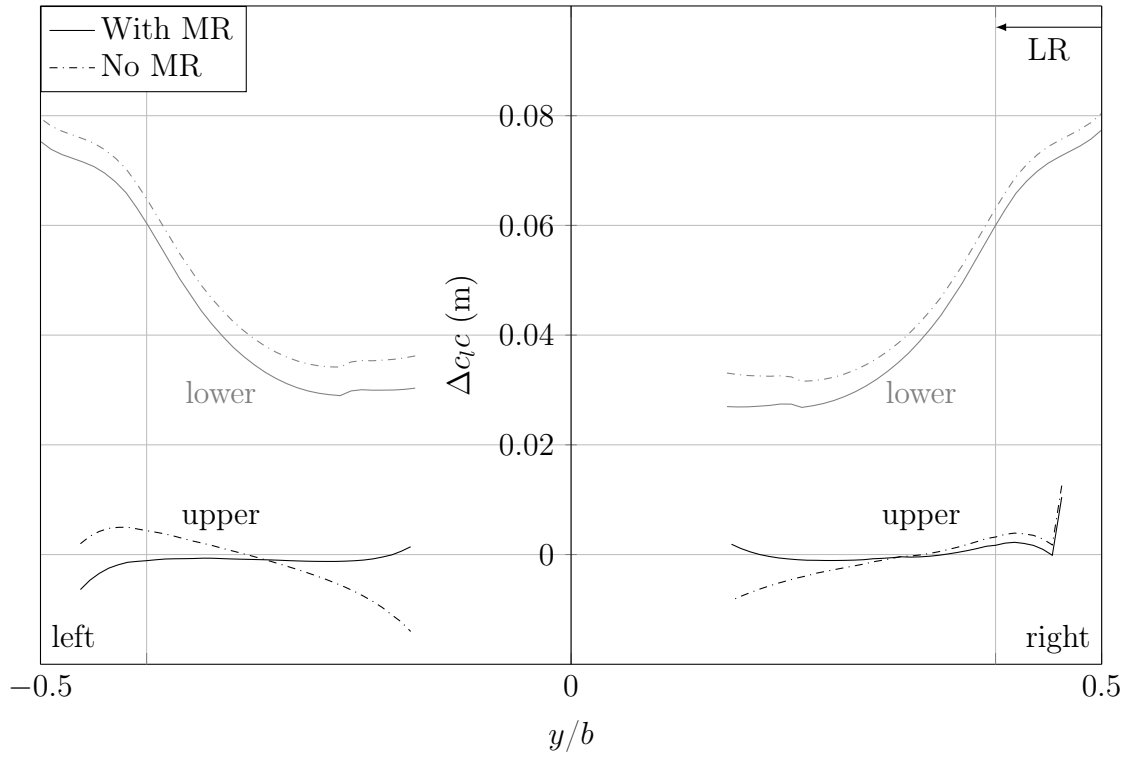

Figure 5.23: Distribution of difference in wing lift induced by lateral rotors with and without main rotor. Section lift coefficient. Averaged over one main rotor revolution. Approximate location of lateral rotors indicated. Adapted from Frey et al. [103].

The vertical flow deflection induced by the lateral rotors was already discussed in Section 5.4 and the respective distribution of $\Delta\alpha$ on planes across the left wings can be observed in Fig. 5.16. While the upper wing's inflow clearly is not affected by the lateral rotor's presence, leading to the relatively unchanged lift distribution in Fig. 5.22, the lower wing experiences an upward deflection of its inflow over the whole wingspan. As the magnitude of this is in fact similar to the change in $\Delta\alpha_{eff}$ of roughly 0.5° that was found to be necessary for the lift increase in Fig. 5.23, this vertical deflection—neglecting the dihedral—is responsible for the change in wing performance.

The characteristic distribution of the vertical flow deflection is caused by the lateral rotors in combination with RACER's specific wing geometry. While the lateral rotors induce a contracting streamtube, at the inboard region the additional radial flow caused by this contraction is somewhat hindered by the presence of the fuselage. Consequently, flow originating from above and below is sucked between the nacelle and the fuselage. However, due to the more upstream position of the upper wing with its positive sweep, additional flow from above is blocked, leading to a concentration of the induced vertical inflow from below. The result of this effect is the upward deflection of the lower wings' inflow and, finally, its increase in lift

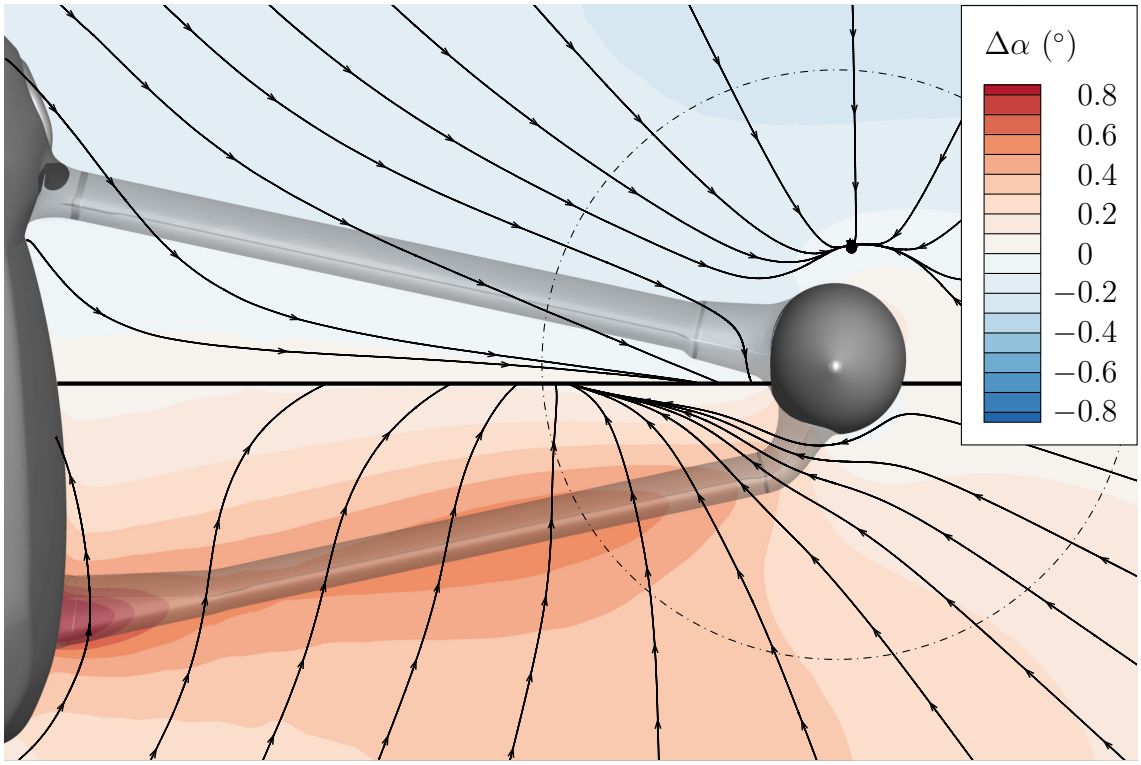

Figure 5.24: Streamlines of velocity difference and distribution of vertical flow deflection induced by lateral rotors on planes in inflow of upper and lower left wing. Averaged over one main rotor revolution. View from ahead [103].

generation. Figure 5.24 illustrates this difference between upper and lower wings with the help of the induced velocities' streamlines on two different planes 0.25 m ahead of the left wings' respective leading edges.

The effect of this can be observed in the distribution of the additional mass flux induced by the lateral rotors, evaluated on a plane roughly spanned by the upper and lower wings' quarter chord lines in Fig. 5.25. It clearly shows a rapid reduction outside the streamtube close to the upper wing. Further below, however, an increased mass flux occurs towards the lower wings' roots due to the aforementioned effect.

As part of a wind tunnel study on fixed-wing propeller aircraft, Patterson and Bartlett [50] observed an increased wing lift at the addition of a propeller to a wing tip–mounted nacelle, which Janus et al. [51] later confirmed with a numerical analysis. They traced it back to the propeller counteracting the wing tip vortex and therefore increasing the wing's effective angle of attack. Especially on RACER's upper wings, similar characteristics cannot be witnessed, as the lift distributions in Fig. 5.22 show no significant difference here. Owing to the box wing configuration acting similar to an endplate, this upstream effect on the upper wings seems to be prevented.

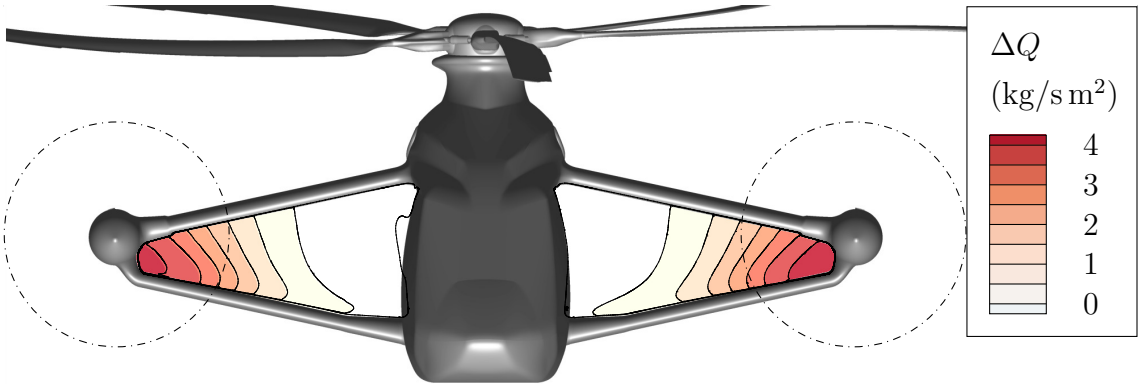

Figure 5.25: Distribution of difference in mass flux induced by lateral rotors between wings. Averaged over one main rotor revolution [103].

On the lower wings, however, the dominating beneficial effect is the aforementioned upward suction of additional flow due to the interaction of the contracting streamtube with the fuselage and the upper wings. This is confirmed with the help of the previously discussed simulations with a reverse sense of rotation on the lateral rotors. As the sole application of this measure results in a significant drop in lateral rotor thrust (see Section 5.5) and consequently a weaker streamtube, the retrimmed configuration with similar net thrust is assessed once again, and the resulting lift distributions are included in Fig. 5.22.

While the upper wings' lift remains unchanged, the lower wings show a notable lift increase compared to the configuration without lateral rotors. Especially close to their roots, almost the level of lift at nominal sense of rotation is reached, while with growing spanwise position the lift benefit is slightly smaller. Most likely, this is caused by the specific lateral rotor thrust distribution at this operating point. As previously shown in Fig. 5.21, at similar net thrust the lateral rotor with reverse sense of rotation generates significantly less thrust in the region between upper and lower wings. Consequently, the streamtube is less developed here, leading to a weaker influence of the aforementioned beneficial effect. This is reflected in the mass flow passing between the wings, listed in Table 5.5, which is significantly larger than without lateral rotors but still does not fully reach the magnitude of the standard configuration and therefore explains the remaining difference in wing lift.

In order to verify the possibility of reproducing the standard configuration's wing lift with reverse lateral rotors, both lateral rotors' pitch angles are retrimmed once again. While the first retrim—aimed at equal lateral rotor thrust—required an additional pitch angle of 6.05° and 7.0° for the left and right lateral rotor, respectively, another increase by 4.25° and 4.0°, respectively, leads to a wing lift almost identical to the nominal lateral rotor sense of rotation. This can be observed in the corresponding wing lift distribution in Fig. 5.22.

Table 5.5: Changes in mass flow between wings. Normalized with full configuration.

	No lateral rotors	Reverse lateral rotors, retrim T_{LR}	Reverse lateral rotors, retrim L_{wings}	Actuator disk
$\Delta\dot{m}_{left}$	$-1.3\,\%$	$-0.3\,\%$	$+0.1\,\%$	$-0.1\,\%$
$\Delta\dot{m}_{right}$	$-1.2\,\%$	$-0.2\,\%$	$+0.2\,\%$	$-0.1\,\%$

In contrast to the first retrim, this does not result in a total lateral rotor thrust similar to the standard configuration but in a similar thrust level in the region between upper and lower wing. Consequently, a comparably strong streamtube is induced here and the mass flow passing between the wings is larger than for the first retrim. While, according to Table 5.5, the offset from the nominal setup is significantly decreased on the left wings, it remains comparably large, yet oppositely signed, for the right wings.

The independence of the lateral rotors' beneficial effect on the wing lift of their sense of rotation finally is examined by replacing the discrete lateral rotors by actuator disks. Thus, the lateral rotor thrust distribution achieved for the standard configuration can be applied while neglecting the tangential (and radial) forces induced by the specific sense of rotation. Table 5.5 illustrates a good agreement of the mass flow passing between the wings—induced by the resulting streamtube—with the full configuration. As the respective wing lift distributions of the setups with discrete lateral rotors and actuator disks in Fig. 5.22 are very similar, the lateral rotors' axial acceleration of the flow is found to be causing this beneficial effect rather than its rotatory influence.

Similar to the main rotor, the lateral rotors not only influence the average lift of the wings but also induce load fluctuations. This can be clearly seen in Fig. 5.26's frequency spectrum of the left wings' lift difference due to the lateral rotors. With the right wings showing similar characteristics, both upper and lower left wings have a distinct lift fluctuation induced by the lateral rotors at their first BPF. Despite being even smaller than the fluctuations induced by the main rotor discussed in Section 5.1 (see Fig. 5.7), the left upper wing's frequency spectrum still features a fluctuation at the first lateral rotor BPF with an amplitude of roughly $0.3\,\%$ of its mean lift, whereas the respective lower wing—also being significantly more affected in mean lift—experiences somewhat larger fluctuations ($0.45\,\%$) and furthermore shows a peak at the second lateral rotor BPF.

Additionally, the presence of lateral rotors induces small lift fluctuations at the first main rotor BPF on both wings which is caused by a second-order effect. As discussed in Section 5.4 and illustrated in Fig. 5.15(a), the lateral rotors are responsible for a thrust difference on the main rotor which, in turn, leads to characteristic lift fluctuations on the wings (see Section 5.1 and Fig. 5.7), the combination of both consequently leading to the fluctuations witnessed in this context.

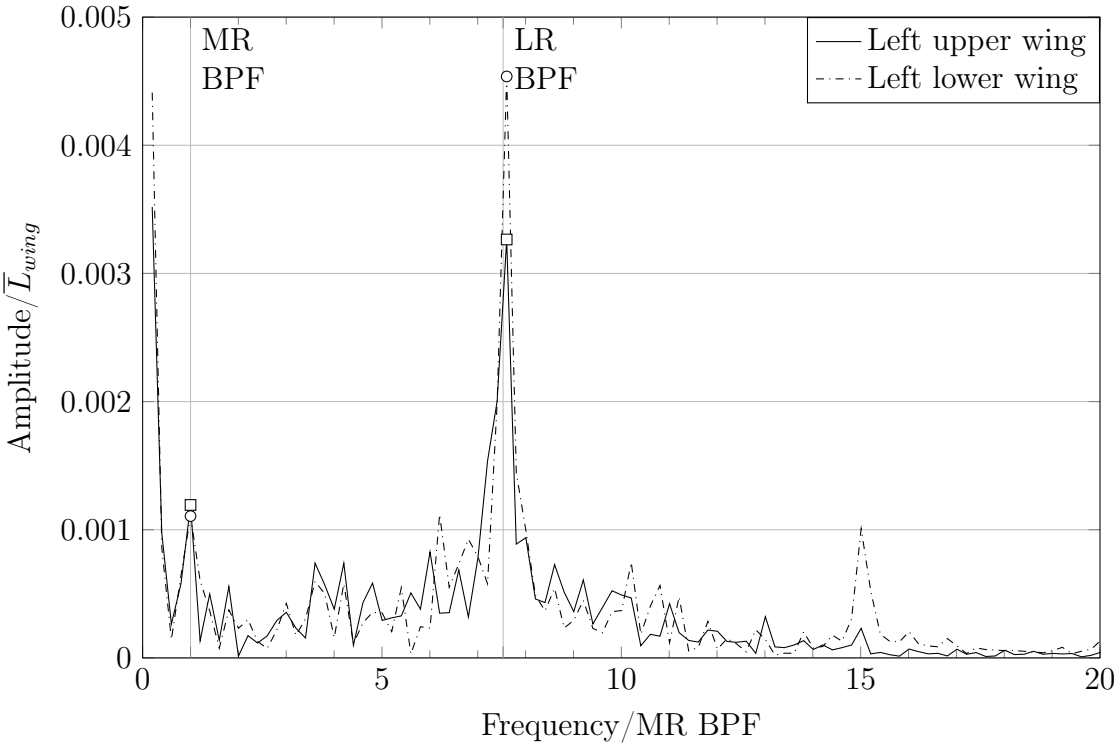

Figure 5.26: Frequency spectrum of lift difference on left wings induced by lateral rotors. Normalized with average lift of respective wing in full configuration [103].

A minor second-order effect can also be discovered in Fig. 5.23's additional distributions of difference in wing lift induced by the lateral rotors in the absence of the main rotor. Compared to the respective change with main rotor present, the upper wings particularly show a difference in their root regions, which was previously observed in Fig. 5.6 and attributed to the influence of the engine inlets with their boundary conditions inducing a slightly differing mass flow (see Section 5.1). As illustrated by the remaining difference between first-order and cumulative effect of the lateral rotors, which is relatively small but extends over the full span of the lower wings, their complex influence on wing inflow described above clearly interacts with the respective downward deflection originating from the main rotor.

5.7 Conclusions

Within this chapter, mutual interactions between the main rotor, wings, and lateral rotors of Airbus Helicopters' compound helicopter RACER were investigated for its cruise flight. By comparing detailed, trimmed CFD results of the full configuration with reduced setups omitting individual components, the fundamental understanding of first- and second order interactions and their effect on the aerody-

namic performance of main rotor, wings, and lateral rotors was improved. From the results presented, the following conclusions are drawn:

1. The main rotor has a first-order effect on the wings' lift generation. Especially the region of highest lift on the main rotor's advancing blades induces a notable decrease of effective angle of attack and, thus, lift on the subjacent left wings, whereas only a small loss was observed on the retreating side.

2. The reverse influence of the wings on the main rotor equally manifests itself mainly on the advancing side where the wings' circulation leads to an increase in effective angle of attack ahead of them and conversely a decrease behind them, resulting in an overall thrust decrease of 9 %. Second-order effects are of minor significance.

3. A tangential velocity in the upper part of the lateral rotors' inflow is induced by the main rotor. With the same orientation as the blades' rotation, they result in a decrease of effective angle of attack and consequently thrust in this region. Significant gain in thrust on the upstroking blades due to a vertical flow deflection originating from the main rotor does not occur as the wings hinder a notable influence in this region via a second-order effect. While with a decrease of 4 % and 1 %, respectively, the influence on lateral rotor net thrust is stronger below the left-hand—advancing—side of the main rotor, the right lateral rotor in contrast experiences larger thrust fluctuations caused by the main rotor, yet still at a small level.

4. Main rotor thrust is decreased by 4 % due to the influence of the left lateral rotor as the contraction of the subjacent streamtube results in a reduced effective angle of attack in the region of the advancing blades located above. A similar effect on the opposite side of the main rotor could not be observed due to the operating conditions on the retreating blades at an advance ratio of over 0.5. As a result of the slightly aft longitudinal position of the lateral rotors, the main rotor does not benefit substantially from the blocking effect of the lateral rotor wakes. The wings' thrust-augmenting influence on the lateral rotors amplifies the latter's interaction with the main rotor as a second-order phenomenon.

5. The convective influence of the wings immensely increases thrust generation on the left and right lateral rotors by 42 % and 52 %, respectively. Both due to a decrease in horizontal inflow velocity in the wings' wakes and a tangential inflow velocity induced by the wing tip vortex, the effective angle of attack of the lateral rotor blades is increased. While the first influence is independent of the lateral rotors' sense of rotation, the second effect specifically is beneficial

for RACER's inboard-up configuration but slightly suffers from a second-order effect caused by the main rotor–induced reduction of wing lift.

6. Exclusively on the lower wings, the lateral rotors induce a lift increase over the whole wingspan. Caused by RACER's specifically swept box wing configuration, the suction of the lateral rotors and the contracting streamtubes in combination with the fuselage induce an upward flow ahead of the lower wings, resulting in an increased effective angle of attack and, consequently, lift. The independence of this effect from the lateral rotors counteracting the wing tip vortices was not only shown by the lacking influence on the upper wings but also with the help of reversely rotating lateral rotors and actuator disks incorporating only axial forces, resulting in a similar lift increase on the lower wings.

6 Aerodynamic Interactions in Hover

Although being specifically designed to extend a helicopter's flight envelope towards flight speeds unreachable for conventional configurations, in order to close the "Mobility Gap", hovering remains a key operating condition for RACER. Consequently, the following chapter is dedicated to the analysis of this flight state in order to complement Chapter 5's effort in gaining a thorough understanding of the mutual effects of the helicopter's main aerodynamic elements. Similar to the analysis on aerodynamic interactions in cruise flight, the following sections discuss the six individual interactional effects between RACER's main rotor, wings, and lateral rotors in hover (see Fig. 4.1) according to the approach highlighted in Chapter 4 and based on the coupled and trimmed CFD simulations described in Chapter 2. In addition to the first-order effects, particular attention is paid to the second-order phenomena of the individual interactions, whose respective denotation—as before in Chapter 5—indicates an influence of the former component on the latter. While this chapter is largely based on Frey et al. [111], a small number of illustrations originate from an earlier version of this publication [113], whereas Section 6.3 contains additional analyses specifically conducted for this thesis.

An overview of the flow phenomena occurring in hover is illustrated in Fig. 6.1 with the help of λ_2 isosurfaces of the vortex structures and a temperature isosurface of the exhaust gases.

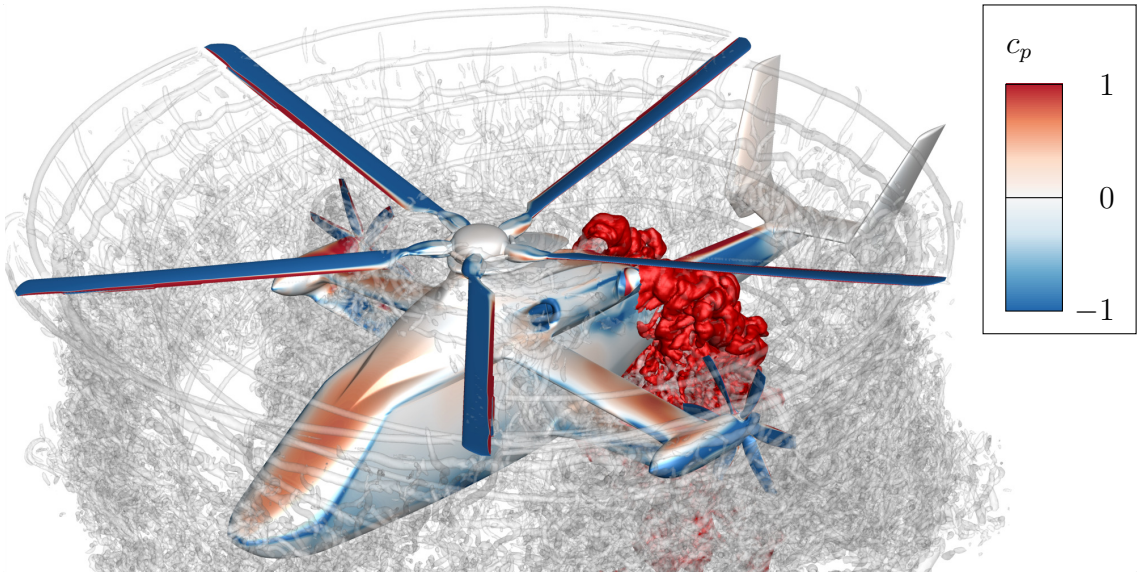

Figure 6.1: λ_2 flow field visualization of RACER in hover with temperature isosurface of exhaust gases and pressure coefficient on helicopter surface, normalized with dynamic pressure of induced velocity [111].

6.1 Main Rotor–Wing Interaction

Due to the lack of horizontal inflow, in hover the wings clearly cannot serve their main purpose of delivering lift. Instead, following Lynn's observation of increased main rotor power and consequently thrust due to the presence of wings in flight tests [60], Orchard and Newman [10], Moodie and Yeo [115], and Ferguson and Thomson [13] have discussed the generation of additional download as a suitable performance criterion. Ground tests of Felker and Light [56] on a rotor-wing combination of a tiltrotor configuration showed this download to amount to as much as 10 % of the total rotor thrust, whereas they found even larger values for compound helicopter configurations. Both was later confirmed by the numerical studies of Tanabe and Sugawara [61], and Tran et al. [58].

RACER's unique box wing configuration is intended to minimize this effect by shielding the lower wings from the main rotor downwash and consequently reducing their download by 50 % according to Blacha et al. [4]. The lower wings' shielding was confirmed in a previous study involving the author of the present thesis [21] as well as by Wentrup et al. [43] who found the upper wings' download to be three times larger than on the lower wings based on uncoupled CFD simulations with main rotor and lateral rotor actuator disks.

Following the approach outlined in Chapter 4, the main rotor's influence on the wing download is examined more deeply by comparing the results of RACER's hover to additional simulations where the main rotor geometry is omitted (see Fig. 4.2(b), left) and consequently no downwash impinges onto the wings. The resulting difference in all four wings' download distribution induced by the main rotor is displayed in Fig. 6.2 in terms of the section lift coefficient $c_l c$. While for the cruise flight's analysis the latter's normalization in Eq. 5.1 was conducted with the dynamic pressure of the free-stream velocity v_∞, the lack hereof in hover necessitates the use of the main rotor's—theoretical—induced velocity v_i instead. As phenomena in the downwash are of particular interest within this study, this velocity is determined for the contracted streamtube rather than the rotor disk:

$$v_i = \sqrt{\frac{2T_{MR}}{\rho_\infty \pi R_{MR}^2}}\,. \tag{6.1}$$

The upper wings mostly show an increase in download difference with increasing spanwise position. This is caused by the thrust distribution of the main rotor with the smallest thrust levels, and consequently induced velocity, towards the blade roots. In contrast, while the induced download on the lower wings is relatively similar to their upper counterparts close to the helicopter fuselage, it significantly decreases at larger spanwise position. This trend can be traced back to the box wing geometry, where even as the upper and lower wings' roots are positioned behind each

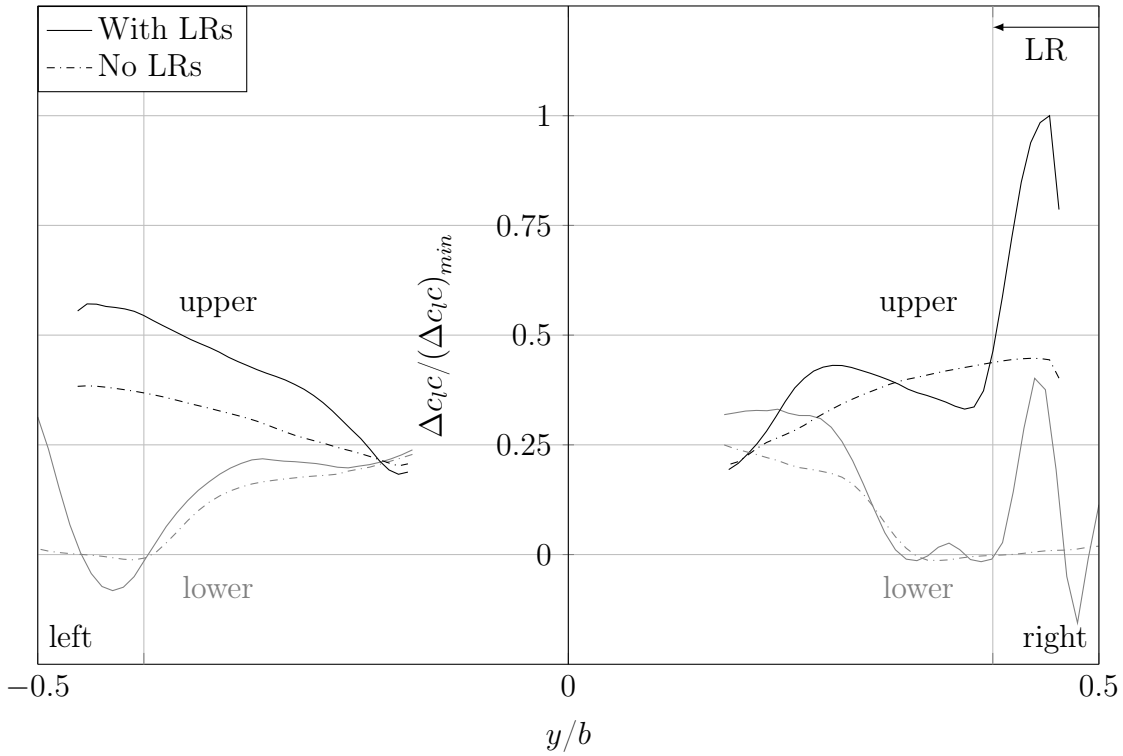

Figure 6.2: Distribution of difference in wing download induced by main rotor with and without lateral rotors. Section lift coefficient, normalized with dynamic pressure of induced velocity and maximum additional download induced by main rotor. Averaged over five main rotor revolutions. Approximate location of lateral rotors indicated [111].

other, due to their opposite sweep, they increasingly overlap with growing spanwise position, until the lower wings are fully shaded close to the lateral rotors.

However, a significant asymmetry is visible particularly in the outer half of the wings. The reason for this is the influence of the lateral rotors which both operate in highly different conditions. While the left lateral rotor generates nominal thrust and consequently induces suction on the adjacent wings, anti-torque generation requires the right lateral rotor to deliver reverse thrust, resulting in a blowing of the right wings' outer sections from geometrical trailing to leading edges.

While a comparison of the download distributions with and without main rotor only allows for an analysis of the cumulative direct and indirect influence of the main rotor onto the wings, following the schematic outlined in Fig. 4.3 the additional omission of the lateral rotors enables the comparison to a purely first-order influence. For this reason, Fig. 6.2 additionally shows the corresponding difference between the two setups respectively lacking lateral rotors, which allows for a comparison and location of first- and second-order effects. Even as the individual effects clearly

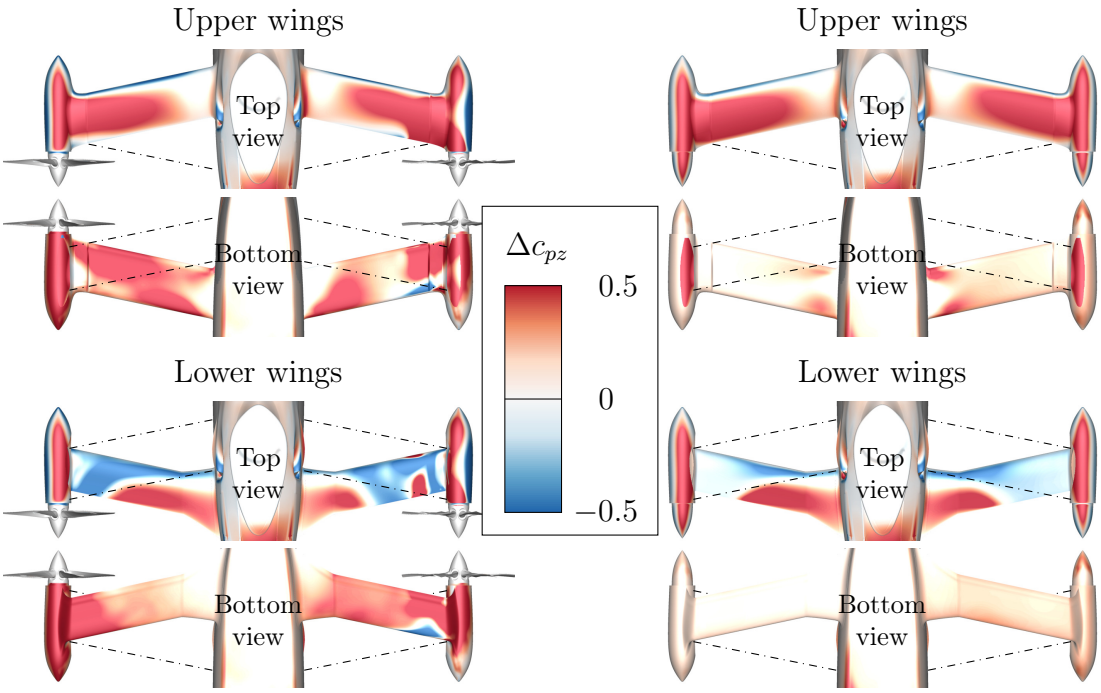

(a) With lateral rotors (b) No lateral rotors

Figure 6.3: Distribution of difference in wing download induced by main rotor with and without lateral rotors. Vertical component of pressure coefficient, normalized with dynamic pressure of induced velocity and vertical component of wall-normal vector (red: download). Averaged over five main rotor revolutions [111].

cannot be directly superposed due to the highly nonlinear nature of the interactions, this approach helps understanding their general principles.

The analysis is supported by distributions of the surface pressure difference induced by the main rotor, both in the presence and absence of lateral rotors, displayed in Fig. 6.3. In order to specifically focus on the surface pressure's contribution to download, the pressure coefficient c_p is normalized with the vertical component of the surface's wall-normal vector n_z:

$$c_p = \frac{p - p_\infty}{\frac{1}{2}\rho_\infty v_i^2}\,, \tag{6.2}$$

$$c_{pz} = c_p n_z\,. \tag{6.3}$$

Similar to what is visible in Fig. 6.2 for the upper wings in the lateral rotors' absence, a slight asymmetry in download generation was even witnessed on an isolated wing below a main rotor by Tanabe and Sugawara [61]. They attributed this to the downwash's swirl and the consequently varying horizontal component of the inflow towards the wing's leading or trailing edge. For the present analysis, the asymmetry

of the first-order effect on the upper wings is clearly increased by their sweep and the presence of the fuselage.

While the direct influence of the main rotor on the left upper wing mainly affects its top side, the indirect effect via lateral rotor not only reduces download at the outer section's trailing edge but overcompensates this by increasing download generation at the wing's lower surface. The mechanism behind this is illustrated in Fig. 6.4, where the change in velocity magnitude induced by the main rotor is displayed on a slice through the left wings. In the absence of the lateral rotors, no large-scale change in velocity is visible between the two wings. In combination with the additional convection through the left lateral rotor, however, a distinct vortex is driven by the downwash shed at the upper wing's trailing edge. While this is a phenomenon of the averaged flow fields, as Fig. 3.5(c) showed the occurrence of unsteady vortical structures of varying scales in the separated flow below the upper wing, the convection induces a region of suction on the upper wing's bottom side, consequently generating download.

A similar effect can also be witnessed on the right upper wing, where the first-order influence of the main rotor on the wing's lower surface is very small, while the second-order influence leads to the increased download in the wing's inner third illustrated in Fig. 6.2. In the outer region, the main rotor downwash heavily interacts with the lateral rotor wake reversely impinging on the wing, which, apart from smaller regions of lift, mostly increases download and causes the significant peaks in the respective spanwise distribution.

On the lower wings' pressure distributions, the effect of the box wing concept is clearly visible. While the main rotor downwash directly impinges on the root region and causes a distinct area of download generation on the wings' upper surface, this effect is eliminated with increasing spanwise position due to the shading through the upper wings. Moreover, as illustrated in Fig. 6.4, the impinging flow is partly deflected around the leading edge, where its acceleration leads to a region of suction and even induces lift. In the presence of the lateral rotors, the aforementioned second-order effect further increases the suction and extends the region of lift.

The second-order effect of the main rotor onto the lower wings is similar to the upper wings. In conjunction with the lateral rotor convection, the main rotor downwash induces download in large parts of the bottom side by generating a vortex. In the right lateral rotor's wake, the induced pressure difference highly varies and leads to the peaks in $\Delta c_l c$ illustrated in Fig. 6.2.

In addition to influencing the compound helicopter's performance in hover, the generation of download on the wings due to the impingement of the main rotor downwash might also be of unsteady nature. For this reason, the difference in the individual wings' vertical force between the full setup and the reduced setup without main rotor is analysed with the help of an FFT. In order to discriminate the direct effect of the main rotor onto the wings from the indirect effect via the lateral

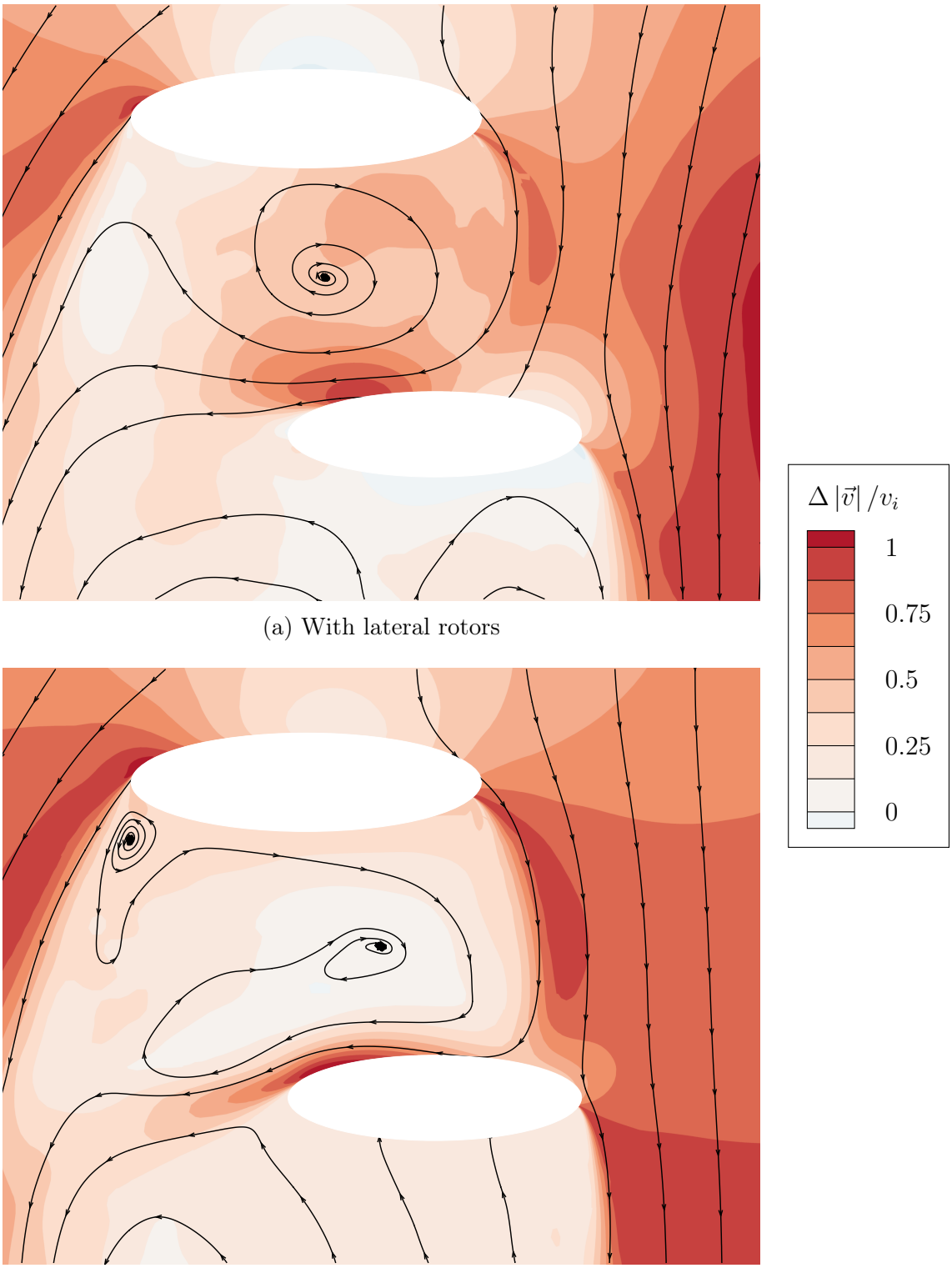

(a) With lateral rotors

(b) No lateral rotors

Figure 6.4: Streamlines of velocity difference and distribution of difference in velocity magnitude induced by main rotor with and without lateral rotors on longitudinal slice through wings at $y/b = -0.33$. Normalized with induced velocity of main rotor. Averaged over five main rotor revolutions [111].

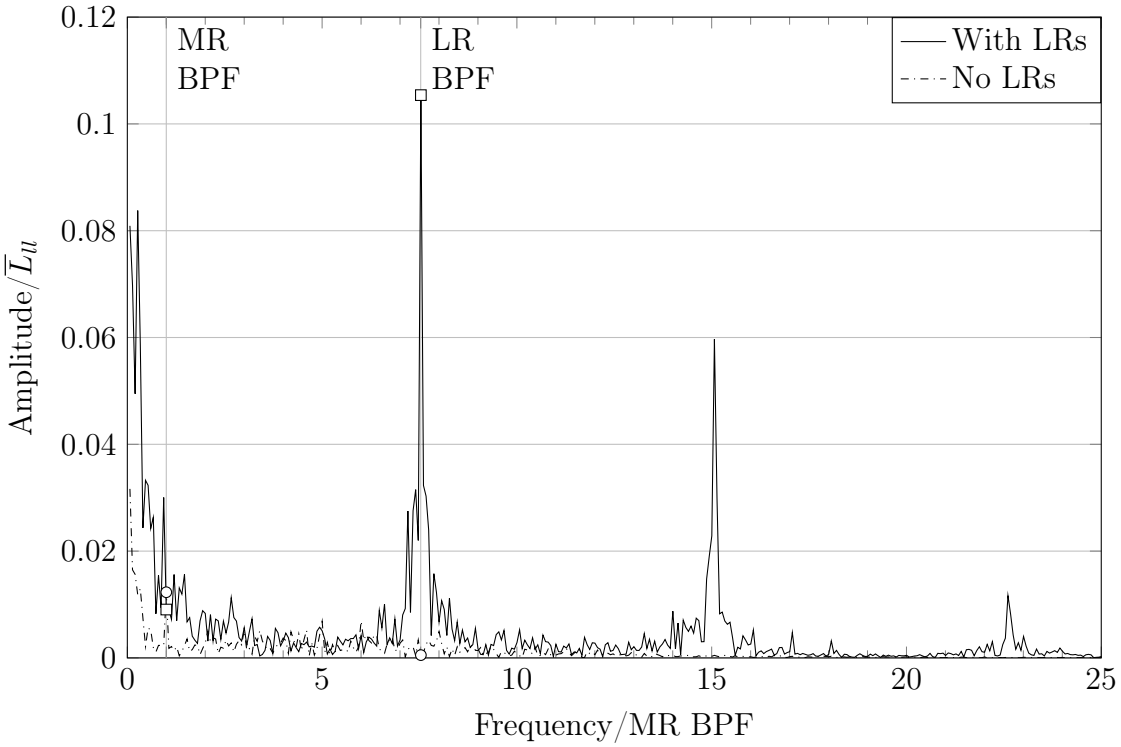

Figure 6.5: Frequency spectrum of download difference on left lower wing induced by main rotor with and without lateral rotors. Normalized with average download of wing in full configuration [111].

rotors, additional frequency spectra are generated from load differences between the two respective setups lacking lateral rotors. Here, both upper wings show very similar characteristics with fluctuations at main rotor BPF of roughly 1 % of the respective download in full configuration caused by the direct interaction. Due to the second-order interaction, additional fluctuations at lateral rotor BPF are accumulated with an amplitude of 2–3 %. With the previously discussed shading of the lower wings from the main rotor downwash, not only their total level of download is significantly smaller than for their upper counterparts but also their susceptibility to load fluctuations at main rotor BPF. Instead, the main rotor's direct influence mirrored in the load analysis with the lateral rotors absent almost exclusively causes low-frequency fluctuations emerging from the upper wings' separated flow. For the left lower wing, this can be observed in the respective frequency spectrum in Fig. 6.5.

However, the cumulative influence of the main rotor not only shows these low-frequency fluctuations but furthermore very distinct peaks at the lateral rotor BPF and its higher harmonics. While they amount to approximately 10 % of this wing's average download, this remains uncritical as their *absolute* level of fluctuations is similarly low like for the upper wings.

With the significantly lower level of thrust of the right lateral rotor and its unfavourable operating conditions, the indirect influence of the main rotor onto the right lower wing shows relatively small download fluctuations at lateral rotor BPF ($\approx 1\,\%$), predominated by the low-frequency influence of the upper wing's separated flow.

6.2 Wing–Main Rotor Interaction

The reverse influence of the wings on the main rotor, in contrast, cannot be of convective nature. Nevertheless, an upstream effect on the main rotor performance can be expected. For this reason, similar to the previous approach, the behaviour of the full RACER configuration is compared to a reduced setup lacking the wings (see Fig. 4.2(b), center).

By omitting the wings, the main rotor thrust decreases by $1.2\,\%$, whereas a slightly smaller power reduction can be observed (see Table 6.1). This clearly shows the occurrence of a positive upstream influence induced by the wings, which was previously also observed on tiltrotor configurations, where Felker and Light [56] found a thrust increase of $3\,\%$ at constant rotor power by adding a wing to their ground tests, with numerical studies of Tanabe and Sugawara [61] as well as Tran et al. [58] showing similar characteristics.

In order to locate the causative effect, the main rotor thrust distributions of both analysed setups are subtracted, and the resulting difference is displayed in Fig. 6.6(a). Not very surprisingly, the additional main rotor thrust induced by the wings originates from the regions above the latter. In the wings' root region, the benefit is smallest, whereas it has its peak towards the tips and above the nacelles.

The reason for these characteristics is the blockage effect—or, as referred to by Felker and Light, "ground effect"—of the wings in the main rotor downwash which can be seen in Fig. 6.7. Here, the averaged flow fields of the full and reduced setups are subtracted and the difference in vertical velocity across the wings is displayed. The stagnation of the downwash at the wings' upper surface manifests itself in a positive induced vertical velocity. However, there is also a significant upstream effect of this stagnation extending to the main rotor disk. This results in a smaller

Table 6.1: Changes in main rotor thrust and power. Normalized with respective configuration with wings.

	No wings, with lateral rotors	No wings, no lateral rotors
ΔT_{MR}	$-1.2\,\%$	$-1.2\,\%$
ΔP_{MR}	$-0.9\,\%$	$-0.9\,\%$

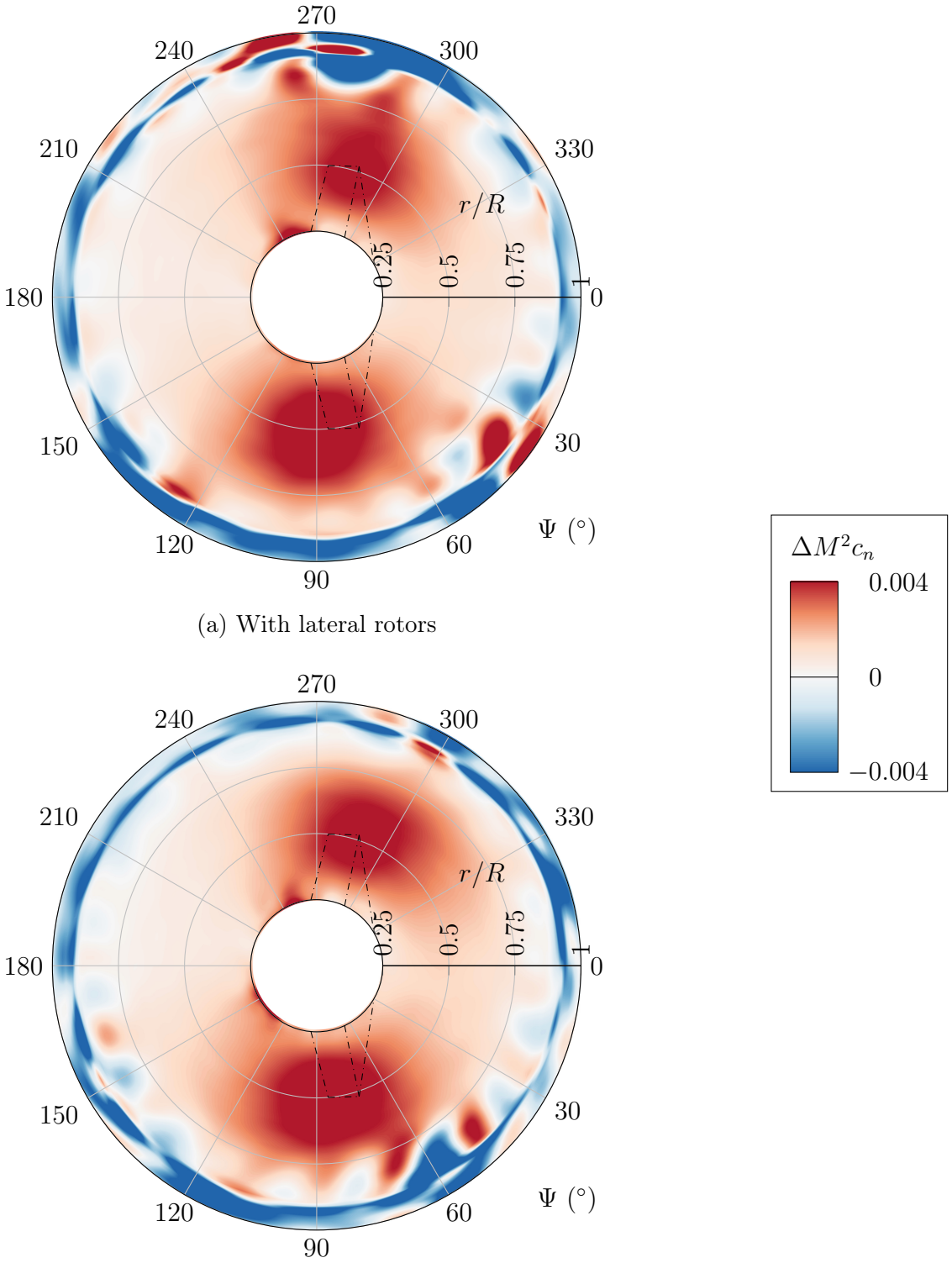

(a) With lateral rotors

(b) No lateral rotors

Figure 6.6: Distribution of thrust difference on main rotor induced by wings with and without lateral rotors. Section normal force coefficient. Averaged over five main rotor revolutions. Frequency filtered above 20/rev. Approximate location of wings indicated. View from above [111].

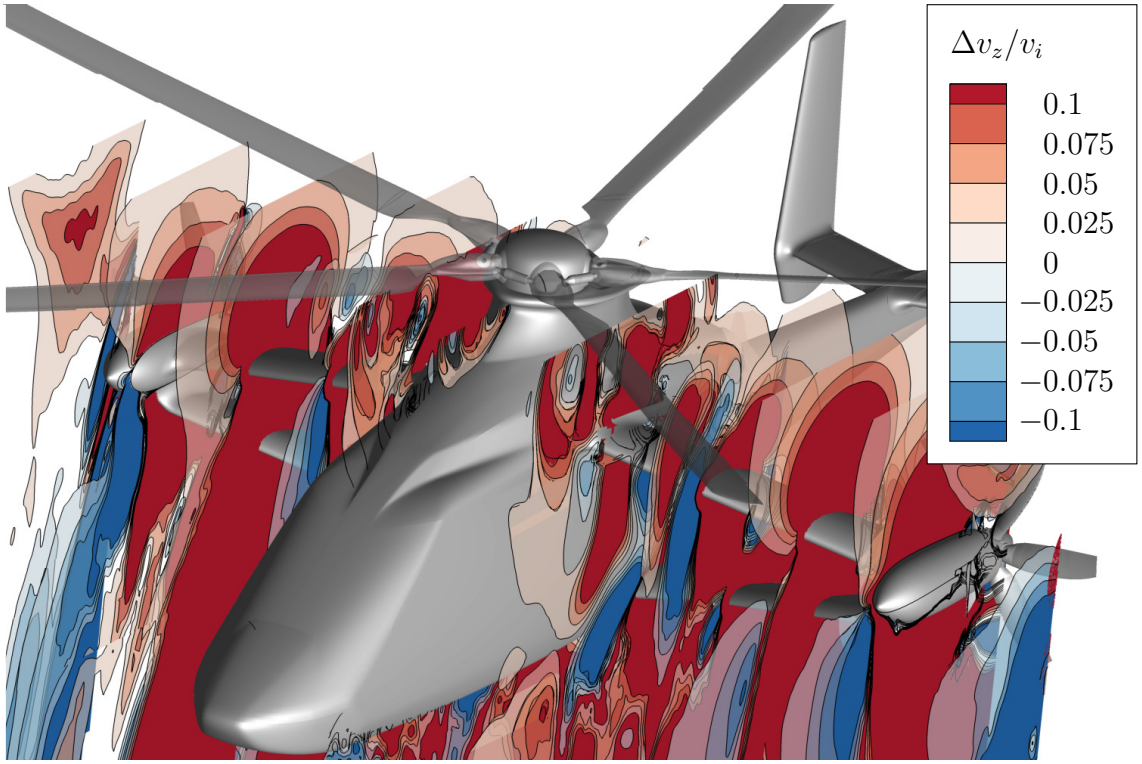

Figure 6.7: Distribution of difference in vertical velocity induced by wings on planes across wingspan. Normalized with induced velocity of main rotor. Values between −0.025 and 0.025 blanked. Averaged over five main rotor revolutions [113].

downward component of the main rotor blade inflow and consequently an increased effective angle of attack and larger thrust. Interestingly, this effect is not largest for the smallest distance between upper wings and main rotor in the root region. In contrast, with increasing spanwise position the growing vertical distance due to the negative dihedral is overcompensated by the larger main rotor thrust level and hence induced velocity with increasing main rotor radial position (see the distribution of pressure difference on upper wings in Fig. 6.3(a) for a similar result).

Furthermore, the additional main rotor thrust extends beyond the geometric wing tips and even the nacelles. This is caused by a similarly extending blockage effect of the wings which not only affects the flow inboard of the nacelles but leads to an outboard deflection of the decelerated flow. Consequently, the beneficial effect of the wings on the main rotor thrust can be observed up to 0.75 R_{MR}.

While, at first sight, this location might be associated with a second-order effect involving the lateral rotors, the latter in fact play no role in this interaction. This becomes obvious when generating the comparable distribution of main rotor thrust difference in Fig. 6.6(b) from two respective setups additionally lacking the lateral rotors (see configurations in Fig. 4.2(b), right and 4.2(c), right). Here, identical regions of thrust increase can be observed; consequently, the characteristics witnessed

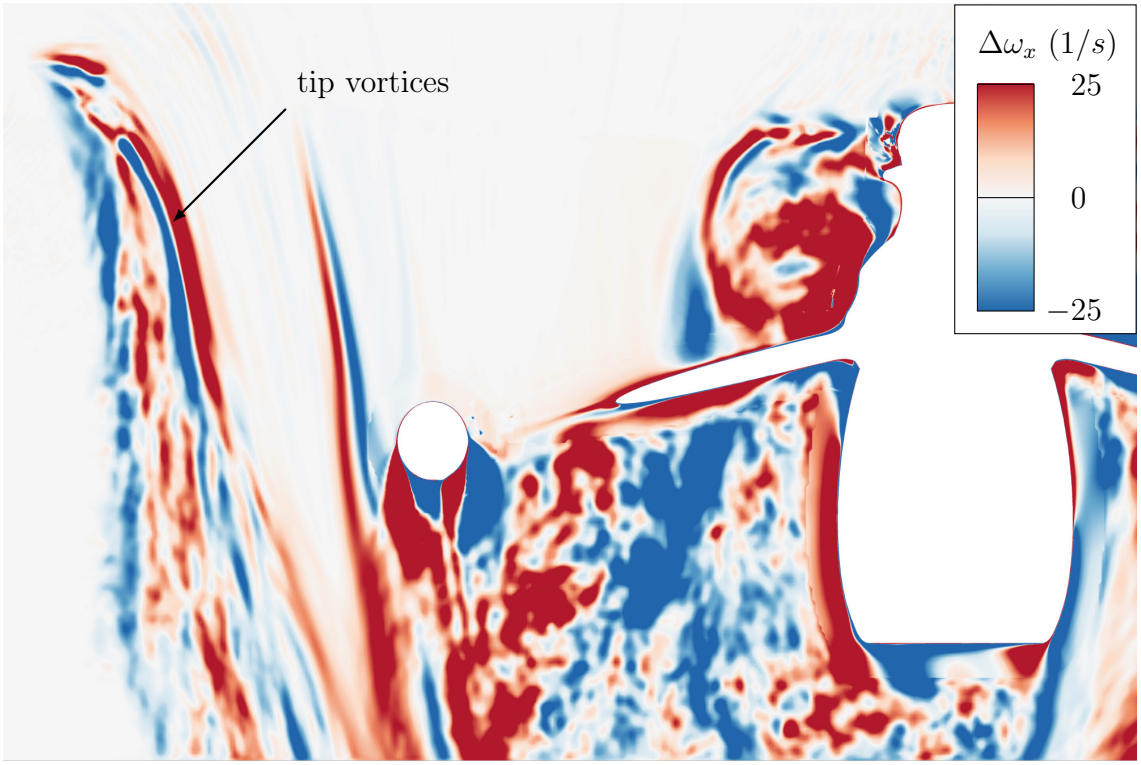

Figure 6.8: Distribution of difference in longitudinal vorticity induced by wings on lateral slice at $\Psi_{MR} = 90°$ (red: counterclockwise). Averaged over five main rotor revolutions. View from behind [111].

in Fig. 6.6(a) can be fully linked to the first-order influence of the wings onto the main rotor. This is additionally supported by the global changes in main rotor thrust and power induced by wings in the lateral rotors' absence, which, according to Table 6.1, are identical to the changes discussed above for lateral rotors present.

Besides the beneficial influence of the wings on the superjacent regions of the main rotor, both with and without lateral rotors the thrust differences in Fig. 6.6 show a decrease over large parts of the main rotor azimuth in its outermost region where trim tabs are attached. This is likely caused by the influence of the wings on the streamtube of the main rotor downwash. Due to the previously discussed blockage effect, this streamtube expands further outboard compared to a flow field without wings. This is illustrated by the difference in longitudinal vorticity induced by the wings on a lateral slice at $\Psi_{MR} = 90°$ in Fig. 6.8, where a distinct outboard shift of the tip vortices can be observed.

The associated streamtube expansion is not strictly limited to the azimuthal positions directly beyond the wings but extends significantly further. As a consequence of the streamtube expansion, the inductive effect of the tip vortices on the following main rotor blades' tip region is affected, where the section superjacent to the vortex core shift experiences a reduction in effective angle of attack due to the change in

vorticity and associated vertical velocities. This might cause the respective thrust reduction observable in Fig. 6.6.

6.3 Main Rotor–Lateral Rotor Interaction

In addition to the main rotor downwash's impingement on the wings, the lateral rotors are equally situated in its streamtube. This makes the analysis of the main rotor's influence on the lateral rotor performance particularly important. Indeed, with +7.8 % (see Table 6.2) the change in the left lateral rotor's thrust when omitting the main rotor is almost double to what was observed in the analysis of cruise flight in Section 5.3 (+4.6 %, see Table 5.2). While this implies a negative effect of the main rotor on the left lateral rotor's thrust, previous studies involving the author of the present thesis [21] as well as by Boisard [44] in contrast found a positive installation effect with a thrust increase of 7 % and 7.72 %, respectively. However, in both cases, the simulation setup comprised an isolated main rotor and an isolated lateral rotor. Consequently, only first-order interactions were represented without the second-order effects via wings.

In order to distinguish between the cumulative main rotor effect mentioned above and its direct effect on lateral rotor performance, additional simulations are conducted omitting the wings, once again with and without main rotor (see configurations in Fig. 4.2(b), center and 4.2(c), left). Here, for the latter a decrease in left lateral rotor thrust of 9.7 % can be observed, confirming Boisard's results with a positive (first-order) installation effect.

A closer analysis of direct and indirect main rotor influence can be conducted with the help of differences in lateral rotor thrust distribution gained by subtracting the respective distributions of setups with and without main rotor. While the differences in the wings' presence (see Fig. 6.9(a)) illustrate the cumulative effect, the respective distributions in the wings' absence in Fig. 6.9(b) only include the main rotor's direct effect. At first sight, for the left lateral rotor relatively similar characteristics can be observed irrespective of the wings. A significant thrust increase near the blade tips occurs in the top half of the lateral rotor disk, while a decrease is visible especially in the last quadrant. By comparing the thrust distributions more closely, however,

Table 6.2: Changes in lateral rotor thrust. Normalized with respective configuration with main rotor.

	No main rotor, with wings	No main rotor, no wings
ΔT_{leftLR}	+7.8 %	−9.7 %
$\Delta T_{rightLR}$	−20.4 %	−20.4 %

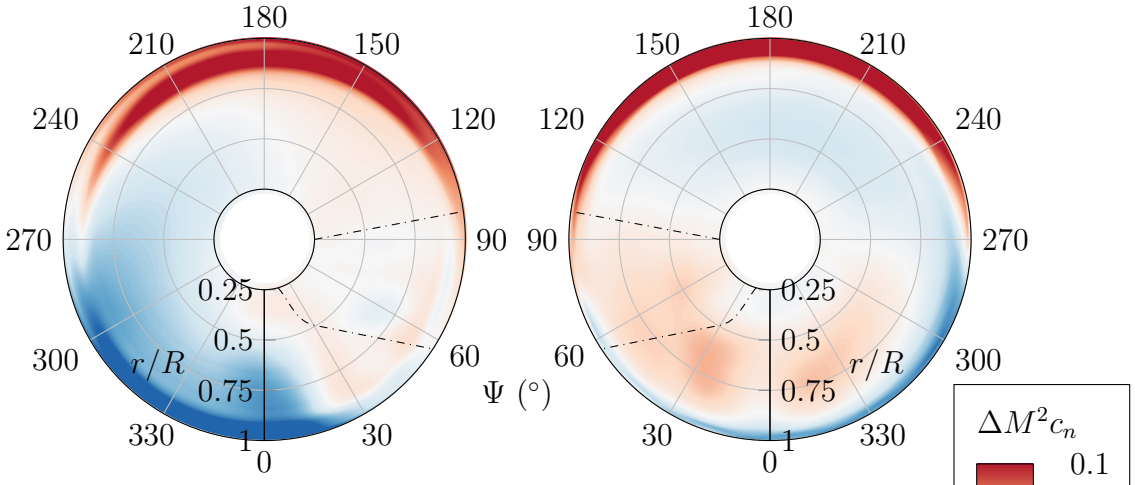

(a) With wings

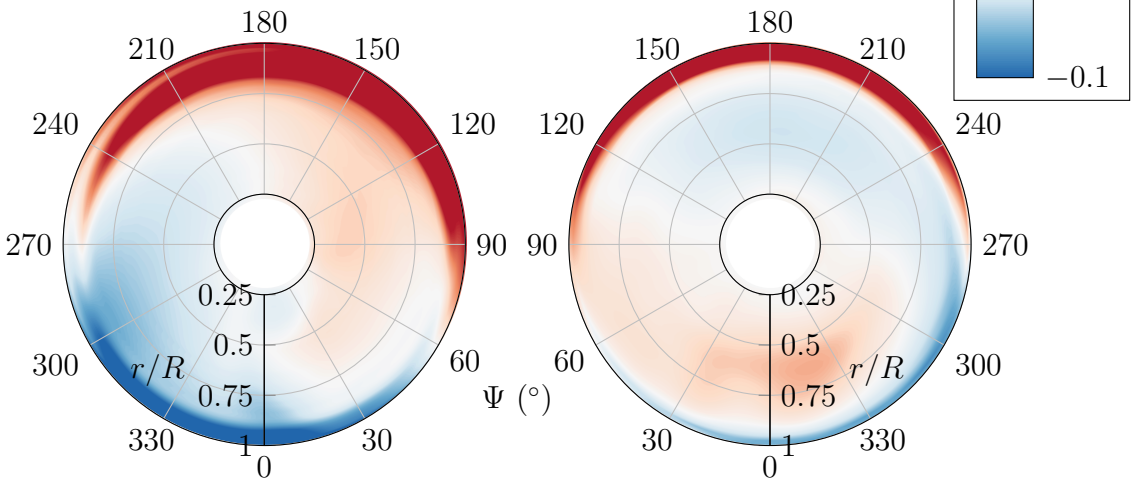

(b) No wings

Figure 6.9: Distribution of thrust difference on lateral rotors induced by main rotor with and without wings. Section normal force coefficient. Averaged over five main rotor revolutions. Approximate location of wings indicated. View from behind [111].

on the upstroking (inner) blades at smaller radial positions additional thrust is only induced in the wings' absence. Consequently, the main rotor's second-order effect on thrust via the wings is of diminishing nature and leads to the previously described thrust-reducing installation effect.

The flow phenomena causing the direct and indirect interactional effects become clearer by analysing the left lateral rotor's inflow for the different setups. Similar to the analysis of interactions in cruise flight in Section 5.5, a discrimination between effects on axial and tangential inflow (see Fig. 5.19) is helpful for understanding the underlying characteristics. For this reason, the changes in effective angle of attack

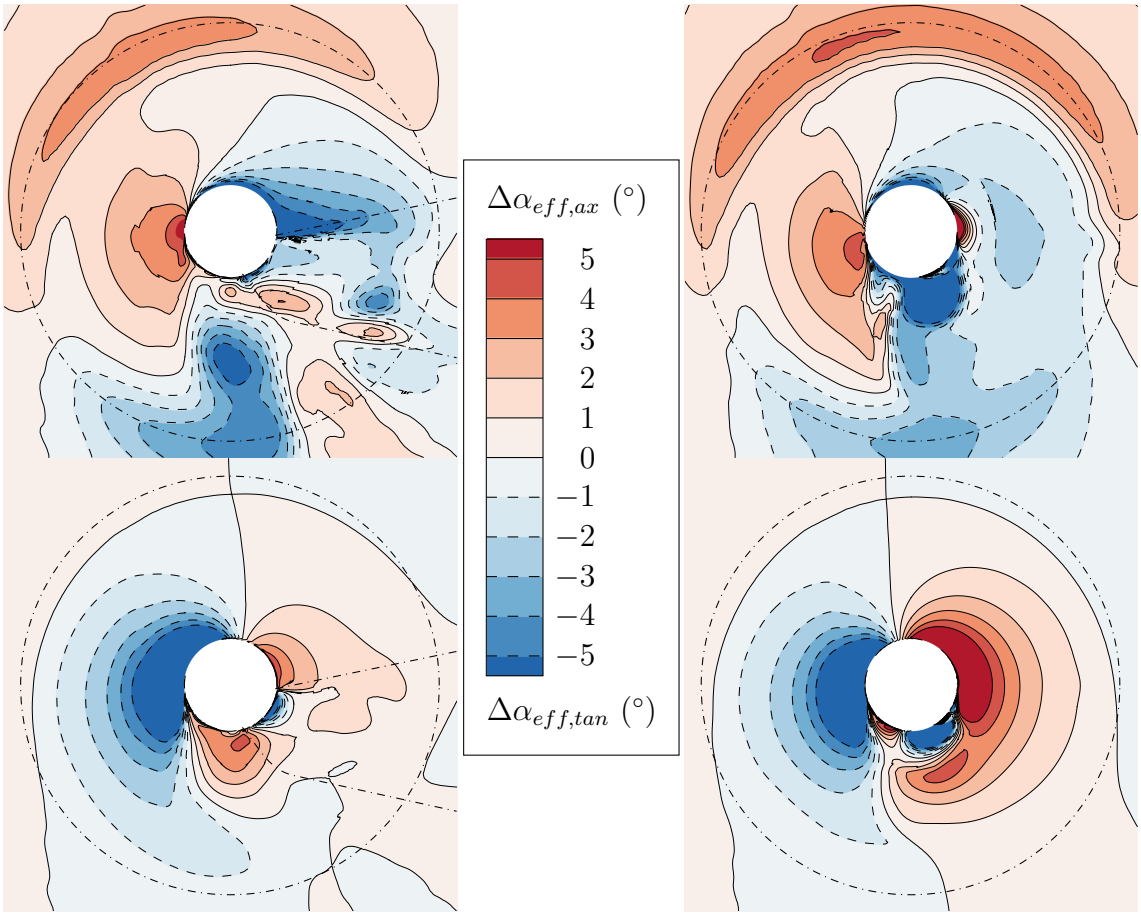

(a) With wings

(b) No wings

Figure 6.10: Distribution of difference in effective angle of attack on left lateral rotor inflow induced by main rotor with and without wings due to effects on axial (top) and tangential (bottom) velocity components. Based on local rotational velocity. Averaged over five main rotor revolutions. Approximate location of wings indicated. View from behind [111].

caused by the main rotor displayed in Fig. 6.10 are divided into their respectively changing velocity components according to Eqs. 5.4 and 5.5.

Without the wings (see Fig. 6.10(b)), an increase in $\Delta\alpha_{eff,ax}$ can be observed in the upper half's blade tip region, causing the respective thrust gain visible in Fig. 6.9(b). This is likely a result of the main rotor's effect on the lateral rotor's wake and more specifically its tip vortices. By deflecting them downward, the induction on the upstream blade regions that are now positioned outboard of the vortex core shifts towards a negative axial velocity and consequently a positive effective angle of attack. The downward deflection of the tip vortices might also be the cause for the slight decrease in $\Delta\alpha_{eff,ax}$ in the lower region of the lateral rotor disk.

Similar sickle-shaped regions, which are characteristic for rotors with non-axial inflow and were extensively witnessed in a prior publication involving the author

of the present thesis on RACER in crosswind conditions [22], can also be observed in the lateral rotor's inflow with wings present. However, additionally, a significant loss in $\Delta\alpha_{eff,ax}$ occurs at the intersection between the upper wing's top side and the nacelle. Here, the main rotor downwash impinges onto the wing (see Fig. 6.3) and is deflected towards the lateral rotor. This leads to an additional axial velocity component and consequently a smaller effective angle of attack.

Additionally to this detrimental effect on $\Delta\alpha_{eff,ax}$, the second-order influence via wings also prevents a positive first-order influence as displayed in Fig. 6.10's distributions of $\Delta\alpha_{eff,tan}$. In the wings' absence, the main rotor downwash relatively symmetrically induces a tangential velocity component in the lateral rotor inflow. For the upstroking (inner) blades, this results in an increase of effective angle of attack, whereas for the downstroking (outer) blades, a reduction can be witnessed. This effect was also described by Stokkermans et al. [47].

With the wings situated in the lateral rotor inflow, however, the positive effect of the main rotor downwash's vertical flow on the upstroking blades is largely eliminated due to the aforementioned axial deflection. For the inflow being channelled between the wings, the rectifying effect leads to an almost negligible $\Delta\alpha_{eff,tan}$ in Fig. 6.10(a).

The combination of the main rotor's direct influence on the lateral rotor inflow's axial and tangential velocity components causes the difference in thrust distribution displayed in Fig. 6.9(b), whereas the addition of the second-order effect prevents or reduces the inboard thrust gain (see Fig. 6.9(a)) and consequently reverses the installation effect on total lateral rotor thrust from positive to negative.

With the lateral rotor's relatively inhomogeneous inflow conditions due to the main rotor, not only the latter's influence on average thrust levels are of particular interest but also their fluctuations are likely to be affected. This effect is assessed by subtracting the time-dependent lateral rotor thrust of the configurations with and without main rotor and conducting an FFT on the resulting difference over three main rotor revolutions, where an almost full number of lateral rotor cycles is achieved. In order to isolate the first-order effect, this process is repeated for the respective configurations without wings. The resulting frequency spectra are displayed in Fig. 6.11.

The main rotor's accumulated direct and indirect effect in the wings' presence shows distinct peaks at both rotors' BPFs. While the amplitude of the fluctuations at lateral rotor BPF is roughly 1.5 % of the average thrust due to the inflow's asymmetry with first-order effects (see Fig. 6.10(b)), the additional second-order effects via wings increase this asymmetry as discussed before (see Fig. 6.10(a)) and consequently also induce larger thrust fluctuations at lateral rotor BPF with amplitudes of 2.5 % of the average thrust.

The frequency spectra's peaks at main rotor BPF, in contrast, are not only smaller but also remain constant between the setups with and without wings. Consequently,

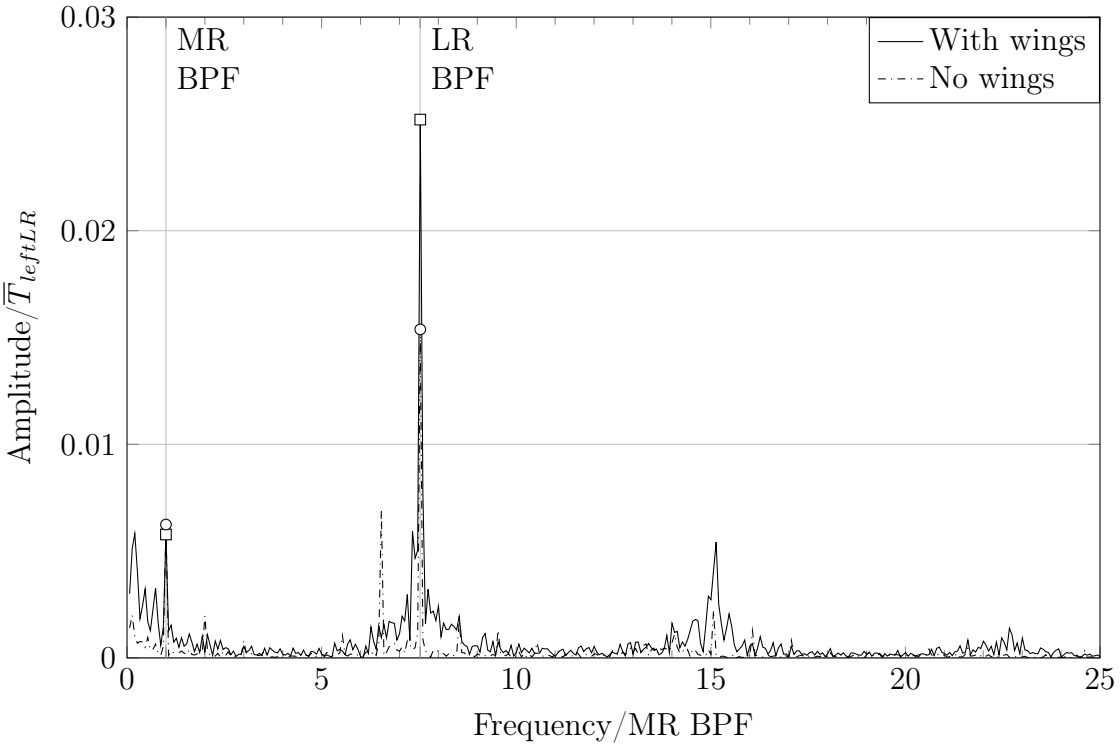

Figure 6.11: Frequency spectrum of thrust difference on left lateral rotor induced by main rotor with and without wings. Normalized with average thrust of lateral rotor in full configuration [111].

they originate from a first-order influence of the main rotor, the nature of which could be twofold: On the one hand, the pressure fields of the passing main rotor blades instantaneously induce velocity fluctuations on the lateral rotor blades; on the other hand, the main rotor downwash shows a distinct stacking of blade wakes with local variations of pressure and velocity, convecting over the lateral rotor disk.

In order to clarify the contribution of these two mechanisms to the thrust fluctuations, additional simulations are conducted with a variation of the lateral rotors' vertical position. For this purpose, the computations on the setup lacking wings (see configuration in Fig. 4.2(b), center) are repeated with a vertical offset on nacelles and lateral rotors of half of the downwash's convective length which becomes manifest in the stacking of main rotor blade wakes and results from the main rotor BPF and the induced velocity v_i. Even though the latter was determined for the contracted downwash in Eq. 6.1, the illustration of the lateral rotors' shift in Fig. 6.12 with its distributions of vorticity magnitude on a lateral slice in the lateral rotor inflow clearly shows the latter's position in relation to the—synchronized—main rotor blade wakes to differ by roughly half of a convective length.

The comparison of the resulting left lateral rotor thrust for the two different rotor positions over one main rotor revolution in Fig. 6.13 is largely dominated by the

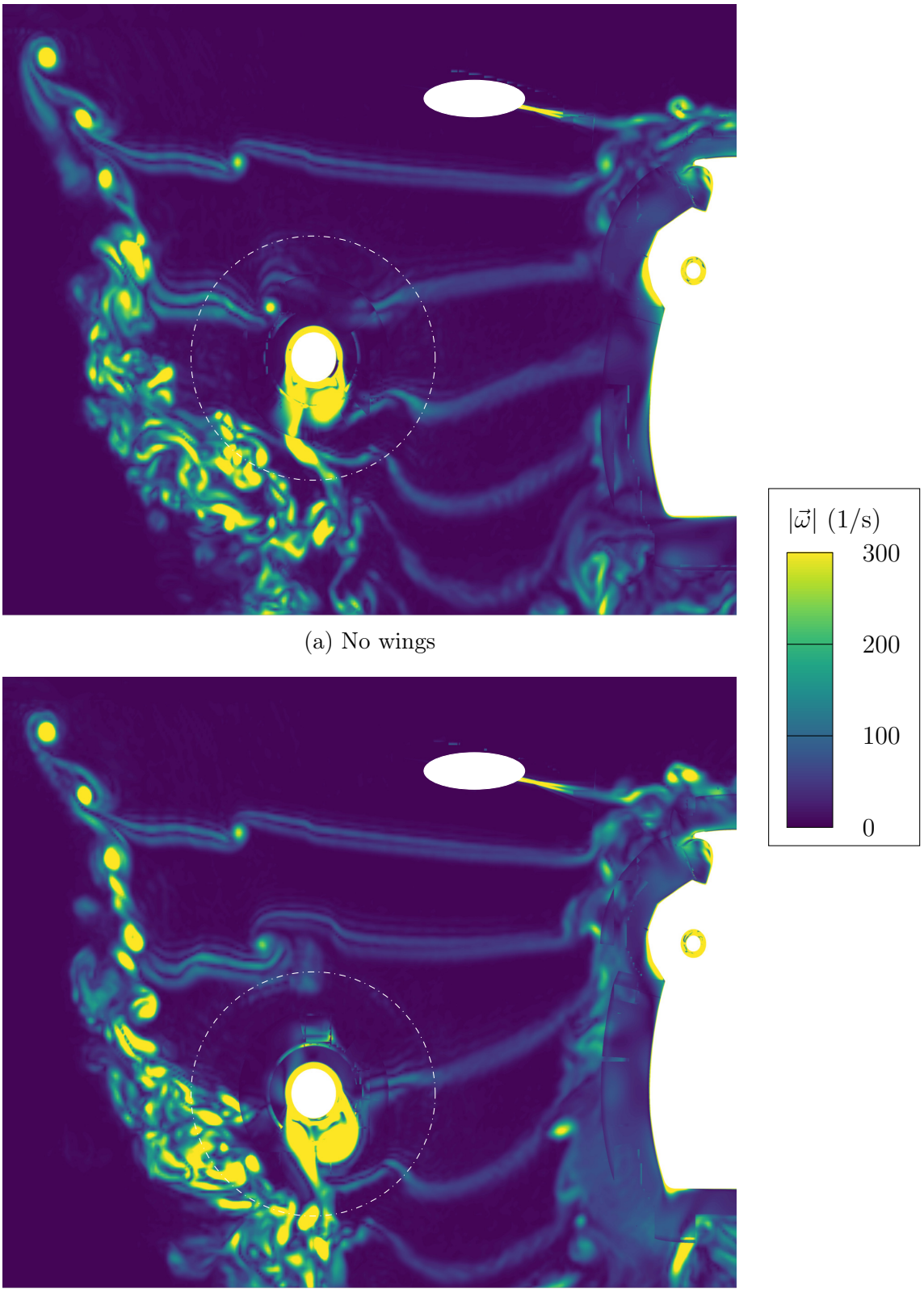

(a) No wings

(b) No wings, lateral rotors shifted vertically

Figure 6.12: Distribution of vorticity magnitude with different lateral rotor positions on lateral slice in lateral rotor inflow. Synchronized with main rotor azimuth.

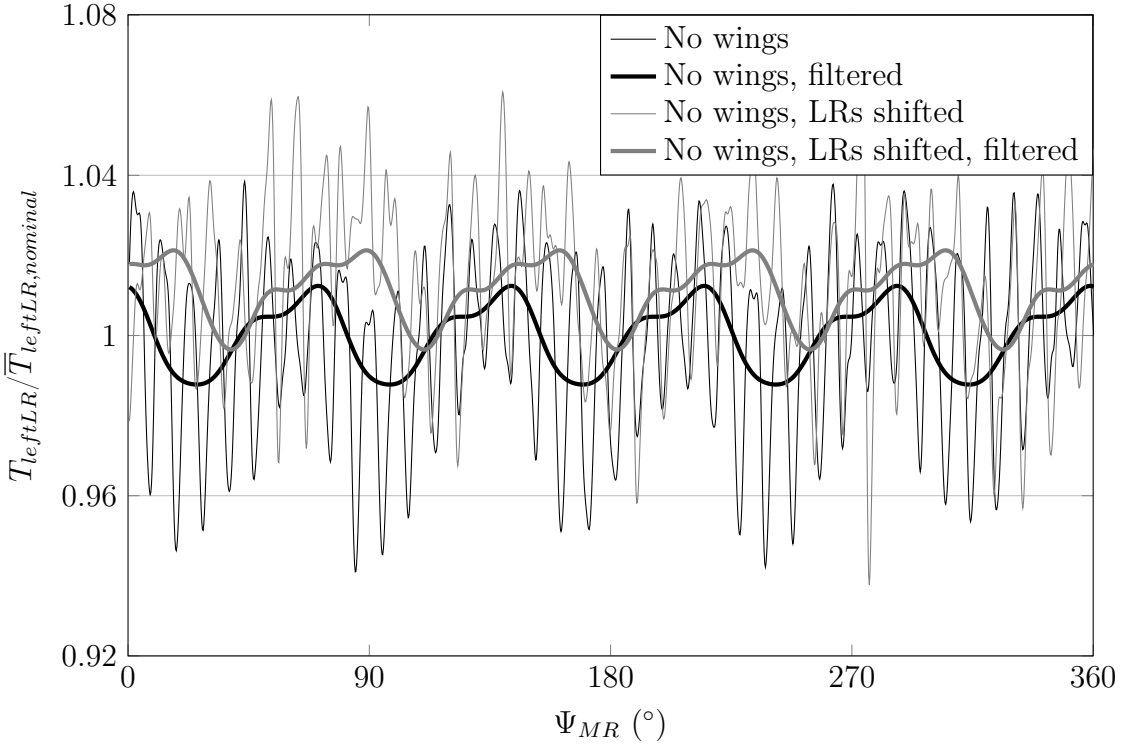

Figure 6.13: Thrust on left lateral rotor with different lateral rotor positions. Normalized with average thrust of lateral rotor in nominal position. Frequency filtered over five main rotor revolutions for main rotor BPF and higher harmonics.

fluctuations at lateral rotor BPF, which was already concluded from the respective amplitudes in Fig. 6.11's frequency spectrum. As this analysis is solely focussed on the main rotor–induced fluctuations, the lateral rotor thrust signals are filtered for the main rotor BPF and its higher harmonics. The resulting fluctuations in Fig. 6.13 not only feature an approximately 1 % larger average thrust for the lower rotor position but also nicely show a phase shift caused by the vertical offset of the lateral rotors.

With roughly 15° of the main rotor azimuth, this is significantly smaller than what could be expected for a purely convection-based mechanism inducing the fluctuations, which would be approximately $\Delta\Psi_{MR} = 36°$ for the five-bladed main rotor and the vertical offset of half the convective length. For fluctuations solely being driven by the main rotor blades' pressure fields, on the other hand, a roughly ten times smaller phase shift would result from their propagation at speed of sound, assuming the respective phase to be dominated by the vertical distance between main rotor and lateral rotors. Consequently, with the occurring phase shift being in between these two theoretical values, the fluctuations at main rotor BPF visible in Fig. 6.11 are clearly caused by a combination of both mechanisms.

Due to its different operating conditions, the right lateral rotor's performance is affected to a different extent by the main rotor. According to Table 6.2, the thrust decreases significantly with the main rotor's omission (−20.4 %). This thrust-augmenting installation effect is fully independent of the wings' presence, as they are situated downstream of the reversely operating right lateral rotor, and agrees with a previous study involving the author of the present thesis [21] that showed a thrust gain of 25 % on an isolated right lateral rotor with the addition of an isolated main rotor.

The lack of second-order effects can also be observed in the distributions of main rotor–induced thrust differences on the right lateral rotor in Fig. 6.9, showing almost identical characteristics with and without wings. Trends similar to the left lateral rotor are visible, with a thrust gain in the top region due to the aforementioned axial influence and a generally slightly higher thrust on the upstroking blades compared to the downstroking blades, caused by the tangential velocity induced by the main rotor.

As a result of the generally deviating thrust distribution, however, the different phenomena are in effect to a varying extent on left and right lateral rotor. This explains the asymmetry of the main rotor's first-order influence in Fig. 6.9(b).

6.4 Lateral Rotor–Main Rotor Interaction

Based on the occurrence of an upstream effect of the wings on the main rotor performance (see Section 6.2), a similar influence of the lateral rotors can be expected. By comparing the main rotor thrust of the full configuration with a reduced setup lacking the lateral rotors (see Fig. 4.2(b), right), however, no change can be determined as specified in Table 6.3.

In order to rule out the compensation of counteracting effects, the respective thrust distributions are subtracted; the resulting main rotor–induced difference is displayed in Fig. 6.14(a). In fact, despite the unaffected total thrust, an influence superjacent to both lateral rotors' positions can be observed. In front of the left lateral rotor, a decrease in main rotor thrust occurs, while above its wake, this reverses into a thrust gain. Even though the characteristics around the right lateral rotor are

Table 6.3: Changes in main rotor thrust and power. Normalized with respective configuration with lateral rotors.

	No lateral rotors, with wings	No lateral rotors, no wings
ΔT_{MR}	+0.0 %	−0.1 %
ΔP_{MR}	−0.4 %	−0.3 %

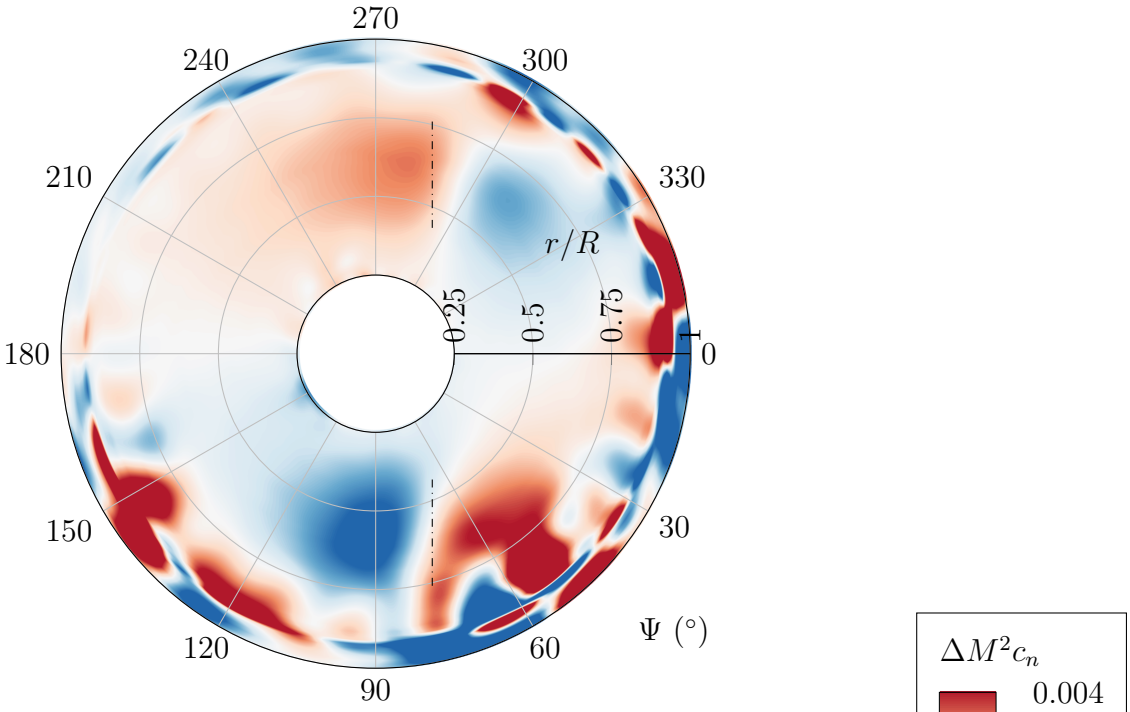

(a) With wings

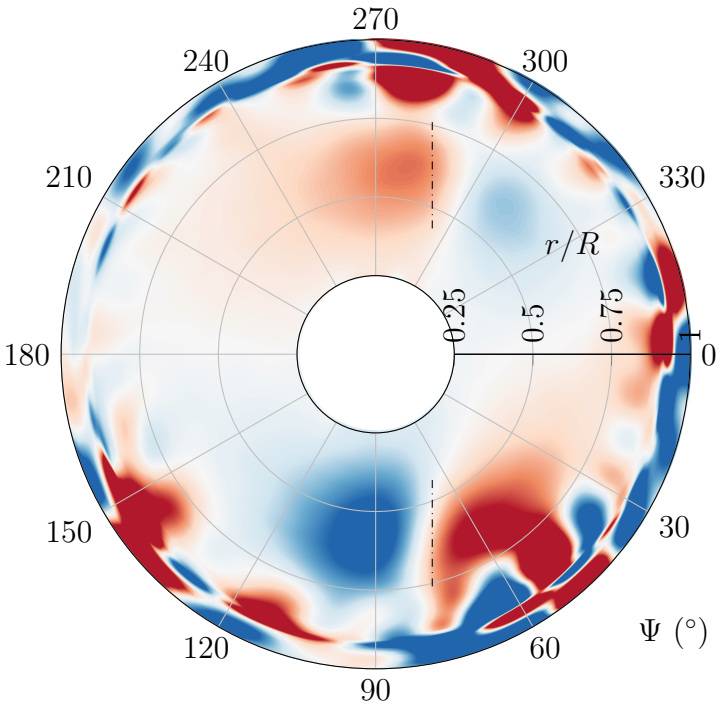

(b) No wings

Figure 6.14: Distribution of thrust difference on main rotor induced by lateral rotors with and without wings. Section normal force coefficient. Averaged over five main rotor revolutions. Frequency filtered above 20/rev. Approximate location of lateral rotors indicated. View from above [111].

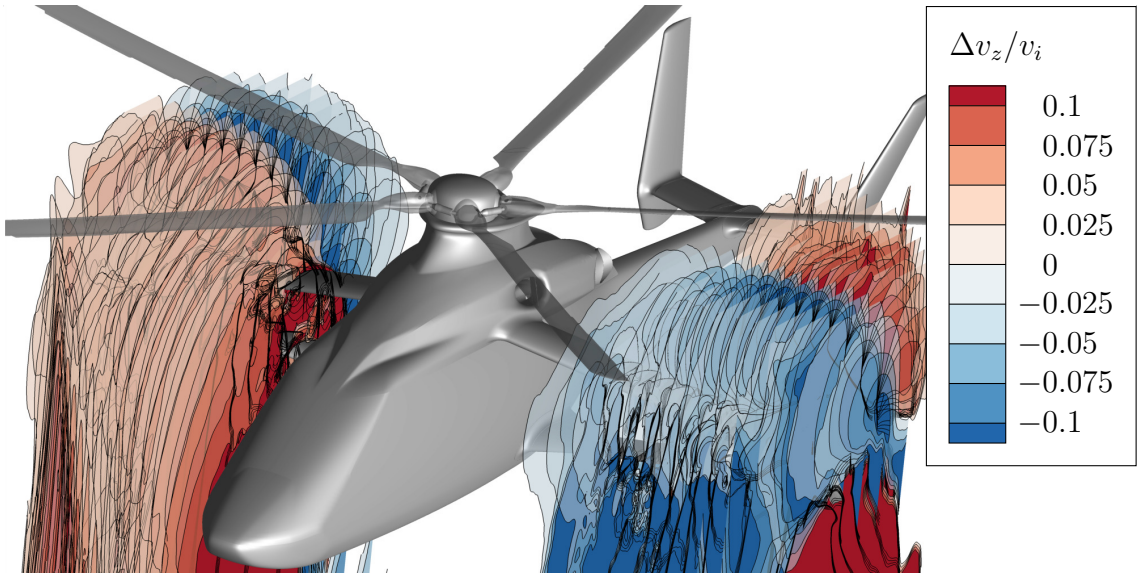

Figure 6.15: Distribution of difference in vertical velocity induced by lateral rotors on planes across wingspan. Normalized with induced velocity of main rotor. Values between −0.025 and 0.025 blanked. Averaged over five main rotor revolutions [111].

inverted, this can be explained by its generation of reverse thrust. Therefore, both lateral rotors equally decrease main rotor thrust in their upstream region, whereas their wakes induce an increase in thrust.

The flow phenomena causing this effect can be observed in Fig. 6.15's illustration of the lateral rotors' influence on vertical flow velocity in their vicinity. Upstream of both lateral rotors, their suction effect induces a downward flow below the main rotor, consequently decreasing the effective angle of attack on the passing main rotor blades and therefore also their thrust. In contrast, the lateral rotor wakes have a blockage effect on the main rotor downwash—similar to the influence of the wings that was observed in Section 6.2—reducing the downward velocity and causing a thrust gain due to a larger effective angle of attack on the main rotor.

Both of these phenomena were already observed in Section 5.4's investigations on cruise flight and accord with results by Boisard [44], whose time history of rotor blade thrust shows a peak before passing the lateral rotor position, followed by a thrust decrease. The positive installation effect he witnessed on total main rotor thrust (+2.83 %), however, cannot be confirmed here. This is not a result of the lack of second-order effects of his isolated setup, as the comparison with results of simulations without wings in Table 6.3 not only shows no direct lateral rotor effect on total main rotor thrust either, but also an almost identical distribution of thrust difference is observed (see Fig. 6.14(b)). Consequently, no such indirect effects via wings can be expected for this interaction. Instead, Boisard's slightly deviating influence on average thrust might be the result of the varying lateral rotor position and the fact that his setup comprised a single lateral rotor instead of two.

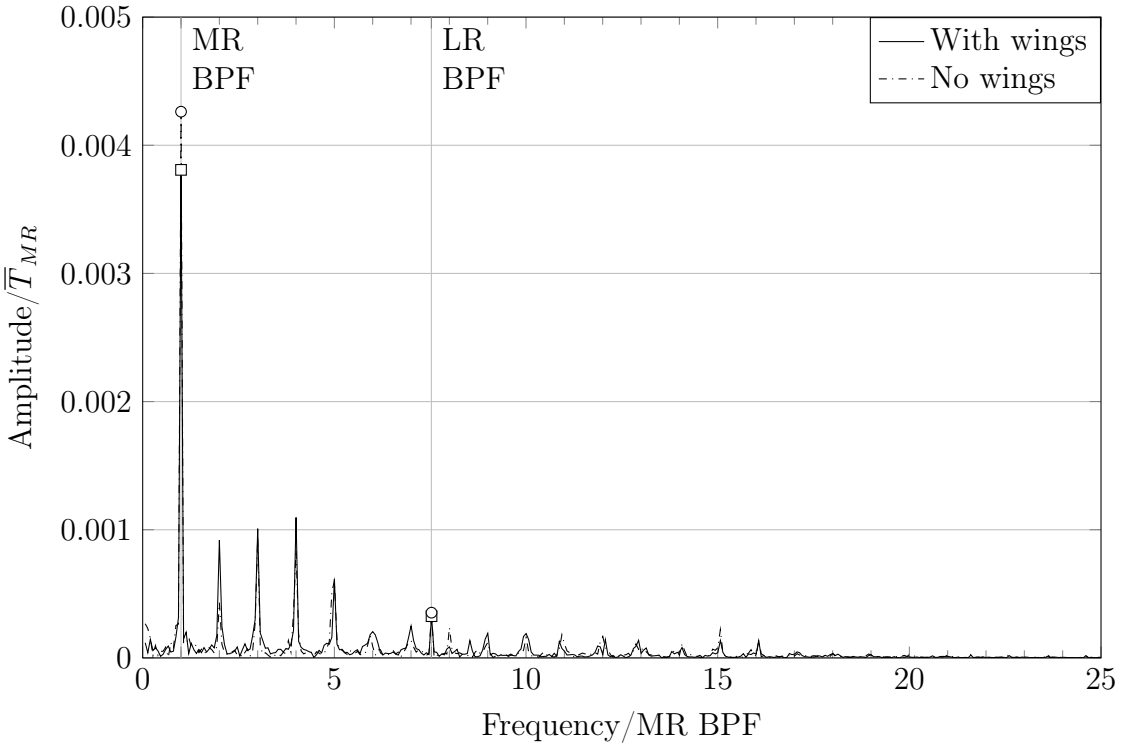

Figure 6.16: Frequency spectrum of thrust difference on main rotor induced by lateral rotors with and without wings. Normalized with average thrust of main rotor in full configuration [113].

In contrast, the findings on lateral rotor–induced changes in average main rotor power agree very nicely with Boisard's results. Here, for the simulations at hand a slight decrease with the omission of the lateral rotors of 0.4 % and 0.3 % was found with and without wings, respectively.

The frequency spectrum of the main rotor's global thrust difference induced by the lateral rotors (see Fig. 6.16) shows hardly any fluctuations with the lateral rotor BPF. This indicates no effect of the lateral rotor blades' rotating pressure fields on the main rotor thrust generation. The upstream effect on the mean flow, however, with the induction of vertical velocities discussed before, is also visible here, as it induces additional fluctuations with the main rotor BPF. At roughly 0.4 % of the average thrust, though, both for wings present and absent, they remain relatively small.

6.5 Wing–Lateral Rotor Interaction

In Section 5.5's investigations on interactions in cruise flight, the wings' influence on the lateral rotors' performance was found to be the strongest interactional effect, manifesting itself in a considerable benefit in lateral rotor thrust. Due to the differing

Table 6.4: Changes in lateral rotor thrust. Normalized with respective configuration with wings.

	No wings, with main rotor	No wings, no main rotor
ΔT_{leftLR}	+14.9 %	−3.8 %
$\Delta T_{rightLR}$	+0.9 %	+0.9 %

operating conditions, lacking horizontal inflow and additional main rotor downwash, the characteristics of the interaction in hover are expected to be of a different nature; nevertheless, owing to the small distance between the components and the upstream placement of the left wings, this effect is of particular interest for the investigations at hand.

Indeed, Table 6.4 shows a significant influence of the wings on the left lateral rotor's thrust. In contrast to the cruise flight, however, it is detrimental, as the thrust increases by 14.9 % with the omission of wings. A thrust-augmenting first-order effect, though, can be observed in the absence of the main rotor (see configurations in Fig. 4.2(b), left and 4.2(c), left).

The completely different characteristics of wing influence on lateral rotor thrust are also visible in the distributions of thrust difference displayed in Fig. 6.17. While the accumulated effect in the main rotor's presence shows a significant decrease of thrust over almost the complete left lateral rotor disk, the first-order effect in Fig. 6.17(b) shows hardly any notable influence.

Similar to the investigations in Sections 5.5 and 6.3, in accordance with the approach illustrated in Fig. 5.19 the causative effects for the thrust difference are divided into influence on axial inflow and tangential inflow and their respective changes in effective angle of attack by applying Eqs. 5.4 and 5.5. In the main rotor's absence (see Fig. 6.18(b)) the first-order influence of the wings is visible in the slightly increased $\Delta\alpha_{eff,ax}$ caused by the decreased axial velocity component in their wakes. Additionally, the lateral rotor's blowing of the wings induces the generation of lift and consequently the formation of a tip vortex around the nacelle. With its sense of rotation reverse to the left lateral rotor's inside-up rotation, this leads to an increase of the effective angle of attack's tangential component over the complete rotor disk and most notably on the transition between upper wing's top side and nacelle. The characteristic distribution of both phenomena is very similar to what was observed in cruise flight in Section 5.5 (see Fig. 5.20) albeit on a much smaller level, due to the lateral rotor inflow being the sole source of wing lift. Additionally taking the variation of dynamic pressure over the lateral rotor blade span into account, both effects in conjunction lead to the difference in thrust distribution witnessed in Fig. 6.17(b).

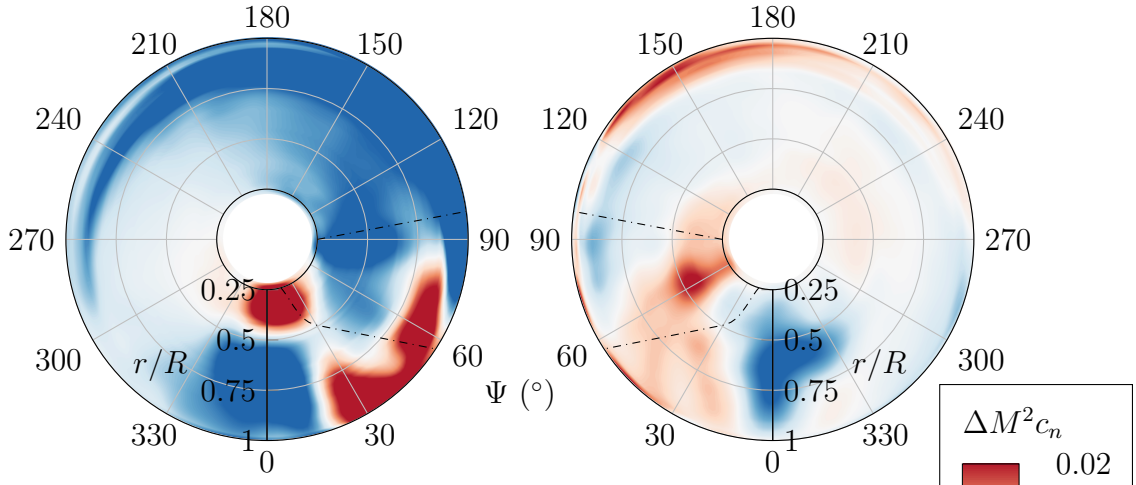

(a) With main rotor

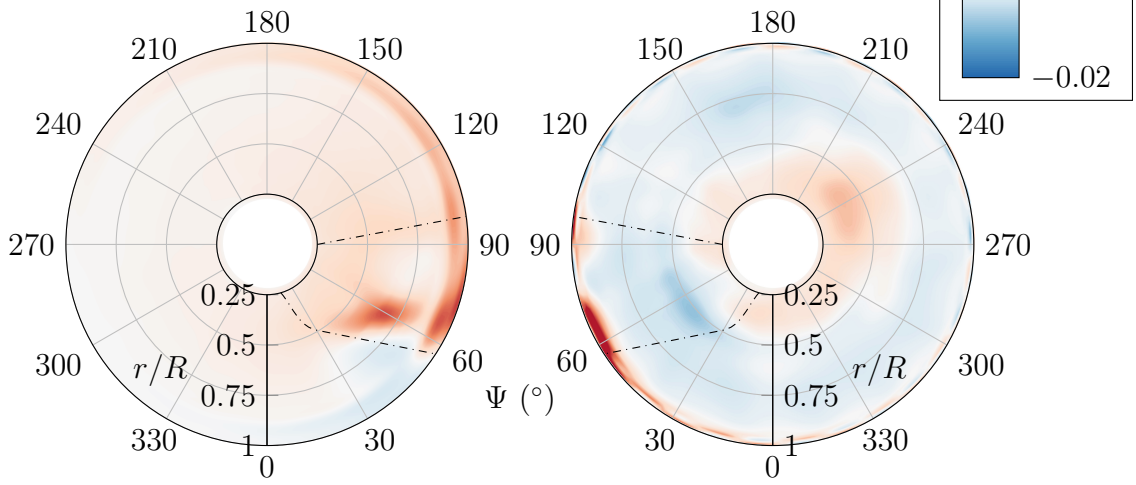

(b) No main rotor

Figure 6.17: Distribution of thrust difference on lateral rotors induced by wings with and without main rotor. Section normal force coefficient. Averaged over five main rotor revolutions. Approximate location of wings indicated. View from behind [111].

With the additional second-order effects via the main rotor, however, the cumulative changes in effective angle of attack (see Fig. 6.18(a)) differ highly from the first-order characteristics. The wing lift induced by the lateral rotor streamtube completely vanishes due to the main rotor downwash and the download resulting from this. Consequently, the wing tip vortex around the nacelle is reversed into a counterclockwise flow. This reduces the effective angle of attack over most of the lateral rotor disk as illustrated by the distribution of $\Delta\alpha_{eff,tan}$.

The beneficial effect of the lower wing's wake remains visible in the distribution of differences in angle of attack caused by changes in axial velocity with the main

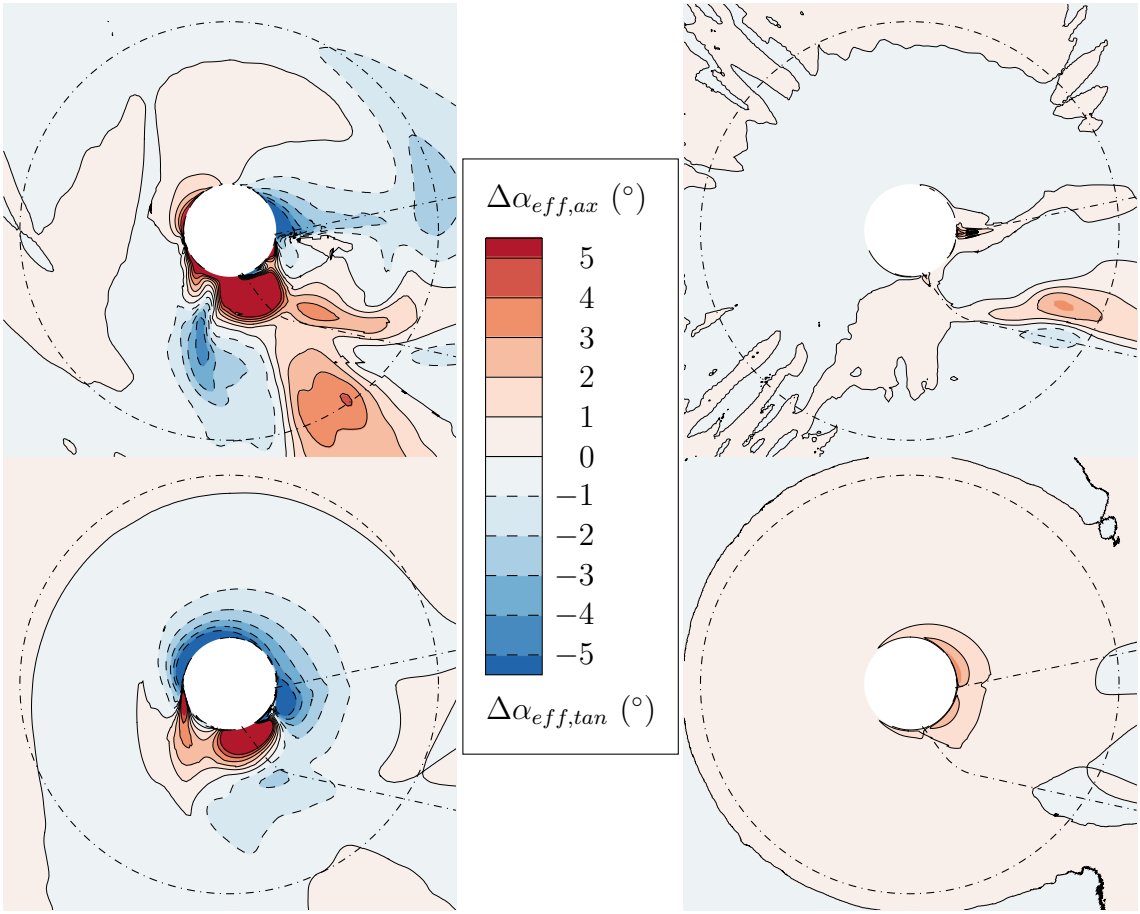

(a) With main rotor

(b) No main rotor

Figure 6.18: Distribution of difference in effective angle of attack on left lateral rotor inflow induced by wings with and without main rotor due to effects on axial (top) and tangential (bottom) velocity components. Based on local rotational velocity. Averaged over five main rotor revolutions. Approximate location of wings indicated. View from behind [111].

rotor present. However, the deflection of the main rotor downwash by the upper wing discussed in Section 6.3 is also visible here, as it leads to a reduction of $\Delta\alpha_{eff,ax}$ along the wing and especially near the nacelle.

The described second-order effects in the main rotor's presence clearly dominate over the direct influence of the wings, explaining not only the difference in Fig. 6.17's distributions for the left lateral rotor but also the changes in total thrust specified in Table 6.4. While generally witnessing the same main rotor–induced phenomena on RACER's left lateral rotor, Stokkermans et al. [47] on the contrary found a positive—cumulative—installation effect of +10.5 % on thrust, in contrast to the present thesis' detrimental installation effect of −13.0 % corresponding to the thrust change of +14.9 % with the omission of the main rotor (see Table 6.4). Even though this presumably can be attributed to the differing anti-torque ratio and consequently

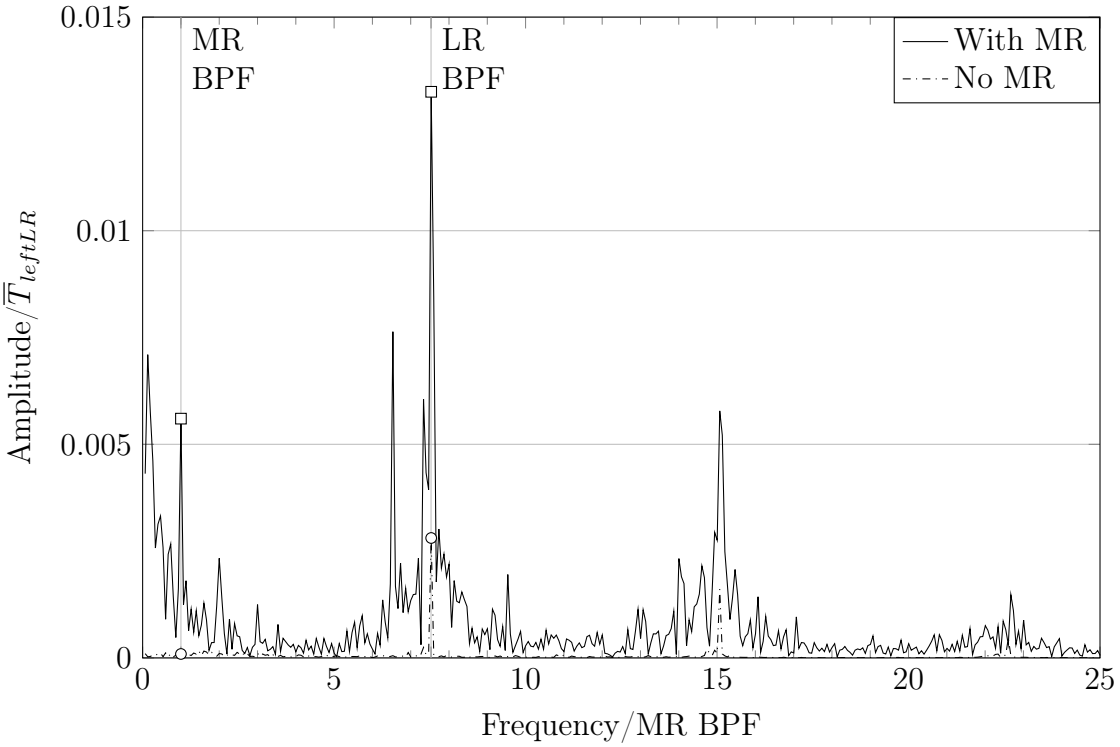

Figure 6.19: Frequency spectrum of thrust difference on left lateral rotor induced by wings with and without main rotor. Normalized with average thrust of lateral rotor in full configuration [111].

thrust level of the lateral rotors, as well as the earlier rotor blade geometry of Stokkermans et al. and their steady-state representation of the main rotor as an actuator disk, this illustrates the susceptibility of this interactional effect and the delicate balance of the underlying phenomena.

In contrast, for the right lateral rotor the wings' effect on total thrust is not only of much smaller scale but—despite the qualitatively differing distributions in Fig. 6.17—also fully independent of the main rotor. This is caused by the lateral rotor's operating condition in reverse thrust, resulting in the wings being situated downstream and therefore only playing a minor role in lateral rotor performance.

With the significant influence on the left lateral rotor's total thrust, also the wings' effect on thrust fluctuations needs to be examined. For this reason, an FFT is conducted on the respective thrust differences between setups with and without wings. The resulting frequency spectra in the main rotor's presence and absence are displayed in Fig. 6.19. The relatively small asymmetry in thrust distribution induced by the wings without the main rotor (see Fig. 6.17(b)) only leads to minor fluctuations at lateral rotor BPF, while naturally no fluctuations at main rotor BPF can occur. With the addition of the main rotor, however, the wings' deflection of the downwash affects the thrust fluctuations at main rotor BPF compared to a lateral

rotor being exposed to an undisturbed downwash, leading to the additional peak in Fig. 6.19. The significantly larger asymmetry in thrust distribution, meanwhile, increases the fluctuations at lateral rotor BPF. At roughly 1.3 % of the left lateral rotor's average thrust in full configuration, the fluctuations remain comparatively small.

6.6 Lateral Rotor–Wing Interaction

In addition to the significant influence of the main rotor on the wings' aerodynamic behaviour (see Section 6.1), also the lateral rotors' effect has to be examined more closely. For this reason, in Fig. 6.20 the spanwise distributions of wing download in full configuration are compared to the respective distributions of a setup without lateral rotors (see Fig. 4.2(b), right) by illustrating the resulting difference induced by the latter.

On the left-hand side, the lateral rotor significantly increases download on the upper wing over its whole span; this effect only vanishes close to the fuselage. In

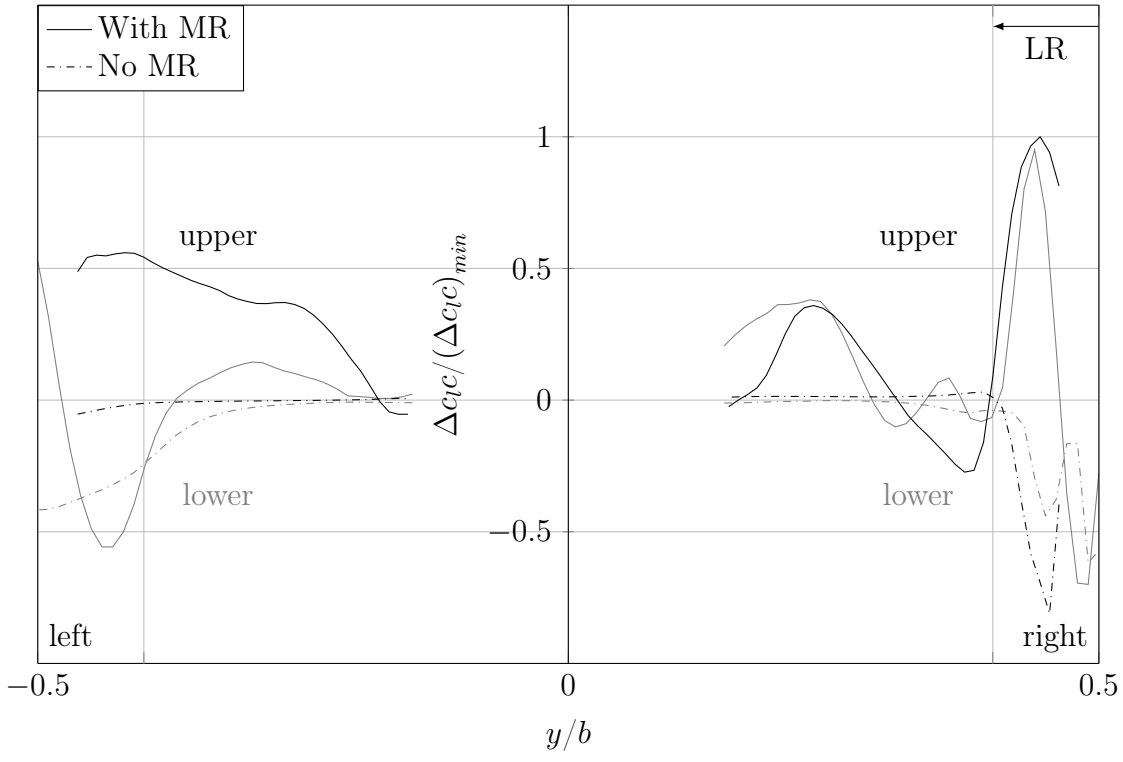

Figure 6.20: Distribution of difference in wing download induced by lateral rotors with and without main rotor. Section lift coefficient, normalized with dynamic pressure of induced velocity and maximum additional download induced by lateral rotors. Averaged over five main rotor revolutions. Approximate location of lateral rotors indicated [111].

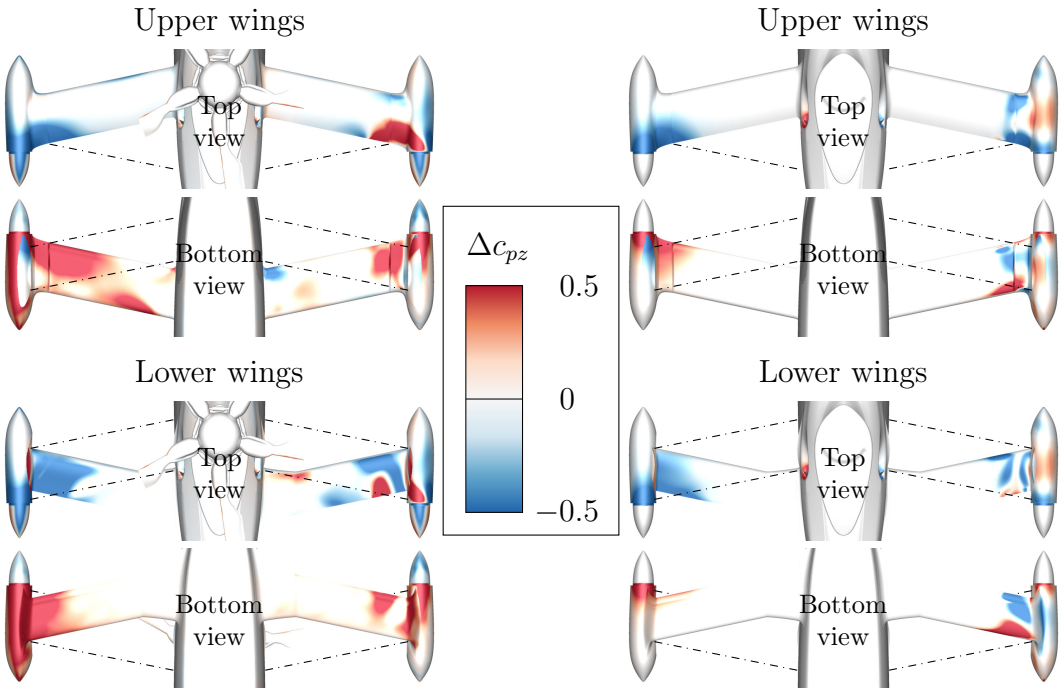

(a) With main rotor (b) No main rotor

Figure 6.21: Distribution of difference in wing download induced by lateral rotors with and without main rotor. Vertical component of pressure coefficient, normalized with dynamic pressure of induced velocity and vertical component of wall-normal vector (red: download). Averaged over five main rotor revolutions [111].

contrast, the lower wing experiences a decrease in download directly upstream of the lateral rotor, whereas this is reversed further inboard.

Due to the different operating condition of the right lateral rotor, generating reverse thrust, different characteristics can be witnessed on the corresponding wings. Their outer sections directly experience the lateral rotor wake, which manifests itself in a peak of additional download on the upper wing, while the lower wing is subjected to a steep gradient in vertical force. Similar to the left-hand side, the lateral rotor's effect significantly extends towards the wings' roots. As illustrated by Fig. 6.20's additional distributions of difference in wing download induced by the lateral rotors in the main rotor's absence (see configurations in Fig. 4.2(b), left and 4.2(c), center), this is clearly an effect of the second-order interactions.

The lateral rotors' first-order influence is mainly limited to the outer section of the wings directly upstream or downstream, respectively. On each wing, lift is generated due to the induced flow over the wings with the lateral rotors' convection. For the right wings, however, this effect is significantly less uniform as the reverse thrust of the corresponding lateral rotor leads to a reverse inflow. This discrepancy is illustrated by the difference in pressure distribution induced by the lateral rotors without the main rotor in Fig. 6.21(b). While close to the left nacelle a convection-

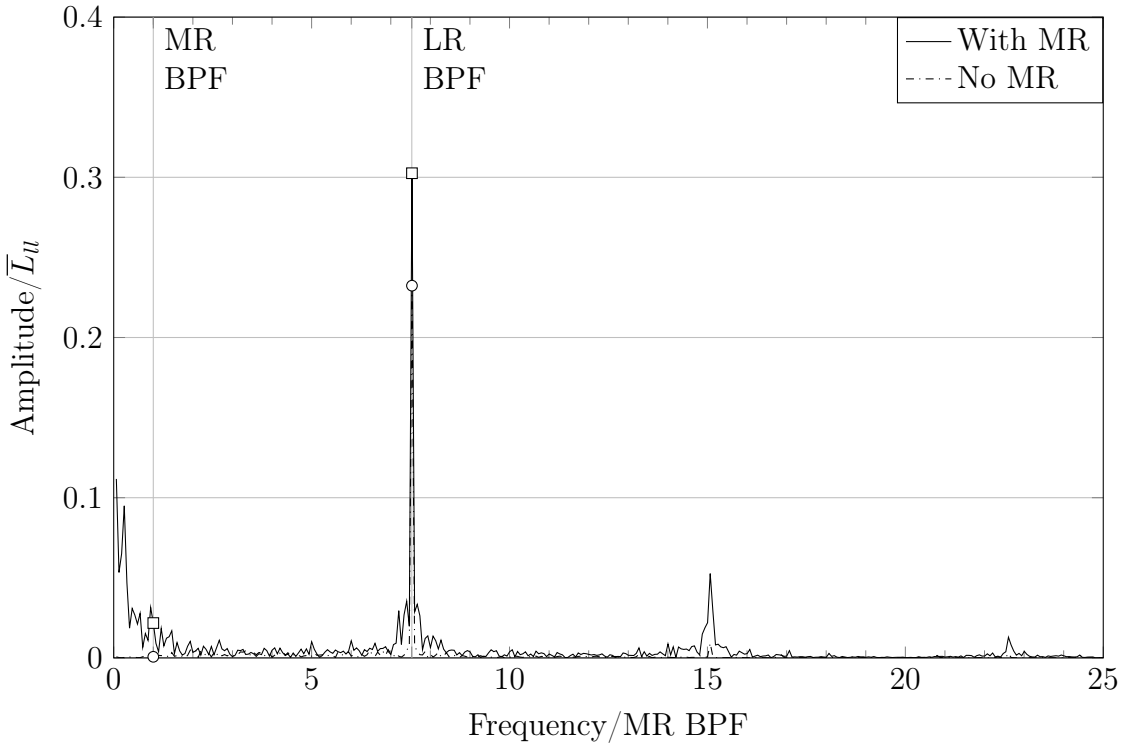

Figure 6.22: Frequency spectrum of download difference on left lower wing induced by lateral rotors with and without main rotor. Normalized with average download of wing in full configuration [111].

induced decrease in static pressure causes the generation of lift on both top sides and a slight download on the upper wing's bottom side, the effect near the right nacelle is scattered due to the unfavourable flow around the wing caused by the blowing from the trailing edge.

The comparison to the cumulative lateral rotor influence in the main rotor's presence (see Fig. 6.21(a)) shows the occurrence of significant second-order effects, accounting for the varying download distributions in Fig. 6.20. On the left upper wing's top surface, the addition of the main rotor downwash hardly changes the influence of the lateral rotor's suction. In contrast, the large area of separated flow on the wing's lower surface caused by the main rotor extends the lateral rotor's area of effect significantly inboard and even extends onto the lower wing, as the combination of both convections leads to the time-averaged formation of a vortex between the wings (see Section 6.1). This also applies to the right wings, even though the flow separation is subjected to reverse inflow here.

Notably, the main rotor downwash's impingement onto the upper wing induces a flow contrary to the reverse lateral rotor flow. The result of this is a stagnation region on the top outer section of the right upper wing, leading to the peak in download visible in Fig. 6.20.

The small distance to the lateral rotors furthermore is likely to influence not only the mean vertical forces of the wings but also lead to fluctuations. The frequency spectra resulting from an FFT of the load difference induced by the lateral rotors with and without main rotor is illustrated in Fig. 6.22 for the left lower wing. The rotating pressure field around the lateral rotor blades clearly provokes load fluctuations at lateral rotor BPF on the upstream positioned wing. With the additional influence of the main rotor downwash, these fluctuations are further increased, whereas the occurrence of low-frequency fluctuations is the result of the lateral rotor's interaction with the separated flow below the wings.

While the induced fluctuations in Fig. 6.22 appear to be relatively large with up to 30 %, this is an effect of the normalization with the full setup's average download of the left lower wing. As explained in Section 6.1, the shielding by the upper wings significantly reduces the lower wings' download. Consequently, the fluctuations' amplitude is not to be considered critical.

6.7 Conclusions

Based on detailed, trimmed CFD simulations of Airbus Helicopters' compound helicopter RACER in hover and the comparison hereof with results from reduced configurations individually omitting main rotor, wings, and lateral rotors, mutual first- and second-order effects of these components were investigated within this chapter in order to improve the fundamental understanding of these interactions and their influence on the respective aerodynamic performance. From the results presented, the following conclusions are drawn:

1. On the upper wings, the main rotor generates significant download, whereas the lower wings benefit from the box wing concept and are extensively shaded from the main rotor downwash. Second-order effects in the presence of the lateral rotors lead to large variations of vertical force in the latters' vicinity and overall to the generation of additional download on wide regions of all wings' bottom sides.

2. Reversely, the blockage effect of the wings in the downwash causes a decrease in vertical velocity up to the main rotor. This becomes manifest in an increased effective angle of attack on the passing main rotor blades and consequently a thrust gain over the wing tips, while the resulting widening of the downwash streamtube with its change in tip vortex convection causes a decrease in thrust close to the blade tips.

3. The first-order influence of the main rotor increases thrust on left and right lateral rotor by 11 % and 26 %, respectively, due to a combination of changes

in tangential and axial inflow. However, as the wings have a significant second-order effect in deflecting the main rotor downwash in the left lateral rotor's inflow, this accumulates to an overall thrust decrease of 7 % on this rotor caused by the main rotor. On the right lateral rotor, in contrast, no such indirect influence arises due to the upstream placement of the reversely operating lateral rotor in relation to the wings.

4. Despite the lack of influence on global main rotor thrust, the lateral rotors induce a distinctive change in main rotor thrust distribution. The suction upstream of both lateral rotors causes a decrease in effective angle of attack in the superjacent regions of the main rotor disk, whereas the blockage effect of the lateral rotor wakes conversely leads to a thrust gain on the main rotor blades passing above.

5. The thrust-augmenting first-order effect of the wings on the left lateral rotor shows similar characteristics to the influence on axial and tangential inflow witnessed in cruise flight, yet on a much smaller level with an increase of 4 %. In the main rotor's presence, however, this is largely reversed into a reduction of the left lateral rotor's effective angle of attack and a decrease of total thrust by 13 % due to the wings. No notable influence of the latter is visible on the right lateral rotor generating reverse thrust.

6. While the lateral rotors' first-order influence induces lift in the wings' regions directly upstream or downstream, respectively, in conjunction with the main rotor downwash their effect extends over the whole wingspan and widely leads to the generation of download. In general, the suction of the left lateral rotor has a more homogeneous effect on the adjacent wings than the blowing of the right lateral rotor.

7 Conclusions and Outlook

In the present thesis, aerodynamic interactions on Airbus Helicopter's compound helicopter RACER were investigated regarding its main aerodynamic components, namely main rotor, wings, and lateral rotors. The necessity for this has arisen with recent years' quest to extend helicopters' operation envelopes towards higher flight velocities by developing novel configurations. The eponymous concepts' underlying mechanisms of thrust and lift compounding have resulted in miscellaneous combinations of rotors and wings, the individual aerodynamic performance of which is highly influenced by mutual interactions. Consequently, the aerodynamics of such a concept's complete system in particular cannot be treated as the sum of its (isolated) parts but requires factoring in the interactional phenomena during various stages of development and operation.

Previous studies on rotor-rotor and rotor-wing interactions on various aircraft have given a broad impression of potential mutual effects but could hardly be directly transferred to RACER's specific combination of main rotor, box wing, and lateral rotors in pusher configuration. For this reason, dedicated analyses were carried out in the course of this work for this particular compound helicopter demonstrator by conducting high-fidelity CFD simulations with the flow solver FLOWer for flight conditions of interest. These were not only based on a highly detailed geometry of RACER, including rotating, discrete main and lateral rotors with elastic blades for the former, engine boundary conditions for exhaust and cooling flows, and deflected flaps on wings and stabilizers, but also on realistic, trimmed flight states. For this purpose, in a prior step FLOWer was loosely coupled to the CA tool HOST, with both of which alternately exchanging flight conditions and main rotor deformation, or aerodynamic loads, respectively, until a converged trim state was reached.

In order to isolate the mutual influence of main rotor, wings, and lateral rotors, CFD simulations of the trimmed flight conditions of interest were not only conducted on the full RACER configuration, but also on reduced setups individually lacking the respective components. Hence, the influence of one component onto another could be determined by comparing the latter's performance in the presence and absence of the former. Repeating this approach while additionally omitting the third protagonist and juxtaposing the resulting direct and cumulative effects furthermore allowed for the discrimination between first- and second-order interactions.

With the operation envelope's extension towards higher flight velocities essentially being the motivation behind the configuration's development, the first flight condition examined in the scope of this thesis was RACER's cruise flight at 220 kts. Based on URANS simulations, a general asymmetry in interactional effects related

to the main rotor was found, with stronger influences originating from and affecting its highly loaded advancing side. The retreating blades, in contrast, are hardly susceptible to any influences and mostly induce load fluctuations on subjacent wings and lateral rotor rather than changes in total lift and thrust, respectively, due to their significantly reduced dynamic pressure and extensive region of reverse inflow at an advance ratio exceeding 0.5.

As another overall trend in cruise flight, first-order effects were found to be largely dominating aerodynamic interactions. With the exception of the main rotor's influence on lateral rotor performance which is changed from thrust-increasing to thrust-reducing by the presence of the wings, second-order interactions proved to play only a minor role by slightly amplifying or damping the direct effects.

Regarding the individual mutual effects, the main rotor's advancing side was observed to significantly reduce lift on the left-hand wings by deflecting their inflow despite the lack of any convective impingement of the downwash. Conversely, the wings' circulation induces an upward deflection ahead of them and vice versa behind them, which leads to an increase or decrease, respectively, of effective angle of attack and consequently thrust in the superjacent regions of the main rotor disk's advancing side. In total, this results in a thrust decrease.

While the main rotor was witnessed to induce a tangential flow in the upper region of the left-hand lateral rotor, co-rotating with the latter's blades and thereby reducing their thrust, the—stronger—opposite first-order effect in the inboard region is prevented by the second-order rectifying influence of the wings, which inverts the overall thrust change into a decrease. Vice versa, a lateral rotor–induced reduction of thrust in a region on the main rotor's advancing side was traced back to the subjacent contracting streamtube of the former and the associated deflection of the flow around it, resulting in a decrease of effective angle of attack on the latter. The blockage effect of the lateral rotor wakes, however, with its lift-increasing influence on superjacent main rotor blades is not strong enough to compensate for this.

Arguably the strongest interactional effects were visible in the wings' influence on lateral rotor performance. Due to the upstream position of the wings, their wakes directly convect through the lateral rotors, where the associated velocity deficit causes an increase of effective angle of attack. This angle, however, experiences an even larger change by the tangential velocity component of the wing tip vortex from which the lateral rotors highly benefit owing to their inboard-up sense of rotation. The substantial thrust increase originating from these two mechanisms is only slightly reduced on the left lateral rotor via a second-order influence caused by the main rotor's asymmetrical reduction of wing lift. Independent of their sense of rotation, the lateral rotors induce a lift gain over the full span of the lower wings, whereas the upper wings remain unaffected as a result of RACER's specifically swept box wing design.

The latter was also found to play an important role in the second flight state examined in the course of this work. With its position in RACER's flight envelope being antipodal to the cruise flight, hover was selected for further analyses on aerodynamic interactions as the underlying phenomena were expected to be of very different nature than the previously observed effects. Furthermore, VTOL remains a key feature of the compound helicopter configuration and therefore requires a thorough assessment of its aerodynamic performance and the possible influence of interactions hereupon. In order to account for the expected flow separation resulting from the downwash's impingement onto the wings and its effect on aerodynamic interactions, DDES simulations were conducted for the analysis of the hover condition.

While the interactional phenomena showed distinct asymmetries similar to cruise flight, this was found to originate not from an asymmetric main rotor loading but from the different operating conditions of the lateral rotors, where the right-hand rotor provides anti-torque by delivering reverse thrust. Consequently, the interactions that have this rotor as their source or target generally have a different characteristic than their left-hand counterparts.

In contrast to the analysis of cruise flight, second-order interactions proved to play a more important role in hover. With the reason for this being the mainly convective nature of interactional phenomena, it clearly becomes manifest in notable differences between first-order and cumulative influences for all interactions except the ones affecting the main rotor.

On the upper wings, the main rotor generates significant download, whereas the lower wings highly benefit from the box wing concept as they are largely shaded from the impinging downwash. Furthermore, second-order effects in the lateral rotors' presence not only lead to strong variations of vertical forces directly upstream or downstream of them but also to additional download in the regions of separated flow on the wings' bottom side. Even as no second-order interactions were observed vice versa, the wings' blockage effect of the downwash decreases vertical velocity up to the main rotor disk and consequently induces a thrust increase in the respective superjacent regions, while the associated widening of the streamtube and consequently different convection of the tip vortices results in a decrease of thrust close to the blade tips.

As a result of the main rotor's influence on axial and tangential velocity components in the lateral rotors' inflow, a positive first-order effect on the latter's thrust was observed. With the additional presence of the wings, however, and the strong second-order effects arising from this, the cumulative effect on left lateral rotor thrust is reversed into a loss, the origin of which is twofold: Not only is the downwash prevented from inducing a beneficial tangential velocity component on the upstroking blades but its deflection by the wings also results in a detrimental axial velocity component of the inflow. In contrast, no such influence was witnessed to emanate

from the—downstream-positioned—right-hand wings. In the lateral rotors' effect on main rotor thrust, conversely, phenomena similar to cruise flight were visible, with a detrimental and beneficial influence, respectively, originating from the upstream suction of the lateral rotors and the blockage effect of their wakes. Owing to the hover's relatively symmetric thrust generation of the main rotor, however, this also becomes manifest in the rotor disk regions above the—reversely-operating—right lateral rotor.

In absence of the main rotor, the suction of the left lateral rotor slightly induces lift on the upstream regions of the wings, which, in turn, leads to an—albeit small—gain of lateral rotor thrust due to effects similar to cruise flight. With the addition of the main rotor downwash, though, its aforementioned deflection reverses this into a notable wing-induced decrease of left lateral rotor thrust, whereas, vice versa, the latter cumulatively also causes additional download over the full span of the left upper wing. Interactions between right-hand wings and lateral rotor significantly differ from this as a result of the rotor's generation of reverse thrust. While hardly any wing-induced upstream effect could be witnessed on right lateral rotor thrust, the blowing of the adjacent outer wing region results in strong spanwise variations of download, particularly in combination with second-order effects via main rotor downwash.

Overall, the present study demonstrated a significant occurrence of interactional effects between RACER's main rotor, wings, and lateral rotors and a clear influence hereof on their individual aerodynamic behaviour, consequently affecting the performance of the complete configuration. The respective nature of these phenomena was shown to be oftentimes a combination of first- and second-order interactions. While the analysis of the antipodal flight conditions of hover and cruise flight should allow for the assessment of large ranges of the operation envelope as a combination of the present results, future studies on additional flight states could not only support this assumption but also investigate the influence of different trim laws and account for interactional phenomena very specific for a particular operation point. The low-speed horizontal flight with its impingement of main rotor blade tip vortices onto wings and lateral rotors would, for example, be well-suited in this regard.

Furthermore, additional studies on similar, yet not identical, compound helicopter configurations would complement the present thesis. Based on an equally detailed, but generic, design and comparable high-fidelity, trimmed CFD analyses, this would also allow for the assessment of a broader range of performance characteristics, like for example FOM or efficiency of the rotors, or drag and L/D of the wings. This was not possible in the present study due to the proprietary nature of the RACER design. Finally, these analyses could provide more insight into the transferability of the present results and support this work's effort of developing a fundamental understanding of aerodynamic interactions.

References

[1] Frain, I., "The King of Heavy Lift—The Sikorsky CH-53K King Stallion," *Vertiflite*, Vol. 64, (4), July 2018, pp. 18–21.

[2] Leishman, J. G., *Principles of Helicopter Aerodynamics*, Cambridge University Press, New York, New York, second edition, 2006. DOI: 10.1017/S0001924000087352

[3] Gudmundsson, S., *General Aviation Aircraft Design: Applied Methods and Procedures*, Butterworth-Heinemann, Boston, Massachusetts, first edition, 2012.

[4] Blacha, M., Fink, A., Eglin, P., and Cabrit, P., "Clean Sky 2: Exploring New Rotorcraft High Speed Configurations," 43rd European Rotorcraft Forum, Milan, Italy, September 2017.

[5] Huot, R., and Eglin, P., "Flight Mechanics of the RACER Compound H/C," Vertical Flight Society 76th Annual Forum, October 2020.

[6] Ormiston, R., "Revitalizing Advanced Rotorcraft Research—and the Compound Helicopter," *Journal of the American Helicopter Society*, Vol. 61, (1), January 2016, pp. 1–23. DOI: 10.4050/jahs.61.011001

[7] Quackenbush, T., Wachspress, D., Yu, M., and Solomon, C., "Modeling of Proprotor/Wing/Flap Interaction for Advanced Vertical Lift Aircraft," Vertical Flight Society 76th Annual Forum, October 2020.

[8] Keller, J., McKillip, Jr., R., Wachspress, D., Lopez, M., Tischler, M., and Juhasz, O., "Linearized Inflow and Interference Models from High Fidelity Free Wake Analysis for Modern Rotorcraft Configurations," Vertical Flight Society 76th Annual Forum, October 2020.

[9] Frain, I., "Paris Airshow Celebrates its 50th," *Vertiflite*, Vol. 59, (5), September 2013, pp. 24–25.

[10] Orchard, M., and Newman, S., "The Fundamental Configuration and Design of the Compound Helicopter," *Journal of Aerospace Engineering*, Vol. 217, (6), June 2003, pp. 297–315. DOI: 10.1243/095441003772538570

[11] Ferguson, K., and Thomson, D., "A Performance Analysis of Compound Helicopter Configurations," American Helicopter Society 70th Annual Forum, Montréal, Canada, May 2014.

[12] Rand, O., and Khromov, V., "Compound Helicopter: Insight and Optimization," *Journal of the American Helicopter Society*, Vol. 60, (1), January 2015, pp. 1–12. DOI: 10.4050/jahs.60.012001

[13] Ferguson, K., and Thomson, D., "Maneuverability Assessment of a Compound Helicopter Configuration," *Journal of the American Helicopter Society*, Vol. 61, (1), January 2016, pp. 1–15. DOI: 10.4050/jahs.61.012008

[14] Reddinger, J.-P., Gandhi, F., and Kang, H., "Using Control Redundancy for Power and Vibration Reduction on a Compound Helicopter at High Speeds," *Journal of the American Helicopter Society*, Vol. 63, (3), July 2018, pp. 1–13. DOI: 10.4050/JAHS.63.032009

[15] Bowen-Davies, G., and Yeo, H., "Performance and Loads Study of a High-Speed Compound Helicopter," *Journal of the American Helicopter Society*, Vol. 63, (3), July 2018, pp. 1–15. DOI: 10.4050/JAHS.63.032004

[16] Lienard, C., Salah el Din, I., Renaud, T., and Fukari, R., "RACER High-Speed Demonstrator: Rotor and Rotor-Head Wake Interactions with Tail Unit," American Helicopter Society 74th Annual Forum, Phoenix, Arizona, May 2018.

[17] Salah el Din, I., Lienard, C., Huot, R., and Fukari, R., "RACER High-Speed Demonstrator: Tail Unit Vertical Fin Aerodynamic Design," American Helicopter Society 74th Annual Forum, Phoenix, Arizona, May 2018.

[18] Pölzlbauer, P., Desvigne, D., and Breitsamter, C., "Aerodynamic design optimization of a helicopter rotor blade-sleeve fairing," *CEAS Aeronautical Journal*, Vol. 10, (3), September 2019, pp. 665–685. DOI: 10.1007/s13272-018-0341-0

[19] Blacha, M., Garcia-Rios, A., and Schelcher, M., "The Challenges for the Integration of the Drive Shaft in the RACER's Wing Configuration," Vertical Flight Society 75th Annual Forum, Philadelphia, Pennsylvania, May 2019.

[20] Thiemeier, J., *Trim Condition Impact on Efficiency and Flight Mechanics of a Compound Helicopter in Cruise Flight*, Ph.D. thesis, Universität Stuttgart, 2005.

[21] Öhrle, C., Frey, F., Thiemeier, J., Keßler, M., and Krämer, E., "Coupled and Trimmed Aerodynamic and Aeroacoustic Simulations for Airbus Helicopters' Compound Helicopter RACER," *Journal of the American Helicopter Society*, Vol. 64, (3), July 2019, pp. 1–14. DOI: 10.4050/jahs.64.032003

[22] Thiemeier, J., Öhrle, C., Frey, F., Keßler, M., and Krämer, E., "Aerodynamic and Flight Mechanics Analysis of Airbus Helicopters' Compound Helicopter RACER in Hover under Crosswind Conditions," *CEAS Aeronautical Journal*, Vol. 11, (1), January 2020, pp. 49–66. DOI: 10.1007/s13272-019-00392-3

[23] Öhrle, C., Frey, F., Thiemeier, J., Keßler, M., Krämer, E., Embacher, M., Cranga, P., and Eglin, P., "Compound Helicopter X^3 in High-Speed Flight: Correlation of Simulation and Flight Test," *Journal of the American Helicopter Society*, Vol. 66, (1), January 2021, pp. 1–14. DOI: 10.4050/jahs.66.012011

[24] Wilke, G., "Variable Fidelity Optimization of Required Power of Rotor Blades: Investigation of Aerodynamic Models and their Application," 38th European Rotorcraft Forum, Amsterdam, Netherlands, September 2012.

[25] Yin, J., and Ahmed, S., "Helicopter Main-Rotor/Tail-Rotor Interaction," *Journal of the American Helicopter Society*, Vol. 45, (4), October 2000, pp. 293–302. DOI: 10.4050/JAHS.45.293

[26] Visingardi, A., Dummel, A., Falchero, D., Pidd, M., Voutsinas, S., and Yin, J., "Aerodynamic interference in full helicopter configurations: Validation using the HeliNOVI database," 32nd European Rotorcraft Forum, Maastricht, Netherlands, September 2006.

[27] Fletcher, T. M., Duraisamy, K., and Brown, R. E., "Aeroacoustic analysis of main rotor–tail rotor interaction," 34th European Rotorcraft Forum, Liverpool, United Kingdom, September 2008.

[28] Jude, D., Jung, Y., Lee, B., and Baeder, J. D., "Challenges and Improvements to Interactional Aerodynamic Analysis using Overset Methods on Modern Computer Architectures," Overset Grid Symposium, College Park, Maryland, October 2018.

[29] Dingeldein, R., "Wind-Tunnel Studies of the Performance of Multirotor Configurations," NACA Technical Note 3236, National Advisory Committee for Aeronautics, Langley Aeronautical Laboratory, Langley Field, Virginia, August 1954.

[30] Ramasamy, M., "Hover Performance Measurements Toward Understanding Aerodynamic Interference in Coaxial, Tandem, and Tilt Rotors," *Journal of the American Helicopter Society*, Vol. 60, (3), July 2015, pp. 1–17. DOI: 10.4050/jahs.60.032005

[31] Klimchenko, V., Sridharan, A., and Baeder, J. D., "CFD/CSD Study of the Aerodynamic Interactions of a Coaxial Rotor in High-Speed Forward Flight,"

35th AIAA Applied Aerodynamics Conference, Denver, Colorado, June 2017. DOI: 10.2514/6.2017-4454

[32] Sharma, K., Brentner, K. S., Jia, Z., Lee, S., and Anusonti-Inthra, P., "Aeroacoustic Predictions of the Free-Wake Model, Vortex Particle Method, and Computational Fluid Dynamics for a Coaxial Rotor System," Vertical Flight Society Technical Conference on Aeromechanics Design for Transformative Vertical Flight, San Jose, California, January 2020.

[33] Juhasz, O., Xin, H., and Tischler, M., "Inflow Based Flight Dynamics Modeling Improvements for the Sikorsky X2 Technology Demonstrator," Vertical Flight Society 76th Annual Forum, October 2020.

[34] Lee, J., Oh, S., Yee, K., and Kim, D.-K., "Numerical Investigation on Overlap Effects of Tandem Rotors in Forward Flight," *International Journal of Aeronautical and Space Sciences*, Vol. 10, (2), November 2009, pp. 63–76. DOI: 10.5139/ijass.2009.10.2.063

[35] Healy, R., Gandhi, F., Mistry, M., and Duffy, M., "A Computational Investigation of Multi-Rotor Interactional Aerodynamics with Hub Lateral and Longitudinal Canting," Vertical Flight Society 76th Annual Forum, October 2020.

[36] Guner, F., Miller, D., and Prasad, J., "Understanding the Effect of Rotor-to-Rotor Interference on CH-47D Helicopter Dynamics," Vertical Flight Society 76th Annual Forum, October 2020.

[37] Stokkermans, T., Usai, D., Sinnige, T., and Veldhuis, L., "Aerodynamic Interaction Effects between Propellers in Typical eVTOL Vehicle Configurations," *Journal of Aircraft*, Vol. 58, (4), July 2021, pp. 1–19. DOI: 10.2514/1.C035814

[38] Zhou, W., Ning, Z., Li, H., and Hu, H., "An Experimental Investigation on Rotor-to-Rotor Interactions of Small UAV Propellers," 35th AIAA Applied Aerodynamics Conference, Denver, Colorado, June 2017. DOI: 10.2514/6.2017-3744

[39] Droandi, G., Syal, M., and Bower, G., "Tiltwing Multi-Rotor Aerodynamic Modeling in Hover, Transition and Cruise Flight Conditions," American Helicopter Society 74th Annual Forum, Phoenix, Arizona, May 2018.

[40] Ventura Diaz, P., Johnson, W., Ahmad, J., and Yoon, S., "The Side-by-Side Urban Air Taxi Concept," AIAA Aviation Forum, Dallas, Texas, June 2019. DOI: 10.2514/6.2019-2828

[41] Alvarez, E., Schenk, A., Critchfield, T., and Ning, A., "Rotor-on-Rotor Aeroacoustic Interactions of Multirotor in Hover," Vertical Flight Society 76th Annual Forum, October 2020.

[42] Bain, L. J., and Landgrebe, A. J., "Investigation of Compound Helicopter Aerodynamic Interference Effects," Technical Report 67-44, U.S. Army Aviation Material Laboratories, Fort Eustis, Virginia, November 1967.

[43] Wentrup, M., Yin, J., Kunze, P., Streit, T., Wendisch, J.-H., Schwarz, T., Pinacho, J.-P., Kicker, K., and Fukari, R., "An Overview of DLR Compound Rotorcraft Aerodynamics and Aeroacoustics Activities within the CleanSky2 NACOR Project," American Helicopter Society 74th Annual Forum, Phoenix, Arizona, May 2018.

[44] Boisard, R., "Aerodynamic Investigation of Rotor/Propeller Interactions on a Fast Rotorcraft," 44th European Rotorcraft Forum, Delft, Netherlands, September 2018.

[45] Decours, J., Bailly, J., Ortun, B., Canard-Caruana, S., Delrieux, Y., Fukari, R., and Guntzer, F., "RACER Aero-Acoustic Propeller Analysis and Design," Vertical Flight Society 75th Annual Forum, Philadelphia, Pennsylvania, May 2019.

[46] Yin, J., Schwarz, T., Wentrup, M., and Guntzer, F., "DLR Analysis on the Noise Emission from the RACER Configuration," 45th European Rotorcraft Forum, Warsaw, Poland, September 2019.

[47] Stokkermans, T., Veldhuis, L., Soemarwoto, B., Fukari, R., and Eglin, P., "Breakdown of aerodynamic interactions for the lateral rotors on a compound helicopter," *Aerospace Science and Technology*, Vol. 101, June 2020, pp. 1–11. DOI: 10.1016/j.ast.2020.105845

[48] Stokkermans, T., *Aerodynamics of Propellers in Interaction Dominated Flowfields*, Ph.D. thesis, Delft University of Technology, 2020.

[49] Miranda, L., and Brennan, J., "Aerodynamic effects of wingtip-mounted propellers and turbines," 4th Applied Aerodynamics Conference, San Diego, California, June 1986. DOI: 10.2514/6.1986-1802

[50] Patterson, Jr., J. C., and Bartlett, G. R., "Evaluation of Installed Performance of a Wing-Tip-Mounted Pusher Turboprop on a Semispan Wing," NASA Technical Paper 2739, National Aeronautics and Space Administration, Scientific and Technical Information Office, Hampton, Virginia, August 1987.

[51] Janus, J., Chatterjee, A., and Cave, C., "Computational Analysis of a Wingtip-Mounted Pusher Turboprop," *Journal of Aircraft*, Vol. 33, (2), March 1996, pp. 441–444. DOI: 10.2514/3.46959

[52] Veldhuis, L., *Propeller Wing Aerodynamic Interference*, Ph.D. thesis, Delft University of Technology, 2005.

[53] Stokkermans, T., Nootebos, S., and Veldhuis, L., "Analysis and Design of a Small-Scale Wingtip-Mounted Pusher Propeller," AIAA Aviation Forum, Dallas, Texas, June 2019. DOI: 10.2514/6.2019-3693

[54] Schollenberger, M., Lutz, T., and Krämer, E., "Position Dependency Between the Aerodynamic Interactions of Wingtip-Mounted Propellers and the Wing-Vortex-System," Aerospace Europe Conference, Bordeaux, France, February 2020.

[55] Jayasundara, D., Jung, Y., and Baeder, J. D., "CFD and Aeroacoustic Analysis of Wingtip-Mounted Propellers," Vertical Flight Society 76th Annual Forum, October 2020.

[56] Felker, F., and Light, J., "Aerodynamic Interactions Between a Rotor and Wing in Hover," *Journal of the American Helicopter Society*, Vol. 33, (2), April 1988, pp. 53–61. DOI: 10.4050/jahs.33.53

[57] Lim, J. W., "Fundamental Investigation of Proprotor and Wing Interactions in Tiltrotor Aircraft," Vertical Flight Society 75th Annual Forum, Philadelphia, Pennsylvania, May 2019.

[58] Tran, S., Lim, J. W., Nunez, G., Wissink, A., and Bowen-Davies, G., "CFD Calculations of the XV-15 Tiltrotor During Transition," Vertical Flight Society 75th Annual Forum, Philadelphia, Pennsylvania, May 2019.

[59] Tran, S., and Lim, J. W., "Investigation of the Interactional Aerodynamics of the XV-15 Tiltrotor Aircraft," Vertical Flight Society 76th Annual Forum, October 2020.

[60] Lynn, R., "Rotor-Wing Interactions," *Journal of Aircraft*, Vol. 3, (4), July 1966, pp. 326–332. DOI: 10.2514/3.43742

[61] Tanabe, Y., and Sugawara, H., "Numerical Simulation of Aerodynamic Interaction Between a Rotor and a Wing," 5th Asian/Australian Rotorcraft Forum, Singapore, November 2016.

[62] Sugawara, H., and Tanabe, Y., "A Study of Rotor/Wing Aerodynamic Interaction at High Speed Flight on a Compound Helicopter," 6th Asian/Australian Rotorcraft Forum, Kanazawa, Japan, November 2017.

[63] Tanabe, Y., Sugawara, H., Kobiki, N., Kobayashi, W., Hayashi, H., and Satou, R., "Experimental and Numerical Investigation of Interaction Between Rotor and Wing at High Advance Ratio," Vertical Flight Society 76th Annual Forum, October 2020.

[64] Brouwers, E., Fillman, M., and Deresz, R., "Advanced AH-64 Compound Wind Tunnel Testing Overview," Vertical Flight Society 75th Annual Forum, Philadelphia, Pennsylvania, May 2019.

[65] Yeo, H., "Design and aeromechanics investigation of compound helicopters," *Aerospace Science and Technology*, Vol. 88, May 2019, pp. 158–173. DOI: 10.1016/j.ast.2019.03.010

[66] Schäferlein (né Kowarsch), U., Keßler, M., and Krämer, E., "Aeroelastic Simulation of the Tail Shake Phenomenon," *Journal of the American Helicopter Society*, Vol. 63, (3), July 2018, pp. 1–17. DOI: 10.4050/jahs.63.032003

[67] Altmikus, A. R. M., Wagner, S., Beaumier, P., and Servera, G., "A Comparison: Weak versus Strong Modular Coupling for Trimmed Aeroelastic Rotor Simulations," American Helicopter Society 58th Annual Forum, Montréal, Canada, June 2002.

[68] Potsdam, M., Yeo, H., and Johnson, W., "Rotor Airloads Prediction Using Loose Aerodynamic/Structural Coupling," *Journal of Aircraft*, Vol. 43, (3), May 2006, pp. 732–742. DOI: 10.2514/1.14006

[69] Wissink, A., Jude, D., Jayaraman, B., Roget, B., Lakshminarayan, V. K., Sitaraman, J., Bauer, A. C., Forsythe, J. R., and Trigg, R. D., "New Capabilities in CREATE-AV Helios Version 11," AIAA Scitech 2021 Forum, January 2021. DOI: 10.2514/6.2021-0235

[70] Pulliam, T. H., "High Order Accurate Finite-Difference Methods: as seen in OVERFLOW," 20th AIAA Computational Fluid Dynamics Conference, Honululu, Hawaii, June 2011. DOI: 10.2514/6.2011-3851

[71] Saberi, H., Khoshlahjeh, M., Ormiston, R. A., and Rutkowski, M. J., "Overview of RCAS and Application of Advanced Rotorcraft Problems," American Helicopter Society 4th Decennial Specialists' Conference on Aeromechanics, San Francisco, California, January 2004.

[72] Johnson, W., "Rotorcraft Aerodynamics Models for a Comprehensive Analysis," American Helicopter Society 54th Annual Forum, Washington, DC, May 1998.

[73] Anderson, W. K., and Bonhaus, D. L., "An Implicit Upwind Algorithm for Computing Turbulent Flows on Unstructured Grids," *Computers & Fluids*, Vol. 23, (1), January 1994, pp. 1–21. DOI: 10.1016/0045-7930(94)90023-X

[74] Tanabe, Y., Saito, S., and Sugawara, H., "Construction and Validation of an Analysis Tool Chain for Rotorcraft Active Noise Reduction," 38th European Rotorcraft Forum, Amsterdam, Netherlands, September 2012.

[75] Celi, R., "HeliUM 2 Flight Dynamic Simulation Model: Development, Technical Concepts, and Applications," American Helicopter Society 71st Annual Forum, Virginia Beach, Virginia, May 2015.

[76] Leishman, J. G., Bhagwat, M. J., and Bagai, A., "Free-Vortex Filament Methods for the Analysis of Helicopter Rotor Wakes," *Journal of Aircraft*, Vol. 39, (5), September 2002, pp. 759–775. DOI: 10.2514/2.3022

[77] Bhagwat, M. J., Ormiston, R. A., Saberi, H. A., and Xin, H., "Application of Computational Fluid Dynamics/Computational Structural Dynamics Coupling for Analysis of Rotorcraft Airloads and Blade Loads in Maneuvering Flight," *Journal of the American Helicopter Society*, Vol. 57, (3), July 2012, pp. 1–21. DOI: 10.4050/JAHS.57.032007

[78] Benoit, B., Dequin, A.-M., Kampa, K., Grünhagen, W. v., Basset, P.-M., and Gimonet, B., "HOST, a General Helicopter Simulation Tool for Germany and France," American Helicopter Society 56th Annual Forum, Virginia Beach, Virginia, May 2000.

[79] Kroll, N., Eisfeld, B., and Bleeke, H. M., "The Navier–Stokes Code FLOWer," *Notes on Numerical Fluid Mechanics*, Vol. 26, (11), 1999, pp. 58–71.

[80] Boniface, J. C., *Calcul d'écoulements compressibles autour de rotors d'hélicoptéres en vol stationnaire ou en vol d'avancement par résolution des équations d'Euler*, Ph.D. thesis, École Nationale Supérieure d'Arts et Métiers, Paris, France, 1995.

[81] Dietz, M., Khier, W., Knutzen, B., Wagner, S., and Krämer, E., "Numerical Simulation of a Full Helicopter Configuration Using Weak Fluid-Structure Coupling," 46th AIAA Aerospace Sciences Meeting and Exhibit, Reno, Nevada, January 2008. DOI: 10.2514/6.2008-401

[82] Embacher, M., Keßler, M., Dietz, M., and Krämer, E., "Coupled CFD-Simulation of a Helicopter in Free-Flight Trim," American Helicopter Society 66th Annual Forum, Phoenix, Arizona, May 2010.

[83] Beaumier, P., Costes, M., Rodriguez, B., Poinot, M., and Cantaloube, B., "Weak and Strong Coupling Between the elsA CFD Solver and the HOST Helicopter Comprehensive Analysis," 31st European Rotorcraft Forum, Florence, Italy, September 2005.

[84] Cambier, L., and Gazaix, M., "elsA—An Efficient Object-Oriented Solution to CFD Complexity," 40th AIAA Aerospace Sciences Meeting and Exhibit, Reno, Nevada, January 2002. DOI: 10.2514/6.2002-108

[85] Pahlke, K., and van der Wall, B. G., "Chimera Simulations of Multibladed Rotors in High-Speed Forward Flight with Weak Fluid-Structure-Coupling," *Aerospace Science and Technology*, Vol. 9, (5), July 2005, pp. 379–389. DOI: 10.1016/j.ast.2005.03.003

[86] Pahlke, K., and van der Wall, B. G., "Progress in Weak Fluid-Structure-Coupling for Multibladed Rotors in High-Speed Forward Flight," 28th European Rotorcraft Forum, Bristol, UK, September 2002.

[87] Smith, M. J., Lim, J. W., van der Wall, B. G., Baeder, J. D., Biedron, R. T., Boyd, Jr., D. D., Jayaraman, B., Jung, S. N., and Min, B.-Y., "The HART II International Workshop: An Assessment of the State of the Art in CFD/CSD Prediction," *CEAS Aeronautical Journal*, Vol. 4, (4), December 2013, pp. 345–372. DOI: 10.1007/s13272-013-0078-8

[88] Meijer Drees, J., "A Theory of Airflow Through Rotors and its Application to Some Helicopter Problems," *Journal of the Helicopter Association of Great Britain*, Vol. 3, (2), July 1949, pp. 79–104.

[89] Embacher, M., Keßler, M., Dietz, M., and Krämer, E., "Capability of Helicopter CFD-Simulation Trimmed to Free Flight Condition to Predict Flight Test Data," 37th European Rotorcraft Forum, Gallarate, Italy, September 2011.

[90] Raddatz, J., and Fassbender, J. K., "Block Structured Navier–Stokes Solver FLOWer," *MEGAFLOW—Numerical Flow Simulation for Aircraft Design*, edited by N. Kroll and J. K. Fassbender, Springer Berlin Heidelberg, Berlin/Heidelberg, Germany, April 2005, pp. 27–44. DOI: 10.1007/3-540-32382-1_2

[91] Blazek, J., *Computational Fluid Dynamics—Principles and Applications*, Butterworth-Heinemann, Oxford, UK, third edition, 2015. DOI: 10.1016/C2013-0-19038-1

[92] Spalart, P. R., and Allmaras, S. R., "A One-Equation Turbulence Model for Aerodynamic Flows," 30th AIAA Aerospace Sciences Meeting and Exhibit, Reno, Nevada, January 1992. DOI: 10.2514/6.1992-439

[93] Wilcox, D. C., "Multiscale Model for Turbulent Flows," *AIAA Journal*, Vol. 26, (11), November 1988, pp. 1311–1320. DOI: 10.2514/3.10042

[94] Menter, F. R., "Two-Equation Eddy-Viscosity Turbulence Models for Engineering Applications," *AIAA Journal*, Vol. 32, (8), August 1994, pp. 1598–1605. DOI: 10.2514/3.12149

[95] Jameson, A., Schmidt, W., and Turkel, E., "Numerical Solution of the Euler Equations by Finite Volume Methods Using Runge Kutta Time Stepping Schemes," 14th AIAA Fluid and Plasma Dynamics Conference, Palo Alto, California, June 1981. DOI: 10.2514/6.1981-1259

[96] Borges, R., Carmona, M., Costa, B., and Don, W. S., "An Improved Weighted Essentially Non-Oscillatory Scheme for Hyperbolic Conservation Laws," *Journal of Computational Physics*, Vol. 227, (6), March 2008, pp. 3191–3211. DOI: 10.1016/j.jcp.2007.11.038

[97] Kowarsch, U., Öhrle, C., Hollands, M., Keßler, M., and Krämer, E., "Computation of Helicopter Phenomena Using a Higher Order Method," *High Performance Computing in Science and Engineering '13: Transactions of the High Performance Computing Center, Stuttgart (HLRS) 2013*, edited by W. E. Nagel, D. H. Kröner, and M. Resch, Springer International Publishing, Cham, Switzerland, January 2014, pp. 423–438. DOI: 10.1007/978-3-319-02165-2_29

[98] Jameson, A., "Time Dependent Calculations Using Multigrid, with Applications to Unsteady Flows Past Airfoils and Wings," 10th AIAA Computational Fluid Dynamics Conference, Honululu, Hawaii, June 1991. DOI: 10.2514/6.1991-1596

[99] Weihing, P., Letzgus, J., Bangga, G., Lutz, T., and Krämer, E., "Hybrid RANS/LES Capabilities of the Flow Solver FLOWer—Application to Flow around Wind Turbines," *Progress in Hybrid RANS-LES Modelling*, edited by Y. Hoarau, S.-H. Peng, D. Schwamborn, and A. Revell, Springer International Publishing, Cham, Switzerland, March 2018, pp. 369–380. DOI: 10.1007/978-3-319-70031-1_31

[100] Frey, F., Herb, J., Letzgus, J., Weihing, P., Keßler, M., and Krämer, E., "Enhancement and Application of the Flow Solver FLOWer," *High Performance Computing in Science and Engineering '18: Transactions of the High Performance Computing Center, Stuttgart (HLRS) 2018*, edited by W. E. Nagel,

D. H. Kröner, and M. Resch, Springer International Publishing, February 2019, pp. 323–336. DOI: 10.1007/978-3-030-13325-2

[101] Schuff, M., Kranzinger, P., Keßler, M., and Krämer, E., "Advanced CFD-CSD Coupling: Generalized, High Performance, Radial Basis Function Based Volume Mesh Deformation Algorithm for Structured, Unstructured and Overlapping Meshes," 40th European Rotorcraft Forum, Southampton, United Kingdom, September 2014.

[102] Kranzinger, P., Kowarsch, U., Schuff, M., Keßler, M., and Krämer, E., "Advances in Parallelization and High-Fidelity Simulation of Helicopter Phenomena," *High Performance Computing in Science and Engineering '15: Transactions of the High Performance Computing Center, Stuttgart (HLRS) 2015*, edited by W. E. Nagel, D. H. Kröner, and M. Resch, Springer International Publishing, Cham, Switzerland, February 2016, pp. 479–494. DOI: 10.1007/978-3-319-24633-8_31

[103] Frey, F., Thiemeier, J., Öhrle, C., Keßler, M., and Krämer, E., "Aerodynamic Interactions on Airbus Helicopters' Compound Helicopter RACER in Cruise Flight," *Journal of the American Helicopter Society*, Vol. 65, (4), October 2020, pp. 1–14. DOI: 10.4050/jahs.65.042001

[104] Le Chuiton, F., "Quasi-Steady Simulation of a Complete EC-145 Helicopter: Fuselage + Main / Tail Actuator Discs + Engines," 31st European Rotorcraft Forum, Florence, Italy, September 2005.

[105] Öhrle, C., Frey, F., Thiemeier, J., Keßler, M., Krämer, E., Embacher, M., Cranga, P., and Eglin, P., "Compound Helicopter X^3 in High-Speed Flight: Correlation of Simulation and Flight Test," Vertical Flight Society 75th Annual Forum, Philadelphia, Pennsylvania, May 2019.

[106] Frey, F., Thiemeier, J., Öhrle, C., Keßler, M., and Krämer, E., "Aerodynamic Interactions on Airbus Helicopters' Compound Helicopter RACER in Cruise Flight," Vertical Flight Society 75th Annual Forum, Philadelphia, Pennsylvania, May 2019.

[107] Öhrle, C., Schäferlein, U., Keßler, M., and Krämer, E., "Higher-order Simulations of a Compound Helicopter using Adaptive Mesh Refinement," American Helicopter Society 74th Annual Forum, Phoenix, Arizona, May 2018.

[108] Keßler, M., *Rotorcraft Flow Simulations—Technology and Results*, Habilitation thesis, Universität Stuttgart, 2019.

[109] Stanger, C., Kutz, B., Kowarsch, U., Busch, E. R., Keßler, M., and Krämer, E., "Enhancement and Applications of a Structural URANS Solver," *High Performance Computing in Science and Engineering '14: Transactions of the High Performance Computing Center, Stuttgart (HLRS) 2014*, edited by W. E. Nagel, D. H. Kröner, and M. Resch, Springer International Publishing, Cham, Switzerland, March 2015, pp. 433–446. DOI: 10.1007/978-3-319-10810-0_29

[110] Letzgus, J., Dürrwächter, L., Schäferlein, U., Keßler, M., and Krämer, E., "Optimization and HPC-Applications of the Flow Solver FLOWer," *High Performance Computing in Science and Engineering '17: Transactions of the High Performance Computing Center, Stuttgart (HLRS) 2017*, edited by W. E. Nagel, D. H. Kröner, and M. Resch, Springer International Publishing, Cham, Switzerland, February 2018, pp. 305–322. DOI: 10.1007/978-3-319-68394-2

[111] Frey, F., Thiemeier, J., Öhrle, C., Keßler, M., and Krämer, E., "Aerodynamic Interactions on Airbus Helicopters' Compound Helicopter RACER in Hover," *Journal of the American Helicopter Society*, Vol. 67, (1), January 2022, pp. 1–17. DOI: 10.4050/jahs.67.012007

[112] Letzgus, J., Gardner, A. D., Schwermer, T., Keßler, M., and Krämer, E., "Numerical Investigations of Dynamic Stall on a Rotor with Cyclic Pitch Control," *Journal of the American Helicopter Society*, Vol. 64, (1), January 2019, pp. 1–14. DOI: 10.4050/jahs.64.012007

[113] Frey, F., Öhrle, C., Thiemeier, J., Keßler, M., and Krämer, E., "Aerodynamic Interactions on Airbus Helicopters' Compound Helicopter RACER in Hover," Vertical Flight Society 76th Annual Forum, October 2020.

[114] Stokkermans, T., Voskuijl, M., Veldhuis, L., Soemarwoto, B., Fukari, R., and Eglin, P., "Aerodynamic Installation Effects of Lateral Rotors on a Novel Compound Helicopter Configuration," American Helicopter Society 74th Annual Forum, Phoenix, Arizona, May 2018.

[115] Moodie, A. M., and Yeo, H., "Design of a Cruise-Efficient Compound Helicopter," *Journal of the American Helicopter Society*, Vol. 57, (3), July 2012, pp. 1–11. DOI: 10.4050/jahs.57.032004